

**56th Scientific Conference for Young Students of Physics and Natural Sciences**

# **Open Readings 2013**

**March 20-23, 2013**

**Vilnius, LITHUANIA**

**Programme and Abstracts**

## **LOCAL ORGANIZING COMMITTEE**

*Students' Scientific Association, Faculty of Physics, Vilnius University, LITHUANIA:*

Vytautas Aukštikalnis

Jonas Beržins

Vytautas Butkus

Eglė Krikštopavičiūtė

Birutė Leiputė

Ugnė Nevedomskaitė

Vytenis Pranculis

Maria Razgutė

Greta Striokaite

Faculty of Physics  
Vilnius University  
Saulėtekio Ave. 9-III, LT-10222 Vilnius  
LITHUANIA

[www.ff.vu.lt](http://www.ff.vu.lt)  
[www.openreadings.eu](http://www.openreadings.eu)

# Contents

Conference programme.....	4
List of poster presentations .....	7
Oral session 1 .....	15
<i>Laser physics and optical technologies</i>	
Oral session 2 .....	20
<i>Semiconductor and condensed matter physics, material sciences</i>	
Oral session 3 .....	28
<i>Spectroscopy, methods and devices for physical diagnostics Functional materials and derivatives, modern technologies</i>	
Oral session 4 .....	34
<i>Chemistry and chemical physics</i>	
Oral session 5 .....	41
<i>Biophysics, medical and environmental physics</i>	
Oral session 6 .....	48
<i>Theoretical physics</i>	
Oral session 7 .....	55
<i>Astrophysics and astronomy Interdisciplinary</i>	
Poster session 1.....	62
Poster session 2.....	108
Poster session 3.....	161
Index.....	210

# Conference programme

20 March  
WEDNESDAY

13:00 CONFERENCE OPENING

INVITED LECTURE

13:10 **Donatas Zigmantas**, *Department of Chemical Physics, Lund University, Sweden*  
**TWO-DIMENSIONAL ELECTRONIC SPECTROSCOPY: WHAT CAN BE LEARNED ABOUT MOLECULES AND MOLECULAR COMPLEXES**

## ORAL SESSION O1

14:00 Eglė Kaziulionytė, Sima Rekšytė, Mangirdas Malinauskas 01-1 16  
**DIRECT LASER FABRICATION OF COMPOSITE MATERIAL 3D MICROSTRUCTURED SCAFFOLDS**

14:15 Tomas Jonavičius, Gabija Kiršanskė, Mangirdas Malinauskas 01-2 17  
**FABRICATION OF 3D METALLIC MICROSTRUCTURE VIA DIRECT LASER WRITING**

14:30 Kirilas Michailovas, Andrejus Michailovas, Valerijus Smilgevicius 01-3 18  
**HIGH AVERAGE POWER, HIGH REPETITION RATE PICOSECOND PULSES AMPLIFIER OUTPUT BEAM QUALITY OPTIMIZATION USING ADAPTIVE MIRROR**

14:45 Simas Butkus, Domas Paipulas, Valdas Sirutkaitis 01-4 19  
**FAST CUTTING AND DRILLING OF TRANSPARENT MATERIALS VIA FEMTOSECOND LASER FILAMENTATION**

15:00 Linas Jonušauskas, Mangirdas Malinauskas 01-5 20  
**FABRICATION AND CHARACTERIZATION OF MICROLENS ARRAYS FOR USAGE IN MULTIFOCUS DIRECT LASER WRITING**

15:30 – 18:00 POSTER SESSION P1

21 March  
THURSDAY

## ORAL SESSION O2

9:00 Steponas Raišys, Karolis Kazlauskas, Marytė Daškevičienė, Tadas Malinauskas, Vytautas Getautis, Saulius Juršėnas 02-1 22  
**INFLUENCE OF PHENYLETHENYL SIDE-MOETIES ON EXCITON DIFFUSION IN TRIPHENYLAMINE COMPOUNDS**

9:15 Akvilė Zabaliūtė 02-2 23  
**MESOPIC BIOLOGICALLY FRIENDLY LIGHT SOURCES BASED ON LIGHT CONVERSION IN PHOSPHORS**

9:30 Augustas Vaitkevičius 02-3 24  
**PHOTOLUMINESCENCE OF INGAN QUANTUM WELLS WITH DIFFERENT WELL PROFILE**

9:45 Mantas Dmukauskas, Arūnas Kadys 02-4 25  
**GROWTH OF DIFFERENT SPATIAL PROFILES InGaN/GaN QUANTUM WELLS BY MOCVD AND RESEARCH**

10:00 Eduardas Gvozdas, Irmantas Kašalynas, Gintaras Valušis 02-5 26  
**MAGNETOTRANSPORT PROPERTIES OF AlGaIn/GaN HETEROSTRUCTURES**

10:15 Armandas Balčytis, Rolandas Tomašiūnas, Raimondas Petruškevičius 02-6 27  
**MODELING OF TEMPERATURE DEPENDENCE OF ALL-OPTICAL POLING TRANSIENTS IN POLYMERS**

## ORAL SESSION O3

11:00 Mantas Ragauskas, Linas Minkevičius, Jonas Matukas, Gintaras Valušis 03-1 29  
**LOW FREQUENCY NOISE CHARACTERISATION OF BOW-TIE DIODES SENSORS FOR TERAHERTZ IMAGING**



11:15	Jelena Aleksejeva, Janis Teteris <b>HOLOGRAPHIC RECORDING IN AZO POLYMER FILMS</b>	03-2	30
11:30	Paulius Naujalis, Danielis Rutkauskas <b>SINGLE MOLECULE SPECTROSCOPY: DNA DETECTION</b>	03-3	31
11:45	Marta Lange, Inga Saknīte, Dainis Jakovels, Janis Spigulis. <b>DETERMINING THE AGE OF BRUISES DEPENDING ON THE BILIRUBIN CONCENTRATION USING SPECTRAL IMAGING</b>	03-4	32
12:00	Inga Saknīte, Valērijs Garancis, Liene Elste, Eriks Zaharans, Janis Zaharans, Oskars Rubenis, Edgars Kviesis, Janis Spigulis <b>MULTI-SPECTRAL IMAGING DEVICE FOR SKIN DIAGNOSTICS</b>	03-5	33
BREAK			
<b><u>ORAL SESSION 04</u></b>			
14:00	Rūta Stankevičiūtė, Artūras Žalga <b>AQUEOUS SOL-GEL SYNTHESIS METHOD: SUITABLE TECHNIQUE FOR THE PREPARATION OF DIFFERENT CERAMIC MATERIALS</b>	04-1	35
14:15	Natalia Boboriko <b>COMPARISON OF PHASE COMPOSITION OF TiO<sub>2</sub>-MoO<sub>3</sub> NANOCOMPOSITE SYSTEMS SYNTHESIZED BY DIFFERENT METHODS</b>	04-2	36
14:30	Ekaterina Kozlovskaya, George Pitsevich, Alex Malevich, Valdas Sablinskas, Vitas Balevicius <b>STUDY OF OH GROUP VIBRATIONS IN THE PYRIDINE -OXIDE/TRICHLOROACETIC ACID COMPLEX IN ACETONITRILE USING FTIR SPECTRA AND 1D AND 2D POTENTIAL SURFACES</b>	04-3	37
14:45	Paweł Tokarz, Jarosław Lewkowski, Anna Krzyczmonik, Katarzyna Ślepokura, Tadeusz Lis <b>STEREOSELECTIVITY OF REACTION BETWEEN SALICYLAMINES AND H- PHOSPHONATES</b>	04-4	38
15:00	Joana Gylytė, Asta Zubrienė, Daumantas Matulis <b>EVALUATION OF LINKED PROTONATION EFFECTS UPON INHIBITOR BINDING TO HUMAN CARBONIC ANHYDRASES</b>	04-5	39
15:15	Akvilė Botyriūtė, Vytautas Smirnovas <b>EPIGALLOCATECHIN-3-GALLATE AS A POTENTIAL INHIBITOR OF INSULIN AMYLOID-LIKE FIBRIL FORMATION</b>	04-6	40
15:30 – 18:00	<b><u>POSTER SESSION P2</u></b>		
22 March FRIDAY			

---

### **ORAL SESSION 05**

9:00	Ilze Dimanta, Jānis Kleperis, Indriķis Muižnieks. <b>BIO-HYDROGEN PRODUCTION EXPERIMENTS USING CRUDE GLYCEROL AS SUBSTRATE WITH DIFFERENT ANAEROBIC MICROORGANISMS</b>	05-1	42
9:15	Justinas Jonušas, Rūta Araminaitė, Vitalijus Karabanovas <b>EFFECTS OF PH ON GLUTATHIONE – CAPPED CdSe QUANTUM DOTS OPTICAL PROPERTIES</b>	05-2	43
9:30	Raminta Marcinonytė, Marija Matulionytė <b>DYNAMICS OF ACCUMULATION OF MES CAPPED GOLD NANOPARTICLES IN CANCER CELLS</b>	05-3	44
9:45	Edita Jazdauskaitė, Vytautas Kulvietis <b>PHOTOSTABILITY OF QUANTUM DOTS AND ITS IMPLICATION IN BIOSAFETY OF NANOMATERIALS</b>	05-4	45
10:00	Urtė Statkutė, Vitalijus Karabanovas <b>IMAGING OF MAGNETIC NANOPARTICLES IN CELLS USING OPTICAL MICROSCOPY</b>	05-5	46
10:15	Karola Panke, Varis Karitāns <b>INFLUENCE OF OPTICAL ABERRATIONS INDUCED IN ONE EYE AND THE ACCOMODATIVE RESPONSE IN THE FELLOW EYE</b>	05-6	47

### **ORAL SESSION 06**

11:00	Maxim Belov, Alex Halavanau	06-1	49
	<b>1D WAVE EQUATION OPENCL-BASED INTEGRATION</b>		
11:15	Laura Baliulytė, Jelena Tamulienė	06-2	50
	<b>QUANTUM-MECHANICAL STUDY OF THE ASPARAGINE MONOHYDRATE FRAGMENTATION BY LOW ENERGY ELECTRONS</b>		
11:30	Darius Stonys	06-3	51
	<b>THEORETICAL INVESTIGATION OF LIGHT ATOMS EXCITATION BY ELECTRON IMPACT</b>		
11:45	Andrius Gelžinis, Leonas Valkūnas, Darius Abramavičius	06-4	52
	<b>TIGHT BINDING MODEL OF THE PHOTOSYSTEM II REACTION CENTER</b>		
12:00	Tomas Andrijauskas, Egidijus Anisimovas, Nathan Goldman, Gediminas Juzeliūnas	06-5	53
	<b>TOPOLOGICAL PROPERTIES OF BAND STRUCTURE OF <math>T_3</math> OPTICAL LATTICE</b>		
12:15	Valdemaras Milkus, Thomas Gajdosik.	06-6	54
	<b>APPLICATION OF THE BOLTZMANN- EINSTEIN EQUATIONS FOR THE DESCRIPTION OF GRAVITINO DARK MATTER</b>		
	<b>BREAK</b>		

### **ORAL SESSION 07**

13:30	Volha Filippenko	07-1	56
	<b>THE TOTAL ENERGY OF THE ELECTRIC FIELD AND THE ENERGY OF THE INTERACTION BETWEEN CHARGES AT SECONDARY SCHOOL</b>		
13:45	Aleksejus Kononovicius, Vygintas Gontis	07-2	57
	<b>BURSTING BEHAVIOR OF THE NON-LINEAR STOCHASTIC MODELS APPLICABLE TO THE FINANCIAL MARKETS</b>		
14:00	Artūrs Stramkaļs	07-3	58
	<b>DESTRUCTION OF COMETS</b>		
14:15	Algimantas Kostas Sabulis, Kastytis Zubovas	07-4	59
	<b>TURBULENT MOLECULAR CLOUD COLLAPSE</b>		
14:30	Aija Laure, Laimons Začs	07-5	60
	<b>RADIAL VELOCITY MEASUREMENTS AND INTERPRETATION OF PROTOPLANETARY NEBULAE</b>		
14:45	Karolis Manfreds Lyvens, Donatas Narbutis	07-6	61
	<b>AUTOMATIC SEARCH FOR STAR CLUSTERS IN LEO A GALAXY</b>		

### **15:00 – 17:00 POSTER SESSION P3**

**23 March  
SATURDAY**

*Energy and Technology Museum  
Rinktinės g. 2*

---

#### **13:00 – 13:50 EXCURSIONS AROUND ENERGY AND TECHNOLOGY MUSEUM**

14:00	CAFÉ SCIENTIFIQUE ABOUT NIKOLA TESLA'S LIFE AND ACHIEVEMENTS
	<b>Edmundas Kuokštis</b> , Faculty of Physics, Vilnius University, Lithuania
	<b>Rimvydas Aleksiejūnas</b> , Faculty of Physics, Vilnius University, Lithuania
16:00	CONFERENCE CLOSING AND AWARDS

# List of poster presentations

20 March  
WEDNESDAY

---

15:30 – 18:00 **POSTER SESSION P1**

Vytautas Šimkevičius <b>MgZnO OPTICAL PROPERTIES</b>	P1-01	63
Nelda Antonovaitė, Vytautas Kučikas <b>3D VISUALISATION OF SINGLE AND MULTIPLE FILAMENTS INDUCED BY ULTRAVIOLET FEMTOSECOND PULSES</b>	P1-02	64
Jonas Berzinš, Mindaugas Gedvilas <b>SCRIBING OF SAPPHIRE WAFERS BY USING PICOSECOND LASER IRRADIATION AT 355 nm AND 1064 nm WAVELENGTHS</b>	P1-03	65
Rimantas Budriūnas, Cord Arnold <b>COLLINEAR SETUP FOR TWO-COLOR HIGH HARMONIC GENERATION</b>	P1-04	66
Gediminas Chaževskis, Domas Paipulas <b>MICROMACHINING OF OPTICAL FIBERS USING ULTRASHORT LASER PULSES</b>	P1-05	67
Aušra Čerkauskaitė, Domas Paipulas <b>PHOTOREFRACTIVE MODIFICATIONS IN LITHIUM NIOBATE CRYSTALS INDUCED BY FEMTOSECOND LASER PULSES</b>	P1-06	68
Juozas Dudutis, Paulius Gečys <b>THIN-FILM CIGS SOLAR CELLS SCRIBING WITH FEMTOSECOND AND NANOSECOND LASERS</b>	P1-07	69
Darius Gailevičius, Vytautas Purlys, Lina Maigytė, Martynas Peckus, Mangirdas Malinauskas, Kęstutis Staliūnas <b>SPATIAL FILTERING BY CHIRPED PHOTONIC CRYSTALS</b>	P1-08	70
Nail Garejev, Julius Darginavičius <b>GENERATION OF ODD HARMONICS IN SOLID MEDIA</b>	P1-09	71
Ieva Gražulevičiūtė, Tomas Tamulevičius, Darius Urbonas, Martynas Gabalis, Raimondas Petruškevičius, Sigitas Tamulevičius <b>NUMERICAL ANALYSIS OF DIFFRACTION GRATING BASED REFRACTIVE INDEX SENSOR</b>	P1-10	72
Aušra Gustainytė, Marius Franckevičius, Loreta Rastenenė, Rimas Vaišnoras, Vidmantas Gulbinas <b>OPTICAL AND STRUCTURAL STUDY OF HYBRID STRUCTURE COMPLEXES COMPOSED OF PHOTOCHROMIC DENDRIMERS AND AG NANOPARTICLES</b>	P1-11	73
Simonas Indrišiūnas, Bogdan Voisiat <b>FABRICATION OF MICRO-SIZE STRUCTURES FOR THZ FILTERS USING SCANNED INTERFERENCE PATTERN</b>	P1-12	74
Aušrinė Jurkevičiūtė, Nerijus Armakavičius, Linas Šimatonis, Dainius Virganavičius, Tomas Tamulevičius, Sigitas Tamulevičius <b>MULTIPLE EXPOSURE HOLOGRAPHIC LITHOGRAPHY FOR TWO-DIMENSIONAL SUB-MICROMETER STRUCTURES</b>	P1-13	75
Krylova L.G., Krylov G.G. <b>TIME-SPACE DISTRIBUTED MODEL FOR DIFFERENT LASER REGIME SIMULATION IN SOLID STATE LASER</b>	P1-14	76
Agnė Marcinkevičiūtė, Rosvaldas Šuminas, Julius Vengelis, Karolina Stankevičiūtė, Valdas Sirutkaitis <b>CONSTRUCTION OF SYNCHRONOUSLY PUMPED FEMTOSECOND OPTICAL PARAMETRIC OSCILLATOR</b>	P1-15	77
Edgaras Markauskas, Paulius Gečys <b>SELECTIVE PATTERNING OF CZTS THIN-FILM SOLAR CELLS BY ULTRA-SHORT LASER INDUCED MATERIAL LIFT-OFF PROCESS</b>	P1-16	78

Simas Melnikas, Simonas Kičas, Rytis Buzelis <b>COATING THICKNESS UNIFORMITY MODULATION IN ION BEAM SPUTTERING PROCESS</b>	P1-17	79
Jevgenij Mitrofanov, Simonas Kičas, Ramutis Drazdys <b>CHARACTERIZATION OF HFO<sub>2</sub>-SiO<sub>2</sub> MIXTURES PRODUCED BY ION-BEAM SPUTTERING TECHNOLOGY</b>	P1-18	80
Andrius Narmontas, Giedrė Marija Archipovaitė <b>EFFECTIVE NONCOLLINEAR SECOND HARMONIC GENERATION EXCITED BY TWO BEAMS</b>	P1-19	81
Sergey Nazarov, Gorbach Dmitry <b>FOUR-WAVE MIXING OF GAUSSIAN AND SINGULAR LIGHT BEAMS IN MEDIA WITH THERMAL NONLINEARITY</b>	P1-20	82
Emilis Pileckis, Donatas Majus <b>SUPERCONTINUUM GENERATION USING 2 mm 30-fs PULSES</b>	P1-21	83
Mindaugas Slivka, Tomas Tolenis, Rytis Buzelis, Ramutis Drazdys <b>HIGH REFLECTIVITY MEASUREMENTS BY CAVITY RING-DOWN TECHNIQUE: EXPERIMENTAL SCHEME AND SENSITIVITY ANALYSIS</b>	P1-22	84
Paulius Stanislovaitis, Valerijus Smilgevičius, Vytautas Šetkus <b>SECOND HARMONIC GENERATION FROM RADIAL AND AZIMUTHAL POLARIZATION BEAMS IN TYPE II NONLINEAR CRYSTAL</b>	P1-23	85
Andrius Subačius, Kęstutis Juškevičius <b>INVESTIGATION AND COMPARISON OF Nb<sub>2</sub>O<sub>5</sub>-SiO<sub>2</sub> MIXTURES PREPARED BY MAGNETRON SPUTTERING AND ELECTRON BEAM EVAPORATION TECHNIQUES</b>	P1-24	86
Kristupas Kazimieras Tikuišis, Albertas Žukauskas, Mangirdas Malinauskas <b>FABRICATION AND CHARACTERIZATION OF MICROFRAXICONS FABRICATED BY DIRECT LASER WRITING</b>	P1-25	87
Ernestas Žeimys, Benas Makauskas, Kęstutis Steponkevičius <b>THIRD-HARMONIC GENERATION IN ATMOSPHERIC AIR</b>	P1-26	88
Evelina Baltakytė, Sandra Tamošaitytė, Dominyka Blaževič, Milda Pučetaitė, Justinas Čeponkus, Valdas Šablinskas <b>CORRECTION OF MIE SCATTERING BACKGROUND APPEARING IN INFRARED ABSORPTION SPECTRA OF URINARY SEDIMENTS</b>	P1-27	89
Jonas Povilas Banys, Milda Pučetaitė, Valdas Šablinskas <b>APPLICATION OF INFRARED REFLECTION MICROSCOPY FOR CHEMICAL IMAGING OF CROSS-SECTIONED URINARY CALCULI</b>	P1-28	90
D. V. Borisevich, G. A. Pitsevich, A. E. Malevich, V. Šablinskas, V. Balevicius <b>3D CALCULATIONS OF THE HYDROXYL GROUP MODES IN THE FREE PYRIDINE n-OXIDE/TRICHLOROACETIC ACID COMPLEX</b>	P1-29	91
Kseniya Bogdanchuk, Dmitry Stepanenko, Vladimir Minchenya <b>MEASUREMENT OF MAGNETOSTRICTIVE PROPERTIES OF MATERIALS BY MEANS OF ULTRASONIC METHOD</b>	P1-30	92
Kęstutis Bučinskas, Maksim Ivanov, Robertas Grigalaitis, Jūras Banys, Eva Sapper, Jürgen Rödel <b>DIELECTRIC AND IMPEDANCE SPECTROSCOPY OF Fe DOPED 0.94(Na<sub>0.5</sub>Bi<sub>0.5</sub>TiO<sub>3</sub>)-0.06BaTiO<sub>3</sub> CERAMICS</b>	P1-31	93
Agnė Čiučiulkaitė, Asta Tamulevičienė, Andrius Vasiliauskas <b>INVESTIGATION OF SILVER CONTAINING DIAMOND LIKE CARBON THIN FILMS EMPLOYING FOURIER TRANSFORM INFRARED SPECTROSCOPY</b>	P1-32	94
Erika Elijošutė, Olegas Eicher-Lorka, Egidijus Griškonis, Dalia Jankūnaitė, Gintaras Denafas <b>STRUCTURAL INVESTIGATION OF [Hg(ScN)N]2-N COMPLEXES IN WATER AND HEAVY WATER SOLUTIONS BY RAMAN SPECTROSCOPY AND THEORETICAL MODELING</b>	P1-33	95
Povilas Kaščionis, Viktorija Lukševičiūtė, Valdemaras Aleksa <b>POVILAS CONFORMATIONAL CHANGES IN IONIC LIQUID-D<sub>2</sub>O MIXTURES USING RAMAN SPECTROSCOPY</b>	P1-34	96
Žygimantas Lackus, Vytautas Bacevičius <b>MAGIC ANGLE SPINNING (MAS) NMR SPECTROSCOPY</b>	P1-35	97

Alina Muravitskaya, Andrei Ramanenka <b>SPECTRAL-LUMINESCENT PROPERTIES OF ALEXA FLUOR 488 MOLECULES NEAR SILVER NANOPARTICLES</b>	P1-36	98
Ieva Puodžiūtė, Justinas Čeponkus <b>EVALUATION OF D AND G RAMAN MODES RATIO FOR THE ANALYSIS OF CARBON NANOTUBE STRUCTURE</b>	P1-37	99
Mantas Stankevičius, Mindaugas Brinkus, Valdemaras Aleksa <b>INVESTIGATION OF ARTWORKS POLYCHROMY USING PIXE ANALYSIS AND RAMAN SPECTROSCOPY METHODS</b>	P1-38	100
Simona Streckaitė, Renata Karpicz, Saulius Grigalevičius <b>PHOTOPHYSICAL PROCESSES OF ORGANIC INDOLO[3,2-B]CARBAZOLE COMPOUNDS</b>	P1-39	101
Anda Svagere, Rolands Zvejnieks <b>STABILITY AND INTENSITY OF SPECTRAL LINES IN HFEDLS WITH ZINC</b>	P1-40	102
Laurynas Tumonis, Rimvydas Venckevičius, Irmantas Kašalynas, Gintaras Valušis <b>SPECTRAL SIGNATURES OF MEDICINE DRUGS IN TERAHERTZ RANGE</b>	P1-41	103
Martynas Velička, Milda Pučetaitė, Valdas Šablinskas <b>ANLYSIS OF CHEMICAL CONSTITUENS OF URINARY SEDIMENTS BY MEANS OF SURFACE ENHANCED RAMAN SPECTROSCOPY</b>	P1-42	104
Artūras Vyšniauskas, Dovilė Čibiraitė, Sandra Pralgauskaitė, Jonas Matukas <b>APPLICATION OF FLUCTUATION ANALYSIS METHOD FOR EVALUATION OF HUMAN CARDIOVASCULAR SYSTEM</b>	P1-43	105
Madara Zinge, Valters Dzelve <b>SELF-MODULATION REGIME STUDIES OF SELENIUM CONTAINING HIGH-FREQUENCY ELECTRODELESS LAMPS</b>	P1-44	106
Tomas Žukauskas <b>SAMPLE TEMPERATURE CONTROLLER</b>	P1-45	107

21 March  
THURSDAY

---

15:30 – 18:00 **POSTER SESSION P2**

Justinas Aleknavičius <b>PHOTOLUMINESCENCE OF INGAN EPITAXIAL LAYERS WITH HIGH INDIUM CONTENT</b>	P2-01	109
Aurina Arnatkevičiūtė <b>INVESTIGATION OF INTERMEDIATE STAGES OF GAN GROWTH: STRAIN TRANSFORMATIONS FROM INTERFACE TO EPI-LAYER</b>	P2-02	110
Darius Bajarūnas, Eugenijus Gaubas <b>DLTS SPECTROSCOPY OF TECHNOLOGICAL AND RADIATION DEFECTS IN SI STRUKTURES</b>	P2-03	111
Jaroslavas Belovickis, Romualdas Rimeika <b>BEHAVIOUR OF ACOUSTIC BEAM GENERATED FROM LEAKY SURFACE WAVE UPON REFLECTION IN YX-LiTaO<sub>3</sub></b>	P2-04	112
Paulius Cicėnas, Tomas Čeponis, Eugenijus Gaubas, Vidmantas Kalendra <b>EPR SPECTROSCOPY OF NEUTRON IRRADIATED STRUCTURES</b>	P2-05	113
Pranciškus Dobrovolskis, Vilma Venckutė <b>ELECTRICAL PROPERTIES OF Li<sub>4x</sub>Ti<sub>1-x-1</sub>P<sub>2</sub>O<sub>7</sub> (X=0.06, 0.1) COMPOUND CERAMICS</b>	P2-06	114
Edgaras Dvinelis, Kristijonas Vizbaras, Augustinas Vizbaras <b>MID-INFRARED PHOTOLUMINESCENCE MAPPING OF ALGAINASSB/QW EPITAXIAL STRUCTURES FOR NEXT GENERATION TYPE-I GASB LASER DIODE DEVELOPMENT</b>	P2-07	115
Adomas Eikevičius, Saulius Tumėnas <b>SPECTROSCOPIC ELLIPSOMETRY OF GaBi<sub>x</sub>As<sub>1-x</sub></b>	P2-08	116
Dainius Gabrielaitis, Marjorie Albino, Michaël Josse, Martynas Kinka, Vytautas Samulionis, Robertas Grigalaitis, Mario Maglione, Jūras Banys <b>DIELECTRIC PROPERTIES OF Ba<sub>2</sub>NdFeNb<sub>3,7</sub>Ta<sub>0,3</sub>O<sub>15</sub> SOLID SOLUTION</b>	P2-09	117

Viktorija Jankauskaitė, Robertas Grigalaitis, Jūras Banys, Mirjana Vijatović Petrović, Jelena Bobić, Biljana Stojanović <b>PROPERTIES OF LANTHANUM, NIOBIUM, MANGANESE DOPED BARIUM TITANATE CERAMICS PRODUCED FROM NANOPOWDERS</b>	P2-10	118
Vytautas Janonis <b>INVESTIGATION OF THERMALLY STIMULATED CONDUCTIVITY AND PHOTOCONDUCTIVITY SPECTRA IN TlBr</b>	P2-11	119
Arnoldas Jasiūnas, Eugenijus Gaubas <b>RECOMBINATION CHARACTERISTICS DEPENDENT ON TECHNOLOGICAL REGIMES OF GAN AND DIAMOND FORMATION</b>	P2-12	120
J. Jovaišaitė, S. Raišys, K. Kazlauskas, R. Reghu, J. V. Gražulevičius, S. Juršėnas <b>ALKYL CHAIN LENGTH EFFECT ON THE FLUORESCENCE PROPERTIES OF TRIPHENYLAMINE DERIVATIVES</b>	P2-13	121
Vaiva Kaveckytė, Irmantas Kašalynas <b>THIN DIELECTRIC FILM LOADING EFFECT ON PLASMONS EXCITATION IN PERFORATED METAL FILMS</b>	P2-14	122
Deividas Kovalenkovas, Tadas Malinauskas <b>MODELLING ELECTRICAL CHARACTERISTICS OF BOW-TIE DIODES</b>	P2-15	123
Oleg Kravcov <b>THE INFLUENCE OF LOCALIZED STATES ON THE OPTICAL PROPERTIES OF SEMICONDUCTORS</b>	P2-16	124
Jevgenij Kusakovskij, Freddy Callens, Henk Vrielinck, Eugenijus Gaubas <b>CHARACTERIZATION OF X-RAY INDUCED ROOM TEMPERATURE UNSTABLE RADICALS IN SUCROSE</b>	P2-17	125
Elena Levchuk, Leonid Makarenko, Olga Lavrova <b>MODELING OF GEOMETRICAL EFFECTS ON SHALLOW DONOR STATES IN MOS-STRUCTURES</b>	P2-18	126
Mažena Mackoīt <b>SPATIALLY RESOLVED LUMINESCENCE IN LGSO:Ce CRYSTALS</b>	P2-19	127
Karolis Madeikis, Linas Minkevičius, Gintaras Valušis <b>ANTENNA-COUPLED INGAAS “BOW-TIE” DIODE DESIGNS FOR TERAHERTZ DETECTION</b>	P2-20	128
Rita Merzliakovaitė, Saulius Antanas Juršėnas <b>FORMATION AND OPTICAL CHARACTERIZATION OF NANOAGGREGATES FORMED BY TRIPLET OLED EMITTERS</b>	P2-21	129
Dovilė Meškauskaitė, Eugenijus Gaubas <b>DLTS SPECTROSCOPY ON Ge DOPED Si DIODES</b>	P2-22	130
Eimantas Mikolajūnas <b>SURFACE PLASMON ENHANCED PHOTOLUMINESCENCE OF InGaN/GaN QUANTUM WELLS</b>	P2-23	131
Grigorij Muliuk, Johan Lauwaert, Henk Vrielinck <b>DLTS INVESTIGATION OF MN-IMPLANTED Ge</b>	P2-24	132
Kristina Gelžinytė, Kazimieras Nomeika <b>OPTICAL STUDY OF EXCITATION-DEPENDENT RECOMBINATION PROCESSES IN VARIOUS (In,Ga)N STRUCTURES</b>	P2-25	133
Žydrūnas Podlipskas <b>INVESTIGATION OF CARRIER DYNAMICS IN (Al,Ga)N LAYERS BY LIGHT INDUCED TRANSIENT GRATING TECHNIQUE</b>	P2-26	134
V. Rumbauskas, A. Mekys, J. V. Vaitkus <b>HALL AND MAGNETORESISTIVITY MEASUREMENTS IN FAST ELECTRON IRRADIATED SILICON</b>	P2-27	135
Aurimas Sakanas, Robertas Grigalaitis, Jūras Banys, Liliana Mitoseriu, Vincenzo Buscaglia, Paolo Nanni <b>BROADBAND DIELECTRIC INVESTIGATION OF BARIUM TITANATE AND NICKEL-ZINC FERRITE COMPOSITE CERAMICS</b>	P2-28	136
Andrius Sakavičius <b>INVESTIGATION OF THE IMPACT OF AU NANOPARTICLES ON THE ELECTRICAL AND CHARGE TRANSPORT PROPERTIES OF A-Si:H SOLAR CELLS</b>	P2-29	137

Ramūnas Songaila, Saulius Tumėnas <b>OPTICAL AND ELECTRICAL CHARACTERIZATION OF VACUUM DEPOSITED THIN ORGANIC LAYERS</b>	P2-30	138
Marius Stasiūnas, Mindaugas Karaliūnas <b>INVESTIGATION OF GREEN PHOTOLUMINESCENCE FROM CdZnO/ZnO AND InGaN/GaN MULTIPLE QUANTUM WELLS</b>	P2-31	139
Alina Svekla <b>FORMATION HYDROGEN-RELATED DONOR IN THE EPITAXIAL SILICON IMPLANTED WITH PROTONS</b>	P2-32	140
Ignas Abromavičius, Valerijus Smilgevičius <b>ANALYSIS OF PARAMETRIC LIGHT GENERATION IN 1500 nm REGION</b>	P2-33	141
Martynas Šoliūnas, Saulius Balakauskas, Vincas Tamošiūnas <b>INVESTIGATION OF Cu(In,Ga)Se<sub>2</sub> LAYER PROPERTIES BY MEANS OF FOURIER SPECTROSCOPY</b>	P2-34	142
Vytautas Tumas, Edmundas Kuokštis, Mindaugas Karaliūnas, Egidijus Anisimovas <b>MECHANISMS OF OPTICAL GAIN IN ZnO CRYSTALS</b>	P2-35	143
Andrius Vaitkūnas, Algirdas Novičkovas, Algirdas Mekys, Vincas Tamošiūnas <b>HIGH POWER LIGHT EMITTING DIODES AS SOURCES FOR NOVEL SOLAR SIMULATORS</b>	P2-36	144
Arūnas Velička, Tomas Čeponis, Eugenijus Gaubas <b>TEMPERATURE AND FLUENCE DEPENDENT VARIATIONS OF STUDY OF CARRIER LIFETIME VARIATIONS IN Si STRUCTURES</b>	P2-37	145
Laura Zurauskaite, Saulius Balevicius <b>ELECTRORESISTANCE OF NANOSTRUCTURED MANGANITE FILMS</b>	P2-38	146
Audronė Žemaitytė, Saulius Kazlauskas <b>SINTERING OF GADOLINIUM DOPED CERIA CERAMICS AND THEIR ELECTRICAL PROPERTIES</b>	P2-39	147
Loreta Žukauskaitė, Maud Barre <b>FABRICATION AND INVESTIGATION OF NASICON-TYPE SOLID ELECTROLYTES</b>	P2-40	148
Sergejus Balčiūnas, Maksim Ivanov, H.Amorín, A. Castro, M. Algeró, Jūras Banys <b>DIELECTRIC PROPERTIES OF NANOGRAIN BSPT CARAMICS</b>	P2-41	149
Paulius Baronas, Saulius Juršėnas, Karolis Kazlauskas, Austra Tomkeviciene, Juozas Vidas Grazulevicius <b>CARBAZOLE AND FLUORENE DERIVATIVES FOR OPTOELECTRONIC APPLICATIONS</b>	P2-42	150
Marek Burakevič, Mantas Ragauskas, Jonas Matukas, Gintaras Valušis <b>TRANSITOR BASED TERAHERTZ SENSORS NOISE CHARACTERISATION</b>	P2-43	151
Rokas Dobužinskas, Kęstutis Arlauskas, Andrius Poškus <b>HYBRID ORGANIC-INORGANIC X-RAY SENSITIVE LAYER FORMATION AND INVESTIGATION OF ELECTRICAL PROPERTIES</b>	P2-44	152
Paulius Eidikas, Andrius Petrulis <b>MULTICOLOUR LED CLUSTERS FOR PHOTOBIOLOGICALLY FRIENDLY SOLID-STATE LIGHTING</b>	P2-45	153
Eriks Elksnis, Atis Skudra, Arturs Viksna <b>DIAMOND SYNTHESIS USING PLASMA CHEMICAL VAPOUR DEPOSITION METHOD ON DIFFERENT SUBSTRATE MATERIALS</b>	P2-46	154
Džiugas Jablonskas, Austė Kuprevičiūtė, Šarūnas Svirskas, Vytautas Samulionis, Jūras Banys, Tonny McNally <b>BROADBAND DIELECTRIC SPECTROSCOPY AND ULTRASONIC INVESTIGATIONS OF COMPOSITES OF POLY(ε-CAPROLACTONE) AND Mo<sub>6</sub>S<sub>3</sub>I<sub>6</sub> NANOWIRES</b>	P2-47	155
Guntars Kitenbergs, Kaspars Ērglis, Oksana Petrichenko, Andrei Tatulchenkov, Fahrettin Gökhan Ergin, Bo Beltoft Watz, Regine Perzynski, Andrejs Cēbers <b>CHARACTERISTIC WIDTH OF THE MAGNETIC FIELD DRIVEN MICRO-CONVECTION IN THE HELE-SHAW CELL</b>	P2-48	156
Regimantas Komskis, Tomas Serevičius, Povilas Adomėnas, Ona Adomėnienė, Renaldas Rimkus, Vygintas Jankauskas, Karolis Kazlauskas, Saulius Juršėnas <b>NEW ASYMMETRIC ANTHRACENE DERIVATIVES FOR OPTOELECTRONIC APPLICATIONS</b>	P2-49	157
Ieva Kranauskaitė, Jan Macutkevič, Jūras Banys, Alain Celzard, Stefano Bellucci <b>DIELECTRIC SPECTROSCOPY OF MEDIUM GRAPHITE LOADED EPOXY RESIN COMPOSITES</b>	P2-50	158

Gediminas Kreiza, Karolis Kazlauskas, Arūnas Miasojedovas, Eglė Arbačiauskienė, Aurimas Bieliauskas, Algirdas Šačkus, Saulius Juršėnas <b>SELF-ASSEMBLY OF FLUORESCENT NANOAGGREGATES BASED ON 1,4-DIVINYLBENZENE DERIVATIVES</b>	P2-51	159
Dalius Petrulionis, Odile Bohnke <b>20 MOL. % Gd<sub>2</sub>O<sub>3</sub> DOPED CeO<sub>2</sub> SOLID ELECTROLYTE 20 MOL. 20 MOL. % Gd<sub>2</sub>O<sub>3</sub> DOPED CeO<sub>2</sub> ELECTRONIC CONDUCTIVITY DEPENDANCE ON OXYGEN ACTIVITY</b>	P2-52	160
22 March FRIDAY		
15:00 – 17:00 <b><u>POSTER SESSION P3</u></b>		
Artis Aberfelds, Laimonis Začš <b>HIGH-RESOLUTION SPECTROSCOPY OF STAR B517569-0011</b>	P3-01	162
Karolina Adelbergytė, Arūnas Kučinskas, Vidas Dobrovolskas <b>OXYGEN ABUNDANCES IN THE OLDEST GALACTIC POPULATIONS</b>	P3-02	163
Jonas Klevas, Arūnas Kučinskas, Hans-Günther Ludwig, Piercarlo Bonifacio, Mathias Steffen, Dainius Prapakavičius <b>PREDICTING ASYMMETRIES AND SHIFTS OF SPECTRAL LINES IN THE METAL-POOR RED GIANT HD 122563</b>	P3-03	164
Edgaras Kolomiecias, Arūnas Kučinskas <b>SILICON ABUNDANCE IN THE ATMOSPHERES OF RED GIANT STARS OF GALACTIC GLOBULAR CLUSTER 47 TUCANAE</b>	P3-04	165
Rokas Naujalis, Rima Stonkutė <b>STAR FORMATION HISTORY OF THE DWARF IRREGULAR GALAXY LEO A</b>	P3-05	166
Edvinas Brilius, Stasys Tamošiūnas <b>CREATING AN ATMOSPHERIC REFRACTIVE INDEX MAP OF LITHUANIA</b>	P3-06	167
Yaroslav Dichenko, Aleksei Yantsevich, Sergei Usanov <b>MODIFIED SUBSTRATE SPECIFICITY OF CYP7B1 R486C MUTANT – A POSSIBLE REASON FOR SPASTIC PARAPLEGIA TYPE 5</b>	P3-07	168
Vilmantas Gėgžna, Jaunius Kurtinaitis, Andrius Brazaitis, Narūnas Porvaneckas <b>THE DYNAMICS OF FEMORAL HEAD BLOOD FLOW AFTER A FEMORAL NECK FRACTURE</b>	P3-08	169
Elena N. Golubeva <b>MITOCHONDRIAL INVOLVMENT IN ASCORBATE-INDUCED CALCIUM IONS RELEASE INTO CYTOSOL OF HEP-2C CELLS</b>	P3-09	170
Tadas Juknius, Tomas Tamulevičius, Ieva Gražulevičiūtė, Dainius Virganavičius, Irena Klimienė, Algimantas Petras Matusėvičius, , Sigitas Tamulevičius <b>THE RESPONSE OF A PURE BACTERIAL CULTURE TO THE EFFECT OF ANTIMICROBIAL AGENTS EMPLOYING A LEAKY MODE DIFFRACTION GRATING WAVEGUIDE SENSOR</b>	P3-10	171
Maryna Hliatsevich, Pavel Bulai <b>THE KINETIC MODEL OF NEUROTRANSMITTER RELEASE FROM PRESYNAPTIC BOUTON</b>	P3-11	172
Justina Kazokaitė, Daumantas Matulis <b>THERMODYNAMICS OF ETHOXZOLAMIDE BINDING TO RECOMBINANT HUMAN CARBONIC ANHYDRASE (CA) VI</b>	P3-12	173
Julia Kirpich, Nina Krylova, Elena Golubeva, Tatsiana Kulahava <b>REDOX-REGULATION OF FUNCTIONAL AND MORPHOLOGICAL CHARACTERISTICS OF CELLS 293, PRODUCING CH3L1 PROTEIN</b>	P3-13	174
Julija Pauraitė, Vidmantas Ulevičius <b>THE INVESTIGATION OF BLACK CARBON IN AEROSOL PARTICLES AND IDENTIFICATION OF ITS ORIGIN</b>	P3-14	175
Nadya Pleshko, Vladimir Krot <b>ELECTROPHORETIC STUDY OF COMPLEXING BETWEEN DNA AND CARBOXYLATED CARBON NANOTUBES</b>	P3-15	176



Deividas Sabonis, Ričardas Rotomskis	P3-16	177
<b>ACTIVATION OF BOVINE SERUM ALBUMIN-GOLD NANOCLOUDS VIA TWO PHOTON EXCITATION</b>		
Olga Simachova	P3-17	178
<b>ELECTROMAGNETIC PULSE INTERACTION WITH A HUMAN SKIN TAKING INTO ACCOUNT PERMITTIVITY DISPERSION</b>		
Ernestas Svirbutavičius, Marius Stalnionis, Marija Matulionytė	P3-18	179
<b>FLUOROMETRIC INVESTIGATION OF AU-BSA-99TC MULTIMODAL IMAGING TRACER</b>		
Gediminas Špogis	P3-19	180
<b>INVESTIGATIONS OF LUMINESCENCE OF SINGLET OXYGEN GENERATED BY THE QUANTUM DOT-SENSITIZER COMPLEX</b>		
Indrė Valiulytė, Mykolas Mikučiūnas, Paulina Vaitkienė, Daina Skiriutė, Arūnas Kazlauskas	P3-20	181
<b>AHR GENE METHYLATION AND PROTEIN EXPRESSION IN DIFFERENT MALIGNANCY GLIOMAS</b>		
Vilmantas Gėgžna, Darius Varanius, Gunaras Terbetas, Aurelija Vaitkuvienė, Juozas Vidmantis Vaitkus	P3-21	182
<b>MULTICURVE RESOLUTION ALGORITHM AND ARTIFICIAL NEURAL NETWORKS APPLIED FOR ANALYSIS OF INTERVERTEBRAL DISC TISSUE AUTOFLUORESCENCE</b>		
Nina Krylova, Nikita Vasilyeu	P3-22	183
<b>INTERDIGITAL CAPACITIVE SENSOR FOR CELLULAR MONOLAYER FUNCTIONAL STATE ANALYSIS</b>		
Brigita Zutere, Kaiva Luse	P3-23	184
<b>USABILITY OF PSYCHOPHYSICAL EXPERIMENT SCHEME IN COLOUR VISION DEFICIENCY CHARACTERIZATION</b>		
Alexandr Bedulin, George Pitsevich	P3-24	185
<b>SPECTRAL AND STRUCTURAL CHARACTERISTICS OF THE METHANOL DIMER IN THE GAS PHASE</b>		
Andrew Bogush, Georgy Pitsevich	P3-25	186
<b>THE TRANSFORMATION OF THE CENTRAL FORCE FIELDS TO THE NATURAL COORDINATES REPRESENTATION</b>		
Justina Dakševič, Jurgis Barkauskas	P3-26	187
<b>TRANSFER OF GRAPHENE OXIDE COATINGS ONTO POLYETHYLENE TEREPHTHALATE SUBSTRATE: A SIMPLEX OPTIMIZATION STUDY</b>		
Gytautas Janulevičius, Artūras Žalga	P3-27	188
<b>SOL-GEL SYNTHESIS AND CHARACTERIZATION OF <math>\text{Ca}_{1-2x}\text{M}_x\text{RE}_x\text{MoO}_4</math> (M = Li, Na, K, Rb AND Cs; RE=Eu, Gd, Sm AND Tb) POWDERS</b>		
Agnė Kalpakovaitė, Tomas Grinys	P3-28	189
<b>FABRICATION OF METAL NANO-ISLANDS AND DETERMINATION OF THEIR PLASMONIC RESONANCE FOR GaN APPLICATIONS</b>		
Helen Khrol, George Pitsevich, Alex Malevich, Valdas Sablinskas, Vitautas Balevicius	P3-29	190
<b>THE INFLUENCE OF SOLVATION EFFECTS IN THE STRUCTURE AND POTENTIAL ENERGY SURFACE OF THE PYRIDINE n-OXIDE/TRICHLOROACETIC ACID COMPLEX</b>		
Vytautas Klimavičius	P3-30	191
<b>NMR MONITORING OF HYDROGEN – DEUTERIUM EXCHANGE IN IONIC SOLUTIONS</b>		
Dovilė Lengvinaitė, Kęstutis Aidas	P3-31	192
<b>QUANTUM CHEMICAL PREDICTIONS OF THE H-1 NMR SPECTRA OF 1-DECYL-3-METHYL-IMIDAZOLIUM IN THE LIQUID PHASES</b>		
Katažyna Mito, Vytautas Smirnovas	P3-32	193
<b>AMYLOID-LIKE FIBRIL ELONGATION FOLLOWS MICHAELIS-MENTEN KINETICS</b>		
Arūnas Pulmanas, Vytautas Daujotis	P3-33	194
<b>DRAG FORCE STUDY OF THE HEXAFLUOROPHOSPHATE SOLUTION LAYER PROPERTIES AT GOLD ELECTRODE SURFACE</b>		
Piotr Zagórski, Andrzej Jóźwiak, Dariusz Cał, Mieczysław W. Płotka	P3-34	195
<b>SYNTHESIS OF PHOSPHORYLATED ISOINDOLINONE DERIVATIVES</b>		
Anton Yermalovich	P3-35	196
<b>MODELING A CARBON NANOTUBE BASED DETECTOR OF MODULATED TERAHERZ RADIATION</b>		

Migle Kišonaite, Asta Zubriene, Daumantas Matulis <b>INTRINSIC THERMODYNAMICS OF BENZENESULFONAMIDES BINDING TO HUMAN CARBONIC ANHYDRASES</b>	<i>P3-36</i>	<b>197</b>
Lukas Matijošaitis, Laurynas Dabašinskas, Arūnas Tuzikas <b>INTELLIGENT STREET LIGHTING</b>	<i>P3-37</i>	<b>198</b>
Virginija Plungytė, Aušra Ungurytė <b>CHARACTERIZATION OF THE CELLS ISOLATED FROM HUMAN ARTICULAR CARTILAGE</b>	<i>P3-38</i>	<b>199</b>
Igor Sivak, George Krylov <b>PATTERN RECOGNITION IN SYNERGETIC COMPUTER</b>	<i>P3-39</i>	<b>200</b>
Justas Trimailovas, Andrius Petrulis <b>SMART SOLID-STATE LIGHTING WITH AN OPTIMAL COLOUR SATURATION AND MINIMAL PHOTOCHEMICAL DAMAGE</b>	<i>P3-40</i>	<b>201</b>
Indrė Urbonaitė <b>PHYTOPLASMA INFECTION IN CUCURBIT SPIT</b>	<i>P3-41</i>	<b>202</b>
Valdas Eimontas, Olga Rancova <b>MODELING OF THE ABSORPTION SPECTRUM OF PHOTOSYNTHETIC LH2 COMPLEX BASED ON THE ALTERNATIVE CRYSTAL STRUCTURE</b>	<i>P3-42</i>	<b>203</b>
Vadim Gerasimov, Juozas Šulskus, Stepas Toliautas <b>INVESTIGATION OF PHOTO EXCITATION PROCESSES IN ORGANIC COMPLEXES WITH IRIIDIUM USING QUANTUM CHEMICAL METHODS</b>	<i>P3-43</i>	<b>204</b>
Rytis Kazakevičius, Bronislovas Kaulakys <b>1/f NOISE WITH DOUBLE POWER LAW FROM NONLINEAR STOCHASTIC DIFFERENTIAL EQUATIONS</b>	<i>P3-44</i>	<b>205</b>
Gintaras Kerevičius <b>REVISED IDENTIFICATION OF THE AUTOIONIZING STATES OF RUBIDIUM ATOM</b>	<i>P3-45</i>	<b>206</b>
Olga Kozlova <b>AB INITIO SIMULATION OF TWO-DIMENSIONAL MOLYBDENUM DISULFIDE WITH VACANCY CLUSTERS</b>	<i>P3-46</i>	<b>207</b>
Rūta Tolytė, Juozas Šulskus, Stepas Toliautas <b>SIMULATION OF ENVIRONMENTAL INFLUENCE ON ELECTRONIC SPECTRA OF BACTERIOCHLOROPHYLL MOLECULES BY FMO METHOD</b>	<i>P3-47</i>	<b>208</b>
Vladimir V. Uglov, Nikolai T. Kvasov, Raman S. Kudaktsin, Yuri A. Petukhou <b>COMPRESSION PLASMA FLOWS AS PERSPECTIVE TOOL FOR SILICON-BASED MATERIALS SYNTHESIS</b>	<i>P3-48</i>	<b>209</b>

# Oral session 1

14:00

Wednesday

---

Laser physics and optical technologies

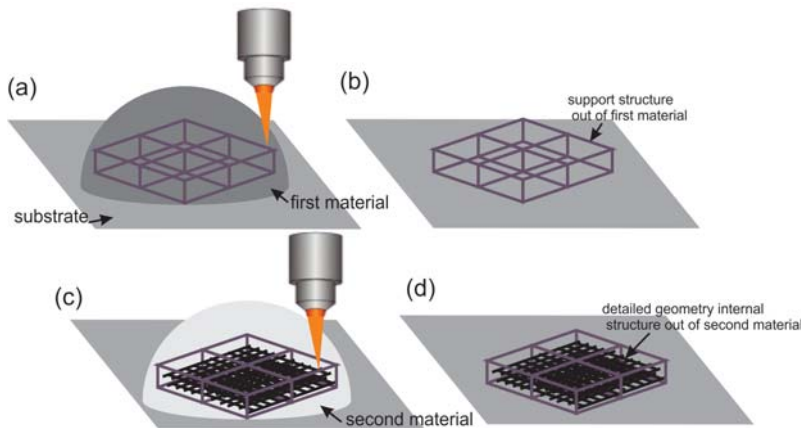
## DIRECT LASER FABRICATION OF COMPOSITE MATERIAL 3D MICROSTRUCTURED SCAFFOLDS

Eglė Kaziulionytė<sup>1</sup>, Sima Rekštytė<sup>1</sup>, Mangirdas Malinauskas<sup>1</sup>

<sup>1</sup>Laser Research Center, Department of Quantum Electronics, Faculty of Physics, Vilnius University,  
Saulėtekio Ave. 10, LT-10223 Vilnius, Lithuania  
[egle.kaziulionyte@ff.stud.vu.lt](mailto:egle.kaziulionyte@ff.stud.vu.lt)

Direct fs laser writing in polymers is a technique based on the phenomenon of multiphoton absorption and subsequent polymerization [1]. It allows the construction of three-dimensional micro- and nanostructures using a wide variety of photosensitive bio-materials [2]. As manufacturing throughput empowers overall structure size of more than 1 mm<sup>3</sup>, this technique becomes especially attractive to fabricate scaffolds for cell studies and tissue engineering applications [3]. In this paper we present direct laser fabrication of 3D microstructured scaffolds consisting out of a few polymeric materials owning different biological properties.

As the sample should be relocated between different steps of fabrication, the direct laser writing system was supplemented by a machine vision. Using this system 3D microporous multicomponent polymer scaffolds out of different organic-inorganic substances have been manufactured. Such composite constructions offer several biological functionalities such as biostability or biodegradation as well as the possibility to micro/nanopattern the surface with various bioactive materials such as proteins [4], all spatially distributed within a structure with 1 – 10  $\mu\text{m}$  features [5]. The potential of this approach is applicable for single or multiple cell adhesion, migration, proliferation and differentiation mechanism study in 3D as well as suggesting the answer for best material and architecture combinations for scaffolding needed in tissue engineering and regenerative medicine.



1 Fig. Direct laser fabrication of a composite scaffold: (a) a support structure with rough geometry giving mechanical strength is fabricated out of one material and is developed (b), then another monomer is poured over the first scaffold and a more detailed geometry is fabricated inside (c). After a second development a composite scaffold made out of two different materials is acquired (d).

- 
- [1] S. Juodkazis, V. Mizeikis, and H. Misawa, Three-dimensional microfabrication of materials by femtosecond lasers for photonics applications. *J. Appl. Phys.* **106**(5), 051101 (2009).
  - [2] M. Malinauskas, D. Baltrikiene, A. Kraniauskas et al., In vitro and in vivo biocompatibility study on laser 3D microstructurable polymers, *Appl. Phys. A*, **108**(3), 751 (2012).
  - [3] P. Danilevicius, S. Rekštyte, E. Balciunas et al., Micro-structured polymer scaffolds fabricated by direct laser writing for tissue engineering, *J. Biomed. Opt.* **17**, 081405 (2012).
  - [4] S. Engelhardt, E. Hoch, K. Borchers et al., Fabrication of 2D protein microstructures and 3D polymer-protein hybrid microstructures by two-photon polymerization, *Biofabrication* **3**, 025003 (2011).
  - [5] F. Klein, B. Richter, T. Striebel et al., Two-component polymer scaffolds for controlled three-dimensional cell culture, *Adv. Mater.* **23**, 1341 (2011).

# FABRICATION OF 3D METALLIC MICROSTRUCTURE VIA DIRECT LASER WRITING

Tomas Jonavičius, Gabija Kiršanskė, Mangirdas Malinauskas

Laser Research Center, Department of Quantum Electronics, Physics Faculty, Vilnius University, Saulėtekio ave. 10,  
LT-10223 Vilnius, Lithuania  
[tomas.jonavicius@ff.stud.vu.lt](mailto:tomas.jonavicius@ff.stud.vu.lt)

There has been a lot of interest recently in the design and fabrication of three-dimensional (3D) metallic micro/nanostructures for applications in micro-electro mechanical systems (MEMS) [1], plasmonics [2], biosensors [3], and optical metamaterials [4]. However, the fabrication of complex, high resolution, fully 3D metallic structures is still a challenging task, since traditional lithographic techniques, involving the layer-by-layer structuring of metallic structures, can only allow the deposition of a few layers or the creation of high-aspect ratio two-dimensional (2D) structures.

As an alternative technology for fabrication of 3D metallic micro/nanostructures ultrafast lasers can be used. There are three main methods: multiphoton reduction of metal ions [5], direct laser writing into a positive-tone photoresist followed by electrochemical deposition of metal [6], and direct laser writing of negative photoresists and subsequent metallization of the 3D nanostructures using electroless plating [7].

The third method has attracted the most attention up-to date and has been chosen for this work. It allows to create dielectric nanostructures with sub-100 nm resolution and metallize them without external source of electric current. It is characterised by the selective reduction of metal ions only at the surface of a catalytic substrate immersed into an aqueous solution of metal ions.

In this report, we present study of possibility to connect two conductive surfaces with metallized polymeric link and defining it's properties. Conductive surfaces were separated by laser ablated dielectric skotch. Zirconium containing organic-inorganic photosensitive material doped with amine metal-binding moieties was used for fabrication of the structure [7]. Then it was chemically metallized with silver and measurements of resistance were made. It was shown that metallized polymeric links are conductive, however, dielectric skotches also were covered with some silver.

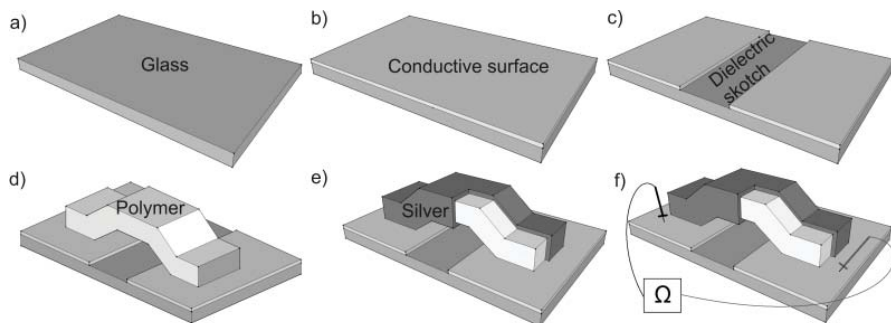


Fig. 1. Main steps of formation of metallized polymeric link.

- [1] J. B. Yoon, B. I. Kim, Y. S. Choi, and E. Yoon, 3-D Litography and metal surface micromachining for RF and microwave MEMS, The Fifteenth IEEE International Conference on Micro Electro Mechanical Systems 2002, ISSN: 1084-6999, 673 - 676 (2002).
- [2] D. K. Gramotnev, S. I. Bozhevolnyi, Plasmonics beyond the diffraction limit, Nat. Photonics **4**(2), 8391 (2010).
- [3] A. V. Kabashin, P. Evans, S. Pastkovsky, W. Hendren, G. A. Wurtz, R. Atkinson, R. Pollard, V. A. Podolskiy, and A. V. Zayats, Plasmonic nanorod metamaterials for biosensing, Nat. Mater. **8**(11), 867871 (2009).
- [4] M. S. Rill, C. Plet, M. Thiel, I. Staude, G. Freymann, S. Linden, M. Wegener, Photonic metamaterials by direct laser writing and silver chemical vapour deposition, Nat. Mater. **7**(7), 543546 (2008).
- [5] Y. Y. Cao, N. Takeyasu, T. Tanaka, X. M. Duan, and S. Kawata, 3D metallic nanostructure fabrication by surfactant-assisted multiphoton-induced reduction, Small **5**(10), 11441148 (2009).
- [6] J. K. Gansel, M. Thiel, M. S. Rill, M. Decker, K. Bade, V. Saile, G. von Freymann, S. Linden, and M. Wegener, Gold helix photonic metamaterial as broadband circular polarizer, Science **325**(5947), 15131515 (2009).
- [7] K. Terzaki, N. Vasilantonakis, A. Gaidukeviciute, C. Reinhardt, C. Fotaki, M. Mamvakaki, M. Farsari, 3D conducting nanostructures fabricated using direct laser writing, Opt. Mat. Expr. **1**, 586-597 (2011).

## HIGH AVERAGE POWER, HIGH REPETITION RATE PICOSECOND PULSES AMPLIFIER OUTPUT BEAM QUALITY OPTIMIZATION USING ADAPTIVE MIRROR

**Kirilas Michailovas<sup>1,2</sup>, Andrejus Michailovas<sup>1,2</sup>, Valerijus Smilgevicius<sup>3</sup>**

<sup>1</sup>EKSPLA, Savanoriu Av. 23 LT-023001, Vilnius, Lithuania

<sup>2</sup>Center for Physical Sciences and Technology, Savanorių Av. 231 LT-02300, Vilnius, Lithuania

<sup>3</sup>Vilnius University Laser Research Center, Sauletekio Av. 10 LT – 10223, Vilnius, Lithuania

[k.michailovas@ar.fi.lt](mailto:k.michailovas@ar.fi.lt)

OPCPA technology provides the means to get high pulse energies, high repetition rates and achieve 5-10fs pulse widths. One of the biggest challenges when producing an OPCPA system is to create a laser that would serve as its pump source as the output beam parameters of an OPCPA system depend very much on the output beam parameters of the pump source. It's very important that the pump source would have a homogenous spatial intensity distribution and high beam quality.

Our main goal was to create a laser amplifier system that would serve as a good pump source for an OPCPA system. We've managed to create a system that provides ~80W average power at 1 kHz repetition rate with pulse widths of ~50ps with intensity distribution resembling a hyper Gaussian distribution of 3<sup>rd</sup> order in the near field [1]. The measured M<sup>2</sup> parameter of the output beam was ~6 for both axes. This led us to an idea of conducting experiments on beam quality optimization. The results of our experiments using an adaptive optics to optimize beam quality are provided in this paper.

Deformable mirror was chosen as our adaptive optical element. It was a 37 channel micro machined membrane mirror with electrostatic actuators made by Flexible Optical B.V. The reflective area of it was circular with a 15mm diameter and the actual working area where the actuators are located was 12 mm in diameter. The reflective area is metallic with additional dielectric coating to provide best reflectance possible.

The mirror was used in 2 different configurations. In one the mirror was used as a replacement for an ordinary planar mirror with high reflectivity dielectric coating that is used as the returning mirror in the last (3<sup>rd</sup>) of the 2-pass amplification stages (Fig. 1a). But usage of this configuration resulted in damage to the active medium of the amplifier during the optimization process. So a layout where the mirror was placed at a small angle to the output beam was chosen for further experiments (Fig. 1b) The feedback for the deformable mirror was provided by reflecting a small fraction of the output beam using 2 wedge shaped glass plates and focusing it using a lens, then a camera (CMOS) is placed close to the beam waist. An algorithm was then run changing the voltages on the actuators and searching for ones that would provide the brightest image and one with smallest dimensions.

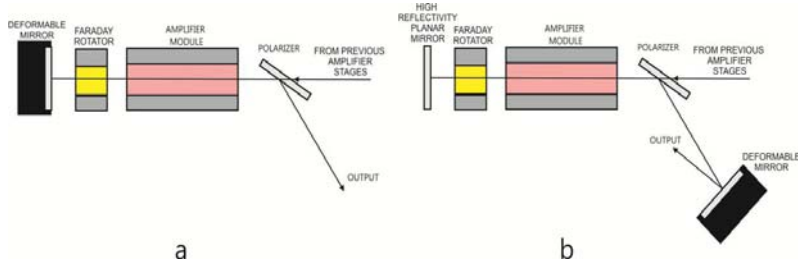


Fig. 1. Simplified layouts of the experiment. a – deformable mirror replacing returning mirror, b – deformable mirror at small angle to the output beam

Using the aforementioned experimental layout the M<sup>2</sup> parameter value of the output beam was reduced from ~6 to ~4 (All M<sup>2</sup> parameter values were obtained using manual z-scan and software provided with the CCD camera). The difference between the intensity distributions at the beam waist was clearly seen using a CCD camera with an obvious change for the better for the optimized beam. Some considerations about use of deformable mirrors will be presented.

[1] K. Michailovas, V. Smilgevicius, A. Michailovas, "Kilohertz rate picosecond pulses amplifier for pumping of OPCPA system", Topical Meeting Advanced Solid-State Photonics (ASSP), Optical Society of America, Washington, DC, 2011), AW4A.3

# FAST CUTTING AND DRILLING OF TRANSPARENT MATERIALS VIA FEMTOSECOND LASER FILAMENTATION

Simas Butkus<sup>1</sup>, Domas Paipulas<sup>1</sup>, Valdas Sirutkaitis<sup>1</sup>

1- Laser Research Center, Vilnius University, Saulėtekio av. 10, Vilnius 10223, Lithuania

[Simas.Butkus@ff.stud.vu.lt](mailto:Simas.Butkus@ff.stud.vu.lt)

Fast microfabrication of transparent materials is becoming essential due to increasing industrial requirements of micrometer scale high-quality devices. Though conventional methods are still applicable, the production of cracks and relatively low fabrication rates may open a new frontier towards industrial application of femtosecond laser microfabrication. A great number of articles have been published on transparent material fabrication where the main material removal mechanism is ablation (front side ablation and water-assisted back side ablation) [1,2]. Alternative fabrication techniques, however, are also present, i.e. transparent material bulk modification caused by tight femtosecond laser pulse focusing and material removal via chemical etching [3]. Although the above mentioned techniques are capable of producing relatively high-quality through holes, the need for high numerical aperture lens focusing and fast motion translation stages can severely prolong the fabrication time. Moreover, in the absence of optimal fabrication parameters, cracks and holes showing slight conicity are probable. The aim of this article is to demonstrate a slightly different femtosecond laser microfabrication technique, where the transparent material samples are covered in a thin film of water and filament formation occurs just before the surface of the sample in the water.

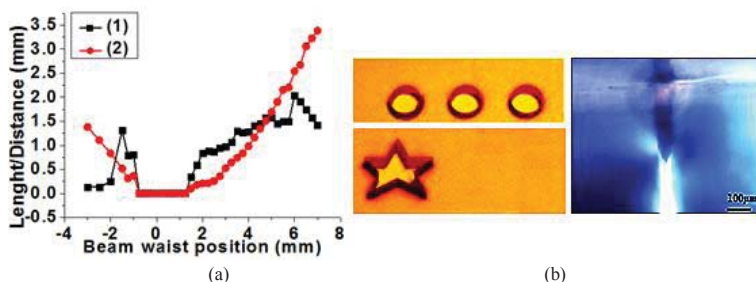


Figure 1 Modified zone length (line 1- black), modified zone distance from the surface of the sample (line 2- red) (a), 2mm wide through holes fabricated in 1mm thick soda-lime glass (b-left), modified zone after 6 hour etching time in 5% HF acid (b-right) in fused silica. (1030 nm, 280 fs, 4.8 W, 25-100 kHz)

Through precise variation of water film thickness and beam waist position relative to the surface of the sample a selective filament formation position is achievable. Due to nonlinear losses of the filament, structural modification zones are formed in fused silica, which are more susceptible to chemical etching than unmodified zones (figure 1 (b-right)), the etching rate was calculated to be 0.44 μm/min in the modified zones. As shown in figure 1(a), depending on the focal position of the beam waist and the thickness of water, modified zones form in different lengths and at different positions relative to the surface. 2 mm wide and 0.5 mm deep through holes were fabricated after laser exposure time of 1 minute and 12h etching in 5% HF acid in fused silica. Surface ablation is observable in figure 1(a) in the overlapping red and black dot areas. Due to self-focusing effects and rapid evaporation of water, material removal rates tend to be substantially higher, 2 mm wide, 1 mm deep through holes were fabricated in soda-lime glass after 2 minutes of laser exposure time (figure 1 (b- left)). Moreover, the possibility of complex shape fabrication has been demonstrated (figure 1 (b-left)). The pentagram is about 1.5 mm wide. Holes fabricated either method show no signs of cracks or conicity.

[1] A. Ran, L. Yan, D. Yan-Ping, F. Ying, Y. Hong and G. Qi-Huang „Laser Micro-Hole Drilling of Soda-Lime Glass with Femtosecond Pulses, *Chinese Phys. Lett.* 21 2465 (2004)

[2] Z. Wu, H. Jiang, Q. Sun, H. Guo, H. Yang and Q. Gong, „Micro-ablation at the front and rear surfaces of a fused silica window by using a femtosecond laser pulse in air“ *Appl. Opt.* 6 671 (2004)

[3] Y. Bellouard, A. Said, M. Dugan and Ph. Bado „Fabrication of high-aspect ratio, micro-fluidic channels and tunnels using femtosecond laser pulses and chemical etching“ *Optics express* 12:10 17 pg 2120-9 (2004)

## FABRICATION AND CHARACTERIZATION OF MICROLENS ARRAYS FOR USAGE IN MULTIFOCUS DIRECT LASER WRITING

Linas Jonušauskas and Mangirdas Malinauskas

Department of Quantum Electronics, Vilnius University, Saulėtekio Ave., 9,  
Vilnius LT-10222, Lithuania  
[linas.jon@gmail.com](mailto:linas.jon@gmail.com)

Direct laser writing (DLW) technique based on multiphoton polymerization is an emerging micro- and nanostructuring technology that allows fabrication of freeform 3D objects [1] with features as small as tens of nanometers [2]. It was shown that this technology is capable of forming various micro- and nanostructures including photonic crystals [3], scaffolds for stem cell growth [4], microoptical elements [5] or combinations of these structures for specific usage [6].

However, this technology still has some drawbacks that limit its capabilities and wide spread usage. One of them is relatively slow fabrication throughput because of point-by-point fabrication nature. Although some microreplication technologies such as UV lithography [7] or soft lithography [8] could be employed to partially overcome this problem, most of these technologies offer only 2.5D or limited 3D geometrical architecture of replicated structures.

In this work we investigate possibility to increase DLW efficiency by using more than one focal point for microfabrication [9]. This could be achieved by adding microlens array in to DLW setup (Fig. 1). Various microlenses for such application are designed then fabricated using conventional DLW setup and characterized. Possible setup for microlens array positioning in DLW setup is proposed. Attempts to achieve multifocus polymerization are made.

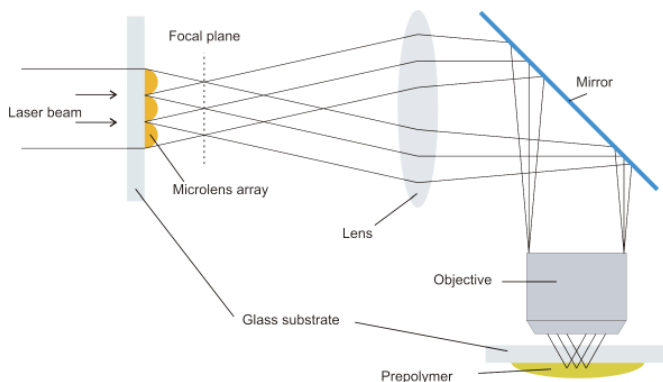


Fig. 1. Basic scheme of optical setup for multifocus polymerization

- [1] S. Juodkazis, V. Mizeikis and H. Misawa, Three-dimensional structuring of resists and resins by direct laser writing and holographic recording, *Adv. Polym. Sci.* **213**, 157-206 (2008).
- [2] M. Emons, K. Obata, T. Binhammer, A. Ovsianikov, B. N. Chichkov and U. Morgner, Two-photon polymerization technique with sub-50 nm resolution by sub-10 fs laser pulses, *Opt. Mater. Express* **273**, 942-947 (2012).
- [3] M. Straub, L.H. Nguyen, A. Fazlic and M. Gul, Complex-shaped three-dimensional microstructures and photonic crystals generated in a polysiloxane polymer by two-photon microstereolithography., *Opt. Mater.* **27**, 359364 (2004).
- [4] M. Malinauskas, P. Danilevicius, D. Baltriukienė, M. Rutkauskas, A. Zukauskas, Kairytė, G. Bickauskaitė, V. Purlys, D. Paipulas, V. Bukelskienė and R. Gadonas, 3D Artificial polymeric scaffolds for stem cell growth fabricated by femtosecond laser., *Lith. J. Phys.* **50**, 75-82 (2010).
- [5] M. Malinauskas, H. Gilbergs, A. Zukauskas, V. Purlys, D. Paipulas and R. Gadonas, A femtosecond laser-induced two-photon photopolymerization technique for structuring microlenses, *J. Opt.* **12** (2010).
- [6] J. Trull, L. Maigyte, V. Mizeikis, M. Malinauskas, S. Juodkazis, C. Cojocar, M. Rutkauskas, M. Peckus, V. Sirutkaitis and K. Staliunas, Formation of collimated beams behind the woodpile photonic crystal, *Phys. Rev.* **84**, 033812 (2011).
- [7] M. Hanm W. Lee, S.-K. Lee and S. S. Lee, 3D microfabrication with inclined/rotated UV lithography, *Sensor. Actuat. A-Phys.* **111**, 14-20 (2004).
- [8] Y. Xia and G. M. Whitesides, Soft lithography, *Annu. Rev. Mater. Sci.* **28**, 153-184 (1998).
- [9] S. Matsuo, S. Juodkazis, H. Misawa, Femtosecond laser microfabrication of periodic structures using a microlens array, *Appl. Phys.* **80**, 683685 (2005).



# Oral session 2

---

09:00  
Thursday

Semiconductor and condensed matter  
physics, material sciences

## INFLUENCE OF PHENYLETHENYL SIDE-MOIETIES ON EXCITON DIFFUSION IN TRIPHENYLAMINE COMPOUNDS

Steponas Rאיšsys<sup>1</sup>, Karolis Kazlauskas<sup>1</sup>, Marytė Daškevičienė<sup>2</sup>, Tadas Malinauskas<sup>2</sup>,  
Vytautas Getautis<sup>2</sup> and Saulius Juršėnas<sup>1</sup>

<sup>1</sup> Institute of Applied Research, Vilnius University, Lithuania

<sup>2</sup> Department of Organic Chemistry, Kaunas University of Technology, Lithuania  
[steponas.raisy@ff.stud.vu.lt](mailto:steponas.raisy@ff.stud.vu.lt)

Organic solar cells are a promising technology for future power generation. Recently the efficiency of bulk heterojunction organic solar cells has been doubled from 4–5% up to 10% by using new materials while keeping the same device structure. However, it is not entirely clear which material properties cause better device performances.

Exciton diffusion is one of the key-processes in the operation of organic solar cells. Excitons or bound electron–hole pairs created in organic semiconductors after absorption of light have to be separated into free charges in order to generate photocurrent. Such a separation is normally achieved at the interface of an electron accepting and electron donating materials. Excitons reach this interface by incoherent hopping, therefore the diffusion length determines the amount of excitons that can contribute to the photocurrent, and consequently, to the device efficiency. To this end, systematic measurements of exciton diffusion length are required to develop the synthetic guidelines for the enhancement of the solar cell efficiency.

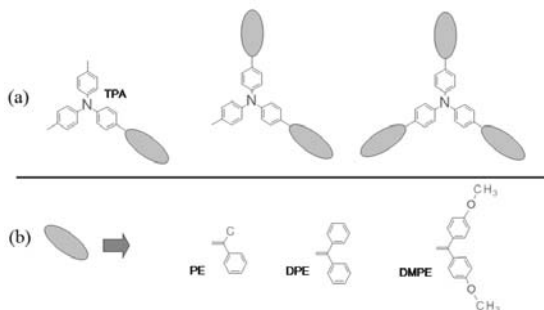


Fig 1. Chemical structure of triphenylamine derivatives (a) and the side-moieties (b).

In this work, exciton diffusion in a series of triphenylamine derivatives, known to possess excellent hole drift mobilities and having different number of 2,2-methylphenylethenyl, 2,2-diphenylethenyl and 2,2-di(4-methoxyphenyl)ethenyl side-moieties, were investigated (Fig. 1). Exciton diffusion was evaluated by measuring fluorescence quenching in the triphenylamine amorphous films with randomly distributed quenchers. In order to determine the exciton diffusion length, Monte Carlo simulation modeling of PL decays in organic semiconductor–quencher blends was performed [1]. The obtained data revealed that the increasing number of side-moieties results in higher exciton diffusion coefficient (up to  $5.4 \cdot 10^{-4} \text{ cm}^2/\text{s}$ ) and in increased exciton diffusion length varying from 3.1 nm to 11.1 nm. Intuitively, the incorporation of more side-moieties into the triphenylamine core makes molecular structure more branchy and should prevent dense molecular packing in the solid state resulting in reduced exciton diffusion length. However, in this particular case, phenylethenyl side-moieties most likely arrange themselves in a densely overlapping pattern, which facilitates exciton diffusion and results in the larger diffusion length.

Due to the large exciton diffusion length and outstanding hole drift mobility (up to  $1.7 \cdot 10^2 \text{ cm}^2/\text{Vs}$ ) [2] triphenylamine derivatives are attractive for application in high performance bulk heterojunction organic solar cells.

[1] O. V. Mikhnenko, H. Azimi, M. Scharber et al, Exciton diffusion length in narrow bandgap polymers, *Energy Environ. Sci.* **5**, 6960–6965 (2012).

[2] T. Malinauskas, D. Tomkute-Luksiene, M. Daskeviciene et al., One small step in synthesis, a big leap in charge mobility: diphenylethenyl substituted triphenylamines, *Chem. Commun.* **47**, 7770–7772 (2011).

## MESOPIC BIOLOGICALLY FRIENDLY LIGHT SOURCES BASED ON LIGHT CONVERSION IN PHOSPHORS

Akvilė Zabiľiūtė

Institute of Applied Research, Vilnius University, Saulėtekio al. 9, bldg. III, Vilnius LT-10222, Lithuania  
[akvile.zabiliute@fdi.lt](mailto:akvile.zabiliute@fdi.lt)

Light emitting diodes (LEDs) are promising sources for all lighting applications. The spectrum of common white LEDs (wLEDs) consists of an intensive peak in a blue region and a broad band in the yellow region. However in 2001, a non-visual photoreceptor in human retina was proven to exist [1]. This receptor responds to blue light and is responsible for biological effects such as alertness, circadian rhythm, blood circulation, etc. While during the day time blue light improves biological performance, in the dark time it can disturb circadian rhythm [1]. For this reason it is important to optimize spectra of LEDs used for outside applications under mesopic conditions. Theoretical optimization of a lightsource for outdoor applications using mesopic photometry is described in ref [2].

In this work, the chromaticity coordinates of spectral power distributions (SPDs) of a blue 440 nm LED and various yellow (garnets, silicates) and orange (silicates, selenides, aluminates) phosphors were calculated. Obtained data was used to model LEDs with SPDs that match the blackbody radiation. The chromaticity coordinates of modeled LEDs are shown in Fig. 1.

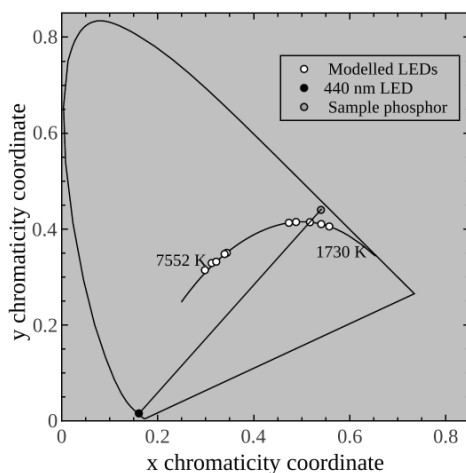


Fig. 1.  $xy$  chromaticity coordinates of modeled LEDs in CIE (1931) chromaticity diagram.

To characterize obtained SPDs, parameters like correlated color temperature (CCT), color rendition index (CRI), luminous efficacy of radiation (LER) and circadian action factor (CAF – the ratio of circadian efficacy of radiation and LER) were calculated. The results for two LEDs with different phosphors are given in the table below:

Phosphor	CCT, K	CAF, blm/W		LER lm/W		CRI	CRI (Mesopic)	
		(0.3 cd/m <sup>2</sup> )	(2 cd/m <sup>2</sup> )	(0.3 cd/m <sup>2</sup> )	(2 cd/m <sup>2</sup> )		(0.3 cd/m <sup>2</sup> )	(2 cd/m <sup>2</sup> )
Garnet	6513	0.636	0.716	385	342	63	85	73
Orthosilicate	2542	0.214	0.208	338	347	55	82	68

The results have shown that light sources, with smaller CCT values have lower values of CAF which means that they affect circadian rhythm less than the ones with high CCT. On the other hand, these kind of light sources tend to have lower values of CRI which makes lighting less pleasant for people. However, under mesopic conditions human ability to differ colors reduces thus the CRI value in this case a bit increases. The obtained results well agree with theoretical values.

[1] D. Lang, Energy Efficient Illumination for the Biological Clock, Proc. SPIE **7954**, 795402 (2011).

[2] A. Žukauskas, R. Vaitėkauskas, P. Vitta, Optimization of solid-state lamps for photobiologically friendly mesopic lighting, Appl. Opt. **51**, 8423–8432 (2012).

## PHOTOLUMINESCENCE IN InGaN QUANTUM WELLS WITH DIFFERENT WELL PROFILE

Augustas Vaitkevičius

Semiconductor Physics Department, Vilnius University, Saulėtekio Ave. 9-III, LT-10222 Vilnius, Lithuania.  
[Augustas.Vaitkevicius@ff.stud.vu.lt](mailto:Augustas.Vaitkevicius@ff.stud.vu.lt)

The band gap of ternary nitride compound, indium gallium nitride, can be adjusted by changing the ratio of indium atoms to gallium atoms. This makes InGaN materials attractive for use in optoelectronics and photovoltaics. InGaN is already widely used in commercially available blue and white light-emitting diodes (LEDs). However, attempts to manufacture LEDs emitting light at longer wavelengths encounter problems due to increased defect density, strong influence of internal electric field, and carrier localization. Thus, carrier dynamics in InGaN epilayers and heterostructures is still under intense study. One of the approaches to reduce the problems caused by increased internal field and defect density is using quantum wells (QWs) with unconventional, nonrectangular shapes.

In this work, the luminescence properties of QWs with three different shapes (rectangular, triangular, and trapezoidal) were compared. The differently shaped multiple quantum well (MQW) structures were grown using metalorganic chemical vapor deposition (MOCVD) on sapphire substrates at the Institute of Applied Research, Vilnius University. QWs with different shapes were grown by changing the growth temperature inside the MOCVD reactor while other growth parameters were maintained constant. The growth temperature and precursor gas flow rate were adjusted to keep the In content at 15-16% in the well bottom and at 8-10% at the top of the potential barrier in all samples. Moreover, the average In content varied along the wafer diameter due to temperature gradient.

The samples have been studied using confocal and atomic force microscopy. *WITec alpha300* microscope system coupled with a spectrometer was used. The photoluminescence spatial distribution was measured in confocal mode with 250 nm spatial resolution. Laser diode *ALPHALAS* emitting at 405 nm was exploited for excitation. Photoluminescence measurements were compared to the results on surface morphology obtained using the *WITec alpha300* system in atomic force microscopy mode.

The study evidenced more homogenous spatial distribution of photoluminescence in samples with triangular and trapezoidal QWs, as compared to rectangular QWs. The spatial distribution of luminescence intensity in different samples is compared in Fig. 1.

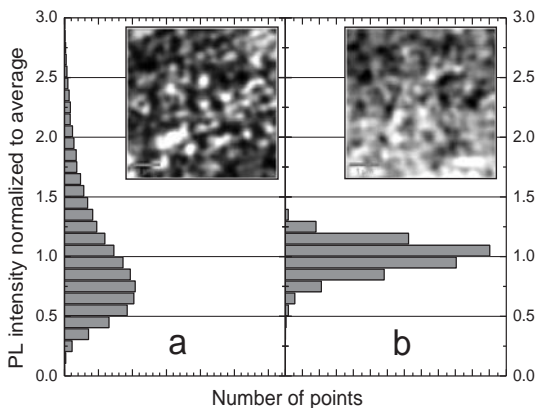


Fig. 1. Histogram of luminescence intensity distribution in rectangular (a) and triangular (b) quantum wells. The corresponding images of luminescence intensity mappings ( $4 \times 4 \mu\text{m}^2$ ) are presented in inserts.

As the indium content was increased, the samples with rectangular QWs exhibited an decrease in photoluminescence intensity and even higher inhomogeneity. Meanwhile, the samples with triangular and trapezoidal QWs showed an increase in photoluminescence intensity and better homogeneity. The correlation between local luminescence intensity and peak energy of the emission band have been calculated but did not show distinct features for different samples.

The investigation of luminescence spatial distribution and surface morphology show that InGaN structures with triangular or trapezoidal quantum wells are promising for development of green-yellow light emitters.

## GROWTH OF DIFFERENT SPATIAL PROFILES INGAN/GAN QUANTUM WELLS BY MOCVD AND RESEARCH

Mantas Dmukauskas<sup>1</sup>, Arūnas Kadys<sup>2</sup>

Institute of Applied Research, Vilnius University, Saulėtekio Ave. 9-III, LT-10222 Vilnius, Lithuania  
[mantasdmuk@gmail.com](mailto:mantasdmuk@gmail.com)

In these days ternary nitride compound, indium gallium nitride (InGaN) alloys are widely used in commercially available blue and white light-emitting diodes (LEDs) and light detectors [1]. The band gap of InGaN can be adjusted by changing the ratio of indium atoms to gallium atoms, that makes InGaN materials attractive for use in optoelectronics and photovoltaics. However, attempts to manufacture LEDs emitting light at longer wavelengths encounter problems due to increased defect density, high influence of internal electric field and carrier localization [2]. Some of the proposed ways to reduce these problems is using protective layers, ramping layers and quantum wells (QWs) with nonrectangular shapes.

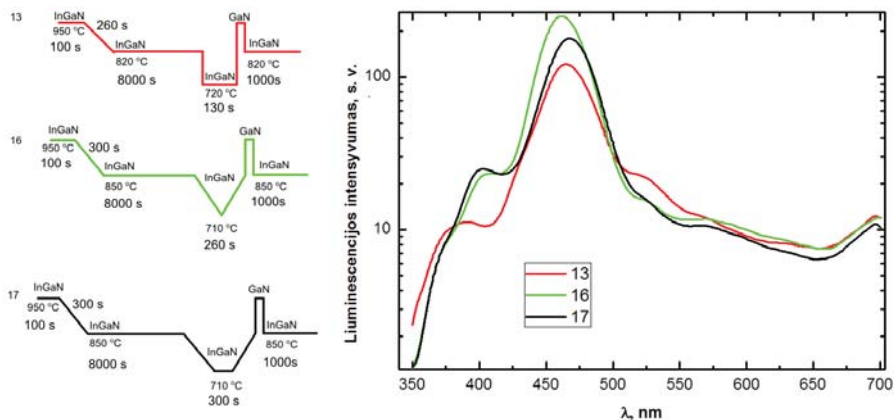


Fig.1. PL dependence on different spatial profile quantum wells.

This work was focused on growth of InGaN multi quantum well structures on GaN templates grown on (0001) sapphire substrates by MOCVD method [3]. In order to improve quality of InGaN layer intermediate layered structures between GaN template and quantum wells were used. Many technological experiments were carried out to find best intermediate structure. The quality of the samples was estimated from photoluminescence measurements. The best results were obtained in samples with intermediate ramped layer (with In gradient) and prolonged first InGaN barrier with triangular-shape multi quantum wells (Fig. 1.).

- [1] J. Wu, W. Walukiewicz, K. M. Yu, J. W. Ager, E. E. Haller, H. Lu, W. J. Schaff, Y. Saito, and Y. Nanishi, "Unusual properties of the fundamental band gap of InN," Applied Physics Letters, vol. 80, no. 21, p. 3967, 2002.
- [2] K. Kazlauskas, G. Tamulaitis, J. Mickevičius, E. Kuokstis, A. Žukauskas, Yung-Chen Cheng, Hsiang-Cheng Wang, Chi-Feng Huang, C. C. Yang, "Excitation power dynamics of photoluminescence in InGaN/GaN quantum wells with enhanced carrier localization", JOURNAL OF APPLIED PHYSICS 97, 013525 (2005)
- [3] Kai Fu, Growth Dynamics of Semiconductor Nanostructures by MOCVD, ISSN 1654-2312, 2009.

## MAGNETOTRANSPORT PROPERTIES OF AlGaIn/GaN HETEROSTRUCTURES

Eduardas Gvozdas<sup>1</sup>, Irmantas Kašalynas<sup>2</sup>, Gintaras Valušis<sup>2</sup>

<sup>1</sup>Faculty of Physics, Vilnius University, Lithuania

<sup>2</sup>Department of Optoelectronics, Center for Physical sciences and Technology, Vilnius, Lithuania  
[eduardas.eg@gmail.com](mailto:eduardas.eg@gmail.com)

Application of terahertz (THz) waves for security, medical diagnostic and imaging needs to develop compact and powerful THz emitters which could operate at room temperature. This work is dedicated to estimate a potential of technology of GaN based structures in developing high electron mobility transistors (HEMT) as possible THz emitters [1].

Magnetotransport measurements in strong magnetic field (up to 10 T) at low temperature (2 K) were performed to determine electron concentration and mobility in MOCVD (Institute of Applied Research, Vilnius University) grown AlGaIn/GaN heterostructures. From magnetoresistance curve analysis at weak magnetic field [2] electron mobility was found to be  $\mu = 2500 \text{ cm}^2 \text{ V}^{-1} \text{ s}^{-1}$ .

It was determined that Shubnikov-de Haas (SdH) oscillations start to appear at  $B = 3.5 \text{ T}$ . Analyzed data of experiment is shown in Fig. 1. It is seen that SdH oscillations' amplitude reflecting electron mobility dependence is sensitive to the direction of the applied magnetic field [3]. The main reason for this inequality is that the sample was placed not in the exact center of the magnetic field.

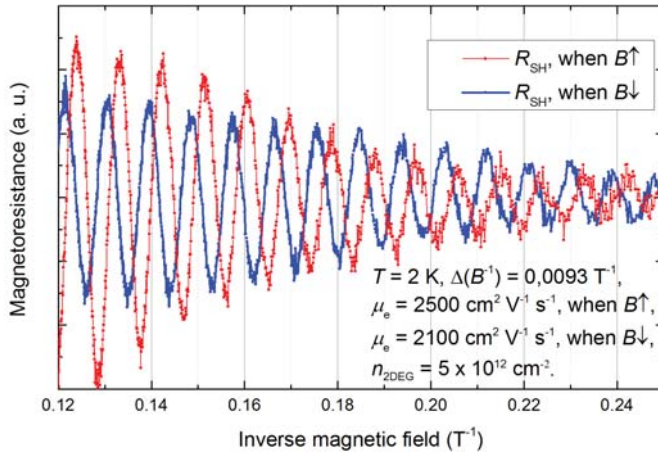


Fig. 1. Measured dependence of the magnetoresistance on the inverse magnetic field in AlGaIn/GaN heterostructure.

From the dependence of magnetoresistance on inverse magnetic field two dimensional electron gas (2DEG) concentration  $n$  was estimated using equation

$$\Delta\left(\frac{1}{B}\right) = \frac{e g_S g_L}{h n}, \quad (1)$$

where  $B$  is the magnetic field strength,  $e$  is the electron charge,  $h$  is the Planck's constant,  $g_S$  and  $g_L$  are electron spin and orbital  $g$ -factors respectively. The concentration of 2DEG is found to be  $5 \times 10^{12} \text{ cm}^{-3}$ .

[1] a. El Fatimy, N. Dyakonova, Y. Meziani, T. Otsuji, W. Knap, S. Vandenbrouk, K. Madjour, D. Théron, C. Gaquiere, M. a. Poisson, S. Delage, P. Prystawko, and C. Skierbiszewski, "AlGaIn/GaN high electron mobility transistors as a voltage-tunable room temperature terahertz sources," *Journal of Applied Physics*, vol. 107, no. 2, p. 024504, 2010.

[2] W. A. Beck and J. R. Anderson, "Determination of electrical transport properties using a novel magnetic field-dependent Hall technique," *Journal of Applied Physics*, vol. 62, no. 2, p. 541, Jul. 1987.

[3] A. Aronov, E. Altshuler, A. Mirlin, and P. Wölfle, "Theory of Shubnikov-de Haas oscillations around the  $\nu=1/2$  filling factor of the Landau level: Effect of gauge-field fluctuations," *Physical Review B*, vol. 52, no. 7, pp. 4708–4711, Aug. 1995.

# MODELING OF TEMPERATURE DEPENDENCE OF ALL-OPTICAL POLING TRANSIENTS IN POLYMERS

Armandas Balčytis<sup>1</sup>, Rolandas Tomašiūnas<sup>1</sup>, Raimondas Petruškevičius<sup>2</sup>

<sup>1</sup> Institute of Applied Research, Vilnius University, Lithuania

<sup>2</sup> Center for Physical Sciences and Technology, Lithuania  
armandas.balcytis@gmail.com

Azo-dye-containing polymeric films are currently the subject of intensive investigations because of their possible application in the areas of optoelectronics, photonics, and optical signal processing such as holographic memories, optical network modulators, switches, frequency converters and other photonic tunable devices [1]. All-optical poling is a novel method for inducing a second order nonlinear optical susceptibility  $\chi^{(2)}$  by light in a centrosymmetric polymer film [2]. Inasmuch as the optical ordering of photoisomerizable molecules is being intensively studied, its theoretical quantification is needed to bridge independent studies in the areas of optics and photochemistry.

In this work a comprehensive theoretical study of all-optical polling transients for chromophores embedded in polymer matrices is presented. A phenomenological model consisting of two coupled orientational diffusion equations for photoexcitation and re-orientation of azo-dye molecules in *trans* and *cis* states was utilized [3]:

$$\begin{cases} \frac{\partial n_t(\Omega)}{\partial t} = -\xi I(\theta) n_t(\Omega) + \phi \int \Phi(\Omega' \rightarrow \Omega) I(\theta') n_c(\Omega') d\Omega' + \frac{1}{\tau_c} \int G(\Omega' \rightarrow \Omega) n_c(\Omega') d\Omega' + D_t \nabla^2 n_t(\Omega) \\ \frac{\partial n_c(\Omega)}{\partial t} = -\phi I(\theta) n_c(\Omega) + \xi \int Q(\Omega' \rightarrow \Omega) I(\theta') n_t(\Omega') d\Omega' - \frac{1}{\tau_c} n_c(\Omega) + D_c \nabla^2 n_c(\Omega) \end{cases}, \quad (1)$$

where  $n_t(\Omega)$  and  $n_c(\Omega)$  are the densities of *trans* and *cis* isomers, respectively, with dipole momentum direction in the angle  $\Omega$ .  $\xi$  and  $\phi$  are the quantum efficiencies of *trans*-to-*cis* and *cis*-to-*trans* photoisomerization, respectively.  $\tau_c$  represents the thermal relaxation lifetime of *cis* isomers.  $G(\Omega' \rightarrow \Omega)$  is the probability for molecules to rotate from  $\Omega'$  to  $\Omega$  in the process of *cis*-to-*trans* thermal recovery.  $Q(\Omega' \rightarrow \Omega)$  and  $\Phi(\Omega' \rightarrow \Omega)$  respectively are probabilities of *trans*-to-*cis* and *cis*-to-*trans* optical transition.  $D_t$  and  $D_c$  are orientational diffusion constants for *trans* and *cis* isomers.

Numerical simulations of all-optical transients where calculated, and their sensitivity to relevant parameters such as orientational diffusion coefficient  $D_t$ , *cis* isomer lifetime  $\tau_c$  (Fig. 1) and excitation rate  $I$  was investigated. Numerical solutions of Eq. (1) were fitted to experimental data of all-optical poling of azophenylcarbazole at temperatures ranging from 140 to 300 K and relevant parameters were extracted.

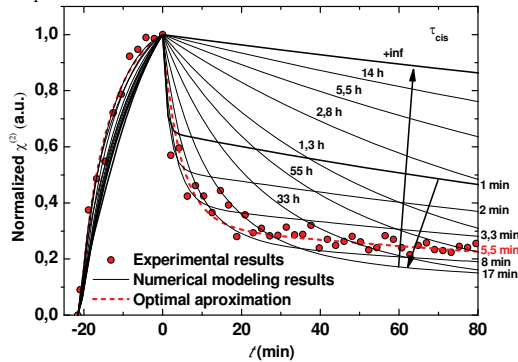


Fig. 1. Comparison of  $\tau_c$  dependent variation of all-optical poling transient simulation results (solid lines) and experimental all-optical poling transient of azophenylcarbazole molecules in polycarbonate at 300 K temperature (dots). Optimal numerical simulation of the experimental transient is presented as a dashed line.

Second order nonlinear optical susceptibility  $\chi^{(2)}$  gratings are created in chromophore doped polymer films by breaking the centrosymmetry of the system using the phenomena of orientational dependent hole burning and photoinduced molecular orientation [2]. By fitting  $\chi^{(2)}$  to experimental data, related linear optical susceptibility  $\chi^{(1)}$  data, which offers complementary information regarding the dynamics of chromophore photoorientation, was extracted.

It was determined, that dark lifetime of the *cis* isomer  $\tau_c$  is the main parameter which underlies the temperature dependent variation of all-optical poling transients in azophenylcarbazole doped polymers.

[1] Z. F. Liu, K. Hashimoto, and A. Fujishima. *Nature* **347**, 658 (1990).

[2] C. Fiorini, F. Charra, J.-M. Nunzi, P. Raimond: *J. Opt. Soc. Am. B* **14**, 1984 (1997).

[3] G. Xu, X. Liu, J. Si, P. Ye, Z. Li, Y. Shen, *Opt. Lett.* **25**, 329 (2000).

# Oral session 3

---

11:00  
Thursday

- Spectroscopy, methods and devices for physical diagnostics
- Functional materials and derivatives, modern technologies



## LOW FREQUENCY NOISE CHARACTERISATION OF BOW-TIE DIODES SENSORS FOR TERAHERTZ IMAGING

Mantas Ragauskas<sup>1,2</sup>, Linas Minkevičius<sup>2</sup>, Jonas Matukas<sup>1</sup>, Gintaras Valušis<sup>2</sup>

<sup>1</sup>Department of Radiophysics, Vilnius university, Lithuania

<sup>2</sup>Center for Physical Sciences and Technology, Lithuania

[Mantas.Ragauskas@ff.stud.vu.lt](mailto:Mantas.Ragauskas@ff.stud.vu.lt)

Electromagnetic radiation responding to frequencies of around  $10^{12}$  Hz (Terahertz, THz) has been quite underdeveloped due to the technological difficulties of creating reliable and compact sources and detectors of radiation. Hence, an important step in order to implement THz imaging systems is to develop sensors that would work effectively at room temperature. Currently, there are three dominating approaches in this activity: field-effect transistors with two-dimensional electron channels, microbolometers and bow-tie diodes.

InGaAs bow-tie diodes – they are called so due to the constructional features of the sensor (Fig. 1) – were found to be rather simple solution for THz detection [1]. The operation principle relies on creation of non-uniform electromagnetic field that arises in the semiconducting leaf of the diode when the incident radiation is concentrated to the latter by the metalized leaf part of the device. As a consequence, inhomogeneous field heats electrons that diffuse away from the necked part and thus generates dc voltage over the terminals.

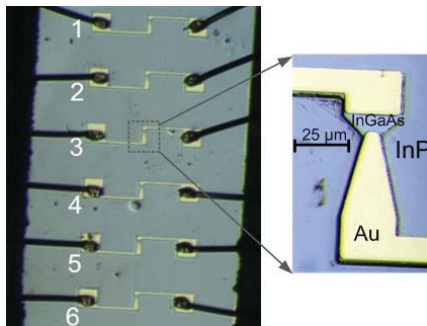


**Fig. 1** Array of six sensors and an image of single sensor. InGaAs is active zone and Au is covered antenna.

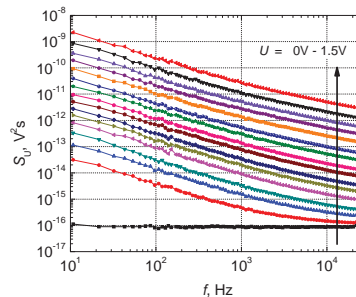


**Fig. 2** Spectral density of voltage fluctuations at room temperature with forward bias current.

By investigating characteristics of low-frequency (10 Hz to 20 kHz) noise it is possible to reveal physical processes behind the operation of sensors, to determine sources of noise and reveal therefore routes to improve noise characteristics of the device [2].

Investigation was carried out for an array composed of the line with 6 detectors (Fig. 1) in lattice temperature ranging from 77 K to 360 K. As it is seen from Fig. 2, at room temperature spectral density of voltage fluctuations varies approximately as  $1/f$  indicating that the origin of noise is superposition of generation and recombination processes in the defects of the structure. With the decrease in temperature, Lorentzian type spectra prevails over  $1/f$  type spectra and within 150 – 200 K all investigated samples exhibit characteristic time ranging from few to hundreds of microseconds. The estimated activation energies were found to be from 0.2 eV to 0.4 eV. These results allow to infer that structural defects are responsible for intensive generation and recombination process.

1. Irmantas Kašalynas, Rimvydas Venckevičius, and Gintaras Valušis, *Continuous wave spectroscopic terahertz imaging with InGaAs bow-tie diodes at room temperature*, *IEEE Sensors Journal*, 2013, Vol. 13, No. 1, 50-54 pages.
2. L. Minkevičius, M. Ragauskas, J. Matukas, V. Palenskis, S. Pralgauskaitė, D. Seliuta, I. Kašalynas and G. Valušis, *InGaAs bow-tie diodes for terahertz imaging: low-frequency noise characterisation*, (Paper 8496-37), Conference 8496 **Terahertz Emitters, Receivers, and Applications III**, 12 – 16 August 2012 San Diego Convention Center, San Diego, California, United States; SPIE Proc. 2012, Vol. **8496**, art. no. 849612, 6 pages.

## HOLOGRAPHIC RECORDING IN AZO POLYMER FILMS

Jelena Aleksejeva, Janis Teteris

Institute of Solid State Physics, University of Latvia  
[aleksejeva.jelena@gmail.com](mailto:aleksejeva.jelena@gmail.com)

In this work surface relief holographic recording in Poly(Disperse Red 1 – methacrylate) thin films polymer was studied. Azo dye DR1 in this compound is chemically bonded to polymer chain what makes mass transport and surface relief formation more efficient and faster. This phenomenon can find further application in optoelectronics, data storage, and telecommunication devices [1-3].

Thin films of Poly(DR1-MA) were prepared using different solvent in order to obtain films with different thickness. For sample preparation different coating methods were used. That effected thickness and quality of the sample.

Holographic recording by solid-state diode-pumped laser with 532 nm wavelength was performed. Read-out by diode laser with 660 nm wavelength was made. Efficient surface relief grating formation was observed using

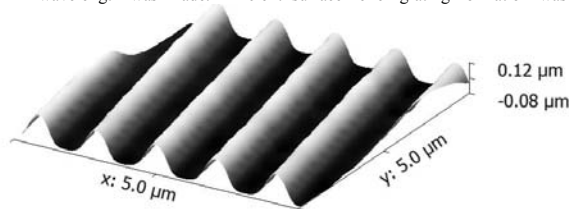


Fig. 1. Surface relief grating recorded in Poly(DR1-MA) thin film.

polarization state of recording beams which gives polarization modulation on the sample surface. Surface relief formation dependence on exposure, recording beam intensity, thickness of the sample and recording beam polarization state was studied. Grating formation was observed in wide range of recording beam intensities, but the depths of grating exceed the thickness of the sample and reached nearly double sample thickness.

Obtained results shows Poly(DR1-MA) copolymer is promising material for holographic recording and applicable in lithography for surface patterning.

[1] C. Fiorini, N. Prudhomme, G. de Veyrac, I. Maurin, P. Raimond, J.-M. Nunzi, *Molecular migration mechanisms for laser induced surface relief grating formation*, *Synthetic materials*, **115**, p. 121-125, (2000).

[2] Shane J. Strutz, L. Michael Hayden, *Effect of* *Journal of Polymer Science: Part B: Polymer Physics*, Vol **36**, p. 2793-2803, (1998).

[3] L. Rocha, V. Dumarcher, E. Malcor, C. Fiorini, C. Denis, P. Raimond, B. Geoffroy, J.-M. Nunzi, *Photo-induced microstructured polymers for the optimization and control of organic devices emission properties*, *Synthetic Metals*, **127**, p. 75-79, (2002).

## SINGLE MOLECULE SPECTROSCOPY: DNA DETECTION

Paulius Naujalis<sup>1</sup>, Danielis Rutkauskas<sup>2</sup>

<sup>1</sup> Department of Medicine, Vilnius University, Lithuania

<sup>2</sup> Center for physical sciences and technology, Lithuania  
[P.Naujalis@GMail.com](mailto:P.Naujalis@GMail.com)

Two decades ago two scientists from USA managed to show that they detected absorption of fluorescence from single molecule [1]. Since then many scientists worldwide are using different techniques to detect and gather different information from single molecules.

In center for physical sciences and technology single molecule spectroscopy was build and has two options to detect single molecules: using wide field and confocal fluorescence microscopies. Short DNA structures were labeled with two different cyanine dyes: Cy3 and Cy5, third group was labeled with both dyes. Cy3 dyes fluorescence at 560 nm wavelength and Cy5 at approximately 660 nm wavelength [2]. For excitation was used 532 nm wavelength solid state laser.

Detection fluorescent light was possible in two ways: using EM-CCD or Avalanche photo diode. Both detectors count photons which hit detector matrix.

Single molecule experiment requires high quality cleanliness - this makes preparation for experiment difficult. Also cyanine dyes react with oxygen. Those two factors lead us to create a sample cell. Two versions of cells were made, but the construction of them were similar. Two microscope slides were separated with Teflon spacer to create a cell between two glass windows. One glass window has two drilled holes where Teflon pipes are connected for flowing liquids. This kind of cell is gently pressed with two plastic frames to seal it.

DNA chains has negative charge, so does the microscope slide after cleaning in plasma cleaner [3]. For this reason slides were functionalized with mono layer in two ways. One with protein poly-L-lysine, other with antigen Anti-digoxigenin. Mechanics of both molecular functionalization are different, but effect is similar, DNA connects to mono layer of protein or antigen. Empty space in cell is filled with buffer which does not have fluorescence signal.

All experiment is automatized with "Lab View" software. Three axial cell table, shutters, detectors, cameras and other electronics are controlled by computer.

Data: it is possible to register spectra, time how long particles were able to fluorescent (dynamics) and compare photon counts of different particles.

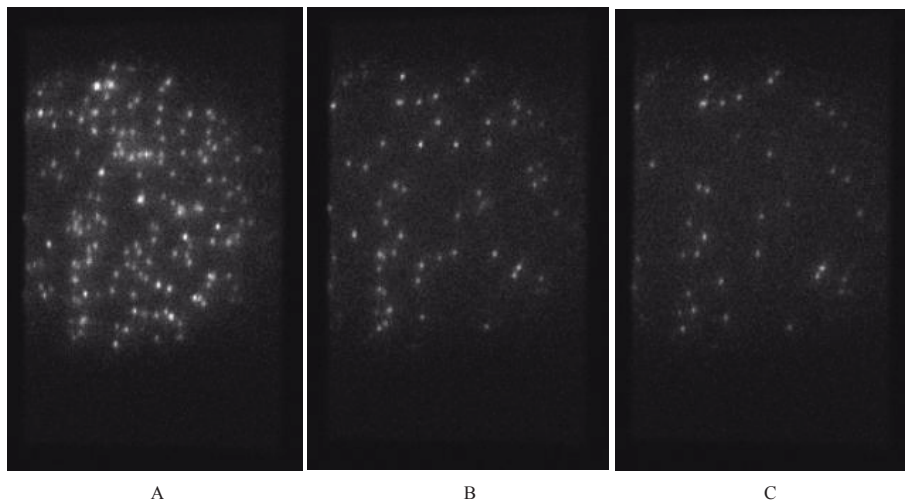


Fig. 1. DNA dye fluorescence decay over 8 seconds.

[1] William Esco (W. E.) Moerner CURRICULUM VITAE 2012

[2] Amersham CyDye (Cy3/Cy5) Reactive Dye Protocols for Post Labelling Aminoallyl-cDNA and Aminoallyl-aRNA For Microarray Applications. UK Healthcare 2009

[3] Plasma cleaning of surfaces. A. Belkind, S. Gershman. Vacuum technology and coating 2008.

## DETERMINING THE AGE OF BRUISES DEPENDING ON THE BILIRUBIN CONCENTRATION USING SPECTRAL IMAGING

Marta Lange<sup>1</sup>, Inga Saknite<sup>2</sup>, Dainis Jakovels<sup>2</sup>, Janis Spigulis<sup>2</sup>

<sup>1</sup> Institute of Biomedical Engineering and Nanotechnology, Riga Technical University, Latvia

<sup>2</sup> Institute of Atomphysics and Spectroscopy, University of Latvia, Latvia

[marta.lange.rtu@gmail.com](mailto:marta.lange.rtu@gmail.com)

Nowadays one of the most important aspects in medicine is fast and non-invasive diagnostics. Optical methods, including spectral imaging are one of them. The aim of this research is to determine bilirubin concentration difference, estimate it to define when exactly the bruise was made or how old it is. [1]

RGB imaging device was used as a simple multispectral camera for image acquisition. Bilirubin concentration distribution maps were obtained from R, G, B image cube. Bilirubin absorption is in the Blue (B), channel and the Red (R) channel can be used as a reference, because both: bilirubin and blood absorption peak is close to the minimum. The Green (G) channel can be used for correction to exclude the blood absorption. [2] MatLab program was used for data processing. To get precise results, MatLab tool for image registration was used: the series of images of the same bruise were put into a 4D matrix, as a result any parameter values can be registered in desired region of image in time. (Fig.1) Later the data was analyzed using Principal component analysis (PCA) tool.

The acquired data gives a great investment in bilirubin concentration statistical estimation, taking into account that more than 300 images of bruises were taken and analyzed of different persons in various parts of the body where the properties of bruising can differ.

To sum up, multispectral imaging in range of 470 nm and 640 nm can be used for detecting bilirubin concentration. Results show that bilirubin concentration maximum reaches its peak at 5th-7th day after trauma that matches the reference, but it can vary due to the dislocation of the bruise, how close it is to the bone area, the mealiness of the tissue, metabolism and volunteer's age, etc. With the data evaluation method it is possible to determine the age of the bruise with +/- 1,5 day precision.

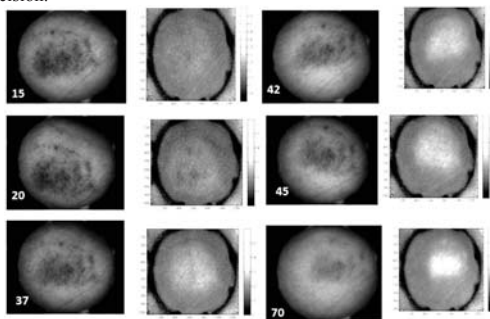


Fig. 1. The changes of bilirubin concentration over time (hours). Female, 23 years old, bruise on the neck, II Fitzpatrick skin type.

[1] Randeberg, L.L. Diagnostic applications of diffuse reflectance spectroscopy, ISBN 82-471-7077-9, Norwegian University of Science and Technology, 2005:100)

[2] I.Saknite, D.Jakovels, J.Spigulis, Distant determination of bilirubin distribution in skin by multi-spectral imaging, Latv J.Phys.Techn.Sci., 2011, No.2, 50-55.

## MULTI-SPECTRAL IMAGING DEVICE FOR SKIN DIAGNOSTICS

Inga Saknīte<sup>1</sup>, Valērijs Garancis<sup>1</sup>, Liene Elste<sup>1</sup>, Eriks Zaharans<sup>1</sup>, Janis Zaharans<sup>1</sup>, Oskars Rubenis<sup>1</sup>, Edgars Kviesis<sup>1</sup>, Janis Spigulis<sup>1</sup>

<sup>1</sup>Institute of Atomic Physics and Spectroscopy, University of Latvia, Latvia  
[inga.saknite@lu.lv](mailto:inga.saknite@lu.lv)

Nowadays, a non-invasive technique for assessment of different skin lesions is a must for medical doctors. For dermatologists, there are already quite a lot of different devices in the market that can be used for skin diagnostics, for example, a dermatoscope, *MelaFind*, *Siascope*, etc. However, dermatologists' experience is that none of these devices is very trustworthy and precise, as well as most of them are very expensive. All of these devices have wires to connect them to a computer or some other screen for data analysis.

In this study, a multi-spectral imaging device is developed and clinically tested. The main advantages of this device are: it is non-expensive, wireless; it gives chromophore maps, as well as different parameter values that are important for dermatologists for skin diagnostics. The first prototype of this device has already been tested clinically and evaluated by dermatologists.

The device is constructed as a cylinder that has all the electronic instalments in one half of it, but the other half consists of a ring of LEDs (450 nm, 545 nm, 660 nm, and 950 nm) with a simple RGB camera in the middle of it [1]. There is a *Start* button and an SD card slot on top of the cylinder. The SD card collects all data and can then be inserted into a PC for analysis of the data by software that has been developed and written in *Matlab*. It is then possible to analyse results of chromophore maps (bilirubin, hemoglobin), as well as maps of different parameters (erythema index, bilirubin index). An example is shown in Figure 1.

The first results of the device shows that it is possible to acquire all the needed parameters for assessment and early diagnostics of different skin lesions, for example, birthmarks, melanoma etc. However, there are some technical advancements still to be done. The future work includes development of the second prototype of this device.

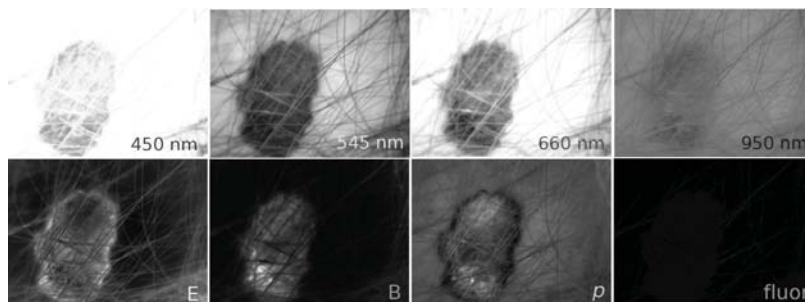


Fig. 1. Skin lesion at different wavelengths (on top) and parameter maps (on bottom): erythema index, bilirubin index, parameter p, fluorescence

---

[1] Jakovels, D., Spigulis, J., Rogule, L. RGB Mapping of Hemoglobin Distribution in Skin. *Proceedings of SPIE*, 2011, vol. 8087, 80872B

# Oral session 4

14:00

Thursday

- 
- Chemistry and chemical physics

## AQUEOUS SOL-GEL SYNTHESIS METHOD: SUITABLE TECHNIQUE FOR THE PREPARATION OF DIFFERENT CERAMIC MATERIALS

Rūta Stankevičiūtė<sup>1</sup>, Artūras Žalga<sup>1</sup>

<sup>1</sup>Department of Inorganic Chemistry, Vilnius University, Lithuania

The sol-gel process is a method to obtain ceramic materials through the condensation in solution of metallo-organics precursors, the condensation of the sol in a gel. In essence, the process begins by hydrolysis and polycondensation of precursors in solution, using a suitable catalyst, to form a colloidal suspension of nanometer scale particles. This sol is then coated onto a surface or cast into a mould, after which further condensation produce a rigid network. Therefore, in the least several decades, sol-gel techniques have been used to prepare variety mixed-metal oxides. In these sol-gel processes, good quality of the oxide products was expected primarily due to the purity of the precursor materials used and chemical homogeneity obtained from the synthesis route [1].

By definition, a sol is a suspension of colloidal particles in a liquid. A sol differs from a solution in that a solution is a single-phase system, whereas a sol is a two-phase, solid-liquid system. Colloidal particles can be in the approximate size range of 1-1000 nm, hence gravitational forces on these particles are negligible and interactions are dominated by short-range forces, such as van der Waals and surface charges. Brownian motion leads to a low energy arrangement, thus imparting stability to the system. If a three dimensional network of the formerly dispersed colloidal particles is formed, the structure is called a gel. Removal of the liquid phase results in the formation of xerogels, which only consist of the solids structure.

The sol can be produced starting both from organic or inorganic precursors, which consist of a metal or metalloid element surrounded by various organic ligands and the whole process is conducted at room temperature. The peculiar thing is that the solid state can be reached at low temperature starting from a solution, and this fact expands greatly the possibility to create new materials or to improve their properties [2].

The technological applications of the sol-gel technique range in a very wide field, because of the versatility and simplicity of the method. The possible applications derive from the various shapes that can be obtained from the gel state and from the compositional and microstructural control of the process, combined with the low processing temperature.

The reason of searching new sol-gel synthesis ways in order to reduce the cost and toxicity of preparation technique also is very desirable. One of the best solutions of these problems is employing the water instead of organic solvents during the main sol-gel synthesis step. As a result aqueous sol-gel synthesis method also could be successfully applied for the preparation of different ceramic compounds. So, this aqueous sol-gel technique is really attractive and compared to other techniques, as it has the advantages of a good control of the starting materials and of the processing parameters, a high purity of the raw materials, and the low temperature of the process [3].

Thus, in this oral presentation we show the aqueous sol-gel synthesis of different molybdates and tungstates combined with alkaline earth metals and different lanthanides. The all obtained samples were characterized by X-ray diffraction (XRD) analysis, scanning electron microscopy (SEM) and UV-Vis spectroscopy. Moreover, the investigation of the influence of two complexing agents, namely tartaric and citric acids, and slightly different starting materials on the characteristics of final oxides was also performed.

**Acknowledgements** This work was partly supported by project "Promotion of Student Scientific Activities" (VP1-3.1-ŠMM-01-V-02-003) from the Research Council of Lithuania (Rūta Stankevičiūtė). This project is funded by the Republic of Lithuania and European Social Fund under the 2007-2013 Human Resources Development Operational Programme's priority 3.

---

[1] T. Klemkiene, R. Raudonis, A. Beganskiene, A. Zalga, I. Grigoravičiute, A. Kareiva, Scandium and gallium substitution effects in the (Y1-xScx)Ba2Cu4O8 and (Y1-xGax)Ba2Cu4O8 superconducting oxides. *Mater Chem Phys* **2010**, 119, 208-213.

[2] Encyclopedia of Inorganic Chemistry, DOI: 10.1002/0470862106.

[3] A. Zalga, Z. Moravec, J. Pinkas, A. Kareiva, On the sol-gel preparation of different tungstates and molybdates. *J Therm Anal Calorim* **2011**, 105, 3-11.

## COMPARISON OF PHASE COMPOSITION OF $\text{TiO}_2\text{-MoO}_3$ NANOCOMPOSITE SYSTEMS SYNTHESIZED BY DIFFERENT METHODS

Natalia Boboriko

Department of Chemistry, Belarusian State University, Minsk, Belarus  
*natchem@tut.by*

Multioxide  $\text{TiO}_2\text{-MoO}_3$  systems with different oxide molar ratio find industrial application as catalysts of dehydration, oxidation, ammoxidation et al. These systems also can be used as gas sensing layers of solid state chemical sensors. Our earlier investigations [1] showed the availability of using  $\text{TiO}_2\text{-MoO}_3$  multioxide systems as gas sensing materials for hydrogen detection. It is widely known, that gas sensing properties of multioxide materials depend on their phase composition. This work is dedicated to the comparison of crystalline phase composition of  $\text{TiO}_2\text{-MoO}_3$  systems, synthesized by three different ways. The first one is traditionally used penetration method, where  $\text{TiO}_2$  powder is impregnated by water solution of ammonium molybdate with subsequent drying and thermal treatment. The second one is colloid-chemical method of synthesis. Colloid-chemical synthesis allows obtaining multioxide materials with developed surface and high level of homogeneity at molecular level, with modified phase composition and controllable structural peculiarities. All this makes it possible to influence physical macroscopic properties of synthesized material, which are dependent on surface and structural features, by the change of synthesis parameters such as the nature of precursors, rate of stirring, pH level and heat treatment conditions. And the third synthetic way is synthesis of  $\text{TiO}_2\text{-MoO}_3$  system by mixing of individual powders of  $\text{TiO}_2$  and  $\text{MoO}_3$  in quantitative ratio with subsequent thermal treatment.

To prepare samples by penetration method pure  $\text{TiO}_2$  powder was used (it was synthesized by drying of  $\text{TiO}_2\cdot n\text{H}_2\text{O}$  sol and its subsequent annealing at 850 °C for 2 hours). Precise amount of  $\text{TiO}_2$  powder was drowned into ammonium paramolybdate aqueous-ammonia solution, dried thereafter at 80 °C and annealed at 450 and 850 °C. Amount of ammonium paramolybdate solution varied to obtain multioxide systems with 1, 5 and 10 mol.%. Colloid-chemical synthesis of  $\text{TiO}_2\text{-MoO}_3$  multioxide materials comprised obtaining of  $\text{TiO}_2\cdot n\text{H}_2\text{O}$  sol on the basis of  $\text{TiCl}_4$  solution in hydrochloric acid and subsequent modification of the obtained sol with calculated amount of ammonium paramolybdate to obtain initial sols for  $\text{TiO}_2\text{-MoO}_3$  system formation with  $\text{MoO}_3$  content of 1, 5 and 10 mol.%. After heating titanium hydrated oxide  $\text{TiO}_2\cdot n\text{H}_2\text{O}$  and ammonium paramolybdate  $(\text{NH}_4)_6\text{Mo}_7\text{O}_{24}$  decomposed to produce  $\text{TiO}_2$  and  $\text{MoO}_3$  correspondingly. After drying samples were heated at 450, 600 and 850 °C. The third set of samples was prepared by mixing of  $\text{TiO}_2$  and  $\text{MoO}_3$  powders with subsequent heating at 450 and 850 °C.

To investigate phase composition of synthesized materials XRD analysis was used. It was established, that phase composition of samples, synthesized by colloid-chemical method depends both on quantitative component ratio in multioxide systems and on the annealing temperature. Addition of molybdenum trioxide to titanium dioxide shifts anatase-rutile transformation to high temperature region. For  $\text{TiO}_2\text{-MoO}_3$  samples annealed at 450 °C and 600 °C crystallographic phase of rutile was not registered, while for pure  $\text{TiO}_2$ , annealed at this temperature, both phases of anatase and rutile were present. Formation of  $\alpha\text{-MoO}_3$  crystal phase is observed after heating samples with 5 and 10 mol.% of  $\text{MoO}_3$  at 600 °C. For sample with 1 mol. % of  $\text{MoO}_3$  masking of  $\alpha\text{-MoO}_3$  phase is distinctive. Annealing at 850 °C leads to the formation of rutile phase only and destruction of crystallographic phase of  $\alpha\text{-MoO}_3$  for all samples.

Samples synthesized by mixing of individual powders of  $\text{TiO}_2$  and  $\text{MoO}_3$  are characterized by the presence of rutile, anatase and  $\alpha\text{-MoO}_3$  crystalline phases after drying at 80 °C and annealing at 450 and 600 °C. Heat treatment at 850 °C leads to the formation of rutile crystalline phase only.

Synthesis by penetration method leads to the formation of rutile crystal phase after heating at 450 °C, rutile and  $\alpha\text{-MoO}_3$  crystal phases after heating at 600 °C and rutile phase after heat treatment at 850 °C.

Thereby the best way to synthesize  $\text{TiO}_2\text{-MoO}_3$  multioxide system with different oxide ratio for gas sensing applications is colloid-chemical method, as this method allows controlling of phase composition of the material by the quantity of  $\text{MoO}_3$  in the system and by the value of the annealing temperature. Use of this method makes it possible to preserve  $\text{TiO}_2$  in anatase crystal phase, which is important for practical applications.

[1] D.I. Mychko, N.E. Boboriko, G.F. Karkotsky, N.S. Dashko Influence of doping materials on titanium dioxide gas sensing properties / Sviridov Readings – 2012. Abstract book. Minsk. 2012. P. 27.



# STUDY OF OH GROUP VIBRATIONS IN THE PYRIDINE N-OXIDE/TRICHLOROACETIC ACID COMPLEX IN ACETONITRILE USING FTIR SPECTRA AND 1D AND 2D POTENTIAL SURFACES

E.Kozlovskaya<sup>1</sup>, G.Pitsevich<sup>1</sup>, A.Malevich<sup>1</sup>, V.Sablinskas<sup>2</sup>, V.Balevicius<sup>2</sup>

<sup>1</sup>Belarusian State University, Minsk, Belarus

<sup>2</sup>Vilnius University, Vilnius, Lithuania

[kozlovskayaen@gmail.com](mailto:kozlovskayaen@gmail.com)

The detailed understanding of short and very short H-bonds with large-amplitude proton dynamics is challenging task that requires joint efforts of the best available experimental techniques and the most advanced theoretical treatments. Pyridine N-oxide (PyO) or its derivatives in the complexes with various acids can be used as very convenient model systems to improve the understanding of the nontrivial physical features of short H-bonding. v. Such systems exhibit in many cases very asymmetric and rather flat H-bond potentials, which allow large-amplitude proton motion with the possible proton transfer through such linkages. The literature sources on computations of the IR spectra even for the simplest complexes with a hydrogen bond using the anharmonic approximation are just a few available.

Computations of the spectral and structural characteristics of trichloroacetic (TCA) and PyO-TCA were performed using the package GAUSSIAN 09 in the approximation B3LYP/cc – pVTZ. B3LYP is one of the approaches in a density functional theory designed to include the exchange and electron correlation effects. As shown by our previous studies, computations in the approximations B3LYP/cc – pVDZ and B3LYP/cc – pVTZ reproduce well frequencies of the harmonic vibrations and the shape of the potential-surfaces for some organic molecules. In the process of optimization of the geometry for these compounds, the fact that minima on the potential surface were reached has been supported by the absence of imaginary frequencies in vibrational spectra. IR spectra of these compounds were computed in the harmonic and anharmonic approximations. In case of the latter the frequency shifts of the fundamental vibrations due to Fermi and Darling-Dennison resonances were included as well.

As seen in Fig. 1, X axis is coincides with the hydroxyl bond lying in the plane XOY. It is clear that motion of the hydrogen atom along the axis X may be associated with the stretching vibration, whereas its motion along the axis Y may be associated with the in-plane and along the axis Z – out-of-plane bending vibrations of the hydroxyl group. During the computations it was assumed that motion of a hydrogen atom is independent of other atoms in the molecule within the potential field formed between two oxygen atoms. We have computed the complex energies at more than 300 points by positioning the hydroxyl atom H<sub>13</sub> at the certain nodes of 1D and 2D meshes, without geometrical optimization of the complex for the remaining geometrical parameters.

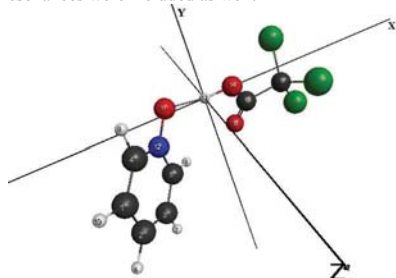


Fig. 1. Equilibrium configuration and direction of the Cartesian axis of the PyO-TCA complex in acetonitrile.

During calculations according [1] the frequencies of hydroxyl group vibrations were found in 1D and 2D approaches. The results are listed in Table 1.

Table 1. Frequencies of the O-H group vibrations in different approaches.

Vibrational mods	1DX (cm <sup>-1</sup> )	1DY (cm <sup>-1</sup> )	1DZ (cm <sup>-1</sup> )	2DXY (cm <sup>-1</sup> )	2DXZ (cm <sup>-1</sup> )	2DYZ (cm <sup>-1</sup> )	Harm. (cm <sup>-1</sup> )	Unharm. (cm <sup>-1</sup> )
$\nu_{OH}$	1070	–	–	1078	1057	–	2105	350
$\delta_{OH}^{ip}$	–	1395	–	1387	–	1392	1472	1414
$\delta_{OH}^{oop}$	–	–	1220	–	1226	1220	1233	1187

As one can see from Table1, the anharmonic frequencies of the bend modes of hydroxyl group are in a good agreement with our results in 1D and 2D approximation. However, this is not so in the case of stretching vibrations. And since, according to the experimental data maximum of the absorption band associated with  $\nu_{OH}$  is located near 1100 cm<sup>-1</sup> it is clear that anharmonic approximation fails to predict the frequency of the stretching vibration of the hydroxyl group in PyO-TCA complex.

[1] G. A. Pitsevich, A. E. Malevich, OPJ Vol. 2, P.332, ( 2012).

## STEREOSELECTIVITY OF REACTION BETWEEN SALICYLALIMINES AND *H*-PHOSPHONATES

Paweł Tokarz<sup>1</sup>, Jarosław Lewkowski<sup>1</sup>, Anna Krzyczmonik<sup>1</sup>, Tadeusz Lis<sup>2</sup>, Katarzyna Ślepokura<sup>2</sup>

<sup>1</sup>Department of Organic Chemistry, University of Łódź, Poland

<sup>2</sup>Department of Chemistry, University of Wrocław  
[paweltokarz.chem@gmail.com](mailto:paweltokarz.chem@gmail.com)

Compounds derived from 1,2-(*R,R*)-diaminocyclohexane (DACH) play a crucial role in the modern chemistry of chiral synthesis. One of the most spectacular substances, derived from this simple amine, are macrocyclic molecules that can be obtained by so-called *cyclocondensation* [1]. Such macrocycles have found numerous applications, only to mention a few – the asymmetric catalysis or the chiral recognition of biologically active agents [2][3].

Until now little is known about modified structures of DACH-based macromolecules, in particular, those containing lipophilic substituents. We have decided to provide a simple and stereoselective method of the introduction of long carbon chains into the macrocyclic moiety. We have used dialkyl phosphites as chain carriers. In this way it was possible for us to introduce two chains per one azomethine bond. We developed a novel synthetic protocol applying use of sodium hydride which gave us diastereoisomeric excesses as high as 99% for acyclic model systems. In case of the large, cyclic systems the problem becomes more complex due to a number of possible isomeric products.

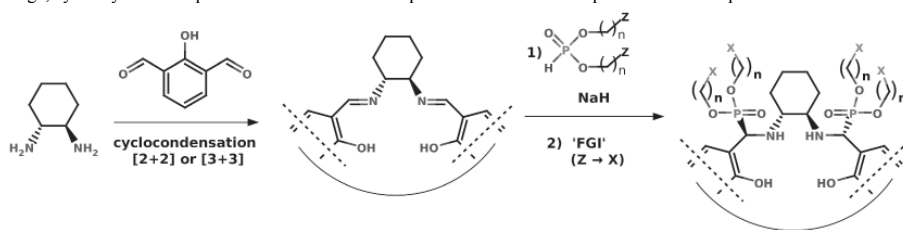


Fig. 1. Synthetic protocol to obtain new chiral molecules and macromolecules.

During the talk our recent achievements in this field will be presented.

- [1] N. E. Borisova, M. D. Reshetova, Y. A. Ustynyuk, Metal-free methods in the synthesis of macrocyclic schiff bases, Chem. Rev. **107**, 46-79 (2007).
- [2] G. Zhou, Y. Cheng, L. Wang, X. Jing, F. Wang, Novel Polyphenylenes Containing Phenol-Substituted Oxadiazole Moieties as Fluorescent Chemosensors for Fluoride Ion, Macromolecules, **38**, 2148-2153 (2005)
- [3] R. D. Hancock, Macrocycles and their selectivity for metal ions on the basis of size, Pure Appl. Chem., **58**, 1445-1452 (1986).

## EVALUATION OF LINKED PROTONATION EFFECTS UPON INHIBITOR BINDING TO HUMAN CARBONIC ANHYDRASES

Joana Gylytė, Asta Zubrienė, Daumantas Matulis

Department of Biothermodynamics and Drug Design, Vilnius University Institute of Biotechnology, Vilnius, Lithuania  
[gylyte@ibt.lt](mailto:gylyte@ibt.lt)

Inhibition of enzymes is important in drug design. Inhibitor interactions with carbonic anhydrases (CA) depend on ionization properties of the inhibitor functional groups and the active site residues in the enzyme. Changes in the protonation of protein, ligand and buffer affect the observed thermodynamic parameters of binding, such as the Gibbs free energy  $\Delta G$ , enthalpy  $\Delta H$ , and entropy  $\Delta S$ . Each binding reaction should be dissected in order to determine the intrinsic thermodynamic parameters that are independent on experimental conditions.

In this work, we present the evaluation of linked protonation reactions upon sulfonamide inhibitor binding to human CAs. There are 12 catalytically active CA isozymes in human body and most of them have been established as therapeutic targets and the sulfonamide inhibitors have been used as diuretics, antiglaucoma agents, antiepileptics, and anticancer agents [1]. The inhibitor binding affinity to a CA was determined using isothermal titration calorimetry (ITC) and the thermal shift assay (TSA, also called ThermoFluor®). ITC is a powerful technique for direct measurement of observed thermodynamic parameters ( $\Delta G$ ,  $\Delta H$ , and  $T\Delta S$ ). TSA is a rapid and sensitive tool to monitor protein stability and determine the Gibbs free energy of inhibitor binding to enzyme. The combined use of these methods provides a detailed picture of the thermodynamics of the protein-ligand interactions.

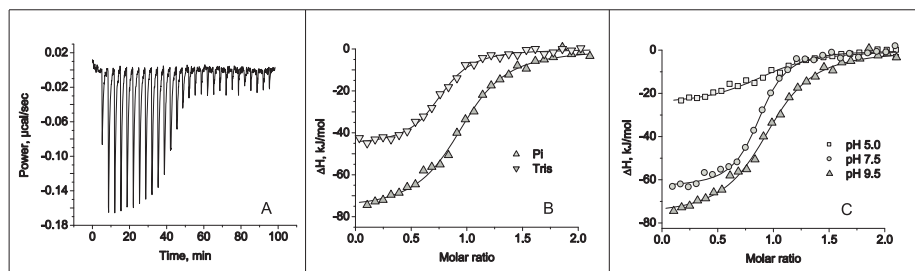


Fig. 1. A panel shows ITC raw data for EZA binding to CAXII in Tris buffer at pH 8.0, 37 °C. B panel shows integrated ITC data for EZA binding to CAXII in phosphate and Tris buffers at pH 9.5, 37 °C. C panel shows integrated ITC data for EZA binding to CAXII at pH 5.0, pH 7.5, pH 9.5 in phosphate buffer, 37 °C.

[1] V. Alterio, A.D. Fiore, K. D'Ambrosio, C.T. Supuran, D.G. Simone, Multiple Binding Modes of Inhibitors to Carbonic Anhydrases: How to Design Specific Drugs Targeting 15 Different Isozymes. *Chemical Review* **112**, 4421-4468 (2012).

## EPIGALLOCATECHIN-3-GALLATE AS A POTENTIAL INHIBITOR OF INSULIN AMYLOID-LIKE FIBRIL FORMATION

Akvilė Botyriūtė, Vytautas Smirnovas

Department of Biothermodynamics and Drug Design, Vilnius University Institute of Biotechnology, Vilnius, Lithuania

Akvile.Botyriute@chf.stud.vu.lt

Amyloid fibril formation is a common event in human protein misfolding disorders, including Alzheimer's, Parkinson's, type-II diabetes and other diseases. In order to treat these disorders scientists are searching for efficient inhibitors which can prevent fibril formation. A number of studies show that (-)-epigallocatechin-3-gallate (EGCG) frequent compound in a green tea can repress amyloid fibril formation of proteins such amyloid-beta, alpha-synuclein and others [1-5].

We checked EGCG influence on recombinant human insulin fibril formation. Contrary to previous studies [1-5] our initial experiments revealed no significant effect using EGCG concentrations up to 5 times higher than insulin. We found out one major difference in experimental conditions. Most of previous inhibition studies were carried out in (or near to) neutral pH [1-4] and ours in pH 2. Having in mind reports of low stability of EGCG in neutral pH [6] we incubated it for 24 hours in neutral pH before using it to insulin fibrillation experiments. In this case inhibition was observed even when EGCG concentration was 10 times smaller than insulin. Therefore we can assert that actual inhibitor of amyloid-like fibril formation is not EGCG but its derivative which occurs over incubation at neutral or higher pH.

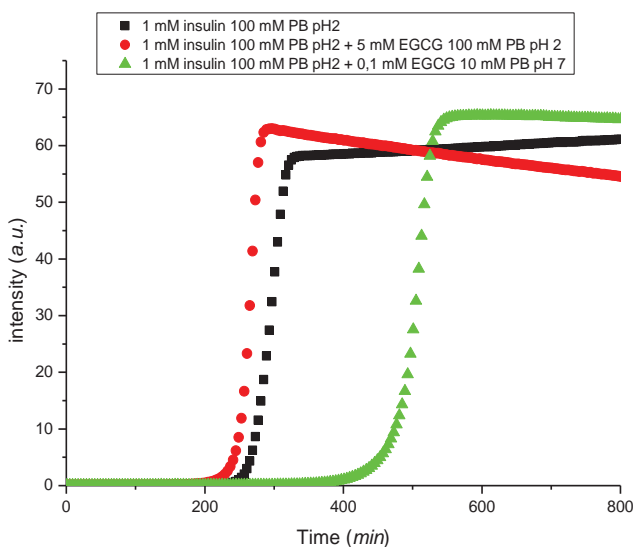


Fig. 1. Insulin amyloid-like fibril formation over time (experimental data of Thioflavin T fluorescence assay).

- [1] D. Ehrnhoefer, J. Bieschke, et al., EGCG redirects amyloidogenic polypeptides into unstructured, off-pathway oligomers, *Nature structural & molecular biology* **15**, 558-566, (2008).
- [2] J. Bieschke, J. Russ et al., EGCG remodels mature  $\alpha$ -synuclein and amyloid- $\beta$  fibrils and reduces cellular toxicity, *Proc Natl Acad Sci U S A* **107**, 7710-7715, (2010).
- [3] A. S. Rambold, M. Miesbauer et al., Green tea extracts interfere with the stress-protective activity of PrP<sup>Sc</sup> and the formation of PrP<sup>Sc</sup>, *Journal of neurochemistry* **107**, 218-229, (2008).
- [4] B. E. Roberts, M. L. Duennwald, et al., A synergistic small-molecule combination directly eradicates diverse prion strain structures, *Nature chemical biology* **5**, 936-946, (2009).
- [5] M. Levy-Sakin, M. Shreberk et al., Targeting insulin amyloid assembly by small aromatic molecules Toward rational design of aggregation inhibitors, *Islets* **1**, 210-215, (2009).
- [6] S. Sang, M. LEE et al., Stability of Tea Polyphenol (-)-Epigallocatechin-3-gallate and Formation of Dimers and Epimers under Common Experimental Conditions, *Journal of agricultural and food chemistry* **53**, 9478-9484, (2005).

# Oral session 5

---

09:00  
Friday

- Biophysics, medical and environmental physics

## BIO-HYDROGEN PRODUCTION EXPERIMENTS USING CRUDE GLYCEROL AS SUBSTRATE WITH DIFFERENT ANAEROBIC MICROORGANISMS

Ilze Dimanta<sup>1</sup>, Jānis Kleperis<sup>2</sup>, Indriķis Muižnieks<sup>1</sup>

<sup>1</sup>Department of Microbiology and biotechnology, Faculty of Biology, University of Latvia

<sup>2</sup>Laboratory of Hydrogen energy materials, Institute of Solid State Physics, University of Latvia

[Ilze.Dimanta@lu.lv](mailto:Ilze.Dimanta@lu.lv)

Hydrogen can be produced from many different sources (e.g. biomass rich in carbohydrates) and in various ways. For hydrogen production in dark fermentation process most commonly used are carbohydrates containing substrates [1].

One of the substrates that can be effectively used for microbial hydrogen production is crude glycerol, which is a by-product from the process of biodiesel production. Because of large quantities of available crude glycerol and the highly reduced nature of carbon in glycerol per se, microbial conversion of it seems to be economically and environmentally viable possibility. Such industrial organic waste product as crude glycerol is perspective for usage in feedstock for hydrogen producing bacteria. The process of biodiesel production results in 41% (w/w) of crude glycerol [2].

Different bacterial isolates (from Microbial Strain Collection of Latvia) were tested for hydrogen gas production in order to find the most effective and suitable bacterial culture for crude glycerol usage. Substrate was sterilized through membrane 0.2µm filter. Substrate concentration was measured by HPLC (High Performance liquid chromatography).

Bacterial cultures were inoculated in 200 ml flasks containing LB (5 g/l yeast extract, 10 g/l tryptone, 10 g/l sodium chloride, 15 g/l Bacto agar). The flasks were aerobically shaken at 37°C for 12 hours at 150 rpm using a multi-shaker PSU-20 (BioSan, Latvia). The bacteria cell number in the overnight culture was titrated at 10-6 dilution. The overnight culture in LB liquid medium was mixed (1:1) with phosphate buffer saline (PBS) pH 7.3 (0.8 g/l NaCl, 0.2 g/l KCl, 1.43 g/l Na<sub>2</sub>HPO<sub>4</sub>, 0.2 g/l KH<sub>2</sub>PO<sub>4</sub> [3] in a vessel sterilized for measurements. The PBS contained a complex trace element medium pH 6.5 (0.039g/l Fe(NH<sub>4</sub>)<sub>2</sub>SO<sub>4</sub>·6H<sub>2</sub>O, 0.172 mg/l Na<sub>2</sub>SeO<sub>3</sub>, 0.02 mg/l NiCl<sub>2</sub>, 0.4 mg/l (NH<sub>4</sub>)<sub>6</sub>Mo<sub>7</sub>O<sub>24</sub> [4]. Argon gas bubbling through the media was used to sustain anaerobic environment.

Evolved gases were collected with the syringe from the tests system serum bottles and tested qualitatively in the mass-spectrometer. Serum bottles were closed with butyl rubber stoppers and aluminium caps. Before use, the bottles were flushed with Argon gas and autoclaved for 60 min at 121°C. Gas concentrations were measured with massspectrometer RGAPro-100.

Results in the report will be discussed in detail.

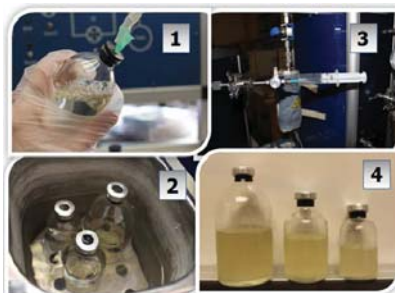


Fig.1. Experimental set-up.

- 
- [1] Hallenbeck P. C. and Ghosh D. Advances in fermentative biohydrogen production: the way forward? *Trends in Biotechnology*, 27, 5 (2009) p.287-297.
- [2] Ito T. Nakashimada Y., Senba K., Matsui T., Nishio N. Hydrogen and ethanol production from glycerol-containing wastes discharged after biodiesel manufacturing process. *Journal of Bioscience and Bioengineering*, 100(3), (2005) p. 260-265.
- [3] Penfold D.W., Forster C.F., Macaskie L.E., Increased hydrogen production by *Escherichia coli* strain HD 701 in comparison with wild -type strain MC4100. *Enzyme and Microbial Technology*, 33, (2003) p.185-189.
- [4] Maeda T., V. Sanchez-Torres., Wood,T.K., Enhanced hydrogen production from glucose by metabolically engineered *Escherichia coli*. *Appl. Microbiol. Biotechnol.*, 77, (2008) p.879-890

# Effects of pH on Glutathione – capped CdSe quantum dots optical properties

Justinas Jonušas<sup>1,2\*</sup>, Rūta Araminaite<sup>1</sup>, Vitalijus Karabanovas<sup>1</sup>

<sup>1</sup>Biomedical Physics Laboratory, Institute of Oncology, Vilnius University, Baublio 3b, LT-08406, Vilnius, Lithuania

<sup>2</sup>Biophotonics group of Laser Research Center, Vilnius University, Sauletekio 9, c. 3, LT-10222 Vilnius, Lithuania  
[justinas.jonusas@ff.stud.vu.lt](mailto:justinas.jonusas@ff.stud.vu.lt)

Last decade, quantum dots (QDs) – nanometric size particles – were considered as promising markers for various purposes in biology, genetics and even medicine as agents in photodynamic therapy and early cancer diagnostics [1].

Recently, few papers have described novel methods for water soluble glutathione (GSH) capped QDs synthesis [2,3]. By using this method, we are able to prepare not only water soluble QDs, but also it enables researchers to develop selective drug delivery systems, were target molecules and drugs are attached to the surface of QDs via bond between GSH and glutathione S – transferase (GST).

Our earlier investigation was focused on optimization of specific conditions during synthesis of CdSe – GSH QDs (pH value was adjusted to 10,64 and heating temperature was 90°C during synthesis) [4]. In mentioned work, we used modified method proposed by Wang et al. [3]. Obtained nanocrystals were almost monodisperse, with size varying from 2 to 4 nm and had crystalline structure. Spectroscopic investigation has showed that synthesized QDs had high PL QY (23 %).

In this work we expand our investigation of GSH capped CdSe QDs by changing the pH value of medium before synthesis reaction. Two additional syntheses were made (pH value of medium before heating solution was adjusted to 8 (synthesis A) and 9 (synthesis B). All other parameters are identical). After synthesis, five samples were prepared in phosphate buffer solution (PB) with different pH value. Photoluminescence spectra of obtained QDs are shown in figure 1. All samples posses PL peak around 500 nm. Highest PL value was obtained from samples with neutral pH value.

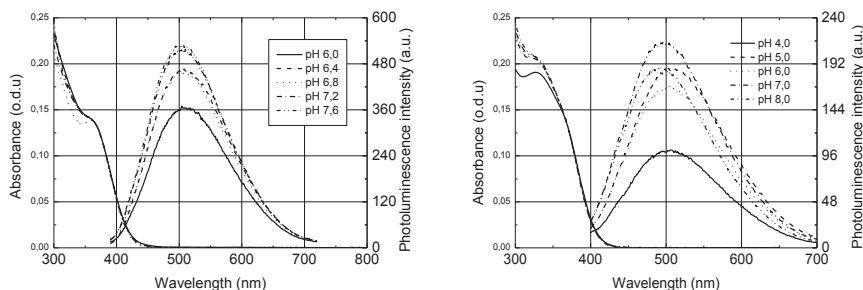


Fig. 1. Absorption and photoluminescence spectra of GSH capped CdSe QDs in PB solutions with different pH values: a) pH = 8, b) pH = 9. All samples were excited with 370 nm wavelength light.

Highest obtained FL QY was ~ 12 %, for samples prepared using QDs from synthesis A. FL QY was much lower (only ~ 4 %) of samples synthesized in medium with higher pH value. First absorption shoulder is visible at 370 nm, for QDs from synthesis A. This shoulder was visible at 330 nm for nanoparticles from synthesis B. Samples from both syntheses stayed stable and dispersed in water more than 11 days, what enables us to use these QDs for biological purposes.

We conclude that pH value of water medium in which nanocrystals are dispersed plays less role than pH value of medium in which QDs are synthesized. QDs synthesized in medium with pH value of 8 obtain much higher PL QY (~ 12 %), than those synthesized in medium with pH value of 9 (~ 4 %).

- Samia, A.C.S., Chen, X.B., Burda, C. Semiconductor quantum dots for photodynamic therapy. *Journal of the American Chemical Society* 125(51), 15736 – 15737 (2003).
- M. Bauml, D. Stamou, J. M. Segura, R. Hovius, H. Vogel. Highly fluorescent streptavidin-coated CdSe nanoparticles: Preparation in water, characterization, and micropatterning. *Langmuir*, 20, 10 (2004), 3828 – 3831.
- J. Yuan, W. Guo, J. Yin, E. Wang. Glutathione-capped CdTe quantum dots for the sensitive detection of glucose. *Talanta*, 77, 5 (2009), 1858 – 1863.
- Jonušas, J., Juralevičiūtė M., Araminaite R., Karabanovas V., Rotomskis R. Characterization of Glutathione – capped CdSe QDs., Medical physics in Baltic states 10 2012, Proceedings of International Conference “Medical Physics 20010” 8 – 10 November 2012, Kauna, Lithuania, p. 58 – 64.

## DYNAMICS OF ACCUMULATION OF MES CAPPED GOLD NANOPARTICLES IN CANCER CELLS

Raminta Marcinytė<sup>1</sup>, Marija Matulionytė<sup>1,2</sup>

<sup>1</sup>Laboratory of Biomedical Physics, Vilnius University Institute of Oncology, Baublio 3A, Vilnius, Lithuania

<sup>2</sup>Biophotonics group of Laser Research Center, Faculty of Physics, Vilnius University, Sauletekio 9, bldg. 3, Vilnius, Lithuania

raminta.marcinyte@gmf.stud.vu.lt

Gold nanoparticles are known for their unique photoluminescence, plasmonic properties [1], easy surface modification and functionalization with wide spectrum of organic molecules and drugs [2], low toxicity to organisms [3]. Due to these properties gold nanoparticles are very promising for cellular imaging, gene therapy, molecular diagnostics and therapy using targeted drug delivery [1]. However, mechanisms of accumulation and cytotoxicity of gold nanoparticles are not completely explored yet, therefore the purpose of this study was to synthesize MES (2-(N-morpholino) etanesulfonic acid) capped gold nanoparticles (Au-MES NP) and analyse their dynamics of accumulation in cancer cells.

Au-MES nanoparticles were synthesized using modified P.C. Chen et. al. synthesis protocol [4]. Spectral properties of Au-MES nanoparticles were analyzed: photoluminescence intensity of Au-MES nanoparticles diluted with cell growth medium was lower in comparison with PL intensity of Au-MES NP diluted with deionized water. This could be due to interaction of Au-MES NP with components of cell growth medium [5]. Accordingly, accumulation of Au-MES nanoparticles in cells can be affected by their interaction with compounds of cell culture medium.

Investigating dynamics of Au-MES NP accumulation of MiaPaCa-2 cancer cells were incubated with Au-MES nanoparticles (volume ratio of cells growth medium to Au-MES nanoparticles solution was 3:1). Confocal fluorescence images (microscope Eclipse TE2000-S,  $\lambda_{\text{exc}} = 404 \text{ nm}$ ) were taken at 3, 6, 9 and 24 hours after the incubation with gold nanoparticles. The adherence to the cell membrane (Fig. 1A, arrow no. 1); formation of granulated clusters (Fig. 1A, arrow no. 2) and localization of granulated clusters at the perinuclear region (Fig. 1A, arrow no. 3) after 3 hours of incubation of Au-MES nanoparticles were recorded. Distribution of Au-MES nanoparticles in cells after 3 hours correlates with stages of endocytosis mechanism. Diffuse distribution (including cell nucleus) with accumulation of Au-MES nanoparticles in several places near plasma membrane were visualized after 6 and 9 hours of incubation. After 24 hours of incubation homogeneous diffuse distribution of Au-MES NP in cancer cells was observed (Fig. 1B).

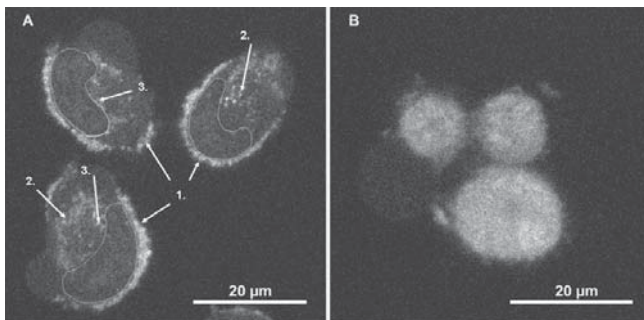


Fig. 1. Confocal fluorescence images of MiaPaCa-2 cancer cells taken after 3 (A) and 24 (B) hours of incubation with MES capped gold nanoparticles. White lines define nuclei, arrows show different localizations of Au-MES NP: 1.- near the cell membrane; 2.- in the cytosol and 3.- at the perinuclear region.

This work was partly supported by project "Promotion of Student Scientific Activities" (VP1-3.1-ŠMM-01-V-02-003) from the Research Council of Lithuania (R.M.). This project is funded by the Republic of Lithuania and European Social Fund under the 2007-2013 Human Resources Development Operational Programme's priority 3.

[1] S. Nie, Y. Xing, G. J. Kim, J. W. Simons, Nanotechnology applications in cancer, *Annu Rev Biomed Eng*, 9, 257–88 (2007).

[2] P. Ghosh, G. Han, M. De, C. K. Kim, V. M. Rotello, Gold nanoparticles in delivery applications, *Advanced Drug Delivery Reviews*, 60, 1307–1315 (2008).

[3] M. W. Cui, J. Li, Y. Zhang, H. Rong, W. Lu, L. J. Jiang, Effects of aggregation and the surface properties of gold nanoparticles on cytotoxicity and cell growth, *Nanomedicine*, 8, 46–53 (2012).

[4] P.C. Chen, S.C. Mwakwari, A.K. Oyeler, Gold nanoparticles: from nanomedicine to nanosensing, *Nanotechnology, Science and Applications*, 1, 47 (2008).

[5] R. Marcinytė, M. Matulionytė, R. Rotomskis, Stability and photostability of MES capped gold nanoparticles, 10<sup>th</sup> international conference on Medical Physics 2012, ISSN 1822-5721, Kaunas University of Technology, 62-66 (2012).



# PHOTOSTABILITY OF QUANTUM DOTS AND ITS IMPLICATION IN BIOSAFETY OF NANOMATERIALS

Edita Jazdauskaitė<sup>1,2</sup>, Vytautas Kulvietis<sup>1,2</sup>

<sup>1</sup> Biomedical Physics Laboratory, Institute of Oncology Vilnius University, Lithuania

<sup>2</sup> Department of Quantum Electronics, Faculty of Physics, Vilnius University, Lithuania  
[edita.jazda@gmail.com](mailto:edita.jazda@gmail.com)

Quantum dots (QD) are photoluminescent semiconductor nanocrystals with specific physicochemical properties which depend on their spatial parameters and chemical composition and which make them advantageous fluorophores for many applications. QD are usually made of heavy metals core and stabilized with biocompatible ligands to reach biostability in biological medium. However under environmental conditions such as UV irradiation organic coatings may be destabilized and heavy metal ions may be released and induce toxicity for the biological systems. It was shown that healthy skin provides a barrier that protects from passage of QD to the organism but skin damages may increase the possibility of QD penetration into the deeper layers. Combined exposure of QD and UV irradiation may lead to the adverse physiological effects in two ways: it might destabilize QD and induce the penetration of the toxic metal ions through skin and/or it might induce dermal damages which decrease the functionality of the skin barrier.

In this study we present the photostability of two types of QD with different structure i.e., CdTe core QD covered with mercaptopropionic acid (CdTe-MPA) and CdSe/ZnS core/shell QD covered with amphiphilic polymer and polyethylene glycol layer (CdSe/ZnS-PEG). We also assessed the accumulation of QD in the skin tissues after topical application under UV irradiation.

Histological examination of UVB irradiated (260-320 nm) skin samples showed that UVB induced skin damage such as: disruption of sebaceous glands, appearance of apoptotic cells, pyknotic nuclei, clear cytoplasm, hyperemia [1]. Spectroscopic investigations revealed that during UVB irradiation photoluminescence (PL) intensity of CdTe-MPA solution increased, the full width at half-maximum of the PL spectrum expanded and the peak of the PL spectrum shifted to the short wave side (Fig. 1A) when compared with the dark conditions. Meanwhile in case of CdSe/ZnS-PEG PL intensity also increased during irradiation but there were no significant changes of spectral shape (Fig. 1B). It shows that nanocrystal structure of these QD was not affected.

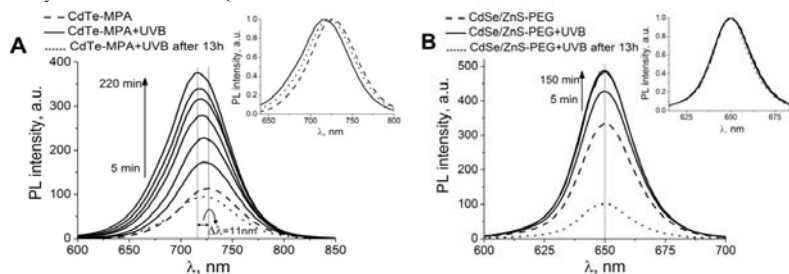


Fig. 1. PL spectra of CdTe-MPA (A) and CdSe/ZnS-PEG (B) QD solutions before UVB irradiation (dash lines), during UVB irradiation (solid lines) and 13 hours after irradiation (dotted lines). Irradiation power 16.8 mW/cm<sup>2</sup>.

Inset: differential normalized spectra showing changes of the spectral shapes.

Spectroscopic changes of the CdTe-MPA QD show that UVB irradiation might damage the core. The degradation of the core is associated with the release of cytotoxic ions. [2] It raises the risk of potential harmful health effects if QD are applied *in vivo*. Differences in photostability between the two types of QD are related to the chemical composition: core/shell structure protects QD from oxidation and polymer ligands are resistant to UV damage.

Confocal fluorescence microscopy revealed that CdSe/ZnS-PEG QD distributed in the *stratum corneum* of the epidermis, in the superficial part of the hair channel and in the skin folds. However, UVB had no significant impact on QD localization in the skin when compared with the control non-irradiated skin samples.

We conclude that UVB irradiation causes temporary PL photoenhancement of CdTe-MPA and CdSe/ZnS-PEG QD. It is followed by shortwave shift of CdTe-MPA QD spectral band indicating the destabilization of the core which is related to the release of toxic heavy metal ions. It raises the risk of potential adverse health effects. Meanwhile CdSe/ZnS-PEG QD retain intact nanocrystal structure under UVB exposure. UVB irradiation does not alter QD localization in mice skin *in vivo* despite of physiological dermal damage.

[1] R. Svobodova, A. Galandakova, J. Sianska et al., DNA damage after acute exposure of mice skin to physiological doses of UVB and UVA light, Arch Dermatol Res, 304(5), 407-412 (2012).

[2] V. Kulvietis, G. Strečkytė, R. Rotomskis, Spectroscopic investigations of CdTe quantum dot stability in different aqueous media, Lithuanian Journal of Physics, 51(2), 163–171 (2011).

## IMAGING OF MAGNETIC NANOPARTICLES IN CELLS USING OPTICAL MICROSCOPY

Urtė Statkutė<sup>1,2</sup>, Vitalijus Karabanovas<sup>1</sup>

<sup>1</sup>Laboratory of Biomedical Physics, Vilnius University Institute of Oncology, Baublio 3A, Vilnius, Lithuania

<sup>2</sup>Biophotonics group of Laser Research Center, Faculty of Physics, Vilnius University, Sauletekio 9, bldg. 3, Vilnius, Lithuania

[urtestatkute@gmail.com](mailto:urtestatkute@gmail.com)

The application of nanotechnology in medicine is a great interest of many researchers. One of the most promising research fields is application of magnetic nanoparticles (MNP) in early cancer diagnostics. Magnetic nanoparticles have unique magnetic properties, such as superparamagnetism, which depend on their size, geometry and chemical composition. Nowadays there are various disciplines, where magnetic nanoparticles could be used, but the main goal is to use magnetic nanoparticles as a contrast agent in oncology. The main issues, which have to be overcome, before using MNP in cancer diagnostics and therapy, are their toxicity, biocompatibility and chemical activity [1]. MNP do not fluoresce, so their imaging using optical microscopy methods, is complicated. In this study, few different imaging methods were applied to detect intracellular localization of superparamagnetic cobalt ferrite nanoparticles (SPIONs).

Firstly, SPIONs were incubated with different cell lines – liver carcinoma (MH-22A), ovarian cancer cells (A278) and fibroblasts (NIH3T3). Then two different imaging methods, such as differential interference contrast microscopy and staining MNP with Prussian blue (Fig.1, a, b), were investigated. Images were obtained using bright field function of confocal microscope.

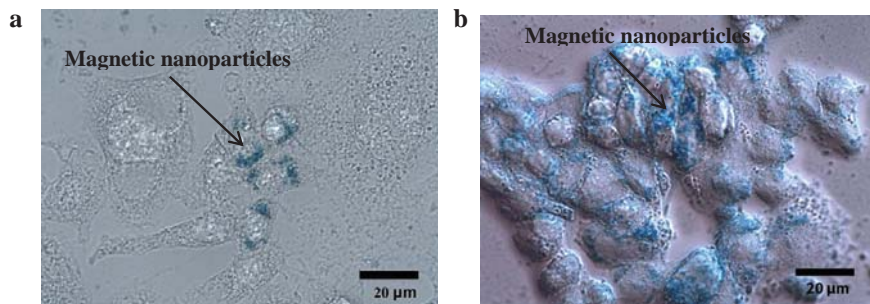


Fig. 1. Images of liver carcinoma and ovarian cancer cells stained with Prussian blue. a – MH-22A, b – A278 treated with cobalt SPIONs. Blue spots show intracellular localization of SPIONs.

Images obtained using differential interference contrast microscopy show, that this method is not suitable for evaluation of intracellular localization of superparamagnetic cobalt ferrite. The main reason is that the light, which passes through cells, is equally absorbed and scattered by vesicles full-filled with MNP or nutrients, so in images intracellular SPIONs appear as the same black spots.

Intracellular labeling of SPIONs with Prussian blue dye showed different amount of accumulated MNP in normal and cancer cell lines. Fig 1 a, b show, that after 24h SPIONs tend to accumulate in the perinuclear region of – MH-22A and A278 cell lines. These results also revealed that MNP are more likely to accumulate in ovarian cancer cells, than in liver carcinoma cells, or fibroblasts. So it would be more efficient to use superparamagnetic cobalt ferrite nanoparticles with ovarian cancer cells, than with other ones.

Acknowledgement: This work was supported by project “Promotion of Student Scientific Activities” (VP1-3.1-ŠMM-01-V-02-003) from the Research Council of Lithuania (U.S.).

[1] An-Hui Lu, E. L. Salabas, and Ferdi Schüth, Magnetic Nanoparticles: Synthesis, Protection, Functionalization, and Application, *Angew. Chem. Int. Ed.*, 46, 1222 – 1244 (2007).

## INFLUENCE OF OPTICAL ABERRATIONS INDUCED IN ONE EYE AND THE ACCOMODATIVE RESPONSE IN THE FELLOW EYE

Karola Panke<sup>1</sup>, Varis Karitāns<sup>2</sup>

<sup>1</sup>University of Latvia, Kengaraga 8, Rīga, LV - 1063

<sup>2</sup>Institute of solid State Physics, Kengaraga 8, Rīga, LV 1063

karola.panke@inbox.lv

For a long time it was not possible to measure higher-order aberrations in the human eye, but since the Shack-Hartmann sensor was fitted for vision science it became possible to make objective, accurate and fast measurements of wave aberrations. Dependence of numerous visual functions on ocular aberrations has been studied [1, 2]. The aim of the research is to study influence of optical aberrations induced in one eye and the accommodative response in the fellow eye. As aberrations affect depth of focus, it is likely that they also play a role in the fluctuations of accommodation [2] and hence contribute to changes of refractive errors throughout the life.

A custom Hartmann-Shack and adaptive optics setup was built to generate and measure wave aberrations. The optical setup is shown in Figure 1. Accommodative response was estimated from wave aberrations for different patterns of aberrations which were induced by an unimorph quartz based deformable mirror. The deformable mirror consists of 24 individual segments. The Hartmann-Shack sensor used has 512 x 512 pixels large CCD matrix. The deformable mirror, Hartmann-Shack wavefront sensor and pupil of the eye were located in the conjugate planes. Measurements were obtained without cycloplegia under natural conditions.

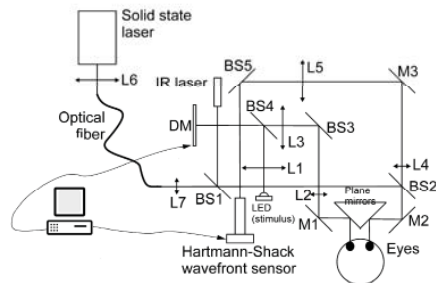


Fig.1 A schematic of Hartmann-Shack and adaptive optics setup. BS – beamsplitter, DM – deformable mirror, L – lens, M – mirror

When different patterns of optical aberrations are induced in one eye small changes in accommodation are occurring in the fellow eye. The area in the brain responsible for control of accommodation receives two separate inputs from the both eyes and choose the smaller amount of accommodation required. However, it seems that accommodation of one eye doesn't depend strongly on the image quality in the fellow eye. The order of changes of accommodation in the fellow eye are few hundredths of a micron. Hypothesis is that lower order aberrations influence accommodation in the fellow eye more than higher order aberrations.

### References

1. Cheng, H., Barnet, J. K., Vilupuru, A. S., Marsack, J. D., Kasthurirangan, S., Applegate, R. A., Roorda, A. (2004). A population study on changes in wave aberrations with accommodation. *Journal of Vision*. 4 (4), 272-280.
2. Gamba, A., Sawides, C., Dorronso, C., Marcos, S. (2009). Accommodation lag and fluctuations when optical aberrations are manipulated. *Journal of Vision*. 9 (6), 1-15.

# Oral session 6

---

11:00  
Friday

- Theoretical physics

## 1D WAVE EQUATION OPENCL-BASED INTEGRATION

Maxim Belov, Alex Halavanau<sup>1</sup>

<sup>1</sup>Faculty of Physics, Belarusian State University, Minsk, Belarus  
mpui@tut.by

In the presented research we discuss the parallel implementation of the method of lines for hyperbolic wave equation with one spatial dimension:

$$\partial_{tt}\phi - \partial_{xx}\phi = 0 \quad (1)$$

We use general purpose graphic processor units (GPGPU) and API of OpenCL library. We illustrated the effectiveness of graphic card use for PDE integration computations by comparing to CPU-based implementations. We used the method of lines as the most simple example for parallel PDE integration. The method allows to construct the solution of desired precision and errors in spatial and time variables and can be easily ammended to 2D and 3D equations.

GPUs are slowly adopted by the computational physics and are still mainly used to speed up Monte Carlo simulations in high energy physics. Implementing Monte Carlo simulations on GPU is natural, because it is obvious how to parallelize the problem [1]. A plenty of computational physics tasks involve solution of PDE, and Solving PDEs is usually significantly harder. Several groups of methods can be pointed out.

First and the most naive approach is to replace all derivatives with appropriate finite differences; this leads to either explicit or implicit methods. The former ones have convergence issues, the latter ones lead to many-diagonal matrix linear equation systems for every time step. One can utilize GPU by applying modern algorithms based on cyclic reduction or recursive doubling. We followed another way of solving PDE which is much more easier to implement and parallelize - the method of lines. If one discretizes the space and leaves the time continuous, he will obtain the system of ordinary differential equations. This system is then can be integrated by any of stepping methods (Runge-Kutta, Adams, etc.) [2]. Depending on discretization scheme some other methods can be constructed, for example the leap-frog and the Crank-Nicholson methods. We have applied the most simple form of the method of lines. Nevertheless, it uses high order schemes and therefore provides us with the robust data. The used finite difference for the second order spatial derivative is following:

$$\frac{d^2\phi_n}{dt^2} \approx \frac{1}{12(\Delta X)^2} (-\phi_{n-2} + 16\phi_{n-1} - 30\phi_n + 16\phi_{n+1} - \phi_{n+2}) \quad (2)$$

It defines corresponding system of  $2N$  first order ordinary differential equations

We decided to use OpenCL API because it works on any GPGPU hardware and supports popular operating systems. Well documented SDK [3] makes the number of applications of this library in computational physics countless. We used our solver to integrate famous non-linear  $\phi^4$  and  $\phi^6$  potential systems and have obtained precise numerical data.

The method of lines utilizes the true parallel manner of PDE integrating and has wide range of applications in hyperbolic, parabolic and mixed-type equations. Our results prove that efficient programming on GPU can sufficiently speed up the process of numerical integration and open parallel computing world to everyone. We plan to extend this technique for higher dimensional systems.

- 
- [1] Daniel Egloff, *High Performance Finite Difference PDE Solvers on GPUs* QuantAlea GmbH, Switzerland, 2010.
  - [2] M. A. Green, *Time Dependent Problems and Difference Methods* Bertil Gustafsson, Heinz-Otto Kreiss, Joseph Oliger. Pure and Applied Math, Wiley, 1996.
  - [3] Accelerated Parallel Processing (APP) AMD SDK

# QUANTUM-MECHANICAL STUDY OF THE ASPARAGINE MONOHYDRATE FRAGMENTATION BY LOW ENERGY ELECTRONS

Laura Baliulytė<sup>1</sup>, Jelena Tamulienė<sup>2</sup>

<sup>1</sup> Vilnius University, Faculty of Natural Sciences, M.K. Ciurlionio st. 21/27, LT-03101 Vilnius, Lithuania

[Laura.Baliulyte@gf.stud.vu.lt](mailto:Laura.Baliulyte@gf.stud.vu.lt)

<sup>2</sup> Vilnius University, Institute of Theoretical Physics and Astronomy, A. Gostauto 12, LT-01108 Vilnius, Lithuania

The studies of the damages amino acids, resulted from the influence of ionizing radiation, are being the hot topic of a series of investigations within last decades. The majority of the above damages are not usually due to the primary high-energy radiation but results from the effect of the secondary low-energy charged particles produced in the course of ionization [1].

The structure of the asparagine monohydrate and its fragment energies of appearance have been studied using the generalized gradient approximation for the exchange–correlation potential in the density functional theory (DFT) as it is described by the Becke's three-parameter hybrid functional, using the non-local correlation provided by Lee, Yang and Parr. The DFT method is commonly referred to as B3LYP [2]– a representative standard DFT method. The cc-pVTZ basis set has been used as well [3]. In this research has been using VU TFAI partners from Institute of Electron Physics, Ukraine experimentally measured mass-spectrum of asparagine monohydrate. This mass-spectrum is published in paper [4]. In order to model the fragmentation processes, the possible fragment anions, cations and fragments with a zero charge both with and without geometry optimization have been analyzed to predict the influence of dissociation energy on the fragmentation processes. For example, according to our calculations and experimentally measured mass-spectrum is determined that mass  $m=13$  a.u. cation is CH. The CH fragments could produced according to the following pathway:  $C_4H_8ON_2O_4 + e \rightarrow CH^+ + (H_2O + H + N_2C_3O_3H_6)^- + e$ . Other fragmentation reactions can be determined on the basis of the data presented in Table 1.

Table 1. Calculated appearance energies (in eV) for the fragments produced from the asparagine monohydrate molecule (<sup>(0)</sup>- fragments of charge):

Fragment	Fragments appeared due to the dissociation of the parent molecule to the fragment in first column	Appearance energies (in eV) *	Appearance energies (in eV) **
CH <sup>(1)</sup>	$(H_2O + H + N_2C_3O_3H_6)^{(1)}$	22.30	16.17
NH <sup>(1)</sup>	$(H_2O + H + C_4N_1O_3H_7)^{(0)}$	22.13	18.34
H <sub>2</sub> N <sup>(1)</sup>	$(H_2O + C_4N_1O_3H_6)^{(1)}$	16.39	15.83
H <sub>2</sub> O <sup>(1)</sup>	$(C_4N_2O_3H_8)^{(0)}$	13.47	12.91
C <sub>2</sub> H <sup>(1)</sup>	$(H_2O + H + H + NH_2 + CO_2H + CN_0H_2)^{(1)}$	29.73	16.33
C <sub>2</sub> H <sub>2</sub> <sup>(1)</sup>	$(H_2O + H + NH_2 + CO_2H + CN_0H_2)^{(1)}$	23.63	16.11
C <sub>2</sub> H <sub>3</sub> <sup>(1)</sup>	$(H_2O + NH_2 + CO_2H + CN_0H_2)^{(1)}$	19.61	13.76
CH <sub>2</sub> N <sup>(1)</sup>	$(H_2O + CO_2H + H + CH_2 + CN_0H_2)^{(1)}$	19.17	10.99
CH <sub>3</sub> N <sup>(1)</sup>	$(H_2O + CO_2H + CH_2 + CN_0H_2)^{(1)}$	14.83	9.59
CH <sub>4</sub> N <sup>(1)</sup>	$(H_2O + CO_2H + CH_2 + CN_0H_1)^{(1)}$	16.96	10.52
C <sub>2</sub> HN <sup>(1)</sup>	$(H_2O + CO_2H + H + H + H + CN_0H_2)^{(1)}$	26.48	18.63
C <sub>2</sub> H <sub>2</sub> N <sup>(1)</sup>	$(H_2O + CO_2H + H + H + H + CN_0H_2)^{(1)}$	26.20	21.66
C <sub>2</sub> H <sub>3</sub> N <sup>(1)</sup>	$(H_2O + CO_2H + H + H + CN_0H_2)^{(1)}$	17.80	14.67
C <sub>2</sub> H <sub>4</sub> N <sup>(1)</sup>	$(H_2O + CO_2H + H + CN_0H_2)^{(1)}$	19.17	8.74
CH <sub>2</sub> O <sub>2</sub> <sup>(1)</sup>	$(H_2O + C_3H_7N_2O)^{(1)}$	18.03	12.37

\*Means that the single point energy calculation of the fragments, taking into account the geometry of the certain part of the asparagine monohydrate molecule, was performed.

\*\*Indicates that the equilibrium geometry structure of the asparagine monohydrate molecule fragments is investigated. Moreover, in this research anions and fragments with zero charge appearance energy have been determined.

[1] S. Cristoni, L.R. Bernardi. Mass. Spectr. Rev., 22 (2003), p. 369.

[2] A.D. Becke. J. Chem. Phys., 98 (1993), p. 5648

[3] R.A. Kendall, T.H. Dunning Jr., R.J. Harrison. Electron affinities of the first-row atoms revisited. Systematic basis sets and wave functions. J. Chem. Phys., 96 (1992), pp. 6796–6806

[4] В.С.Вукстич, Л.Г.Романова, А.В.Снегурский Определение атомарного состава изобарных ионов при масс-спектрометрическом исследовании моногидрата L-аспарагина straipsnyje publikuotame Письма в ЖТФ.2012;38(7).

# THEORETICAL INVESTIGATION OF LIGHT ATOMS EXCITATION BY ELECTRON IMPACT

Darius Stonys

Institute of Theoretical Physics and Astronomy, Vilnius University, Lithuania  
darius.stonys@ff.stud.vu.lt

The probability of an atom excitation during a collision with an electron is defined by the collision cross section. Cross sections are important in modelling various processes occurring in plasma physics. However, their experimental values still possess a high degree of uncertainty, therefore imposing a need of theoretical data.

In the Department of the Theory of Atom of ITPA VU, the programs for calculating excitation cross sections exploring various wavefunction bases using Born approximation have been developed. To evaluate the performance of these programs, several light atoms (H, He and Li) were chosen, all of whom have broad and verified data in NIST database [1]. Two radial orbital bases were chosen for calculations, non-relativistic (HF) and quasirelativistic (QR) one. In case of helium and lithium, correlation effects were taken into account by using the transformed radial orbital method [2,3]. However, since the main cross section data from NIST [4] was additionally scaled, the same scaling procedure was performed in our calculations. The one-configuration Dirac-Fock method (DF) was applied in [4], therefore their results were scaled using the experimental values of oscillator strengths. However, in our work, a multi-configuration method is used, requiring no additional scaling. The programs calculated cross sections for excitations to any level, so our calculation data had to be summed in order to get the results analogous to those in NIST databases.

We see a very close agreement with the data from [4] in almost every case. For our cross sections, the relative mean square deviations are: hydrogen -  $1s \rightarrow 2p$  0,22% (HF) and 0,22% (QR),  $1s \rightarrow 3p$  0,22% (HF) and 0,22% (QR),  $1s \rightarrow 4p$  0,21% (HF) and 0,22% (QR); helium -  $1s^2 \rightarrow 1s2p$  1,52% (HF) and 1,59% (QR),  $1s^2 \rightarrow 1s3p$  9,94% (HF) and 0,74% (QR); lithium -  $1s^2 2s \rightarrow 1s^2 2p$  2,11% (HF) and 1,76% (QR),  $1s^2 2s \rightarrow 1s^2 3p$  34,17% (HF) and 34,47% (QR). The atoms under consideration have small nuclear charges, therefore the HF and QR results are very close to each other. But the QR results agree with those from [4] even better. Most likely, this agreement occurs because the DF relativistic functions were used in [4]. Our results agree better with those from [4] than any other author's results given in [1]. The only major difference appears in lithium  $1s^2 2s \rightarrow 1s^2 3p$  excitation. Currently, it is difficult to determine which results are more accurate because no other theoretical or experimental data are available. These discrepancies may only be eliminated with additional investigation. The dependence of excitation cross sections on the energy of incident electron is given in Figures 1-4.

Overall results indicate that the methods and programs in use are suitable and accurate to produce reliable data for electron-impact excitation of light atoms.

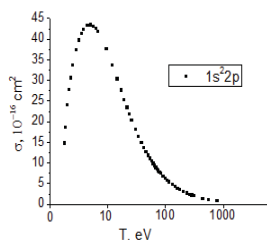


Fig. 4. Li excitation cross section.

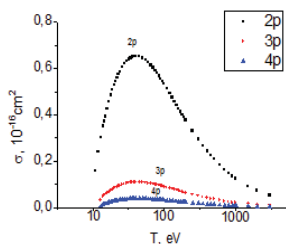


Fig. 1. H excitation cross sections.

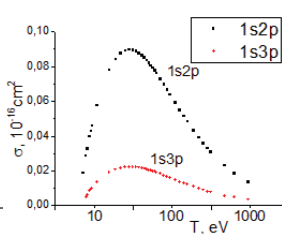


Fig. 2. He excitation cross sections.

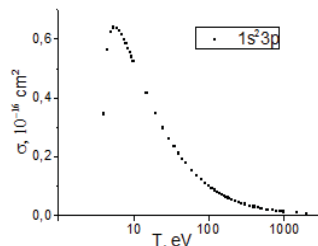


Fig. 3. Li excitation cross section.

[1] [http://physics.nist.gov/PhysRefData/Ionization/atom\\_index.html](http://physics.nist.gov/PhysRefData/Ionization/atom_index.html).

[2] P. Bogdanovich, Nuclear Instruments and Methods **B 235**, 92 (2005).

[3] P. Bogdanovich, Physica Scripta **78**, 045301 (2008).

[4] P. M. Stone, Y.-K. Kim, J. Res. Natl. Inst. Stand. Technol. **107**, 327 (2002).

# TIGHT BINDING MODEL OF THE PHOTOSYSTEM II REACTION CENTER

Andrius Gelzinis<sup>1</sup>, Leonas Valkūnas<sup>1,2</sup>, Darius Abramavičius<sup>1,3</sup>

<sup>1</sup>Department of Theoretical Physics, Faculty of Physics of Vilnius University, Sauletekio Avenue 9, build. 3, 10222 Vilnius, Lithuania

<sup>2</sup>Center for Physical Sciences and Technology, Savanoriu Avenue 231, 02300 Vilnius, Lithuania

<sup>3</sup>State Key Laboratory of Supramolecular Complexes, Jilin University, 2699 Qianjin Street, Changchun 130012, PR China  
andrius.gelzinis@ff.vu.lt

Photosynthesis is a process in which light energy is captured and stored by an organism. Plants use water and carbon dioxide to produce carbohydrates and oxygen. This reaction is driven by light captured from the Sun. Inside chloroplasts various various pigment-protein complexes participate in this reaction. The first steps in the process is done by photosystem II (PSII), which oxidizes water to molecular oxygen [1]. The reaction center (RC) of the PSII uses light energy to perform the initial charge separation, a prerequisite for water oxidation.

In this work we present a model of PSII RC based on the tight binding framework [2], which consistently describes both molecular excitons and charge transfer states. Our model is illustrated in Fig. 1a. It is derived from the modeling of experimental two dimensional optical spectra at 77 K [3]. Simulations based on our model captures all the main experimental feature present in the experimental data: the peak pattern, the lineshapes and time traces. This is achieved by including two charge separation pathways and correlations of both static disorder and fast fluctuations of the energy levels of charge transfer states.

Using our model, we calculate evolution of the states of the PSII RC. We find two timescales of charge separation (see Fig. 1b) at 77 K. Fast component  $\tau_1 \approx 1.5$  ps is assigned to energy equilibration in core pigments and slower component  $\tau_2 \approx 30$  ps is assigned to excitation transfer from the peripheral chlorophylls to the system core.

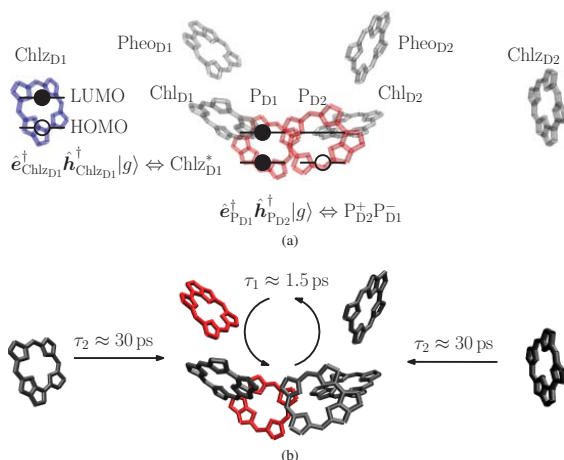


Fig. 1. a) Illustration of the tight-binding model of the PSII RC. Here full circles represent electrons and open circles represent holes. b) Illustration of timescales of charge transfer in PSII RC.

[1] R. E. Blankenship, *Molecular Mechanisms of Photosynthesis* (Wiley-Blackwell, 2002).

[2] D. Abramavicius and S. Mukamel, *J. Chem. Phys.* **133**, 184501 (2010).

[3] A. Gelzinis, L. Valkunas, F. D. Fuller, J. P. Ogilvie, S. Mukamel, D. Abramavicius, Tight binding model of the photosystem II reaction center: application to the two dimensional electronic spectroscopy, *New J. Phys.*, *submitted*.



# **TOPOLOGICAL PROPERTIES OF BAND STRUCTURE OF $T_3$ OPTICAL LATTICE**

Tomas Andrijauskas<sup>1</sup>, Egidijus Anisimovas<sup>1,2</sup>, Nathan Goldman<sup>3</sup>, Gediminas Juzeliūnas<sup>1</sup>

<sup>1</sup>Institute of Theoretical Physics and Astronomy, Vilnius University, Lithuania

<sup>2</sup>Department of Theoretical Physics, Vilnius University, Lithuania

<sup>3</sup>Center for Nonlinear Phenomena and Complex Systems, Université Libre de Bruxelles, Belgium  
tomas.andrijauskas@tfai.vu.lt

Since the discovery of the quantum Hall effect, topological properties of band structure of periodic quantum systems has been a very interesting topic in condensed matter physics. Ultra-cold atoms in optical lattices are periodic quantum systems, similar to electrons in condensed matter, that can have interesting topological phases. In particular, the quantised Hall conductance of each magnetic band is directly related to the topological Chern number [1], which is given by the following integral over the closed Brillouin zone manifold,

$$c_n = \frac{i}{2\pi} \int_{\text{BZ}} d^2k \left( \frac{\partial \langle u_{\mathbf{k},n} |}{\partial k_x} \frac{\partial |u_{\mathbf{k},n}\rangle}{\partial k_y} - \frac{\partial \langle u_{\mathbf{k},n} |}{\partial k_y} \frac{\partial |u_{\mathbf{k},n}\rangle}{\partial k_x} \right), \quad (1)$$

where  $n$  is the band number,  $|u_{\mathbf{k},n}\rangle$  is a vector, corresponding to the periodic part of Bloch state. The quantised Hall conductance of  $N$  filled bands, that are well separated from higher bands, is proportional to the sum of Chern numbers of all filled bands:  $\sigma_H \sim \sum_{n=1}^N c_n$ . The Chern number is insensitive to various perturbations of the system and is related only to the bulk system properties. This allows to use it by characterising various topological system phases.

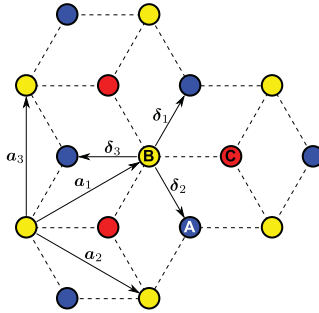


Fig. 1.  $T_3$  lattice, which consists of hexagonal (A and B) and triangular (C) sub-lattices.  $\mathbf{a}_1$  and  $\mathbf{a}_2$  are the lattice vectors.

In our work we numerically analyse the topological properties of band structure of the  $T_3$  optical lattice (Fig. 1) using a tight-binding model. This lattice consists of hexagonal and triangular sublattices, connected with complex hopping elements. Such optical lattice for ultra-cold atoms can be made by using three overlapping laser beams, positioned in a plane at the angles  $2\pi/3$ . Maxima of the created electric field intensity make a triangular lattice, while minima make a hexagonal lattice. Because of dynamic second order Stark effect ultra-cold atoms feel an effective potential, proportional to the field intensity. Two-electron atoms, such as ytterbium or alkaline-earth atoms, feel the triangular or hexagonal lattice depending on their internal state (spin-singlet  $^1S_0$  or long-lived spin-triplet  $^3P_0$ ). One can couple such two internal states with an additional laser light and induce hopping between the two sub-lattices [2].

In the presentation we describe phase diagrams of various topological phases of  $T_3$  optical lattice and show its similarity to the simpler hexagonal lattice with complex hopping elements [3]. Since the  $T_3$  optical lattice can be described by three-level system, it gives more different topological Chern insulator phases than the two-level hexagonal lattice.

- 
- [1] M. Kohmoto, Zero modes and the quantized Hall conductance of the two-dimensional lattice in a magnetic field, Phys. Rev. B **39**, 11943 (1989).
  - [2] F. Gerbier and J. Dalibard, Gauge fields for ultracold atoms in optical superlattices, New J. Phys. **12**, 033007 (2010).
  - [3] N. Goldman, E. Anisimovas, F. Gerbier, P. Öhberg, I. B. Spielman and G. Juzeliūnas, Measuring topology in a laser-coupled honeycomb lattice: from Chern insulators to topological semi-metals, New J. Phys. **15**, 013025 (2013).

# Application of the Boltzmann- Einstein equations for the description of gravitino dark matter

Valdemaras Milkus<sup>1</sup>, Thomas Gajdosik<sup>1</sup>

<sup>1</sup>Faculty of Physics, Vilnius University, Lithuania

[valdemaras.milkus@ff.stud.vu.lt](mailto:valdemaras.milkus@ff.stud.vu.lt)

The gravitino is a hypothetical particle postulated in the theory of local supersymmetry (supergravity). It is the superpartner of the graviton and interacts with the other particles only gravitationally [1]. The gravitino acquires its mass after the supersymmetry breaking. Because of the model dependence, the range of allowed gravitino mass is very wide. In various publications it is stated that the gravitino can be either stable or unstable. In our case we assume the gravitino to be stable so that it would be suitable candidate for the lightest supersymmetric particle and so the particle of the dark matter.

We calculate the squared amplitudes and the decay widths for the processes of the gravitino production in the decays of other particles (Fig. 1 and Fig. 2). These amplitudes are suppressed by a factor of the Planck mass-squared.

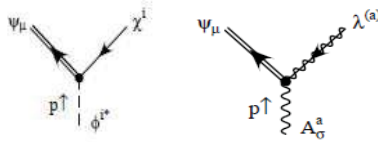


Fig. 1 and Fig. 2. Feynman diagrams for the decays of the scalar and the vector particles.

We find the squared amplitudes for the decay of the scalar and vector particles, producing the gravitinos. For example, in case of the sfermion ( $\phi$ ) decay to the fermion ( $\chi$ ) and gravitino ( $\psi$ ) we find the squared amplitude:

$$\langle |M_1^2| \rangle = \frac{16}{3M_P^2} \left( \frac{[m_\phi^2 - m_\chi^2 - m_\psi^2]^2}{4m_\psi^2} - m_f^2 \right) (m_\phi^2 - m_\chi^2 - m_\psi^2). \quad (1)$$

And in the case of vector particle ( $A$ ) decay to gravitino and gaugino ( $\lambda$ ) we get

$$\langle |M_2^2| \rangle = \frac{4m_\lambda m_\psi m_A^2}{M_P^2} + \frac{2}{3M_P^2} \left[ m_A^2 - \frac{(m_A^2 - m_\lambda^2 + m_\psi^2)^2}{m_\psi^2} \right] (m_A^2 - m_\lambda^2 - m_\psi^2). \quad (2)$$

Together with the gravitino production in the decays, we find the production rate for the gravitinos in case of 2→2 scattering events for gauge bosons- through the interaction of gluons or  $W^\pm$ . Contrarily to previous authors [2], we don't use the simplifications and do not ignore any of particle masses in order to define the nowadays gravitino density (at the low energy scale).

When we have all the necessary squared amplitudes, we make the system of coupled Boltzmann-Einstein equations. In this system we include the variation of the Hubble constant, which depends on the scale parameter and the matter content of the universe. We get the relation of the Hubble constant with the densities of particles from the solutions of the Einstein's field equation. We encode all the necessary equations using the *Mathematica 7.0* program.

Our next goals are to calculate the collision terms for the particle processes, include them into the Boltzmann- Einstein equations and to solve numerically this system of equations. The solution will show the variation of the gravitino density through the thermal history of the universe and we will get the bounds on the range of the gravitino mass in case of stable gravitino. The results will be published in the final master thesis.

[1] T. Moroi "Effects of the Gravitino on the Inflationary Universe" arXiv:9503210v1 [hep-ph].

[2] A. Ferrantelli, "Gravitino phenomenology and cosmological implications of supergravity," arXiv:1002.2835 [hep-ph].

# Oral session 7

---

13:30  
Friday

- Astrophysics and astronomy
- Interdisciplinary

# THE TOTAL ENERGY OF THE ELECTRIC FIELD AND THE ENERGY OF THE INTERACTION BETWEEN CHARGES AT SECONDARY SCHOOL

Volha Filippenko<sup>1</sup>

<sup>1</sup>Department of Physics, Belarusian State University, Belarus

VSME-111@yandex.ru

Energy of electric field is one of the most difficult subjects for understanding at secondary school. Therefore, its careful consideration is required for proper explanation. However, several difficulties occur during discussion of this subject. The most important of them is related to calculation of total energy of the electric field [1].

Let us consider a system of two electric charges  $q_1$  and  $q_2$ . Distance between them is supposed to be equal  $r$ . To calculate the energy of their interaction the following expression is widely used at secondary school:

$$W(r) = \frac{1}{4\pi\epsilon_0} \frac{q_1 q_2}{r}. \quad (1)$$

On the other hand, the expression for total energy of the electric field is known to be

$$W = \int_V w_k \Delta V_k \quad (2),$$

where  $w = \epsilon_0 \frac{E^2}{2}$  – electric energy density.

Following questions can be discussed in the framework of elective course of physics:

1. To find out the relation between total field energy and energy of charges' interaction;
2. To prove the energy of charges' interaction can be expressed as a sum of the energies of charges' interaction in pairs.

Total field energy calculated as follows

$$W = \int_V w_k \Delta V_k = \int_V \frac{\epsilon_0}{2} (\vec{E}_{1k} + \vec{E}_{2k})^2 \Delta V = \int_V \frac{\epsilon_0}{2} \vec{E}_{1k}^2 \Delta V_k + \int_V \frac{\epsilon_0}{2} \vec{E}_{2k}^2 \Delta V_k + 2 \int_V \frac{\epsilon_0}{2} \vec{E}_{1k} \cdot \vec{E}_{2k} \Delta V_k. \quad (3)$$

Summands  $\int_V \frac{\epsilon_0}{2} \vec{E}_{1k}^2 \Delta V_k$  and  $\int_V \frac{\epsilon_0}{2} \vec{E}_{2k}^2 \Delta V_k$  denote energies of fields created by charges  $q_1$  and  $q_2$

respectively.

As a result of this work the following expression for relation between total field energy and energy of charges' interaction have been obtained:

$$W_{int.} = 2 \int_V \frac{\epsilon_0}{2} \vec{E}_{1k} \cdot \vec{E}_{2k} \Delta V_k = \frac{q_1 q_2}{4\pi\epsilon_0 r} = U. \quad (4)$$

Equations (1), (4) define energy of charges' interaction to be the part of total field energy (2), (3).

Let us consider total energy of a system of charges  $q_k$ . by the way mentioned before:

$$\begin{aligned} W &= \int_V w_k \Delta V_k = \int_V \frac{\epsilon_0}{2} (\vec{E}_{1k} + \vec{E}_{2k} + \vec{E}_{3k} + \dots)^2 \Delta V_k = \int_V \frac{\epsilon_0}{2} \vec{E}_{1k}^2 \Delta V_k + \int_V \frac{\epsilon_0}{2} \vec{E}_{2k}^2 \Delta V_k + \int_V \frac{\epsilon_0}{2} \vec{E}_{3k}^2 \Delta V_k \\ &+ \dots + 2 \int_V \frac{\epsilon_0}{2} \vec{E}_{1k} \cdot \vec{E}_{2k} \Delta V_k + 2 \int_V \frac{\epsilon_0}{2} \vec{E}_{1k} \cdot \vec{E}_{3k} \Delta V_k + 2 \int_V \frac{\epsilon_0}{2} \vec{E}_{2k} \cdot \vec{E}_{3k} \Delta V_k + \dots = \\ &= W_1 + W_2 + W_3 + \dots + U_{12} + U_{13} + U_{23} + \dots \end{aligned} \quad (5)$$

Summands  $\int_V \frac{\epsilon_0}{2} \vec{E}_{1k}^2 \Delta V_k$ ,  $\int_V \frac{\epsilon_0}{2} \vec{E}_{2k}^2 \Delta V_k$ , ... are constant because of constant charges  $q_k$ .

Therefore, total energy of system is equal to sum of the energies of charges' interaction in pairs and field energy of charges themselves.

Greater understanding of electric field energy of charges unusual nature and energy of their interaction can be achieved in the framework of approach discussed above.

[1]A. Słabadzianuk, V. Filippenko Energy of electric field and energy of electric charges' interaction, Physics: teaching problems, 33-45 (2012).

## BURSTING BEHAVIOR OF THE NON-LINEAR STOCHASTIC MODELS APPLICABLE TO THE FINANCIAL MARKETS

Aleksejus Kononovicius<sup>1</sup>, Vyngintas Gontis<sup>1</sup>

<sup>1</sup>Institute of Theoretical Physics and Astronomy, Vilnius University, Lithuania  
[aleksejus.kononovicius@gmail.com](mailto:aleksejus.kononovicius@gmail.com)

Most of the currently prevailing economic theories were developed rather long time ago. For example classical economic research is considered to be started by A. Smith back in the XVIII century, while the foundations of neoclassical economics were formulated by many prominent researchers in the end of XIX century and in the begging of XX century. Consequently it should not be surprising that these theories are often overly simplistic and tend to disagree with the observations [1, 2]. The situation is very different today - one can obtain loads of the high-frequency empirical data and process it in anyway desired, one can also create complex computer models and build a bridge between theory, experiment and empirical observations.

The empirical analysis enabled mathematicians, physicists and economists to extend the applications of stochastic calculus to the financial markets and create stochastic models [3, 4, 5, 6]. The models have seen various applications and thus they are able to reproduce different aspects of the empirical time series.

Our group has proposed a general class of stochastic differential equations [7],

$$dx = \left( \eta - \frac{\lambda}{2} \right) x^{2\eta-1} dt + x^\eta dW. \quad (1)$$

This class of stochastic differential equations can be used as a base model for the dynamics of the trading activity [8] and absolute returns [9]. The obtained time series successfully replicated the empirical probability and spectral densities. Furthermore this class of stochastic differential equations can be used as a model for the flicker noise observed in very distinct fields.

Our recent work [10] has suggested that the model can be analyzed, and applied in risk management, in the terms of bursting behavior. In this contribution we will discuss the statistics of the above-the-threshold (i.e. burst duration), below-the-threshold (i.e. inter-burst) times and of the other related features of the empirical and model time series. The developed framework might provide insights to the nature of the systemic risk, the fast-growing bubbles and the flash crashes, consequently serving as an excellent tool in the real time policy making.

- 
- [1] R. H. Nelson, *Economics as Religion: From Samuelson to Chicago and Beyond* (University Park: Pennsylvania State University Press, 2001).
  - [2] J. P. Bouchaud, Economics needs a scientific revolution, *Nature* **455**, 1181 (2008).
  - [3] K. C. Chan, G. Andrew Karolyi, F. A. Longstaff, A. B. Sanders, An Empirical Comparison of Alternative Models of the Short-Term Interest Rate, *The Journal of Finance* **XLVII**, 1209-1227 (1992).
  - [4] J. A. Hernandez, R. M. Benito, J. C. Losada, An adaptive stochastic model for financial markets, *Chaos, Solitons and Fractals* **45**, 899-908 (2012).
  - [5] M. Jeanblanc, M. Yor, M. Chesney, *Mathematical Methods for Financial Markets* (Springer, Berlin, 2009).
  - [6] H. Zi-Gang, C. Yong, Z. Yong, W. Ying-Hai, Description of dynamics of stock prices by a Langevin approach, *Chinese Physics* **16**, 975 (2007).
  - [7] J. Ruseckas, B. Kaulakys, Tsallis distributions and 1/f noise from nonlinear stochastic differential equations, *Physical Review E* **84**, 051125 (2011).
  - [8] V. Gontis, B. Kaulakys, J. Ruseckas, Trading activity as driven Poisson process: comparison with empirical data, *Physica A* **387**, 3891-3896 (2008).
  - [9] V. Gontis, J. Ruseckas, A. Kononovicius, A long-range memory stochastic model of the return in financial markets, *Physica A* **389**, 100-106 (2010).
  - [10] V. Gontis, A. Kononovicius, S. Reimann, The class of nonlinear stochastic models as a background for the bursty behavior in financial markets, *Advances in Complex Systems* **15**, 1250071 (2012).

## DESTRUCTION OF COMETS

Artūrs Stramkals<sup>1</sup>

<sup>1</sup> Department of Physics, Faculty of Natural Sciences and Mathematics, Daugavpils University, Latvia  
[arturs.stramkals@gmail.com](mailto:arturs.stramkals@gmail.com)

The aim of the work is to research phenomena that can cause partial or complete decay of comets, such as solar wind, thermal radiation and collisions with other objects.

Scenarios of erosion of comets have been viewed and theoretically modelled in this study, applying approximations within the Solar system. Researches in this field are actual, especially nowadays, due to the fact that astronomers have been observing increased number of comets and asteroids in the Solar system, especially in proximity from Earth, for a few decades already. A work with information sources: books, publications, Internet material; calculations has been done during the research, modelling before mentioned situations within the Solar system.

An in-depth study of this topic can serve as a basis for developing a method of prediction for dynamic evolution of comets.

## TURBULENT MOLECULAR CLOUD COLLAPSE

Algimantas Kostas Sabulis<sup>1</sup>, Kastytis Zubovas<sup>2</sup>

<sup>1</sup>Faculty of Physics, Vilnius University, Lithuania

<sup>2</sup>Department of Physics and Astronomy, University of Leicester, UK

[algimantas.sabulis@ff.stud.vu.lt](mailto:algimantas.sabulis@ff.stud.vu.lt)

Cold and dense molecular hydrogen clouds serve as Galactic stellar nurseries. Stars are thought to form from dense molecular cores embedded deep within such clouds. What processes counteract the turbulence, which dominates the cloud, initiates collapse and trigger star formation? Several models have been proposed [1]. In this work we investigate if collapse of molecular clouds can be initiated and/or enhanced by external pressure of hot ISM (interstellar medium) surrounding the cloud. Numerical models of molecular clouds enable us to explore deep interiors of such structures, simulate processes that occur during collapse. This information is crucial for our understanding of dynamical processes with timescales much longer than human lifetimes that contribute to star formation.

Numerical SPH/N-body models were employed to simulate the dynamical evolution of such systems, using the Gadget code [2]. Static, homogenous models of molecular clouds supported by turbulence were embedded in hot ISM of various temperatures. We found that  $10^4\text{K}$  temperature and  $1\text{cm}^{-3}$  density ISM is sufficient to compress the cloud and initiate collapse. Collapse of such system creates a shock wave propagating inwardly, towards the center of the cloud. The shocked gas is compressed 4-5 times; such a dense environment enhances formation of gravitationally bound structures.

It was shown that models with highest ISM temperature form gravitationally bound structures fastest, most of gravitationally bound clumps in such models form within the propagating shock wave. Models with ISM temperature value that would keep cloud and hot ISM in equilibrium form gravitationally bound clumps in a shell around the cloud. Finally, models that were embedded in ISM colder than necessary to maintain equilibrium were disrupted and gravitationally bound structures formed in such conditions were only a consequence of turbulence.

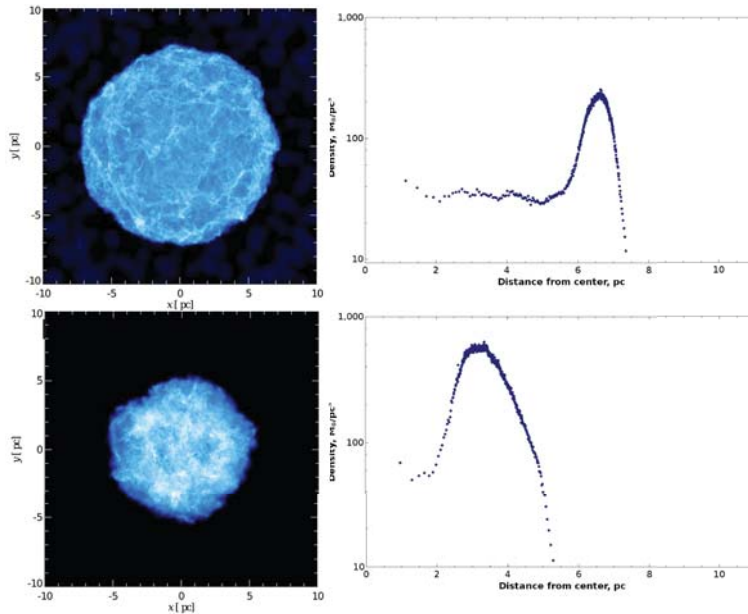


Fig. 1. Molecular cloud collapse. Density plots and radial profiles are given for  $t = 0.23$  and  $t = 0.47$  Myr.

[1] C.F. McKee, E.C. Ostriker, Theory of Star Formation, 2007, ARA&A, 45, 565

[2] V. Springel, The cosmological simulation code GADGET-2, 2005, MNRAS, 364, 1105

## PROTOPLANETARY NEBULAE'S RADIAL VELOCITY MEASUREMENTS AND INTERPRETATION

Aija Laure<sup>1</sup>, Laimons Začs<sup>1</sup>

<sup>1</sup> Faculty of Physics and Mathematics, University of Latvia, Latvia  
[aija.laure@gmail.com](mailto:aija.laure@gmail.com)

Protoplanetary nebula (PPN) is the transition phase between AGB (*asymptotic giant branch*) and planetary nebula, when large mass-losses stopped, but the star is not hot enough to emit sufficient quantity of Lyman-continuum photons to ionize dropped surrounding envelope of AGB star and become a planetary nebula [1].

The protoplanetary nebula phase is an important but still poorly understood stage in the evolution of low- and intermediate-mass stars. And up to now it has not been known how the decrease of the mass-loss rates takes place. Radiation pressure on dust particles is believed to be a major reason for the stellar wind from asymptotic giant branch (AGB) stars leading to high rates of mass-loss. The presence of hot dust and the appearance of emission lines in some PPNs seem to be the result of recent mass loss. [2]

The monitoring of radial velocity and luminosity of group of post-AGB stars confirms the existence of pulsations. Protoplanetary nebulae in Hertzsprung-Russell diagram cross the Cepheid instability strip and part of the transition phase stars could be regular variables [3].

The most active gas in pulsation of Cepheids is helium. Doubly ionized helium is more opaque than singly ionized helium. The more helium is heated, the more ionized it becomes. At the dimmest part of a Cepheid's cycle, the ionized gas in the outer layers of the star is opaque, and so is heated by the star's radiation, and, due to the increased temperature, begins to expand. As it expands, it cools, and so becomes less ionized, therefore more transparent, allowing the radiation to escape. Then the expansion stops, and reverses due to the star's gravitational attraction. The process then repeats.

Within FP7 project POSTAGBinGALAXIES, which is led by PhD in Physics Laimons Začs, radial velocity measurements have been coordinated, in order to maximize number of observations and make them relatively regular on time scale, what in turn is very important for analysis of pulsating periods. The radial velocity have been measured using the CORAVEL spectrometer mounted on the 1.65 m telescope at the Moletai Observatory (Lithuania), 1.2-m telescope at Dominion Astrophysical Observatory (DAO) in Canada and with spectrograph Hermes on the 1.2-m Flemish Mercator telescope at La Palma (Canary Islands).

Results of radial velocity monitoring of protoplanetary nebulae IRAS22272+5435 and IRAS 22223+4327 made in observatories mentioned above show:

- periodic component in changes of Doppler velocity, which could be interpreted as stellar pulsations;
- the characteristics of pulsations significantly differ from observed in typical variable stars – Cepheids;
- that common models of pulsations describe observations incorrectly, so there is a need to improve them.

To achieve the project's goal, it is necessary to make observations of statistically important selection of PPN.

---

[1] Kwok S., 1993. Proto-planetary Nebulae. *Annu. Rev. Astron. Astrophys.*, **vol.31**, pp.63-92.

[2] Začs L., Sperauskas J., Musaei F.A., Smirnova O., Yang T.C., Chen W.P., Schmidt M., 2009. Dynamical Phenomena in the Atmosphere of the Protoplanetary Nebulae IRAS 22272+5435. *The Astrophysical Journal*, **vol.695**, pp.203-207.

[3] Winckel H., 2003. Post-AGB Stars. *Annu. Rev. Astron. Astrophys.*, **vol.41**, pp.391-427.



## Automatic search for star clusters in Leo A galaxy

Karolis Manfreds Lyvens<sup>1,2</sup>, Donatas Narbutis<sup>1,2</sup>

<sup>1</sup> Center for Physical Sciences and Technology, Lithuania

<sup>2</sup> Vilnius University, Lithuania

[karolis.lyvens@ff.stud.vu.lt](mailto:karolis.lyvens@ff.stud.vu.lt)

Leo A dwarf irregular galaxy is a metal poor, gas rich, and one of the most isolated galaxies in the Local Group. Since stars have been forming recently in Leo A, its young stellar populations are still clustered. Investigation of star clusters may provide insight into conditions of their formation, because the fraction of gravitationally bound clusters is large in star-burst galaxies and small for quiescent star formation in low-density galaxies [1].

We have implemented an automatic method to identify stellar over-densities [2] for star cluster detection and applied it to Leo A galaxy. Star clusters can be resolved into individual stars with Hubble Space Telescope (*HST*) at the distance of Leo A, enabling us to perform stellar surface number density analysis.

By simulating star cluster observations, we have shown that such analysis is capable of finding clusters even in crowded stellar fields of the central part of the galaxy. We constrained detectability of clusters as a function of their age, mass, and size, and position in the galaxy.

The method was applied on the *HST* Advanced Camera for Surveys observations [3] of the Leo A galaxy. Several star cluster candidates have been found (one of which is shown in Fig. 1). Physical parameters of star clusters have been derived in order to link their properties to the recent star formation event in the galaxy.

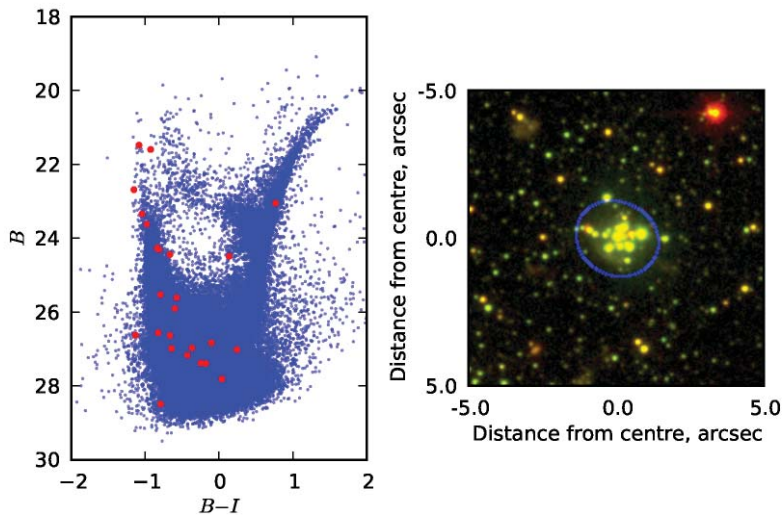


Fig. 1. Star cluster candidate in the Leo A galaxy. Left panel shows colour-magnitude diagram of all stars in the catalogue (blue points) based on observations by [3]. Red points indicate stars residing within the blue ellipse shown in the right panel, which consists of  $B$  (green) and  $I$  (red) pass-bands of *HST* images. High luminosity main sequence stars suggest that the cluster is of young age.

[1] Kruijssen, J. M. D. 2012, MNRAS, 426, 3008

[2] Koposov, S., Belokurov, V., Evans, N. W., et al. 2008, ApJ, 686, 279

[3] Cole, A. A., Skillman, E. D., Tolstoy, E., et al. 2007, ApJL, 659, L17

# Poster session 1

17:00  
Wednesday

---

- Laser physics and optical technologies
- Spectroscopy, methods and devices for physical diagnostics

## Optical properties of MgZnO alloys

Vytautas Šimkevičius, Edmundas Kuokštis, Mindaugas Karaliūnas

<sup>1</sup>Semiconductor Physics Department, Vilnius University, Sauletekio Ave. 9-III, LT-10222 Vilnius, Lithuania  
[vsimkeviciuss@gmail.com](mailto:vsimkeviciuss@gmail.com)

Recently, optoelectronic devices operating in UV region attracts much attention for their potential applications in flame sensing, chemical/biological agents detection, missile plume sensing, air and water purification, etc.[1] For this purpose, visible light blind photodetectors are being developed. In order to increase their efficiency, temperature stability is looking for new material for their production. MgZnO alloys may be used in the manufacture of such photodetectors.

Compared with others materials ZnO based semiconductors can be grown at lower temperature. However, because ZnO and MgO different crystal structure phase separation occurs. ZnO buffer layer is used to make suitable crystal structure for the growing of MgZnO layer. In this way it is possible to grow single – phase hexagonal structure MgZnO with a bandgap energy 4.65eV.[2] To use this material in optical devices, it is necessary to know precisely the energy band structure and optical properties. In this work, series of  $\text{Mg}_x\text{Zn}_{1-x}\text{O}$  epitaxial layers with different Mg quantity ( $x = 0.025; 0.166; 0.303; 0.318$ ) grown by MBE has been investigated.

This work aim was to find MgZnO band gap energy using diffuse reflectance spectroscopy. Results of diffuse reflectance are shown in (fig.1) could be seen sharp absorption edge at 3.33 eV energy and smaller ones in deeper UV region.

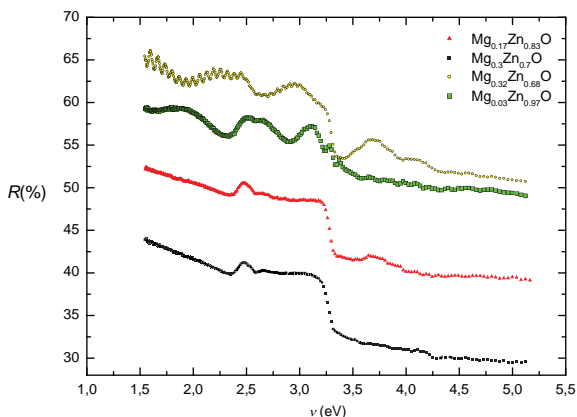


Fig. 1. Measured diffuse reflectance spectra

It was found that increasing the amount of magnesium band gap energy increases from 3.41 eV to 4.25eV. A phase segregation occurs at ~30% Mg. Increasing Mg content also increases the Stoke shift.

[1] T. Tut, M. Gokkavas, A. Inal, and E. Ozbay, Appl. Phys. Lett. 90, 163506 2007.

[2] Leah Bergman, Jeanne L. McHale (2012) Handbook of luminescent semiconductor materials, LLCRC Press :149-151.

## 3D VISUALISATION OF SINGLE AND MULTIPLE FILAMENTS INDUCED BY ULTRAVIOLET FEMTOSECOND PULSES

Nelda Antonovaite<sup>1</sup>, Vytautas Kucikas<sup>1</sup>

<sup>1</sup>Department of Quantum Electronics, Faculty of Physics, Vilnius University, Lithuania

[nelda.antonovaite@ff.stud.vu.lt](mailto:nelda.antonovaite@ff.stud.vu.lt)

[vytautas.kucikas@ff.stud.vu.lt](mailto:vytautas.kucikas@ff.stud.vu.lt)

Light filament is a dynamic optical pulse structure with an intense central core, which is able to propagate distances much larger than typical diffraction length and keep the narrow pulse width without external channeling mechanism [1]. When the input power is far above the critical power self-focusing ( $P_{cr}$ ) in nonlinear medium, the beam breaks up into a large number of filaments [2]. Light filaments display interesting and unique features such as white light spectrum, conical emission, sub-diffractive propagation, pulse shortening and splitting, etc. It is important to visualize light filaments in space and time domains to get better understanding of nonlinear phenomena governing light-matter interaction.

In this work spatial and temporal dynamics of single and multiple filaments formed in water by propagation of an intense 100 fs pulse with wavelength of 400 nm are studied. Three dimensional mapping method with high spatial (1  $\mu\text{m}$ ) and temporal (30 fs) resolution [3], based on cross-correlation via difference-frequency generation was used for visualising spatiotemporal intensity profiles of the filaments. The typical profiles, which were recorded at the input power of 5 and 11  $P_{cr}$  are shown in Fig. 1 (a) and (b), respectively. At the input power of 5  $P_{cr}$ , the filament shows pulse splitting and occurrence of concentric ring structure at ( $t = 0$ ), which breaks up into multiple filaments at 11  $P_{cr}$ . Dynamics of filaments were visualised in two and three dimensions including the isointensity surface of multiple filaments, in which transformation from a single filament to multiple filaments is captured in detail.

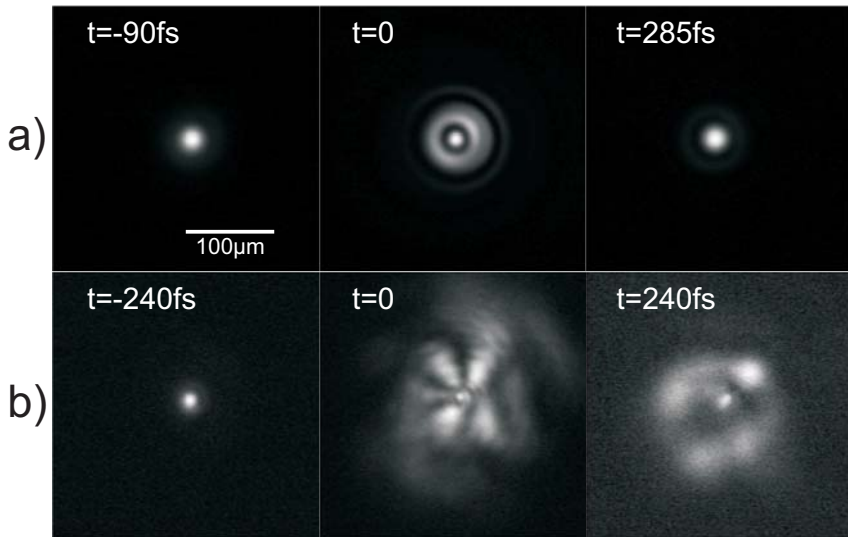


Fig. 1. Spatiotemporal profiles of light filament at input power of (a) 5  $P_{cr}$  and (b) 11  $P_{cr}$ . The negative, zero and positive delay times correspond to the leading, central and trailing parts of the filament, respectively.

- 
- [1] A. Couairon, A. Mysrowicz, Femtosecond filamentation in transparent media, *Phys.Rep.* **441**, 49-189 (2007).
  - [2] G. Tamosauskas, G. Fibich, B. Ilan, Multiple filamentation induced by input-beam ellipticity, *Opt Lett.* **29**, 1126-1128 (2004).
  - [3] D. Majus, V. Jukna, G. Tamosauskas, G. Valiulis, A. Dubietis, Three-dimensional mapping of multiple filament arrays, *Phys. Rev. A* **81**, 043811 (2010).

## SCRIBING OF SAPPHIRE WAFERS BY USING PICOSECOND LASER IRRADIATION AT 355 NM AND 1064 NM WAVELENGTHS

Jonas Berzins, Mindaugas Gedvilas

Center for Physical Sciences and Technology, LT-02300 Vilnius, Lithuania  
jonasberzins@gmail.com

The scribing of sapphire wafers is one of those areas where the correct usage of laser technologies might be the best tool for the optimization of the process [1, 2].

The development of light emitting diodes requires the most efficient technology of basis for the epitaxial GaN structuring. The unique physical, chemical and optical properties of a single crystal sapphire ( $\text{Al}_2\text{O}_3$ ) such as structural fit between sapphire and GaN crystals, transparency at a wide range of wavelengths and a high thermal conductivity makes it an excellent material for the application [3].

In opposition to the widely used industrial methods: a blade dicing with a diamond disk or a laser ablation using nanosecond lasers at the range of ultraviolet wavelengths of irradiation, operating with a picosecond laser offers us a higher precision together with a new way to separate the pieces of the LED chips – the stealth dicing [4]. The greatness of this method is an internal processing that keeps us from any surface damage while still optimizing the process itself (Fig. 1).

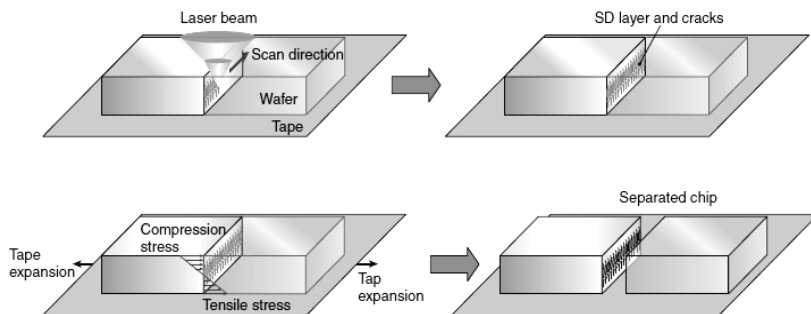


Fig. 1. Principal scheme of the stealth dicing (reproduced from [5]).

In this work, the intra-volume scribing of sapphire wafers with the picosecond laser pulses was investigated under various conditions of pulse energies and distances between laser pulses at 355 nm and 1064 nm wavelengths. The experiments led us to a significant improvement in the scribing of sapphire wafers. The stealth dicing was approved as the best method while it brought us to the foundation of an optical scribing system using both, 355 nm and 1064 nm, wavelengths at once.

- 
- [1] A. Tamhankar, R. Patel, *J. Laser Applications*, 2011, 23, 032001.
  - [2] D. Karnakis, E.K. Illy, M.R.H. Knowles, E. Gu, M.D. Dawson, *Proc. SPIE*, 2004, 5366, 207-211.
  - [3] W.A. Melton, J.I. Pankove, *J. Cryst. Growth*, 1997, 178, 168-173.
  - [4] F. Fukuyo, K. Fukumitsu, N. Uchiyama, *Proc. LPM2005*, Williamsburg, USA, 2005.
  - [5] [http://jp.hamamatsu.com/resources/products/etd/pdf/SD\\_tech\\_forMEMS\\_TLAS9005E02.pdf](http://jp.hamamatsu.com/resources/products/etd/pdf/SD_tech_forMEMS_TLAS9005E02.pdf)

# COLLINEAR SETUP FOR TWO-COLOR HIGH HARMONIC GENERATION

Rimantas Budriūnas<sup>1,2</sup>, Cord Arnold<sup>2</sup>

<sup>1</sup>Faculty of Physics, Vilnius University, Lithuania

<sup>2</sup>Department of Physics, Lund University, Sweden  
[rimantas.budriunas@ff.stud.vu.lt](mailto:rimantas.budriunas@ff.stud.vu.lt)

High harmonic generation (HHG) is a process in which bursts of coherent ultraviolet and/or soft x-ray radiation are generated by firing intense laser pulses into dilute gases. These bursts can last below 100 attoseconds ( $1\text{as} = 10^{-18}\text{s}$ ), making HHG radiation bursts the shortest currently known electromagnetic pulses. One improved scheme of HHG is two-color high harmonic generation, when the driving laser pulse is used in conjunction with its second harmonic. This has several desirable effects, such as raising the total generation efficiency and producing even-numbered harmonics, otherwise absent in HHG spectra [1].

Two-color high harmonic generation requires precise control over the polarizations of the driving pulses and the time delay between them [2]. While this is readily achieved by splitting the fundamental and second harmonic beams and performing the necessary operations on the beams separately, such setups are tedious to align. We designed, constructed and tested a collinear optical system that could replace a two-color interferometer.

A schematic drawing of the setup is shown in fig. 1. The setup is optimized for use with Ti:Sapphire lasers operating in the 750-850nm wavelength range. First, the second harmonic is generated in a BBO ( $\beta$ -Barium Borate) crystal. The 800nm pulse is delayed with respect to the 400nm pulse by a plate made from calcite. It is followed by a crystalline quartz plate that works as a zero-order  $\lambda/2$  waveplate at 800nm and a  $1 \cdot \lambda$  waveplate at 420nm. The polarization of the 800nm pulse is rotated by  $90^\circ$ , while the polarization of 400nm light is unchanged. Finally, because of the limited bandwidth of the waveplates, a series of glass wafers as thin as  $100\mu\text{m}$  are used to clean the polarization of the pulses by reflecting the electric field components polarized in the unwanted direction as HHG efficiency is severely reduced if the driving pulses have elliptical polarization.

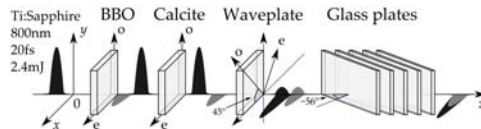


Fig. 1. Schematic drawing of the collinear two-color HHG setup

An example of a high harmonic spectrum generated using this setup is shown in fig. 2. A one-color HHG spectrum produced in the same system from only the 800nm pulse is also shown for comparison.

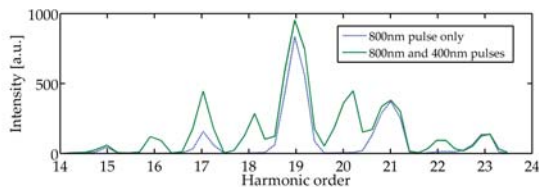


Fig. 2. Spectra of high harmonics generated with the setup in a jet of argon

The collinear system is a suitable replacement of a two-color interferometer. Even though about 10% of the second harmonic pulse energy is lost due to the finite bandwidth of the waveplate, the setup is efficient enough to reliably generate high harmonics in the two-color regime. Furthermore, the setup is very easy to operate. Most importantly, the switching time between one- and two-color HHG experiments has been reduced to a few minutes, which will allow researchers to try more experiments in both one- and two-color modes.

- [1] J. Mauritsson, P. Johnsson, A. L'Huillier et al., Attosecond Pulse Trains Generated Using Two Color Laser Fields, *Physical Review Letters* **97**, 013001-1 - 013001-4 (2006).
- [2] H. Eichmann, A. Egbert, S. Nolte, Polarization Dependent High-Order Two Color Mixing, *Physical Review A* **51**, 3414-3417 (1995)

## MICROMACHINING OF OPTICAL FIBERS USING ULTRASHORT LASER PULSES

Gediminas Čažėvskis<sup>1</sup>, Domas Paipulas<sup>1</sup>

<sup>1</sup> Laser Research Center, Vilnius University, Saulėtekio a. 10, LT-10223 Vilnius, Lithuania

[gediminas.chazevskis@gmail.com](mailto:gediminas.chazevskis@gmail.com)

Over the past decade laser systems, emitting ultrashort pulses, have established themselves in the scientific and industrial market. Laser pulses with pulse durations, ranging from a few picoseconds to tens of femtoseconds, have found their applications in medicine, spectroscopy, atmospheric measurements, warfare and etc. One of the most rapidly developing ultrashort laser pulse applications is micromachining. Ultrashort pulse laser systems are powerful tools for micromachining any material, because they emit high energy pulses, which are able to reach intensities needed to induce nonlinear optical processes when focused. Ultrashort pulse micromachining has some advantages over other machining techniques: reduction of heat diffusion around the focal volume, elimination of plasma absorption and elimination of material's liquid phase during the interaction of the pulse and matter. These advantages allow creating precise micro/nano scale structures.

Since the invention of the optical fibers they are widely used in telecommunications as the information transferring tools, however, rapidly evolving ultrashort pulse laser systems added a few more applications. Micromachined optical fibers are used as optical gas, temperature, mechanical strain, refractive index change, evanescent field, pressure and etc. sensors [1]. Micro Fabry-Perot [2], Mach Zender, Sagnac interferometers, as well as Bragg diffraction gratings are also formed with laser micromachining – it is clear, that demand of micromachined optical fibers is increasing. There are many publications, describing micromachining of fibers using low, from 1 to 3 kHz pulse repetition rate laser systems [1], but there are almost no publications describing the use of high repetition rate, up to hundreds of kilohertz laser systems, which would allow to significantly increase the micromachining speed and precision. In this work we demonstrate the possibility to precisely form various micro structures in optical fibers using high repetition rate ultrashort pulse laser system.

In this experiment a femtosecond PHAROS laser system, emitting 1030 nm wavelength, 300 fs duration pulses with a repetition rate of 100 kHz is used to fabricate microstructures in the multimode quartz fiber. Two different fabrication algorithms are examined, first one being the “repeated line” and the second one – the “repeated rectangular spiral”. Laser beam is focused through a 0,42 numerical aperture lens to the surface of the fiber. A view of the micromachined zone is observed with a CCD camera. Results, obtained using “repeated line” algorithm show that a very narrow, from around 2 to 3  $\mu\text{m}$ , and deep, from around 12 to 35  $\mu\text{m}$  grooves can be formed even after single translation of the sample (Fig. 1). A possibility of forming highly rectangular grooves with a surface roughness of  $\pm 3 \mu\text{m}$ , which could be suitable for interferometric applications, was also demonstrated (Fig. 2).

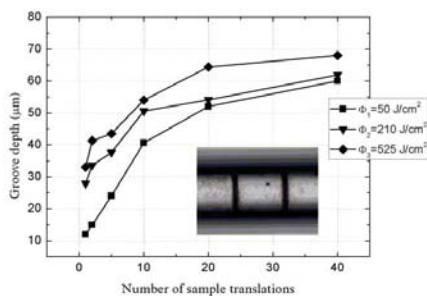


Fig. 1. Groove depth dependence on the number of sample translations using different laser energy fluences.

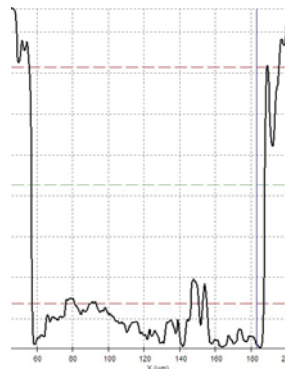


Fig. 2. Highly rectangular groove, formed using a “repeated rectangular spiral” algorithm.

[1] R. R. Gattass, and E. Mazur, Femtosecond micromachining in transparent materials, *Nature Photonics* **2**(4), 219-225 (2008).

[2] Y. Rao, M. Deng, D. Duan, X. Yang, T. Zhu, and G. Cheng, Micro Fabry-Perot interferometers in silica fibers machined by femtosecond laser, *Opt. Express*, **15**(21), 14123-14128 (2007).

## PHOTOREFRACTIVE MODIFICATIONS IN LITHIUM NIOBATE CRYSTALS INDUCED BY FEMTOSECOND LASER PULSES

Aušra Čerkauskaitė<sup>1\*</sup>, Domas Paipulas<sup>1</sup>

<sup>1</sup> Laser Research Centre, Vilnius University, Saulėtekio Ave. 10, LT-10223 Vilnius, Lithuania  
[ausra.cerkauskaite@ff.stud.vu.lt](mailto:ausra.cerkauskaite@ff.stud.vu.lt)

Rapidly growing development in laser physics has led to many applications becoming relevant to the industrial market, and it is expected that the advent of efficient laser sources and the use of materials that exhibit high order nonlinearities should be combined in order to disseminate in new areas. Therefore, the class of nonlinear phenomena based on photorefractive effects in electro-optical crystals will undoubtedly play a major role for modern applications.

Photorefractive effects are based on the transposition of a light pattern into a refractive index pattern. Thus, when coherent high intensity laser beams interfere in the volume of a material, a photoinduced space charge field is generated which modulates a refractive index via the electro-optic effect. The photoinduced change of the refractive index in lithium niobate crystals is reversible and may be optically erased or thermally annealed [1]. This effect in  $\text{LiNbO}_3$  is of interest for many applications, such as holographic data storage, volume holographic memories, wavelength division multiplexing, optical detection systems of ultrasonic waves, double exposure interferometry, etc [2].

However, the change of the refractive index recorded in  $\text{LiNbO}_3$  by femtosecond laser pulses has not been studied completely and detailed knowledge about the microscopic processes occurring in these materials is still unknown. For this reason, the main goal of the current research was to induce photorefractive modifications in undoped and lithium niobate doped with iron ( $\text{LiNbO}_3:\text{Fe}$ ) crystals by illumination with near infrared wavelength (1030 nm), 300 fs pulse duration laser radiation focused through a 0.42 numerical aperture lens to the volume of the crystal (Fig. 1). Also, the dependence of modification appearance on fabrication parameters, such as pulse energy, repetition rate and focusing depth was analyzed. Later, modified crystal was irradiated with intense ultraviolet (UV) light to test modifications stability. Photorefractive modifications induced in pure lithium niobate crystal completely vanish after sufficient UV exposure. In iron-doped lithium niobate case, the erasure of recorded modifications becomes more complicated, as additional zones of modified optical properties start to appear in a laser pulse track almost across all crystal length after UV exposure. These zones indicate that defect-formation is present in the crystal even at low laser pulse energies. We demonstrate that such modifications can be erased using thermal annealing procedure (Fig. 2).

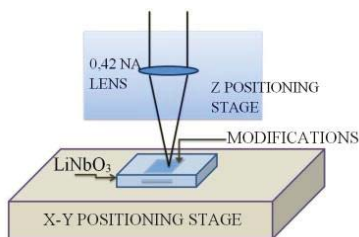


Fig. 1. The principal scheme of the experiment.

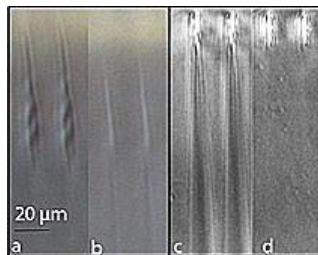


Fig. 2. Modifications in the volume of the  $\text{LiNbO}_3:\text{Fe}$  crystal (a) before and (b) after UV exposure; (c) additional modified zones that appear in the laser path after UV radiation; (d) same area of  $\text{LiNbO}_3:\text{Fe}$  crystal after thermal annealing (1 h at 100°C).

This work was partly supported by project "Promotion of Student Scientific Activities" (VP1-3.1-ŠMM-01-V-02-003) from the Research Council of Lithuania (A. Č.). This project is funded by the Republic of Lithuania and European Social Fund under the 2007-2013 Human Resources Development Operational Programme's priority 3.

[1] T. Volk and M. Wohlecke, *Lithium Niobate: Defects, Photorefractive and Ferroelectric Switching* (Springer, 2008).

[2] K. Buse, Light-induced charge transport processes in photorefractive crystals I: Models and experimental methods, *Appl. Phys. B* 64, 273–291 (1997).



## THIN-FILM CIGS SOLAR CELLS SCRIBING WITH FEMTOSECOND AND NANOSECOND LASERS

Juozas Dudutis, Paulius Gečys

Center for Physical Sciences and Technology, Savanoriu ave. 231, LT-02300, Vilnius, Lithuania

[juozas.dudutis@gmail.com](mailto:juozas.dudutis@gmail.com)

Global demand for energy is increasing. The direct conversion of sunlight into electrical energy can be the most potential alternative to fossil fuels and a preferred method for clean and safe energy production in the future [1, 2]. Thin film solar cell technologies have raised the expectation that photovoltaics will be able to compete with traditional energy production methods due to expected lower processing costs [2]. Among various thin film absorbers the main interest are amorphous Si, CdTe and CuInSe<sub>2</sub> and its alloys with Ga and/or S [1]. CIGS thin film solar cells have a high optical absorption coefficient and a tunable band gap [2].

CIGS solar cells have to be divided into smaller cells interconnected in series to avoid high currents and heat releasing. Three scribing processes are needed to form interconnect: P1 separates the molybdenum back contact, P2 connects the front contact with the back contact of the neighboring cell and P3 is necessary for the electrical separation of the conductive window [3].

In our experiments we focused on P3 scribing process to expose the molybdenum back contact. Three thin-film structures with different front contacts were processed: ITO/ZnO/CdS/CIGS/Mo/PI, ZnO/CdS/CIGS/Mo/PI, ZnO:Al/ZnO/CdS/CIGS/Mo/PI. The best scribing regimes with the lowest damage to the molybdenum back contact were found and ablation thresholds with different number of laser pulses were measured for all samples.

CIGS thin film solar cells were scribed by changing laser scanning speed, repetition rate and pulse energy. Two experimental setups were used for the ablation and scribing processes. In the femtosecond system thin-film structures were scribed using PHAROS laser (300 fs, 100 kHz repetition rate, 1032 nm wavelength). The laser beam was focused with an objective lens with a focal length of 50 mm and XYZ stage was used for sample positioning. In the nanosecond system structures were processed with BALTIC HP laser (10 ns, 10 – 100 kHz repetition rate, 1064 nm wavelength), the laser beam was positioned with a galvanometer scanner and focused with an objective lens with a focal length of 80 mm. The scribing process was evaluated with an optical microscope and scanning electron microscope (SEM), chemical compounds were characterized with the x-ray energy dispersion spectrometer (EDS).

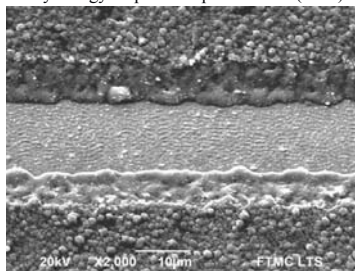


Fig. 1. SEM image of the P3 scribe in ZnO:Al/ZnO/CdS/CIGS/Mo/PI structure: 4.1 μJ, 100 kHz, 180 mm/s.

The best results with the femtosecond laser were achieved using 2.7 μJ – 7 μJ laser pulse energy and 60 – 160 mm/s laser scanning speed for ITO/ZnO/CdS/CIGS/Mo/PI sample, 1.1 μJ – 3.8 μJ pulse energy and 40 – 200 mm/s scanning speed for ZnO/CdS/CIGS/Mo/PI sample and 1.5 μJ – 6.6 μJ pulse energy and 70 – 250 mm/s scanning speed for ZnO:Al/ZnO/CdS/CIGS/Mo/PI sample. We achieved less than 42 % melted edge compared to the whole width of the femtosecond laser scribe. While working with a nanosecond laser a clean scribe was not achieved and melted area was bigger compared to scribing with a femtosecond laser. Also melted edge area depended on the laser pulse energy and scanning speed. Results showed that scribing with lower laser pulse energy and slower scanning speed decreases melted area and provided sharper edges.

[1] Viswanathan S. Saji, Ik-Ho Choi, Chi-Woo Lee, Progress in electrodeposited absorber layer for CuIn<sub>1-x</sub>Ga<sub>x</sub>Se<sub>2</sub> (CIGS) solar cells, *Solar Energy* 85, 2666–2678 (2011).

[2] M. Kaelin, D. Rudmann, A.N. Tiwari, Low cost processing of CIGS thin film solar cells, *Solar Energy* 77, 749–756 (2004).

[3] F. Kessler, D. Herrmann, M. Powalla, Approaches to flexible CIGS thin-film solar cells, *Thin Solid Films* 480–481, 491–498 (2005).

## SPATIAL FILTERING BY CHIRPED PHOTONIC CRYSTALS

Darius Gailevičius<sup>1</sup>, Vytautas Pūrys<sup>1</sup>, Lina Maigytė<sup>2</sup>, Martynas Peckus<sup>3</sup>,  
Mangirdas Malinauskas<sup>1</sup>, Kęstutis Staliūnas<sup>2,4</sup>

<sup>1</sup>Department of Quantum Electronics, Vilnius University, Lithuania

<sup>2</sup>Departament de Física i Enginyeria Nuclear, Universitat Politècnica de Catalunya, Spain

<sup>3</sup> Center for Physical Sciences and Technology, Lithuania

<sup>4</sup> Institució Catalana de Recerca i Estudis Avançats (ICREA), Spain

[darius.gailevicius@ff.stud.vu.lt](mailto:darius.gailevicius@ff.stud.vu.lt)

Photonic crystals are periodic dielectric structures that have been an object of great interest for over two decades. The spatial periodic modulation of the refractive index inside such structures enables the presence of photonic bandgaps. Such photonic bandgaps allow the realization of photonic crystals as temporal light filtering devices, by allowing the propagation of light whose wavelength does not correspond to forbidden Bloch modes [1]. Recently the appearance of photonic bandgaps for certain geometries of photonic crystal structure has been predicted that would allow such devices to function as highly compact spatial beam filtering devices [2].

In this report, we present experimental proof of improved filtering efficiency by using a modified known photonic crystal geometry (2D woodpile), that does not possess a photonic bandgap. Such gapless crystals have been predicted theoretically and are characterized by the fact that they do not require as large longitudinal periods or as high refractive index modulation as the gap-based crystals [3], therefore can be realized with less technological difficulty. Due to the lack of a bandgap such crystals suffer from the effect of reversed scattering, when light propagates over too many crystal layers, which is a result of mode coupling. In order to reduce unwanted mode interactions and increase filtering angles, in addition to other filtering parameters, we employed linear modulation of the longitudinal crystal period (chirping) [3]. First experimental proof of an improved filtering effect in chirped gapless photonic crystals is introduced.

Photonic crystals were fabricated under different conditions and with different geometric parameters by utilizing the method of direct femtosecond laser writing technique [4] inside soda-lime glass samples. After fabrication crystals were irradiated with a focused 633 nm laser beam and the far field spatial (angular) intensity distribution behind the crystal was measured. The improvement of filtering efficiency and increase in filtering angles in comparison with the unchirped crystals have been observed and are in sufficient agreement with the theoretical values.

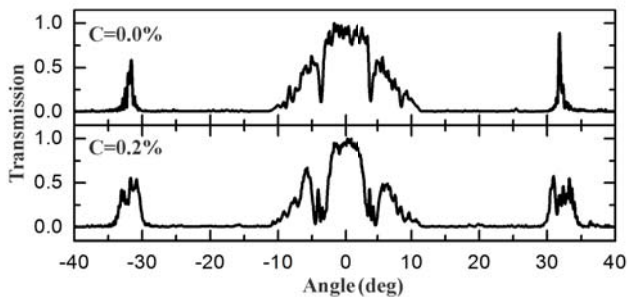


Fig. 1. Angular transmission profiles for varying chirp parameter  $C = \Delta d / \bar{d}$ , where  $\Delta d$  is the difference in distance between two consecutive crystal layers and  $\bar{d}$  is the average distance between layers throughout the whole photonic crystal.

- 
- [1] J. D. Joannopoulos, S. G. Johnson, J. N. Winn, R. D. Meade, *Photonic Crystals: Molding the Flow of Light*, 2nd ed. (Princeton University Press, USA, 2008).
  - [2] E. Colak, A. O. Cakmak, A. E. Serebryannikov and E. Ozbay, Spatial filtering using dielectric photonic crystals at beam-type excitation, *J. Appl. Phys.* **108**, 113106 (2010).
  - [3] K. Staliūnas and V. J. Sánchez-Morcillo, Spatial filtering of light by chirped photonic crystals, *Phys. Rev. A* **79**, 053807 (2009).
  - [4] D. Paipulas, *Refractive Index Modification in Glasses and Crystals with Ultrashort Laser Pulses*, (VU press, Vilnius, 2011).

## GENERATION OF ODD HARMONICS IN SOLID MEDIA

Nail Garejev<sup>1</sup>, Julius Darginavičius<sup>5</sup>

<sup>1</sup> Department of Quantum Electronics, Faculty of Physics, Vilnius University, Saulėtekio Ave. 9-III, LT-10222 Vilnius, Lithuania

[nail.garejev@ff.stud.vu.lt](mailto:nail.garejev@ff.stud.vu.lt)

The generation of harmonics depends on the nonlinear susceptibilities of media and those susceptibilities can be measured using harmonic generation. The aim of this work was to generate higher odd harmonics in solid media without inducing optical damage in the process.

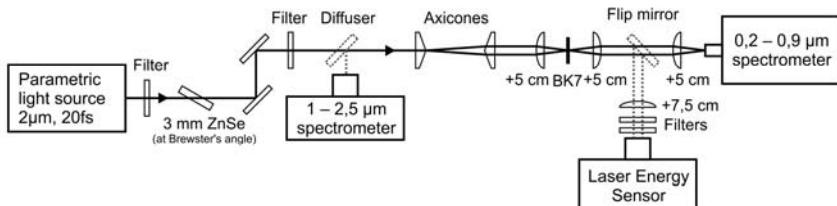


Fig. 1. Experimental setup.

We used a parametric light source, which delivered 20 fs, 50 μJ pulses at 2 μm. ZnSe crystal was used to compensate dispersion in lens and axicones and generate harmonics from shorter, higher intensity pulse. Diffuser was a temporary part of setup, used to divert original pulse to MIR spectrometer. Axicones generated ring-shaped laser beam, which was then sharply focused into the sample. Sharp focusing allowed generating harmonics while avoiding the generation of supercontinuum. 4f system (two +5 cm lens) was used to collect the generated harmonics into the optical fiber connect to spectrometer. Flip mirror could be used to measure the energies of individual harmonics with filters and energy sensor. We used 0.15 mm BK7 glass sample, as it gave the best results compared to other available samples.

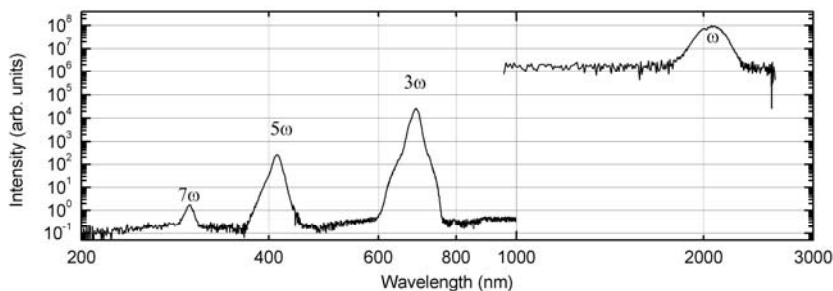


Fig. 2. The spectra of harmonics and original pulse.

During the experiment, 3rd, 5th and 7th harmonics were generated in BK7 glass sample. We have measured the relative energies of harmonics ( $E_{\omega}/E_{3\omega} \approx 1000$ ;  $E_{3\omega}/E_{5\omega} \approx 150$ ;  $E_{5\omega}/E_{7\omega} \approx 190$ ) and their bandwidths ( $\Delta f_{\omega} = 13$  THz;  $f_{3\omega} = 11$  THz;  $\Delta f_{3\omega} = 19.5$  THz;  $\Delta f_{5\omega} = 29$  THz). Our ability to measure 9th and higher harmonics was limited by the aberrations in 4f lens system, optical damage when using higher energy pulses and the limited sensitivity of spectrometer. More experiments are planned with alternative setups and samples.

[1] J. Darginavičius, N. Garejev, and A. Dubietis, Generation of carrier-envelope phase-stable two optical-cycle pulses at 2 μm from a noncollinear beta-barium borate optical parametric amplifier, Opt. Lett. 37, 4805–4807 (2012).

# NUMERICAL ANALYSIS OF DIFFRACTION GRATING BASED REFRACTIVE INDEX SENSOR

Ieva Gražulevičiūtė<sup>1</sup>, Tomas Tamulevičius<sup>1,2</sup>, Darius Urbonas<sup>3</sup>, Martynas Gabalis<sup>3</sup>,  
Raimondas Petruškevičius<sup>3</sup>, Sigita Tamulevičiūtė<sup>1,2</sup>

<sup>1</sup> Physics Department, Kaunas University of Technology, Lithuania

<sup>2</sup> Institute of Materials Science, Kaunas University of Technology, Lithuania

<sup>3</sup> Department of Laser Technology, Center for Physical Sciences and Technology, Lithuania

[Ieva.Grazuleviciute@stud.ktu.lt](mailto:Ieva.Grazuleviciute@stud.ktu.lt)

The understanding of the sharp features in the reflectance spectrum obtained employing a sub-wavelength period diffraction grating based refractive index sensor requires numerical analysis of a theoretical model which includes the surface relief and material properties of a grating sensor chip and optical properties of the analyte.

The sub-wavelength (428 nm) period sinusoidal relief sensor chip was fabricated employing holographic lithography and dry etching of a 230 nm thickness SiO<sub>2</sub> doped diamond like carbon film deposited on fused silica (FS) substrate. The white TM and TE polarized light reflectance measurements (0°, 10°, 20°) were performed employing custom build motorized angular reflectance measurement stand and CCD spectrometer ( $\lambda=360\text{--}860\text{ nm}$ ) [1]. For normal incidence reflectance measurements a 45° inclined fused silica window was placed in the optical path of an incident beam. The reflectance spectra and electric field distribution for the sensor chip in contact with air and distilled water were simulated employing commercially available “GSolver” and “Comsol” software based on Rigorous Coupled Wave Analysis (RCWA) and Finite Element Method (FEM) respectively. The basic structure of the grating is depicted in the inset of Fig. 1 a. Due to the symmetry of the structure in  $x$  and  $z$  directions the simulations were done in 2D (the periodic boundary conditions were used). In case of the RCWA method the grating region  $d_g$  was divided into 13 layers to approximate the profile to an arbitrary degree of accuracy. The electromagnetic boundary conditions were applied at the interfaces among all regions and the individual grating layers.

Fig. 1 a depicts the experimental and simulated reflectance spectrum of TM polarized light for 10° angle of incidence. It demonstrates characteristic peaks employed for the sensing applications. The existence of the peaks can be understood analyzing the  $E_z$  field distribution obtained for the wavelengths corresponding to the peak positions (Fig. 1b, c). These phenomena are called resonance type Wood’s anomalies. They are present due to guided modes which may be supported by the waveguide grating (Fig. 1b, c). In our case due to the periodic modulation and the asymmetry in the guide supported modes are leaky modes and thus it cannot be maintained on the waveguide grating [2]. The resonance peak is highly dependent on the grating parameters especially the refractive index contrast at the FS/DLC and analyte/DLC interfaces.

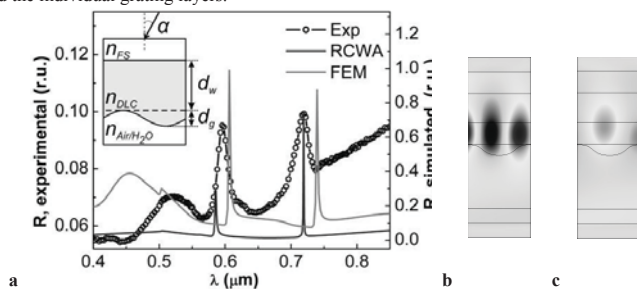


Fig. 1. (a) Experimental and simulated reflectance spectrum of TM polarized light from the grating in contact with air obtained for  $\alpha = 10^\circ$  angle of incidence (inset depicts one period of the sinusoidal grating structure).  $E_z$  field distribution for  $\alpha = 10^\circ$  of a wavelength corresponding to left (606 nm, b) and right (741 nm, c) peak.

[1] T. Tamulevičius, et al., Application of holographic sub-wavelength diffraction gratings for monitoring of kinetics of bioprocesses, Applied Surface Science, 258, 9292–9296 (2012).

[2] J. Hu, C.R. Menyuk, Understanding leaky modes: slab waveguide revisited, Advances in Optics and Photonics, 1, 58–106 (2009).

## OPTICAL AND STRUCTURAL STUDY OF HYBRID STRUCTURE COMPLEXES COMPOSED OF PHOTOCHROMIC DENDRIMERS AND AG NANOPARTICLES

Aušra Gustainytė<sup>1,2</sup>, Marius Franckevičius<sup>2</sup>, Loreta Rastienienė<sup>1</sup>, Rimas Vaišnoras<sup>1</sup>,  
Vidmantas Gulbinas<sup>2</sup>

<sup>1</sup>Liquid Crystals Laboratory, Lithuanian Educological University, Studentų st. 39, LT-08106 Vilnius, Lithuania

<sup>2</sup>Institute of Physics, Center for Physical Sciences and Technology, Savanorių Ave 231, LT-02300 Vilnius, Lithuania  
*gustainyteausra@gmail.com*

Hybrid structure dendrimer-silver nanoparticle is attractive for organics solar cells. Metallic nanostructures supporting surface plasmons can be used to trap light in thin-film solar cells. Ability to produce physically thin but also optically thick photovoltaic absorbers can revolutionize photovoltaic devices. This becomes possible by using light trapping through the resonant scattering and concentration of light in arrays of metal nanoparticles, or by coupling light into surface plasmon polaritons and photonic modes that propagate in the plane of the semiconductor layer [1]. Silver nanoparticles are attractive for photovoltaics for various reasons. Silver metal has the highest thermal and electrical conductivity among metals and has excellent optical properties. Dendrimers are relatively new in this field, but they are showing potential in regulating shape and size of the nanoparticles.

In this work silver nanoparticles were prepared in first-generation PPI dendrimer, five-generation PPI and five-generation PAMAM by the steric stabilization or more specifically speaking by the dendrimer-assisted nanoparticle synthesis method.

Silver nanoparticles in the dendrimer matrix were found to be stable and their size was not dependent on generation of dendrimer. The characteristic extinction peak at 406-420 nm corresponds to a plasmon band. The plasmon spectrum of nanoparticles is affected by the nature of the metal and the status of aggregation of the particles. The presence of silver size nanoparticles has been evaluated by means of optical absorption and structural measurements (Fig. 1).

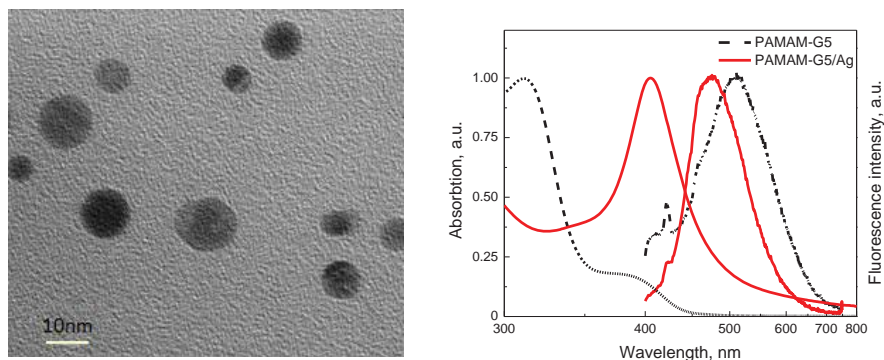


Fig. 1. Absorption, fluorescence spectra and TEM image of PAMAM-G5/ silver composites prepared with 1:30 molecular weight of  $\text{AgNO}_3$  in THF solution. The figure sizes were adjusted for direct comparison of the sizes of nanoparticles.

**Acknowledgement:** The authors are grateful to prof. Remigijus Juškėnas and Rokas Kondrotas for the technical support in the TEM measurements.

[1] Annie Castonguay, Ashok K. Kakkar. Dendrimer templated construction of silver nanoparticles. // *Advances in Colloid and Interface Science* 160 (2010) 76-87.

# FABRICATION OF MICRO-SIZE STRUCTURES FOR THZ FILTERS USING SCANNED INTERFERENCE PATTERN

Simonas Indrišius<sup>1</sup>, Bogdan Voisiat<sup>1</sup>

<sup>1</sup> Center for Physical Sciences and Technology, Savanoriu Ave. 231, Vilnius LT-02300, Lithuania

[s.indrius@ar.fi.lt](mailto:s.indrius@ar.fi.lt)

Precise structuring of thin metal films is required in various technological fields, for example in manufacturing of filters for terahertz radiation [1]. Micro structuring can be performed using direct laser writing. This method offers high production flexibility but requires long fabrication times, especially if structuring of large area is required. Multi-beam interference patterning provides means to overcome shortages of the direct laser ablation. By interference of laser beams it is possible to manufacture 2D and 3D periodic structures [2].

Shape of the periodic structure depends on the number of the beams and their parameters (intensity, phase, polarization [2, 3]). The main drawback of the interference lithography method is that it can create only certain periodic patterns if parameters of individual beams are not controlled. Therefore patterning using scanning of interference pattern is proposed as a versatile method for fabrication of various periodic patterns. Four or six interfering beams provide intensity distributions, consisting of periodically arranged high intensity spikes (Fig. 1 (a) and Fig. 1 (b)). Periodical arrays of holes can be ablated in thin metal film using such intensity distributions. Sample movement between laser shots in precise steps, smaller than array period, allows overlapping of the ablated holes. Various shapes from ablated or not ablated material can be manufactured using such method.

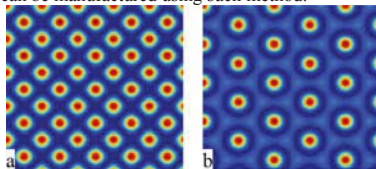


Fig. 1. Intensity distributions of 4 (a) and 6 (b) interfering beams.

Experiments were conducted using nanosecond laser NL220 (Ekspla Ltd., 532 nm, 500 Hz, 10 ns). The laser beam was split into six beams by the diffractive optical element (DOE, Holo/Or Ltd). Sample movement between laser shots was implemented using the piezoelectric 3-axis positioning system PIHera (Physical Instruments) with the minimal programmable step of 10 nm. The 100 nm-thick Cr film deposited on glass substrate by thermal evaporation and the 30 nm-thick Au and 20 nm-thick Ni films deposited on silicon substrates by plasma deposition were patterned using scanning of the 6-beam interference pattern.

The best patterning resolution was achieved on 100 nm-thick Cr film, due to the highest ablation threshold. On this film, the slit-shaped and cross-shaped structures were produced (Fig. 2 (c) and Fig. 2 (d)).

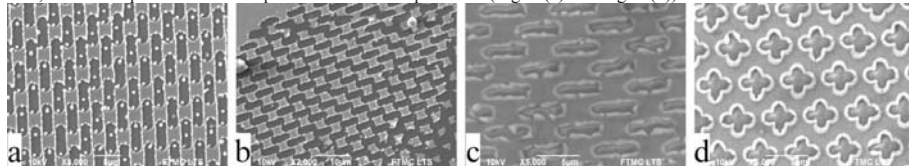


Fig. 2. The slit-shaped structures on Au film (a), the slit-shaped structures on Ni film (b), the slit-shaped structures on Cr film (c), and the cross-shaped structures on Cr film (d).

Thin film structuring using scanned interference pattern can be employed in fabrication of terahertz mesh filters. Mesh filter is a thin metal film in which openings of certain geometry is perforated. Behavior of filters depends on their geometry. Periodical metal matrix with cross-shaped slits can be used as band pass filters for terahertz and infrared radiation [1]. Transmission properties of cross-shaped structure fabricated on Cr films were simulated using ANSYS HFSS software. The peak frequency of 52.5 THz and width of the transmission band of 17.37 THz were estimated.

The thin metal film patterning technique using scanning of interference pattern allows obtaining complicated structures. This method offers higher production speed than the direct laser writing and permits fabrication of complex structures. Such structures can be used as filters for THz and infrared radiation.

- [1] A. M. Melo, A. L. Gobbi, M. H. O. Piazzetta, et al., Cross-Shaped Terahertz Metal Mesh Filters: Historical Review and Results, *Advances in Optical Technologies* **2012**, 1-12 (2012).
- [2] H. Misawa, T. Kondo, S. Juodkazis, et al., Holographic lithography of periodic two- and three-dimensional microstructures in photoresist SU-8, *Optics Express* **14**, 7943 (2006).
- [3] S. Beckemper, J. Huang, A. Gillner, et al., Generation of Periodic Micro- and Nano-structures by Parameter-Controlled Three-beam Laser Interference Technique, *Journal of Laser Micro/Nanoengineering* **6**, 49-53 (2011).



## MULTIPLE EXPOSURE HOLOGRAPHIC LITHOGRAPHY FOR TWO-DIMENSIONAL SUB-MICROMETER STRUCTURES

Aušrinė Jurkevičiūtė<sup>1</sup>, Nerijus Armakavičius<sup>1</sup>, Linas Šimatonis<sup>2</sup>, Dainius Virganavičius<sup>3</sup>,  
Tomas Tamulevičius<sup>1,3</sup>, Sigitas Tamulevičius<sup>1,3</sup>

<sup>1</sup>Department of Physics, Kaunas University of Technology, Lithuania

<sup>2</sup>Gymnasium of Kaunas University of Technology, Lithuania

<sup>3</sup>Institute of Materials Science of Kaunas University of Technology, Lithuania

[Ausrine.Jurkeviciute@stud.ktu.lt](mailto:Ausrine.Jurkeviciute@stud.ktu.lt)

Diffraction optical elements showing high diffraction efficiencies have good optical quality for practical use [1]. Complex diffraction patterns require two-dimensional (2D) periodical structures that can be realised employing holographic lithography. There are two approaches how 2D structures can be realised employing holographic lithography: employing an interference pattern simultaneously generated by multiple beams or using multiple exposures of an interference optical field produced by two beams [2].

In this work we present 2D 0.4 – 1.1  $\mu\text{m}$  period structures fabricated in positive tone photoresist layer employing multiple exposure holographic lithography technique. Different regular patterns were obtained changing the sample rotation angle between exposures and number of exposures. The resulting multiple exposure interference pattern intensities were calculated and the experimental angles were selected according to the targeted structures.

Fabricated structures were analyzed employing optical (see Fig. 1 a)) and scanning electron microscopy (SEM, see Fig. 1 b)). The diffraction efficiencies of diffraction maximums were measured (see Fig. 1 c)) and the spatial distribution of diffraction maximums was compared with Fast Fourier transformations (FFT) of SEM micrographs (see Fig. 1 d)).

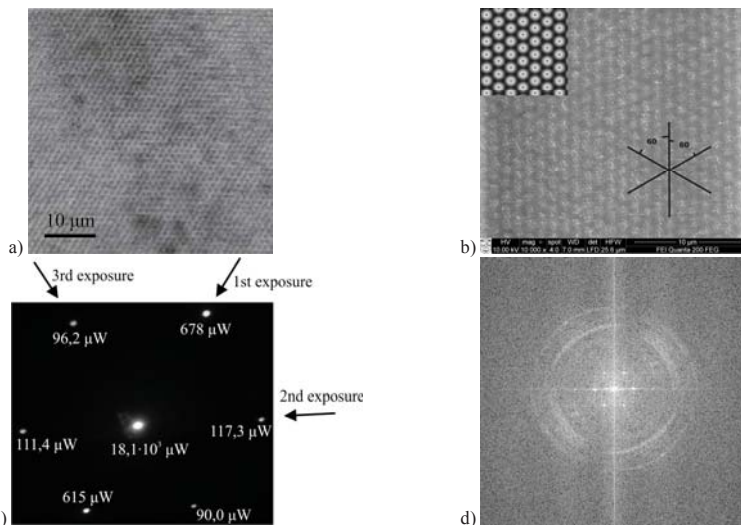


Fig. 1. Analysis of the 1.1  $\mu\text{m}$  period 2D structure fabricated employing three exposures with two sample rotations of  $60^\circ$ : a) optical microscope micrograph (scale bar 10  $\mu\text{m}$ ); b) SEM micrograph with lines indicating three axis of the structure (scale bar 10  $\mu\text{m}$ ) and calculated interference pattern (inset); c) camera image of 405 nm wavelength laser light diffraction pattern together with numbers representing measured intensities of the diffracted light (arrows indicate the diffraction patterns related to the order of exposure); d) FFT of SEM micrograph.

We have fabricated structures with period of 385 nm (angle of incidence:  $33^\circ$ ) and 1.1  $\mu\text{m}$  (angle of incidence:  $10.5^\circ$ ). As seen in optical microscope images the fabricated periodical structures are even over large area. SEM micrographs show that calculated and fabricated structures are very similar. We have shown that multiple exposure holographic lithography is an effective method for fabrication of 2D periodic structures.

- [1] T. Tamulevičius, S. Tamulevičius, M. Andrulevičius, E. Griškonis, L. Puodžiukynas, G. Janušas, A. Guobienė, Formation of periodical microstructures using interference lithography, *Experimental Techniques*, 32: 23-28 (2008).
- [2] L. Suslik, D. Pudis, J. Skriniarova, I. Martineck, I. Kubicova, J. Kovac, 2D photonic structures for optoelectronic devices prepared by interference lithography, *Physics Procedia*, 32: 807-813 (2012).

## TIME-SPACE DISTRIBUTED MODEL FOR DIFFERENT LASER REGIMES SIMULATION IN SOLID-STATE LASER

Liubou Krylova, George Krylov

Faculty of Physics, Belarusian State University, Minsk, Belarus

[krylova\\_lubou@mail.ru](mailto:krylova_lubou@mail.ru)

The application sphere of solid state lasers is very broad because these lasers can generate in infrared region of spectrum. The configurations of these lasers are rather different. They can have resonator length from few cm up to several meters; they can use glasses or crystals as active medium. The pump scheme can also vary. Also they can operate in two different lasing regimes: continuous wave regime and pulse regime.

Nowadays two models are often utilized. Namely, concentrated model is used for simulation of dynamic characteristics of laser, and space distributed model is used for simulation of power characteristics. Earlier we have shown [1] that time-space distributed model perfectly describes continuous wave lasing in solid-state lasers. This model allowed us [2] to obtain the optimal characteristics of Er-Yb continuous wave laser.

In this research we applied time-space distributed model for simulation of various pulse regime of neodymium laser. Moreover, we have shown that it is possible to adiabatically eliminate the population of absorber ions from the model equation system. Finally, stability analysis allowed us to estimate the regions in parametric space, where different regimes exist.

- 
- [1] Burov L.I., *Influence of spatial inhomogeneity of pump energy distribution on output characteristics of Yb:Er laser with end pump*. Krylov G.G., Krylova L.G. Nonlinear Phenomena in Complex Systems, N 13 V. 4. , pp. 368-380, 2010
  - [2] Burov, L. I., *Optimization of Yb-Er microchip laser parameters*. Krylova, L. G. Journal of Applied Spectroscopy, Volume 79, Issue 3, pp.376-381, 2012



## CONSTRUCTION OF SYNCHRONOUSLY PUMPED FEMTOSECOND OPTICAL PARAMETRIC OSCILLATOR

Agnė Marcinkevičiūtė<sup>1</sup>, Rosvaldas Šuminas<sup>1</sup>, Julius Vengelis<sup>1</sup>, Karolina Stankevičiūtė<sup>1</sup>, Valdas Sirutkaitis<sup>1</sup>

<sup>1</sup>Laser Research Center, Faculty of Physics, Vilnius University, Lithuania  
[agne.marcinkeviciute@ff.stud.vu.lt](mailto:agne.marcinkeviciute@ff.stud.vu.lt), [rosvaldas.suminas@ff.stud.vu.lt](mailto:rosvaldas.suminas@ff.stud.vu.lt)

Optical parametric oscillators (OPO) pumped by femtosecond laser pulses are universal devices providing tunable radiation in a wide spectral range. Such radiation is used for investigation of various ultrafast processes in biochemistry, photochemistry, spectroscopy, etc. In order to achieve parametric generation of high repetition rate low energy picosecond or femtosecond pulses synchronous pumping must be used. Synchronous pumping technique involves such OPO cavity adjustment that the time required for the generated pulse to complete one round trip in the cavity is inversely proportional to the repetition rate of pump pulses.

During parametric generation process pump radiation is converted into two lower frequency parametric waves called signal and idler. Generated wavelengths are defined by the conservation of energy and momentum [1], also known as the phase matching conditions, which can be used to calculate the wavelengths of generated waves (Eq. (1), Eq. (2)).

$$n_p w_p = n_s w_s + n_i w_i \quad (1)$$

$$\frac{1}{\lambda_p} = \frac{1}{\lambda_s} + \frac{1}{\lambda_i} \quad (2)$$

Today, most of the commercially available SPOPOs are pumped by fundamental or second harmonic radiation of Ti:sapphire laser. During past few years the great breakthrough of Yb:KGW laser systems was observed. The use of Yb:KGW laser as a pump source for SPOPO might lead to cheaper and more compact high repetition rate tunable light source.

In our study, we used second harmonic radiation (515 nm) of a femtosecond “Pharos” oscillator providing 105 fs pulses at 76 MHz repetition rate with the average output power of 4 W at fundamental (1030 nm) wavelength. Furthermore, in order to implement parametric generation, a nonlinear medium is required. In our SPOPO we used a  $\beta$ -barium borate (BBO) crystal (5x5x2 mm) cut for type-I interaction at  $\theta=22.2^\circ$ ,  $\phi=90^\circ$  angles and coated with anti-reflective (AR) coating for pump (515 nm) and parametric (630-1030 nm) radiation. We used a singly resonant oscillator [2] thus mirrors were highly reflecting at only one of the parametric waves (the signal wave in our case).

Wavelength tuning can be achieved by rotation of nonlinear crystal or by changing the length of SPOPO cavity. When the cavity length is tuned, synchronous pumping condition is satisfied for a different wavelength. As seen in Fig. (1), we achieved signal wave tuning in a 760-980 nm range. We have also measured the output powers at different signal wavelengths and determined generation thresholds. Moreover, a dependence of signal wavelength on resonator length increment was measured.

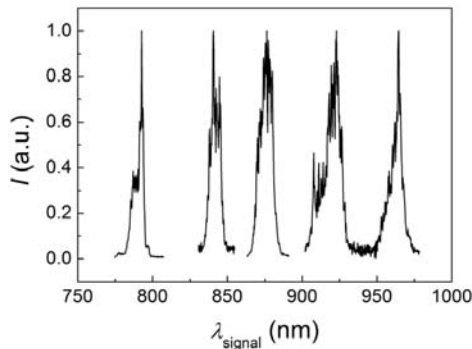


Fig. 1. Normalized signal spectra of SPOPO based on BBO at different wavelengths

[1] “Optical Parametric Oscillators” M. Ebrahimzadeh & M. H. Dunn. OSA Handbook of Optics Vol IV Ch 22 (McGraw Hill, 2001).

[2] “Parametric light generation” M. Ebrahimzadeh Phil. Trans. R. Soc. Lond. A 2003 361, 2731-2750 doi: 10.1098/rsta.2003.1284

## SELECTIVE PATTERNING OF CZTS THIN-FILM SOLAR CELLS BY ULTRA-SHORT LASER INDUCED MATERIAL LIFT-OFF PROCESS

Edgaras Markauskas\*, Paulius Gečys

Center for Physical Sciences and Technology, Savanoriu Ave. 231, Vilnius, LT-02300, Lithuania  
[edgaras.markauskas@gmail.com](mailto:edgaras.markauskas@gmail.com)

Rapidly growing thin-film photovoltaic market is based on the CIGS technology - the most efficient technology for converting sunlight into electricity. On the other hand, the commercialized high-volume production of CIGS-based modules has some limitations due to the scarcity of indium and gallium and the environmental issues associated with Selenium [1]. To overcome these limitations, it has been proposed that CIGS can be replaced by  $\text{Cu}_2\text{ZnSn}(\text{S},\text{Se})_4$  (CZTS) kesterite compound while keeping remaining structure elements the same [2]. This technology shows efficiencies up to 11.1% [3] for small scale devices.

The manufacturing costs and CZTS cell efficiency are critical factors for the wider applicability in terms of economical point of view. Efficiency of thin-film solar cells with a large active area might be maintained if small segments are interconnected in series in order to reduce photocurrent and resistance losses, and laser scribing is crucial for performance of the device. Previous investigations revealed some disadvantages of the direct laser ablation technique. Even working with femtosecond pulsed lasers it is almost impossible to avoid melted area formation at the edges of the laser scribed trench and degradation of electrical properties of the device.

For this we proposed laser induced material lift-off process for the front side scribing of the CZTS solar cells. Using proper laser wavelength, it is possible to control laser energy coupling in the complex film layer structure. High absorption at inner interface of the layers triggers localized rapid temperature rise which facilitates localized spallation of the films rather than evaporation. This material lift-off process enables to process thermally sensitive films as all the laser affected material is mechanically removed from the laser ablation area [4].

Ablation and scribing experiments were carried out with fundamental harmonics of the picosecond laser (Atlantic, 1064 nm, 10 ps, 50-500 kHz from EKSPLA).

Two types of multilayer structure of the CZTS solar cells were investigated: (i) complete structure consisting of TCO top-contact,  $\text{Cu}_2\text{ZnSn}(\text{S},\text{Se})_4$  absorber layer, molybdenum back-contact and soda-lime-glass as a substrate and (ii) incomplete CZTS/Mo/SLG structure without top-contact.

Single pulse ablation and scribing experiments were performed on thin-film CZTS structure in order to find optimal conditions for the Mo back-contact exposure in both P2 and P3 processes. It was determined that at specific experimental conditions with sufficient laser beam focus off-set, constant and high repeatability lift-off craters could be formed (Fig. 1).

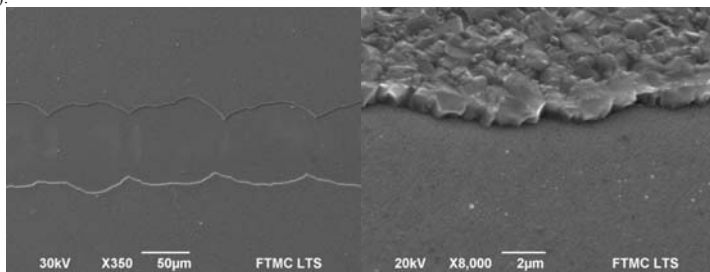


Fig. 1 SEM image of the P2 scribe in CZTS/Mo/SLG sample.

For trench scribing experiments, the P2 and P3 process speeds were limited by our scanning optics and were set to 1 m/s with laser repetition rates from 8 to 10 kHz depending on the process. Experimental results showed the potential of reaching high through output material lift-off based scribing processes for the CZTS thin-film solar cells with picosecond lasers.

[1] H. Katagiri, K. Jimbo, et al., Development of CZTS-based thin film solar cells, *Thin Solid Films* **517**, 2455-2460, (2009).

[2] I. Repins, C. Beall, et al., Co-evaporated  $\text{Cu}_2\text{ZnSnSe}_4$  films and devices, *Solar Energy Materials and Solar Cells* **101**, 154-159, (2012).

[3] T. K. Todorov, J. Tang, et al., Beyond 11% Efficiency: Characteristics of State-of-the-Art  $\text{Cu}_2\text{ZnSn}(\text{S},\text{Se})_4$  Solar Cells, *Advanced Energy Materials*, (2012).

[4] G. Račiukaitis, S. Grubinskas, et al., Selectiveness of laser processing due to energy coupling localization: case of thin film solar cell scribing, *Applied Physics A: Materials Science & Processing*, 1-6, (2012).

# COATING THICKNESS UNIFORMITY MODULATION IN ION BEAM SPUTTERING PROCESS

Simas Melnikas, Simonas Kičas, Rytis Buzelis.

Center for Physical Sciences and technology, Lithuania  
[Simonas.kicas@ftmc.lt](mailto:Simonas.kicas@ftmc.lt)

Optical coatings are widely used to reflect, split or modify laser beams in optical systems. Some coatings are relatively straightforward to make, while others, e.g. large diameter lenses, curved substrates, linear variable filters, Gaussian mirrors must satisfy higher requirements. One of these requirements is thickness uniformity or nonuniformity [1]. Moreover thickness uniformity is essential for production of identical optical coatings stacks. The purpose of this research was to investigate, improve and change thickness uniformity of ion beam sputtering (IBS) deposition technique.

IBS deposition system consists of ion gun, sputtering material target and substrate palette. Layer thickness uniformity is strongly increased by rotating substrate holder. However, this is usually not enough. Without rotation film thickness distribution mostly meets Gaussian distribution. In this research it was noticed and experimentally checked that thickness distribution can be approximately evaluated by function  $S(x,y)$ , Eq. (1), where  $R(x,y)$  is correction function.  $S(x,y)$  function is shown in Fig. 1 and substrate palette is depicted by a black square.

$$S(x,y) = A_1 \exp \left( -\left( \frac{x-x_0}{g_x} \right)^2 - \left( \frac{y-y_0}{g_y} \right)^2 \right) + R(x,y) \quad (1)$$

Function  $S(x,y)$  provides all the information about sputtering intensity in all substrate palette area. It was used to investigate and change thickness uniformity in sputtering process with rotational motion. Coating thickness was modulated by using shadowing mask technique - precise form metal plates [2]. Precise mask, cut using laser machining system, covers slice of sputtered particle's flow to substrate palette. It was experimentally demonstrated that this method can be used to obtain various film thickness profiles.

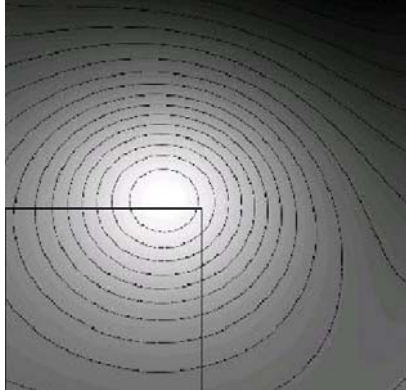


Fig. 1. Function  $S(x,y)$ . Experimental thickness was measured from area separated with black lines.

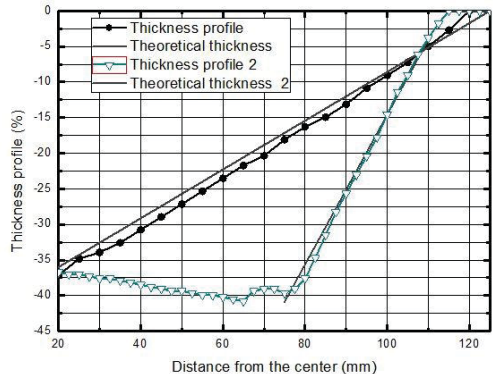


Fig. 2. Theoretical thickness profiles and experimental results.

In this research several shadowing masks were prepared and tested. Each of them had to influence different film thickness profiles. Two profiles (theoretical profile and experimental data) are shown graphically in Fig. 2. Distance was measured from the center of substrate palette.

Shadowing mask technique is universal and easily applicable. If research is done accurately, almost any thickness profile may be obtained.

- [1] Francisco Villa, Amalia Martinez, and Luis E. Regalado, Correction masks for thickness uniformity in large-area thin films, *Appl.Opt.* 39(10), 1602-1610 (2000)
- [2] H. A. Macleod, "Layer uniformity and thickness monitoring" in *Thin Film Optical Filters*, 3rd ed. (Institute of Physics 2001), pp. 488-497.

## CHARACTERIZATION OF $\text{HfO}_2$ - $\text{SiO}_2$ MIXTURES PRODUCED BY ION-BEAM SPUTTERING TECHNOLOGY

Jevgenij Mitrofanov, Simonas Kičas, Ramutis Drazdys

Center for Physical Sciences and technology, Lithuania

[Simonas.kicas@ftmc.lt](mailto:Simonas.kicas@ftmc.lt)

Optical coatings are thin solid films on surfaces of optical substrates which change their optical properties. Today these layers can be prepared by various deposition techniques. However main problems of optical properties are related to their structural properties (inhomogeneity, stress, defects and roughness of the surface). Thin film optical coatings made by ion beam sputter (IBS) deposition have great optical properties such as high refractive index, low absorption, and low scattering [1]. Even so present day applications require higher performance coatings such as those employed in high power lasers and laser gyroscopes where reflectance and stability are important factors [2]. Mixed composition films show modification of structure and better optical properties. Composite thin films consisting of the mixture of two or more materials have a wide range of applications. Mixtures with adjustable refractive index are important in the preparation of many optical devices such as *Rugate filters*, *Notch filters* and integrated optical waveguides. Also, knowing the compositional dependence of the absorption edge is necessary to define the spectral range where mixtures are transparent and thus useful for optical coatings in which absorption must be avoided.

In this work 0 %, 25 %, 50 %, 75 % and 100 % hafnia fraction  $\text{HfO}_2$ - $\text{SiO}_2$  mixtures films were fabricated by IBS technology using argon ions to sputter materials from  $\text{Hf/SiO}_2$  target. Each film thickness - 6 QWOT at 355 nm wavelength were deposited. Refractive index (Fig. 1) and extinction coefficient dispersions (Fig. 2) of materials with different volumetric fractions in coatings were analyzed using spectrophotometric data. The X-ray photoelectron spectroscopy (XPS) method was used to obtain the information about the chemical composition and atomic fractions of the coatings. The structure has been evaluated through X-ray diffraction (XRD) and the surface roughness - through atomic force microscope (AFM) data. The profilometry measurements has been applied also to evaluate the stress of mixtures.

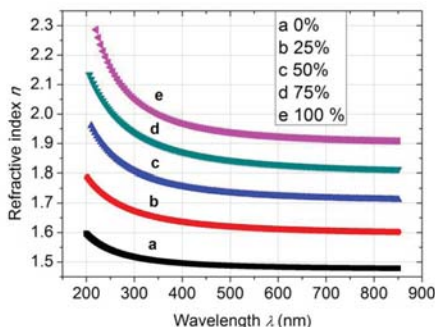


Fig. 1.  $\text{HfO}_2$  -  $\text{SiO}_2$  mixtures refractive index  $n$  dispersion for different  $\text{HfO}_2$  fraction.

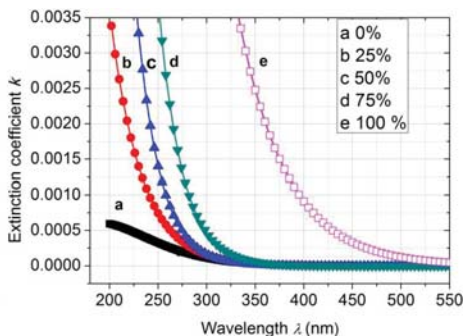


Fig. 2.  $\text{HfO}_2$  -  $\text{SiO}_2$  mixtures extinction coefficient  $k$  dispersion for different  $\text{HfO}_2$  fraction.

It was been shown, that use of mixtures decrease extinction coefficients. Refractive index  $n$  evenly dependent of  $\text{HfO}_2$  fraction in contrast to the  $k$ . It should be noted, that use of mixtures decrease stress. Additionally *ex-situ* annealing process also reduce residual stress and extinction. Investigated characteristics of deposited mixtures was used to design a high reflectivity mirrors for 355 nm wavelength.

- [1] B.J.Pond, J.I.DeBar, C.K.Carniglia and T.Raj, Stress reduction in ion beam sputtered mixed oxide films, *Appl.Opt.* **28** (14), 2800-2805 (1989).
- [2] P. J. Martin, Review Ion-based methods for optical thin film deposition, *Journal of Materials Science* **21**, 1-25 (1986).

## EFFECTIVE NONCOLLINEAR SECOND HARMONIC GENERATION EXCITED BY TWO BEAMS

Andrius Narмонтas, Giedrė Marija Archipovaitė

Department of Quantum Electronics, Faculty of Physics, Vilnius University, Saulėtekio Ave. 9-III, LT-10222 Vilnius, Lithuania

[andrius.narmontas@ff.stud.vu.lt](mailto:andrius.narmontas@ff.stud.vu.lt)

Second harmonic generation (first time demonstrated by P.A. Franken [1] in 1961) is a well-known process which is widely used for effective frequency conversion in laser systems, pulse duration measurements etc. There are two cases of SHG process realization: collinear and noncollinear. Noncollinear second harmonic generation has a few advantages. The beam directions of fundamental and second harmonic waves are spatially separated behind the crystal, therefore no additional filtration of radiation is required. Additional filtration using either filters, dichroic mirrors or diffractive/dispersive optical elements usually leads to energy losses so noncollinear SHG technique offers a potentially higher frequency conversion efficiency. It is especially important while generating higher (for example 4th) harmonics because of the formation of colour centers in transparent condensed medium by UV radiation. The other reason to use noncollinear SHG is a possibility to use pump radiation from two separate laser sources [2]. Using two separate laser sources as a pump for SH generation enables to reach higher pump energies. It is important because the pulse energy of an energy source is limited by maximal pulse intensity in a laser medium. Larger active elements must be used to increase output pulse energy. This causes additional problems: inhomogeneous pump beam, thermal management of active medium, etc. So using two energy sources as two pump beams for SHG allows to reach higher SH pulse energies and better conversion efficiency.

During this work KDP ( $\text{KH}_2\text{PO}_4$ ) type-II 4 cm length crystal was pumped by two separate laser sources (each beam had up to ~4 mJ pulse energy, ~75ps pulse duration and repetition rate of 1kHz), see Fig. 1 for details. Using configuration of noncollinear SHG with angle of 5,7 degrees between the pumping beams an effective frequency doubling (up to 49%) with generated SH pulse energy of 3,9 mJ was demonstrated (see Fig. 2).

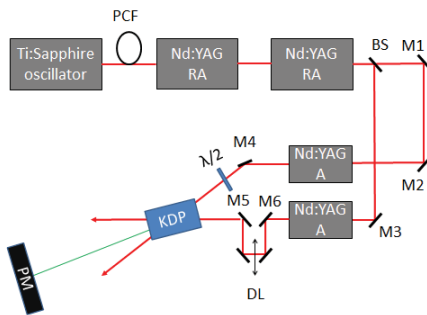


Fig.1 Scheme of SH pulse energy measurement.

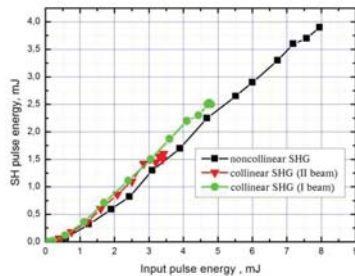


Fig.2 SH pulse energy dependence on input pulse energy.

[1] P.A.Franken, A.E.Hill, C.W.Peters, and G.Weinreich, Generation of optical harmonics, *Physical Review Letters* **7**, 118-119 (1961).

[2] A. Michailovas, S. Mikalauskas, K. Regelskis, V. Smilgevičius, Method and device for combining laser beams, European patent No. EP 2 194 426 (2010).

# Four-wave mixing of Gaussian and singular light beams in media with thermal nonlinearity

Sergei Nazarov<sup>1</sup>, Dmitri Gorbach<sup>1</sup>

<sup>1</sup>Department of Laser Physics and Spectroscopy, Belarusian State University, Belarus  
[sanazarov@tut.by](mailto:sanazarov@tut.by)

The multiwave interactions in media with thermal nonlinearity offering the possibility for transformations of the characteristics of laser radiation (phase, polarization, topological charge, etc.) are of great interest for the researchers and technologists.

To realize four-wave mixing (FWM), two beams, reference and signal, were directed at a small angle into a nonlinear medium to record a dynamic hologram. Reading of the hologram was performed by the beam directed precisely to meet the reference beam, the diffracted beam formed with a wavefront identical to that of the signal beam was propagating in the counter direction, and the phenomenon of wavefront conjugation was the case [1].

A nonlinear medium was represented by ethanol solution of the Rhodamine 6G dye. The experimental wavelength of laser radiation used (532 nm) was falling within the absorption band of this dye. Thermal nonlinearity was exhibited due to absorption of the pulsed radiation and local heating of the solution. During the experiments the nanosecond laser pulses had the repetition rate 10 Hz at the mean power of laser radiation 50 mW.

The main objective of this work was to establish optimum concentrations of the Rhodamine 6G dye solution in ethanol upon FWM with the use of Gaussian and singular light beams varying their intensities.

Fig. 1 shows the experimental results obtained.

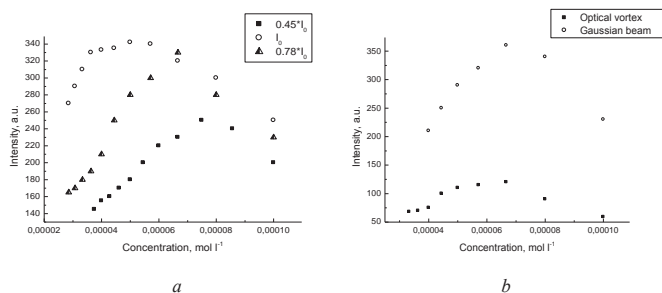


Fig. 1. Intensity of the diffracted beam as a function of the Rhodamine 6G dye concentration for different intensities of the Gaussian signal wave (*a*) and for different types of the signal wave (*b*)

In Fig. 1, *a* it is seen that the diffraction efficiency is lowering as the signal wave intensity decreases, probably due to lower absorption of the energy and lower heat release. In the process an optimum concentration of the solution is growing. At the same time, the use of different signal waves (Gaussian and singular) has no significant effect on the optimum concentration that is about  $6.7 \cdot 10^{-5} \text{ mol} \cdot \text{l}^{-1}$ . It should be noted that the efficiency of FWM for a Gaussian signal wave is higher than that of the singular one. Higher interaction efficiency for the Gaussian signal beam is caused by the use of Gaussian reference and reading waves, making it possible to realize effective overlapping of all these three Gaussian light beams within the nonlinear medium volume. When an optical vortex is used as a signal wave, the region of a maximum Gaussian-beam intensity falls within the region with a minimal intensity of the optical vortex to result in lowering of the interaction efficiency.

Based on the conducted experimental studies, optimum values of the concentration for the Rhodamine 6G dye solution on FWM with the use of Gaussian and singular light beams as a signal wave have been determined

## SUPERCONTINUUM GENERATION USING 2 $\mu\text{m}$ 30-fs PULSES

Emilis Pileckis, \* Donatas Majus

Department of Quantum Electronics, Vilnius University, Lithuania

[emilis.pileckis@stud.ff.vu.lt](mailto:emilis.pileckis@stud.ff.vu.lt)

Today intense ultrashort light pulses' interaction with matter is still a hot topic in optics despite decades of studies. One of the most exciting phenomena is white-light continuum (supercontinuum or SC) generation, which is manifested by large asymmetric spectral broadening. Supercontinuum generation is governed and accompanied by many nonlinear effects, such as pulse-splitting, filamentation, multiphoton absorption, X-waves, soliton formation and others.

For a long time, 800 nm and 1064 nm pulse wavelengths were dominantly used [1], but for now new challenges attract attention, such as infrared (IR) SC generation, which imply longer central wavelengths. The region from 2.5  $\mu\text{m}$  to longer wavelengths (so-called "molecular fingerprint" region) is drawing particular interest for recent studies [2, 3].

The goal of the current study is to compare IR SC generated in several materials and to find some clues on the their applicability for SC generation. 2  $\mu\text{m}$  central wavelength and 30 fs duration pulses, generated by noncollinear beta-barium borate optical parametric amplifier, were used as a pump. Different materials, including calcium fluoride (CF), fused silica (FS) and yttrium aluminium garnet (YAG) were used.

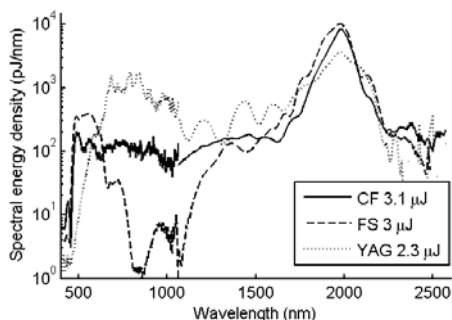


Fig. 1. Measured spectra generated in materials

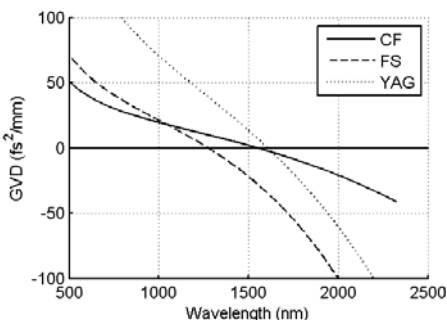


Fig. 2. Group velocity dispersion (GVD) for the used materials [4]

The results show connection between zero-dispersion wavelength and qualitative features of the spectra. Longer anomalous dispersion spectral region is related to long and energetic blue tail formation stop.

- [1] M. Bradler and E. Riedle, „Supercontinuum generation in laser host materials with pulse durations over the entire femtosecond regime“, CLEO Europe 2011, IEEE Conference Publications, DOI:[10.1109/CLEOE.2011.5942446](https://doi.org/10.1109/CLEOE.2011.5942446)
- [2] F. Silva, D. R. Austin, A. Thai, M. Baudisch, M. Hemmer, D. Faccio, A. Couairon and J. Biegert, Multi-octave supercontinuum generation from mid-infrared filamentation in a bulk crystal, *Nature Communications* **3**, 807 (2012).
- [3] E. O. Smetanina, V. O. Kompanets, S. V. Chekalin, A. E. Dormidonov and V. P. Kandidov, “Anti-Stokes wing of femtosecond laser filament supercontinuum in fused silica”, *Optics Letters* **38**, 1, pp. 16-18 (2013)
- [4] <http://refractiveindex.info> (2012 01 17)



# HIGH REFLECTIVITY MEASUREMENTS BY CAVITY RING-DOWN TECHNIQUE: EXPERIMENTAL SCHEME AND SENSITIVITY ANALYSIS

Mindaugas Slivka, Tomas Tolenis, Rytis Buzelis, Ramutis Drazdys

Institute of Physics, Center for Physical Sciences and Technology, Savanorių ave. 231, LT-02300 Vilnius, Lithuania  
[slivka.mindaugas@gmail.com](mailto:slivka.mindaugas@gmail.com)

Highly reflective mirrors are commonly used in laser gyroscopes, high sensitivity spectroscopy, high power lasers, etc. Accurate determination of such mirrors reflection coefficients is important and often challenging task. Currently, the most reliable widely used method for precise measurements of high reflectivity is Cavity Ring-Down (CRD) technique. It is highly sensitive laser measurement technique with immunity to the power fluctuation of light source and rather simple experimental set-up.

CRD is based upon determining the exponential decay of laser pulse in a stable optical resonator. Measured decreasing light intensity can be described by formula [1]:

$$I(t) = I_0 \exp\left(-\frac{t}{\tau}\right), \quad (1)$$

where  $I$  is light intensity,  $I_0$  – initial light intensity,  $t$  – time,  $\tau$  – time taken for the intensity of light to fall to 1/e of the initial intensity or so called ring-down time which can be expressed as

$$\tau = -\frac{2d}{c \ln R_1 R_2}, \quad (2)$$

where  $d$  is cavity length,  $c$  – speed of light,  $R_1$  and  $R_2$  – reflection coefficients of cavity mirrors. Reflection coefficients of cavity mirrors are determined by fitting parameters of Eq. (1) to measurement data (Fig. 1.).

In this work pulsed-CRD experimental scheme (Fig. 2.) was set-up. Pulsed Nd:YAG laser source generating wavelength of 1064 nm was employed. Second harmonic with a wavelength of 532 nm was generated for the experiment. For ring-down cavity plano-concave mirrors were used. High reflectivity optical coatings ( $R > 99.5\%$ ) were produced by using ion beam sputtering (IBS) technology on fused silica substrates. Measurement sensitivity to cavity length and laser source power was investigated. The variation of measured reflectance coefficients of the order of 0.01% was obtained. Various resonator configurations were tested by using different types of substrates. Measurements showed that the results are independent of cavity geometry and configuration. The influence of defects in optical coatings and dust particles to measured reflectance coefficient was observed. Significant decrease in measured values of reflectance coefficients was noticed, because of the increased losses.

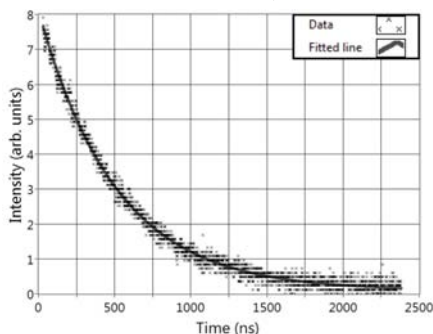


Fig. 1. Fitted exponential decay signal.

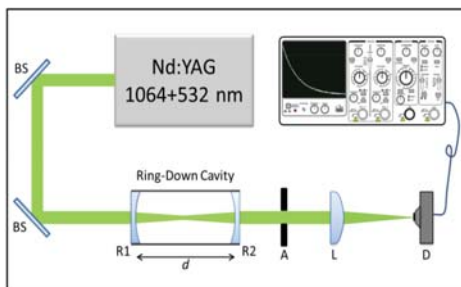


Fig. 2. Experiment scheme. BS – beam splitter, R1, R2 – cavity mirrors, A – aperture, L – lens, D – photodiode detector,  $d$  – cavity length.

- [1] G. Sridhar, S. K. Agarwalla, S. Singh, L. M. Gantayet, Cavity ring-down technique for measurement of reflectivity of high reflectivity mirrors with high accuracy, *Pramana*, **75** (issue 6), 1233-1239 (2010).
- [2] K. Yamada, T. Yamazaki, N. Sei, R. Suzuki, T. Ohdaira, T. Shimizu, M. Kawai, M. Yokoyama, T. Mikado, T. Noguchi, S. Sugiyama, H. Ohgaki, Saturation of cavity-mirror degradation in the UV FEL, *Nuclear Instruments and Methods in Physics Research Section A: Accelerators, Spectrometers, Detectors and Associated Equipment*, **393**, 44-49 (1997).



## SECOND HARMONIC GENERATION FROM RADIAL AND AZIMUTHAL POLARIZATION BEAMS IN TYPE II NONLINEAR CRYSTAL

Paulius Stanislovaitis<sup>1</sup>, Valerijus Smilgevičius<sup>1</sup>, Vytautas Šetkus<sup>1</sup>

<sup>1</sup> Department of Quantum Electronics, Vilnius University, Lithuania  
voveraitis@gmail.com

In this paper, we investigate theoretically and experimentally second harmonic generation (SHG) in type-II nonlinear crystal, pumped by radial and azimuthal polarization beams.

Radial and azimuthal polarization beams can be expressed as a superposition of two Hermite-Gaussian (HG) HG01 and HG10 modes of orthogonal polarizations [1,2]. In paraxial approximation, the complex envelope of radial and azimuthal polarization beams can be written as Laguerre-Gaussian (LG) LG01 mode. We analyze a type II nonlinear interaction. For this purpose, it is convenient to express radial and azimuthal polarization beams as a superposition of e and o polarizations. We assume that our first harmonic beam consists of radial and azimuthal polarization beams with “weight coefficients”  $\alpha$  and  $\beta$  correspondingly, which are real and obey relation  $\alpha^2 + \beta^2 = 1$ . In this case, o and e components can be expressed as :

$$A_e = A_0 (\alpha x + \beta y) / \left( W_0 \left( 1 + i \frac{z}{l_{de}} \right)^2 \right) \cdot e^{\frac{-x^2 + y^2}{W_0^2 (1 + i \frac{z}{l_{de}})}} ; (1)$$

$$A_o = A_0 (\alpha y - \beta x) / \left( W_0 \left( 1 + i \frac{z}{l_{do}} \right)^2 \right) \cdot e^{\frac{-x^2 + y^2}{W_0^2 (1 + i \frac{z}{l_{do}})}} . (2)$$

In type II nonlinear interaction, phase matching condition is satisfied for interaction  $o+e=e$  or  $o+e=o$ , depending on crystal. In a simple case, neglecting walk-off and pump depletion, equation that describes SHG, can be written :

$$\frac{\partial A_2}{\partial z} = \frac{i}{2k_2} \nabla_T^2 A_2 + i\sigma_3 A_o A_e e^{-i\Delta k z} , (3)$$

Where  $A_2$  is complex envelope of second harmonic beam,  $\nabla_T^2$  is transverse component of the Laplacian operator and  $\sigma_3$  is a nonlinear interaction coefficient, which is a parameter of the crystal. In Eq. (3), only type II interaction is considered. From Eq. (3) it can be shown, that the spatial structure of the second harmonic beam is like HG11 mode :

$$I \propto |\xi \eta e^{-q(\xi^2 + \eta^2)}|^2 , (4)$$

Where  $\xi = (\alpha x + \beta y)/W_0$ ,  $\eta = (\alpha y - \beta x)/W_0$ ,  $W_0$  is waist radius of Gaussian envelope and  $q$  is a variable, dependent only on  $z$  coordinate.  $\xi$  and  $\eta$  are rotated cartesian coordinates. When  $\alpha$  and  $\beta$  are real and obey the relation  $\alpha^2 + \beta^2 = 1$ , we can regard them as  $\alpha = \cos \Psi$ ,  $\beta = \sin \Psi$ , where  $\Psi$  is rotation angle around  $z$  axis. If  $\alpha = 1$  and  $\beta = 0$ , we have a radial polarization beam. Then  $\xi = x/W_0$  and  $\eta = y/W_0$ . The theoretical and experimental intensity distributions of the second harmonic beam are shown in Fig. 1.



Fig. 1. Theoretical (a) and experimental (b) intensity distributions of second harmonic, generated from radial polarization beam in type II nonlinear crystal.

- 
- [1] A.V. Nesterov, V.G. Niziev, V.P. Yakunin. „Generation of high – power radially polarized beam“, J. Phys. D: Appl. Phys., Vol. 32, pg. 2871-2875 (1999)  
 [2] R. Oron, S. Blit, N. Davidson, A.A. Friesem, Z. Bomzon, E. Hasman. „The formation of laser beams with pure azimuthal or radial polarization“, Appl. Phys. Lett., Vol. 77 (21), pg. 3322-3324 (2000)  
 [3] Q. Zhan , “Cylindrical vector beams: from mathematical concepts to applications ”, Advances in Optics and Photonics, Vol. 1, pg. 1-57 (2009)

# INVESTIGATION AND COMPARISON OF Nb<sub>2</sub>O<sub>5</sub>-SiO<sub>2</sub> MIXTURES PREPARED BY MAGNETRON SPUTTERING AND ELECTRON BEAM EVAPORATION TECHNIQUES

Andrius Subačius<sup>1</sup>, Kęstutis Juškevičius<sup>2</sup>

<sup>1</sup> Faculty of Physics, Vilnius University, Sauletekio ave. 9-III, LT-10222, Vilnius, Lithuania

<sup>2</sup> State scientific research institute Center for Physical Sciences and Technology Savanoriu ave. 231, LT-02300 Vilnius, Lithuania

subacius.andrius@gmail.com

Composite thin films consisting of the mixture of two materials have a wide range of applications [1-3]. The possibility to tailor the refractive index of materials is very attractive and has motivated the development of structures like gradient refractive index coatings. Mixture coatings present particular advantages, like reduced scattering losses, better mechanical properties [4] and higher resistance against radiation [5].

Nb<sub>2</sub>O<sub>5</sub>-SiO<sub>2</sub> mixture coatings were deposited on fused silica by two different techniques: magnetron sputtering (MS) and electron beam ion assisted deposition (EB IAD) method. In basic magnetron sputtering process a target is bombarded by energetic ions generated in glow discharge plasma. The bombardment process causes the removal of target atoms, which then condense on a substrate as a thin film. Examples include hard, wear-resistant, low friction, well-adhered coatings. The particles evaporated by electron beam are less energetic than sputtered. To compensate the lack of particles energy additional ion assistance is used. It helps to achieve better optical, physical and mechanical thin film properties.

Single layers of pure materials and three mixtures were deposited. Transmittance measurements were performed in spectral range from 250 to 1300 nm. Refractive index and extinction coefficient were calculated using “OptiChar” from transmittance spectra. Fig. 1 shows determined refractive index of Nb<sub>2</sub>O<sub>5</sub>-SiO<sub>2</sub> mixtures prepared by two different deposition techniques. Decreasing Nb<sub>2</sub>O<sub>5</sub> fraction influences decrease of refractive index. Surface roughness of coated and bare substrates was measured by atomic force microscope (AFM). To characterize the structure and stoichiometry of layer X-ray diffraction (XRD) and X-ray photoelectron spectroscopy (XPS) measurements were done. To determine band gap of mixtures Tauc’s model was used.

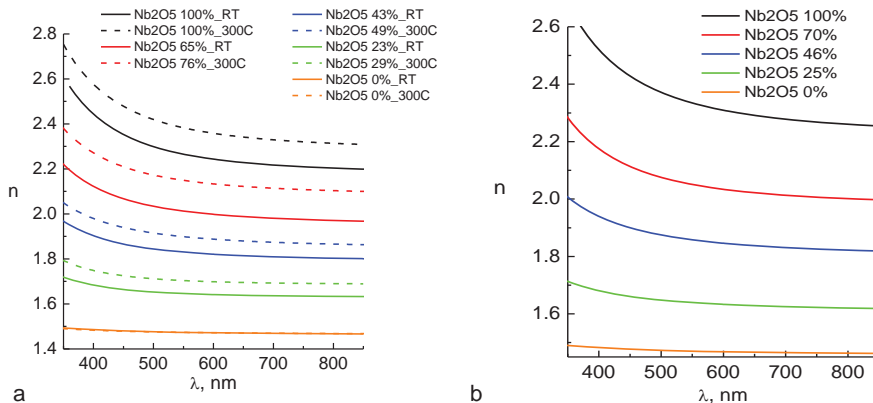


Fig. 1. Refractive index (n) of Nb<sub>2</sub>O<sub>5</sub>-SiO<sub>2</sub> mixtures prepared by magnetron sputtering (a) and electron beam evaporation (b).

[1] K. Starke, L. O. Jensen, M. Jupé, D. Ristau, G. Abromavicius, K. Juskevicius, R. Buzelis, and R. Drazdys, 75040B (2009).

[2] B. Mangote, L. Gallais, M. Zerrad, M. Commandré, L. H. Gao, F. Lemarchand, M. Lequime, A. Melnikaitis, J. Mirauskas, V. Sirutkaitis, S. Kikas, T. Tolenis, R. Drazdys, M. Mende, L. Jensen, H. Ehlers, and D. Ristau, 816815 (2011).

[3] Cheng-Chung Lee, Chien-Jen Tang, and Jean-Yee Wu, Appl. Opt. **45** (7), 1333 (2006).

[4] Cheng-Chung Lee, Chuen-Lin Tien, and Jin-Cherng Hsu, Appl. Opt. **41** (10), 2043 (2002).

[5] V. J. Jordi Sancho-Parramon , Hrvoje Zorc, Thin Solid Films 516, 5478 (2008).

# FABRICATION AND CHARACTERIZATION OF MICROFRAXICONS FABRICATED BY DIRECT LASER WRITING

Kristupas Kazimieras Tikuišis<sup>1</sup>, Albertas Žukauskas<sup>1</sup>, Mangirdas Malinauskas<sup>1</sup>

<sup>1</sup> Department of Quantum Electronics, Vilnius University, Lithuania  
[nanopolimerizacija@gmail.com](mailto:nanopolimerizacija@gmail.com)

A Bessel beam is well known in optics for its ability to: i) propagate distances much greater than the Rayleigh range not undergoing diffraction and ii) concentrate a considerably greater intensity in its central spot than an equivalent Gaussian beam. The radius of a central spot can be almost arbitrary small. Bessel beams therefore has applications in various fields: long focal depth optical elements, optical traps, laser processing, medical imaging etc [1]. It was demonstrated that Bessel beams can be produced by use of annular apertures, Fabri-Perot cavities in combination with annular apertures, computer generated holograms or conical prisms called axicons [2]. The latter are the most usually employed nowadays as they are the most efficient and produce the smoothest axial intensity distribution [1]. However, the material exhibits light absorption (which may be substantial in UV or IR spectral regions) that might be undesirable in applications such as optical communication and laser processing. It is therefore more advantageous to use fraxicon instead. A fraxicon is a recently proposed hybrid optical element based on axicon and design principles of Fresnel lenses (Fig. 1 (a), [3-4]). It is faster to make, requires less material, is lighter, thinner and hence has less absorption and dispersion. To the best of our knowledge, there are no reports on succesful fabrication of microscale fraxicons.

In this report we present fabrication and characterization of microfraxicons. We apply direct laser writing based on two-photon photopolymerization to ensure a flexible and precise fabrication in microscale [5]. Microfraxicons are created of a hybrid organic-inorganic photopolymer SZ2080 known for its thermal, chemical stability and low shrinkage after development. Scanning electron microscope (SEM) image of 10° base angle fraxicon is showed in Fig. 1 (b). Microfraxicons base angles  $\gamma$  are 5° and 10°, segmentation periods  $d$  14,4  $\mu\text{m}$  and 7,2  $\mu\text{m}$ , respectively; radiuses  $R$  are 28,8  $\mu\text{m}$ . Their geometrical parameters are characterised by SEM and optical profilometer. We apply digital holography technique to characterise Bessel beams produced by those fraxicons. It allows a full wavefield reconstruction in any axial plane from a single measurement in contrary to the usual procedure of measuring the intensity in every plane of interest. Optical performance modeling using scalar diffraction theory and finite-difference time-domain method is presented. These fraxicons are suitable for use in microprocessing or integrated nanophotonics.

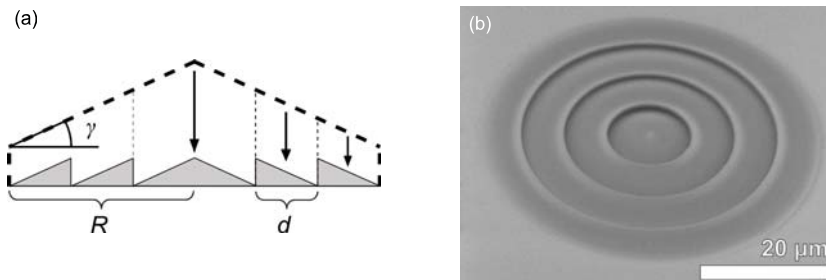


Fig. 1. (a) Transforming an axicon into a fraxicon. Here  $\gamma$  is base angle,  $R$  – radius,  $d$  – segmentation period. Dashed line marks the contour of an axicon, solid fill – fraxicon. (b) SEM image of 10° base angle 29  $\mu\text{m}$  radius and 7  $\mu\text{m}$  segmentation period microfraxicon.

- [1] D. McGloin, K. Dholakia, Bessel beams: diffraction in a new light, *Contemp. Phys.* **46**(1), 15-28 (2005).
- [2] A. Žukauskas, M. Malinauskas, C. Reinhardt et al., Closely packed conical microlens array fabricated by direct laser photopolymerization, *Appl. Optics* **51**(21), 4995-5003 (2012).
- [3] I. Golub, Fresnel axicon, *Opt. Lett.* **31**(12), 1890-1892 (2006).
- [4] K. Gourley, I. Golub, B. Chebbi, First experimental demonstration of a Fresnel axicon, *Proc. SPIE* **7099** (70990D-1), (2008).
- [5] M. Malinauskas, G. Kiršanskė, S. Reikšytė et al., Nanophotonic lithography: a versatile tool for manufacturing functional three-dimensional micro-/nano-objects, *Lith. J. Phys.* **52**(4), 312-326 (2012).

# THIRD-HARMONIC GENERATION IN ATMOSPHERIC AIR

Ernestas Žeimys, Benas Makauskas, and Kęstutis Steponkevičius

Vilnius University Laser Research Center, Saulėtekio Ave. 10, LT-10223 Vilnius, Lithuania

[ernestas.zeimys@ff.stud.vu.lt](mailto:ernestas.zeimys@ff.stud.vu.lt)

Optical harmonic generation is a fundamental process for laser frequency conversion to shorter wavelengths [1]. In recent years, much attention has been paid to harmonic generation in gases because it is a promising method for achieving high intensity, short wavelength coherent light pulses, useful for potential applications in atmospheric pollutants detection through third-harmonic (TH) induced-fluorescence [2] and high-resolution biological imaging [3].

In our experiments TH was generated in atmospheric air by focused femtosecond laser pulses. All experiments were performed using a Ti:sapphire laser system, which generates ultrashort pulses of 100 fs (FWHM) duration with a central wavelength at 800 nm and repetition rate of 1 kHz. Fluorescence images produced by the TH beam on the paper screen, placed in front of the laser beam after the focal plane of focusing lens were registered by the CCD camera. At high laser pulse energies (more than 1 mJ per pulse) a bright blue central spot surrounded by a ring has been observed on the screen (see Fig. 1a). Far-field divergence of the generated TH wave was measured using nine different focal length focusing lenses. It was found that TH ring divergence decreases increasing the lens focal length.

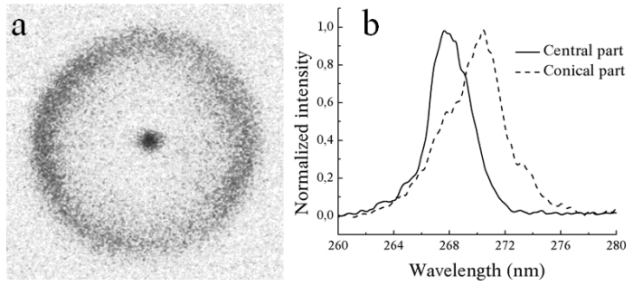


Fig. 1. (a) Typical inverted TH fluorescence image on the paper screen registered by the CCD camera; (b) typical spectra of TH central (solid line) and conical (dashed line) parts.

In addition to these measurements the dependence of TH generation efficiency on the focal length  $L$  of focusing lens was also registered. It has been found that TH generation efficiency increases with the fundamental pulse energy and is inversely proportional to  $L$ . Maximal achieved conversion efficiency to TH signal was about  $10^{-4}$  for  $L = 30$  cm. Spectral characteristics of TH were measured with a spectrometer “Ocean Optics”. During these measurements conical and central parts of TH signal were focused into the fiber delivering light to the spectrometer. It was found that the peak wavelength of conical TH part (about 270 nm) was dependent on the pump intensity and red-shifted in respect with the peak wavelength of the central TH part (Fig. 1b), while the peak wavelength of central TH part was always about 267 nm, which corresponds to the  $1/3$  of the fundamental wavelength. This red-shift of the TH peak wavelength was explained as a result of the influence of laser-created plasma on the refraction index of air.

In conclusion, the spectral, spatial and energy conversion characteristics of TH generated in atmospheric air by focused femtosecond laser pulses have been investigated. Obtained results indicate that such frequency tripling in air and other gases can be used as an efficient source of coherent UV and VUV light pulses.

**Acknowledgements.** E. Ž. acknowledges support by project “Promotion of Student Scientific Activities” (VP1-3.1-ŠMM-01-V-02-003) from the Research Council of Lithuania. This project is funded by the Republic of Lithuania and European Social Fund under the 2007-2013 Human Resources Development Operational Programme’s priority 3.

- [1] N. Aközbek, A. Iwasaki, A. Becker, M. Scalora, S. L. Chin, C. M. Bowden, Third-Harmonic Generation and Self-Channelling in Air Using High-Power Femtosecond Laser Pulses, *Phys. Rev. Lett.* **89** (14), 14391 (2002).
- [2] F. Théberge, N. Aközbek, W. Liu, J. Filion, S. L. Chin, Conical emission and induced frequency shift of third-harmonic generation during ultrashort laser filamentation in air, *Opt. Commun.* **276**, 298-304 (2007).
- [3] D. Yelin and Y. Silberberg, Laser scanning third-harmonic-generation microscopy in biology, *Opt. Express* **5** (8), 169-175 (1999).

## CORRECTION OF *MIE* SCATTERING BACKGROUND APPEARING IN INFRARED ABSORPTION SPECTRA OF URINARY SEDIMENTS

Evelina Baltakytė, Sandra Tamošaitytė, Dominyka Blaževič, Milda Pučetaitė, Justinas Čeponkus, and Valdas Šablinskas

Faculty of Physics, Vilnius University, Saulėtekio av. 9, LT-10222 Vilnius, Lithuania  
[evelina.baltakyte@ff.vu.lt](mailto:evelina.baltakyte@ff.vu.lt)

Urinary stone disease is common worldwide with prevalence of about 10 % of human population [1]. A key condition for urolithiasis to start is urine oversaturation with some specific chemical components, which leads to crystal growth and aggregation. Early discovery together with the identification of the exact chemical composition of urinary sediments could be crucial for taking appropriate preventive measures that inhibit kidney stone formation or growth processes. Optical microscopy, which is now the “gold standard” applied for the analysis, is unreliable as various crystals with the same chemical composition can have different physical appearance and vice versa.

The analysis of the recorded IR spectra allows obtaining objective information about chemical composition of the sediments even if they are multi-component. However, crystals of small size (10 – 100  $\mu\text{m}$ ) are strongly scattering the IR radiation. Therefore, the spectra are often distorted by scattering effects (peak shifts, first-derivative features of the bands and/or baseline oscillations) which can influence the results of the analysis by limiting complete characterization of the deposits, particularly, when they are multi-component. Such effects have been previously observed in the IR spectra of biological cells and human lymph node tissue [2, 3].

Transmission mode of the IR microscope Hyperion 3000 combined with IR spectrometer Vertex 70 was employed to record the IR absorption spectra of the urinary sediments. We analyzed urine samples of 136 healthy persons' urinary sediment. Urine samples were collected and were centrifuged leaving mostly urea and urine sediments in the samples. Then, after being placed on a filter (Whatman 542), the urine was left for 24 hours to dry. Then, the isolated crystals of the sediments were collected from the surface of the filter and transferred to the transparent for IR radiation plate (ZnSe) to analyze them.

We used the correction algorithm described in [3] for the correction of IR spectra of urinary sediments. The spectral corrections were performed using MATLAB package. Every IR spectrum measured was compared to the corresponding reference pure chemical compound spectrum (recorded using KBr pellet technique).

The results presented in figure 1 display an example of optical image of urinary deposit crystal constituted from brushite and corresponding IR absorbance spectrum obtained after crushing it between two ZnSe plates. Baseline oscillations and first-derivative effect can be observed in the spectrum which suggests the presence of the *Mie* scattering.

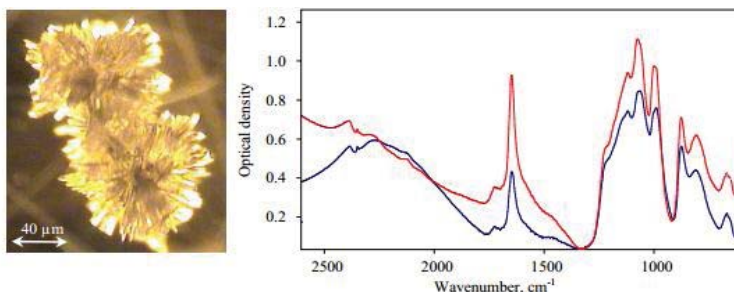


Fig. 1. Optical image of brushite urinary crystal before the crushing (left) and corresponding IR absorbance spectrum (obtained after crushing the crystal) before (right, red) and after (right, blue) the *Mie* scattering Correction

The spectrum obtained after the correction procedure is presented in figure 1. It can be seen that optical density the scattering effects are considerably diminished. Similar results were obtained by applying the correction procedure to the spectra of the sediments of various compositions. The analysis of the corrected spectra provides more reliable results and thorough characterization of the sediments can be performed.

In this work we have deduced that quality of infrared absorption spectra of urinary sediments can be improved when correction of the spectral baseline is performed by taking *Mie* scattering effects into account; thus, reliable chemical analysis can be carried out.

- 
- [1] A. Hesse, R. Siener, “Current aspects of epidemiology and nutrition in urinary stone disease”, *World J Urol* 15, 165-171 (1997).  
[2] P. Bassan, A. Kohler, H. Martens, J. Lee, E. Jackson, N. Lockyer, P. Dumas, M. Brown, N. Clarke, P. Gardner, “RMieS-EMSC correction for infrared spectra of biological cells: Extension using full *Mie* theory and GPU computing”, *J Biophoton* 3(8-9), 609-620 (2010).  
[3] B. Bird, M. Miljkovic, M. Diem, “Two step resonant *Mie* scattering correction of infrared micro-spectral data: human lymph node tissue”, *J Biophoton* 3(8-9), 597-608 (2010).

# Application of Infrared Reflection Microspectroscopy for Chemical Imaging of Cross-sectioned Urinary Calculi

Jonas Povilas Banys, Milda Pucetaite, Valdas Sablinskas

Faculty of Physics, Vilnius University, Sauletekio av. 9, LT-10222 Vilnius, Lithuania  
[jonas.banys@ff.vu.lt](mailto:jonas.banys@ff.vu.lt)

Chemical imaging is an important technique in various fields of study. It provides information about chemical composition and structure of the analyzed sample. Infrared (IR) spectral imaging in specular reflection mode, however, is suffering from the fact that the spectral bands (so called *Reststrahlen* bands) in the specular reflection spectra resemble first derivative of the absorption spectrum and they are shifted towards lower wavenumbers [1]. Standard *Kramers–Kronig* (KK) procedure used to recreate absorption spectral bands from the *Reststrahlen* bands is not applicable to correct the raw spectra of urinary calculi as they contain diffuse reflection component arising from rough surface of the cross-section. In this work, urinary stones with various surface roughnesses were analyzed by infrared microspectroscopy and the bands in different spectral regions were used to create chemical images in order to determine the influence of the diffuse reflection to the imaging results. For study the influence of the diffuse reflection to the imaging results, the cross-sectioned stone was polished with sand paper of various roughnesses. The measurement with the optical profilometer allowed determining the degree of roughness after each polishing: P220 - 20  $\mu\text{m}$ , P240 - 15  $\mu\text{m}$ , P400 - 7-10  $\mu\text{m}$ , polishing glass - 5-10  $\mu\text{m}$ . The influence of the diffuse reflection to the reflection spectra can be estimated when the KK transform is applied. The amount of the diffuse reflection decreases when the ratio of the wavelength of the incident radiation with the size of the surface roughness increases. The results of the KK transform applied to each spectral band reveal that the longer wavelength of the spectral band is better correction of its shape after KK transform which in turn increases quality of chemical image of the surface.

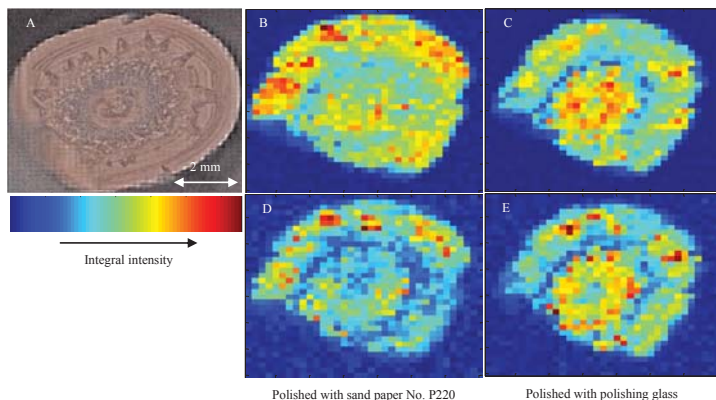


Fig. 1. Optical (A) and chemical (B-E) images of urinary stone, constituted from calcium oxalate and apatite: B, C – images obtained by integrating the spectral band at  $1318\text{ cm}^{-1}$  ( $\nu_{\text{as}}\text{C=O}$ ) of calcium oxalate; D, E – images obtained by integrating the spectral band at  $782\text{ cm}^{-1}$  ( $\delta(\text{O-C=O})$ ) of calcium oxalate.

The chemical imaging results are presented in figure 1. The images, representing distribution of calcium oxalate, obtained for the stone with roughness size of 20  $\mu\text{m}$  reveal clear difference (Fig. 1 B, D): when the spectral band corresponding to a longer wavelength is used to create the chemical image, the contrast is higher and the boundaries of calcium oxalate domains can be distinguished. When the surface roughness becomes smaller the chemical images obtained from different spectral bands are of similar quality (Fig. 1 C, E). It can also be seen in figure 1, that the smaller roughness of the surface, is reasoning higher resolution of the chemical images. In this work, we have demonstrated that the results of the chemical imaging depend significantly on the amount of the diffuse reflection contributing to the infrared reflection spectra. However, by choosing an appropriate spectral band at largest possible wavelength in comparison to the size of the roughness, reliable chemical imaging results can be obtained.

[1] M. Claybourn "External Reflection Spectroscopy" in *Handbook of Vibrational Spectroscopy*, J. M. Chalmers, P. R. Griffiths (Eds.), Vol 2, (John Wiley & Sons, Chichester, 2001) 969-981.

## 3D calculations of the hydroxyl group mods in the free pyridine n-oxide/trichloroacetic acid complex

D. V. Borisevich<sup>1</sup>, G. A. Pitsevich<sup>1</sup>, A. E. Malevich<sup>1</sup>, V. Sablinskas<sup>2</sup>, V. Balevicius<sup>2</sup>

<sup>1</sup>Belarusian State University, Minsk, Belarus

<sup>2</sup>Vilnius University, Vilnius, Lithuania

[dmitriyborisevich@gmail.com](mailto:dmitriyborisevich@gmail.com)

It is known, that vibrations of light atoms, and especially with the participation of the hydrogen atom are anharmonic. This is due to the fact that the displacement amplitudes of the light atoms in the excited vibrational states are large enough. At the same time, the quadratic representation of the potential energy as a function of natural origin is valid only if the small deviations of the atoms from their equilibrium positions. Accounting the third and fourth derivatives of natural coordinates in the expansion of the potential energy, and the use of perturbation theory can adequately account for the effects of anharmonicity in the calculation of the vibration frequencies of C-H and O-H bonds in the free molecules. In the case of short and very short of the hydrogen bonds anharmonic approximation are often not able to correctly predict the values of the vibration frequencies of O-H bond. In such cases, a more detailed analysis of the potential surface. Earlier [1] we performed 1D and 2D calculations and anharmonic calculations of vibrational frequencies of the hydroxyl group of the investigated complex. Comparative analysis of the calculated data allowed us to estimate the values of the vibrational frequencies for the 3D dimension and to combine advantages of the anharmonic approximation of dimension  $D = 3N-6$  with the results of 1D and 2D calculations.

According to the approach developed in [1], the calculation of vibrations of hydroxyl groups was made under the assumption that the motion of the hydrogen atom is in the field created by the other stationary atoms of the complex. Based on this three-dimensional approximation of the potential surface was calculated for the different positions offset hydroxyl proton without geometry optimization on the remaining structural parameters. Energy calculation was carried out in the approximation B3LYP/cc-pVTZ by means of quantum chemical package GASSIAN 09. The values of the potential energy were obtained in 2310 points of a three-dimensional lattice sites. At the same time, more than in 700 nodes energy is found directly by quantum chemical calculations, and in more than 1500 sites - by interpolation. The results are presented in Tab.1.

Tab.1 Frequencies of the O-H group vibrations in different approach

Vibration mods	Typ of approach								
	1DX (cm <sup>-1</sup> )	1DY (cm <sup>-1</sup> )	1DZ (cm <sup>-1</sup> )	2DXY (cm <sup>-1</sup> )	2DXZ (cm <sup>-1</sup> )	2DYZ (cm <sup>-1</sup> )	3DXYZ (cm <sup>-1</sup> )	Harm. (cm <sup>-1</sup> )	Unharm. (cm <sup>-1</sup> )
$\nu_{OH}$	2265			2244	2338		2313	2822	2204
$\delta_{OH}^{ip}$		1416		1381		1426	1404	1489	1418
$\delta_{OH}^{oop}$			1038		962	1045	989	1003	959

So, by numerically solving the three-dimensional Schrödinger equation were determined frequency of the O-H group stretching and bending vibrations, whose values were, respectively, 2313 cm<sup>-1</sup>, 1404 cm<sup>-1</sup> and 989 cm<sup>-1</sup>. It is shown that the previously proposed [1] approaches to the estimation of frequencies of these vibrations in the 3D approach on the basis of 1D and 2D approximations are very satisfactory.

[1] G.A.Pitsevich, A.E.Malevich, V.Sablinskas, I.U.Doroshenko, V.E.Pogorelov, V.Balevicius J. Spec-trosc. Dyn. 2013, 3: 19



## MEASUREMENT OF MAGNETOSTRICTIVE PROPERTIES OF MATERIALS BY MEANS OF ULTRASONIC METHOD

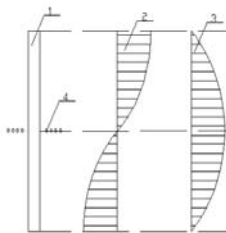
Kseniya Bogdanchuk<sup>1</sup>, Dmitry Stepanenko<sup>1</sup>, Vladimir Minchenya<sup>1</sup>

<sup>1</sup>Belarussian national technical university, Belarus  
[phantomsmall@rambler.ru](mailto:phantomsmall@rambler.ru)

Phenomenon of magnetostriction permanently attracts attention of physicists and engineers from perspective of design of new instruments and technical devices. Magnetostriction provides possibility of measurement of various physical quantities including stress, strain, elastic properties of materials, magnetic fields, magnetization etc. Magnetostrictive effect is used in various transducers and sensors. Magnetostrictive transducers are used in ultrasonic nondestructive evaluation as broadband sensors of vibrations and in acoustoelectronics as filters and resonators. Magnetostrictive sensors of level are widely used for measurement of gasoline level in underground reservoirs of gas stations. Magnetostrictive materials are also used for energy harvesting and in precision actuators for micro- and nano-positioning. In all above-listed applications one should know magnetostrictive properties of material used in sensor or actuator in order to provide highest efficiency of its operational characteristics.

There are several methods for measurement of magnetostriction [1]: method of electric wire strain gauges, hydraulic method, method of mechano-optical lever, interference method, measurement by means of ferroelectric transducer. The main drawback of the above-listed methods consists in the need for measurement of small deformations of the sample and application of highly-sensitive sensors of deformations.

This work considers measurement of magnetostrictive properties of materials by means of ultrasonic method. This method is based on generation of longitudinal standing ultrasonic wave in the sample of studied material made in the form of bar with constant diameter. Ultrasonic wave can be generated by means of piezoelectric transducer and preferably have frequency in the range 20-40 kHz. Length of the sample should be no less than half-wavelength of ultrasonic waves at the given frequency. Inductive sensor used for measurement is placed in nodal plane of vibratory displacements. Sensitive element of the sensor is made in the form of planar inductive coil generating EMF during vibrations of the sample. Generation of EMF is related to inverse magnetostrictive effect consisting in alteration of sample magnetization during its deformation. Application of planar coil provides spatial resolution (locality) of measurements, i.e. possibility of measurement of magnetization change in any arbitrarily chosen section of studied sample. Sensor is placed in the node of vibratory displacements, since it corresponds to maximum (antinode) of vibratory stresses (Fig. 1).



1 – sample, 2 – distribution of amplitude of vibratory displacements, 3 – distribution of amplitude of vibratory stresses, 4 – sensor

Fig. 1. Schematic representation of ultrasonic measurement of magnetostrictive properties.

Sensitivity of the sensor can be calculated using amplitude of vibratory stresses and amplitude of EMF generated in output of the sensor. Amplitude of vibratory stresses  $\sigma$  can be related to the amplitude of vibratory displacements  $\xi$  by means of equation  $\sigma = kE\xi$ , where  $k = 2\pi f/c$  is wavenumber,  $f$  is frequency,  $c$  is speed of sound,  $E$  is elastic modulus. Amplitude of vibratory displacements is measured by means of microscope and can be made relatively large in comparison with deformations generated during traditional measurements of magnetostriction. Since sensitivity of the sensor depends on magnetostrictive properties of material, we can determine these properties from the sensitivity calculated by means of above-described algorithm. Sensitivity of the sensor also depends on frequency of vibrations and number of turns of inductive coil. This enables measurement of weak magnetostrictive properties, when sufficiently large frequency of vibrations and number of turns are provided. For example, we successfully measured magnetostrictive properties of 316L stainless steel.

[1] R. Grössinger et al., Accurate measurement of the magnetostriction of soft magnetic materials. Online: <http://sxs.ifp.tuwien.ac.at/forschung/herbert.sassik/Dateien/magnetostr.pdf>



## DIELECTRIC AND IMPEDANCE SPECTROSCOPY OF Fe DOPED 0.94(Na<sub>0.5</sub>Bi<sub>0.5</sub>TiO<sub>3</sub>)-0.06BaTiO<sub>3</sub> CERAMICS

Kęstutis Bučinskas<sup>1</sup>, Maksim Ivanov<sup>1</sup>, Robertas Grigalaitis<sup>1</sup>, Jūras Banys<sup>1</sup>, Eva Sapper<sup>2</sup>, Jürgen Rödel<sup>2</sup>

<sup>1</sup>Faculty of Physics, Vilnius University, Lithuania

<sup>2</sup>Institute of Materials Science, Technische Universität Darmstadt, Germany  
kestutis.bucinskas@ff.stuf.vu.lt

Ever since the discovery of piezoelectric effect, piezoelectric materials have been rapidly developed and widely used. The most widely used piezoelectric materials are Pb(Zr,Ti)O<sub>3</sub>(PZT)-based ceramics because of their superior piezoelectric properties. However due to legislative enforcements, representatively the European RoHS/WEEE regulations [1], lead-free piezoelectric materials have been extensively studied last decade. Among the studied materials, (1-x)(Na<sub>0.5</sub>Bi<sub>0.5</sub>TiO<sub>3</sub>)-xBaTiO<sub>3</sub> ceramic family has been of particular interest because of the similar piezoelectric properties to PZT ceramics [2].

In the present work the dielectric and impedance properties of Fe doped 0.94(Na<sub>0.5</sub>Bi<sub>0.5</sub>TiO<sub>3</sub>)-0.06BaTiO<sub>3</sub> ceramics in 20Hz-1GHz frequency range and 300-500K temperature range are investigated. The measurements of dielectric permittivity were performed during freezing cycle with 1K/min temperature variation rate. Conductivity was calculated using dielectric permittivity data. Fig. 1 shows frequency dependency of the real part of complex conductivity. Experimental data was fitted with generalized Jonscher's law [3]. The best fits were obtained for 403K-500K temperature range. One conductivity process was distinguished with Arrhenius behavior of  $\sigma_{DC}$  and possible cause of conductivity process is discussed.

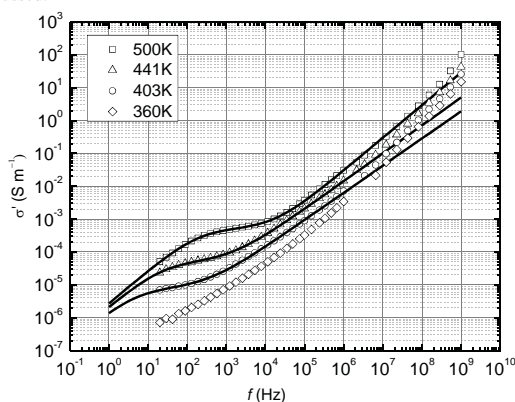


Fig. 1 Frequency dependency of real part of complex conductivity of Fe doped 0.94(Na<sub>0.5</sub>Bi<sub>0.5</sub>TiO<sub>3</sub>)-0.06BaTiO<sub>3</sub> ceramics

[1] EU-Directive 2002/95/EC: Restriction of the use of certain hazardous substances in electrical and electronic equipment (RoHS). Official Journal of the European Union 46 (L37) pp. 19-23 (2003).

[2] Thomas R. Shrout, Shujun J. Zhang, Lead-free piezoelectric ceramics: Alternatives to PZT? J. Electroceram. 19, pp 111-124 (2007).

[3] I. I. Popov, R. R. Nigmatullin, A. A. Khamzin, and I. V. Lounev, Conductivity in disordered structures: Verification of the generalized Jonscher's law on experimental data, J. Appl. Phys. 112, 094107 (2012).

# INVESTIGATION OF SILVER CONTAINING DIAMOND LIKE CARBON THIN FILMS EMPLOYING FOURIER TRANSFORM INFRARED SPECTROSCOPY

Agnė Čiučiulkaite<sup>1</sup>, Asta Tamulevičienė<sup>1,2</sup>, Andrius Vasiliauskas<sup>2</sup>

<sup>1</sup>Physics Department, Kaunas University of Technology, Studentų g. 50, LT 51368 Kaunas, Lithuania

<sup>2</sup>Institute of Materials Science, Kaunas University of Technology, Savanorių pr. 271, LT 50131 Kaunas, Lithuania  
[agne.ciučiulkaite@yahoo.com](mailto:agne.ciučiulkaite@yahoo.com)

Diamond like carbon (DLC) is the amorphous form of carbon (a-C:H), that consists of non-negligible fracture of  $sp^3$  bonding [1]. DLC possess many useful properties such as high mechanical hardness, optical transparency, etc. [1], however it has some significant drawbacks like high compressive stresses, gained due to  $sp^3$  bonding of carbon atoms. Doping with other elements can improve the original properties of a-C:H films. It was reported that silver inclusions can moderate the mechanical and optical properties of the films [2,3]. Optical properties can be changed in a wide range depending on the Ag concentration. It was shown that incorporation of Ag gives the reduced transparency and optical band gap of the films [3]. This effect was associated with the structural change to  $sp^2$  phase. One of the techniques to determine the phase change is Fourier transform infrared (FTIR) spectroscopy. The inclusion of metallic particles into carbon matrix is an additional tool for analysis as metal-surface selection rules for IR absorption must be taken into account [4]. Some absorption bands are strengthened and others are absent or weakened when molecules are adsorbed onto metallic surface or nanometer sized particles [4].

In this work we present an analysis of the structure of DLC films doped with different amount of silver employing FTIR spectroscopy in a 4000 – 400  $cm^{-1}$  range. Nanocomposites were deposited on quartz by unbalanced magnetron sputtering of silver target. Mixture of acetylene and argon was used in reactive sputtering. Varying Ar/C<sub>2</sub>H<sub>2</sub> gas ratio and deposition time, different silver doping level of DLC films was achieved. Films with Ag content from 0.6 to 34.3 at.% were analyzed.

The IR spectra of different films are shown in Fig. 1. The main vibrational bands observed in the spectra were attributed to C-H stretching (3100 – 2800  $cm^{-1}$ ), C-H bending (870 – 650  $cm^{-1}$ ) and CO<sub>2</sub> stretching (2400 – 2250  $cm^{-1}$ ). To determine the structure of the films, the C-H stretching region was analyzed in more detail. Fig. 2 shows the region of interest. It was observed that the increase of Ag concentration reduces the intensity of C-H stretching vibration dramatically. Further this peak was deconvoluted into the different C-H<sub>x</sub> stretching modes in terms of hybridization and bond configuration and  $sp^3/sp^2$  ratio was calculated.

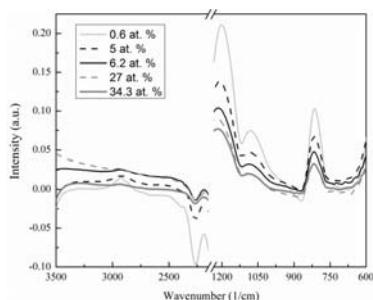


Fig. 1. IR spectra of DLC-Ag nanocomposite films with varying concentration of incorporated Ag from 0.6 at.% to 34.3 at.%.

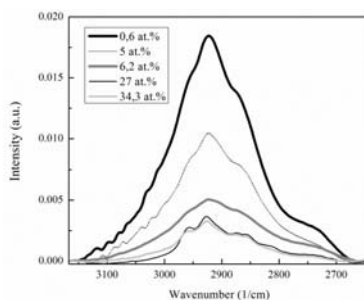


Fig. 2. C-H stretching region of DLC-Ag nanocomposite films with different concentration of incorporated Ag (0.6 – 34.3 at.%) after baseline correction.

[1] J. Robertson, Diamond-like amorphous carbon, *Materials Science and Engineering R* **37**, 129-281 (2002).

[2] Ch. Wang, X. Yu, M. Hua, Microstructure and mechanical properties of Ag-containing diamond-like carbon films in mid-frequency dual-magnetron sputtering, *Applied Surface Science* **256**, 1431-1435 (2009).

[3] Sk. F. Ahmed, M. W. Moon, K. R. Lee, Effect of silver doping on optical property of diamond like carbon films, *Thin Solid Films*, **517**, 4035-4038 (2009).

[4] P. Hlidek, J. Hanuš, H. Biederman, D. Slavinská, J. Pešička, Composite Ag/C:H:N films prepared by planar magnetron deposition, *Thin Solid Films* **516** 4581-4586 (2008)

# STRUCTURAL INVESTIGATION OF $[\text{Hg}(\text{SCN})_n]^{2-n}$ COMPLEXES IN WATER AND HEAVY WATER SOLUTIONS BY RAMAN SPECTROSCOPY AND THEORETICAL MODELING

Erika Elijošaitė<sup>1</sup>, Olegas Eicher-Lorka<sup>2</sup>, Egidijus Griškonis<sup>1</sup>, Dalia Jankūnaitė<sup>1</sup>, Gintaras Denafas<sup>1</sup>

<sup>1</sup>Kaunas university of technology, Radvilėnų pl. 19, LT-50254, Kaunas, Lithuania

<sup>2</sup>Center for Physical Sciences and Technology, Savanorių pr. 231, LT-02300, Vilnius, Lithuania

E-mail: [erika.elijosiute@stud.ktu.lt](mailto:erika.elijosiute@stud.ktu.lt)

The thiocyanate – containing metal complexes are considered to be the most investigated systems because of their diverse supramolecular networks and particular properties. The SCN<sup>-</sup> ion is an ambidentate ligand and the final bonding mode depends also on the metal charge, other coordinated ligands and steric effects [1]. To the best of our knowledge we were not aware of data of the assignments of Raman vibrational spectra of  $[\text{Hg}(\text{SCN})_n]^{2-n}$  molecules based on theoretical calculations and taking into account a different solvation models. Previously we performed the analysis of calculated and experimental Raman spectra of  $[\text{Hg}(\text{SCN})_n]^{2-n}$  complexes in aqueous solution [2]. For better performance of the assignments of fundamental vibrational modes of each  $[\text{Hg}(\text{SCN})_n]^{2-n}$  complex as well as verification of the interaction of water ligands with  $\text{Hg}^{2+}$  ion, the isotopic substitutions play an important role. It is necessary to know how much each vibrational frequency in a molecule changes when a heavy isotope is substituted for a light one [3]. In this work, we present the results obtained by comparing D<sub>2</sub>O/H<sub>2</sub>O exchange influence on the simulated and experimentally observed Raman spectra.

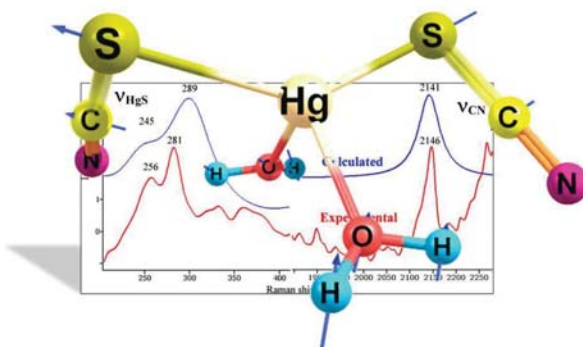


Fig. 1. Experimental and calculated Raman spectra of  $\text{Hg}(\text{SCN})_2$  complex in D<sub>2</sub>O solution with the visualisation of  $\nu_{\text{Hg-S}}$  vibrational mode

The performed calculations and experimental analysis of H<sub>2</sub>O replacement to D<sub>2</sub>O showed that the frequency of  $\nu_{\text{CEN}}$  stretching vibration of each  $[\text{Hg}(\text{SCN})_n]^{2-n}$  molecule is not sensitive to isotopic exchange. However, it is obvious that the isotopic substitution has substantial influence to the  $\nu_{\text{Hg-S}}$ . It should be noted that the vibrations at the 250 – 300 cm<sup>-1</sup> region are complex vibrations of Hg-S and Hg-O stretching. Due to performed calculations and experimental analysis of isotopic substitution, we were able to identify the second  $\nu_{\text{Hg-S}}$  vibrational mode in the case of  $\text{Hg}(\text{SCN})_2$ . This double-peak character also was displayed in calculated Raman spectra of  $\text{Hg}(\text{SCN})_2$  when the solvent is H<sub>2</sub>O, but could not be observed in the experimental Raman spectra.

Generally the isotopic changes have played an important role in performing better vibrational assignments. The D<sub>2</sub>O/H<sub>2</sub>O exchange analysis supported that the  $\text{Hg}^{2+}$  ion in the all complexes is four-coordinated. Additionally, it allowed to observe the second  $\nu_{\text{Hg-S}}$  vibrational mode which was overlaid by H<sub>2</sub>O molecules in the case of  $\text{Hg}(\text{SCN})_2$ .

[1] B. Machura, I. Nawrot, K. Michalik, Novel thiocyanate complexes of cadmium(II) – Synthesis, spectroscopic characterization, X-ray studies and DFT calculations, *Polyhedron* **30**, 2619-2626 (2011).

[2] E. Elijošaitė, O. Eicher-Lorka, E. Griškonis, D. Jankūnaitė, G. Denafas, Intrinsic view of  $[\text{Hg}(\text{SCN})_n]^{2-n}$  particles in the aqueous solution: DFT calculations and Raman spectroscopic study, *Nanochemistry and Nanomaterials*, International Conference of Young Chemists, 2012, ISBN 978-609-459-138-9, Vilnius university, p. 24 (2012).

[3] G. Jancso, *Isotope effects, isotope separation and isotope fractionation*, *Radiochemistry and nuclear chemistry* **1**, Encyclopedia of Life Support Systems (EOLSS).

# INVESTIGATION OF CONFORMATIONAL CHANGES IN IONIC LIQUID- D<sub>2</sub>O MIXTURES USING RAMAN SPECTROSCOPY

Povilas Kaščionis<sup>1</sup>, Viktorija Lukševičiūtė<sup>1</sup>, Valdemaras Aleksa<sup>1</sup>

<sup>1</sup>Department of General Physics and Spectroscopy, Vilnius University, Lithuania  
[povilas.kascionis@ff.stud.vu.lt](mailto:povilas.kascionis@ff.stud.vu.lt), [viktorija.lukseviciute@ff.stud.vu.lt](mailto:viktorija.lukseviciute@ff.stud.vu.lt)

Publications to date show that replacing an organic solvent by an ionic liquid can lead to cleaner and cheaper industrial chemistry processes [1]. Recently, there has been a growing interest in the study of room temperature ionic liquid (RTIL)-water solutions. This is partly because the presence of a small amount of water can affect the dynamics of the RTILs in mixtures [2]. Raman spectroscopy has been used to observe influence of H/D exchange on conformational equilibrium in low concentration ( $X_M = 0.01$  mol.) 1-butyl-3-methyl imidazolium chloride-D<sub>2</sub>O mixture. From sampled Raman spectra anomalous intensity change between imidazolium ring vibrational bands at 600 cm<sup>-1</sup> and 620 cm<sup>-1</sup> attributed to *gauche* and *trans* conformers (Fig 1 a, b) respectively was observed (Fig. 2) We suspect that the process of H/D exchange (Fig. 1 a) directly influences the equilibrium between these conformers in mixtures. This process correlates well in time with the results of theoretical calculations. Intensity changes of  $\nu_{1007}$  and  $\nu_{1023}$  bands in region of 990-1030 cm<sup>-1</sup> (Fig. 1 c) remains as an object of discussions.

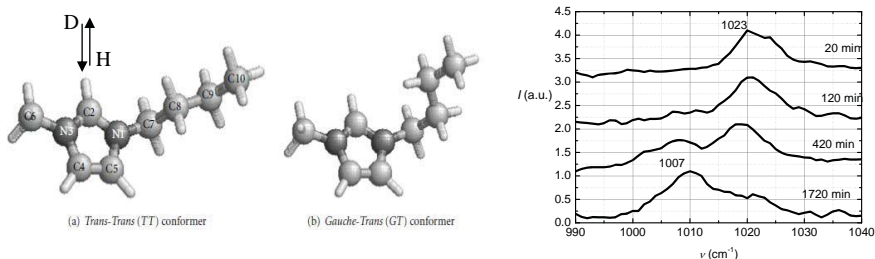


Fig.1. Different conformers of 1-butyl-3-methyl imidazolium cation (a, b) and observed Raman spectral change of  $\nu_{1007}$  and  $\nu_{1023}$  bands in time (c).

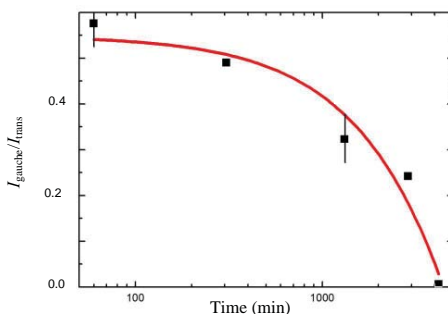


Fig. 2. Intensity change between 620 cm<sup>-1</sup> and 600 cm<sup>-1</sup> bands attributed to *trans* and *gauche* conformers respectively.

- 
- [1] P. Wasserscheid, W. Keim, Ionic liquids – New “Solutions” for Transition Metal Catalysis, *Angew. Chem. Int. Ed.* **39**, 3772-3789 (2000).  
 [2] N. Hatano, M. Watanabe et al., Anomalous Conformational Change in 1-butyl-3-methylimidazolium Tetrafluoroborate-D<sub>2</sub>O Mixtures, *Physical Chemistry A* **116**, 1208-1212 (2012).

## Magic Angle Spinning (MAS) NMR Spectroscopy

Žygimantas Lackus, Vytautas Bacevičius

Department of general physics and spectroscopy, Vilnius University, Lithuania

[z.lackus@gmail.com](mailto:z.lackus@gmail.com)

[akvavyte@gmail.com](mailto:akvavyte@gmail.com)

Even though NMR spectrometry techniques reached a considerably high level upon its origins, its application was limited to research of liquid state materials for a long period of time. In solid state materials we get a wide structureless NMR band. This is due to more complex inner interactions. The main reason for this broadening of the signal is the reciprocity of spins as magnetic dipoles, which hide other spectral structures of weaker interactions, thus making them uninformative.

The local magnetic field, caused by the  $i$  nucleus at the location of the  $j$  nucleus:

$$B_i = \mu r_{ij}^{-3} (3 \cos^2 \theta_{ij} - 1); \quad (1)$$

If the angle in the spin pair is

$$\theta_{ij} = \cos^{-1} \frac{1}{\sqrt{3}} = 54^\circ 44'; \quad (2)$$

then the reciprocity disappears. But only a small portion of the nuclei meets this criterion.

In liquids, where the molecular movement shifts the positions and orientations of the molecules at a high rate, the local fields average value becomes equal to zero. However, in solid state materials this field will have different values in different locations of the body. If we were to rotate the spin pair  $ij$  around any axis, then the components of the vector  $\mathbf{r}_{ij}$ , which are perpendicular to the axis of rotation averages themselves and becomes equal to zero. The effect value of the  $\mathbf{r}_{ij}$  vector becomes equal to its projection rotation axis. Thus, if we were to turn the whole spin ensemble at an angle of  $54^\circ 44'$  compared to the external polarizing field  $\mathbf{B}_0$ , the broadening of the resonance band due to the dipole interactions is negated.

Magic Angle Spinning (MAS) is used routinely in the most of solid state NMR experiments, where its primary task is to remove the effects of chemical shift anisotropy and to assist in the remove of heteronuclear dipolar-coupling effects. It also used to narrow lines from quadrupolar nuclei and it is increasingly the method of choice for removing the effects of homonuclear dipolar coupling. It requires very high spin rate.

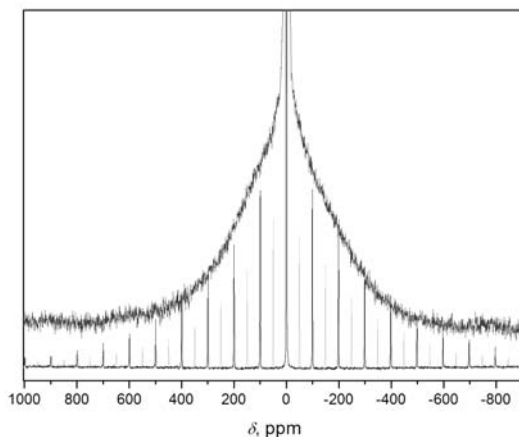


Fig. 1.  $^{79}\text{Br}$  MAS NMR spectrum of spin rate 10 kHz (with spikes) and without spinning (gradual). The measurements were made with Bruker Ascend 400WB NMR spectrometer.

The aim of the report is to review MAS method in NMR spectrometry and present its possible applications in scientific research.

[1] Dr. Shaoxiong Wu.-M. Ng, 1 Dand 2D NMR Experiment Methods, April 14, 2011.

[2] V. Balevičius, L. Kintys, G. A. Misiūnas, Magnetinio rezonanso spektrometrija, Vilniaus universiteto leidykla, 2000.

## SPECTRAL-LUMINESCENT PROPERTIES OF ALEXA FLUOR 488 MOLECULES NEAR SILVER NANOPARTICLES

Alina Muravitskaya<sup>1</sup>, Andrei Ramanenka<sup>1</sup>

<sup>1</sup> Department of Physics, Belarusian State University, Belarus

[alica.mur@mail.ru](mailto:alica.mur@mail.ru)

Plasmon-enhanced luminescence of molecular probes in plasmonic nanostructures is a highly developing field providing a number of new methods in chemical and biomedical analysis. The proximity of a metal nanobody gives rise to an increase in local electromagnetic radiation intensity, changes the probability of spontaneous photon emission, and also promotes multiple enhancement of nonradiative relaxation of an excited state [1]. All three effects result from local modification of the dielectric function of space upon insertion of a metal nanobody which is capable to support plasmon oscillation. Theoretical model of luminescence enhancement/quenching for luminophores near metal spherical nanoparticles stated that there is a strong correlation between intensity of fluorescence and silver particle size as well as distance “fluorophore – metal” [2].

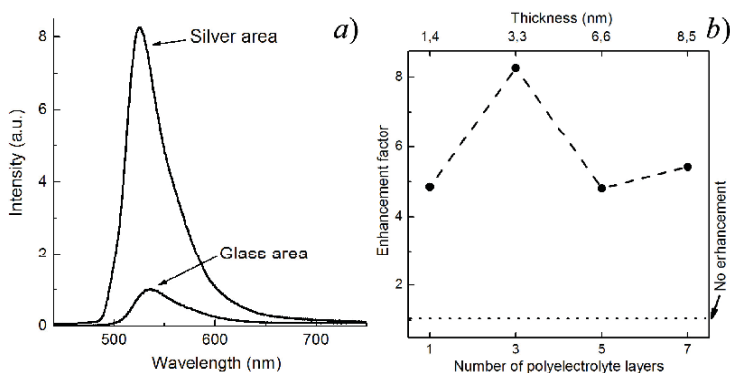


Fig. 1. a) Enhancement of Alexa Fluor 488 luminescence b) Enhancement factors ( $I_{Ag}/I_{glass}$ ) found for samples with different spacers

In this paper we investigated plasmon-enhanced luminescence of Alexa Fluor 488 molecules that are widely used in biomedical applications. For this purpose multilayer nanostructures “silver nanoparticles – polyelectrolytes – Alexa Fluor 488 molecules” were prepared. The distance between molecules and metal nanoparticles was controlled by varying number of counter-charged polyelectrolyte layers. Average diameter of the particles was about 40 nm (the optical density spectrum features the maximum near 415 nm) according to scanning electron microscopy data. The dielectric spacer was developed only up to 1, 3, 5 and 7 polyelectrolyte layers because of the diminution of the plasmonic effects with distance increasing. It was found that all fabricated and examined silver containing samples enhanced Alexa Fluor 488 luminescence in comparison to the reference samples with the same polyelectrolytes layers on glass substrates without silver coatings. Photoluminescence intensity of Alexa Fluor 488 molecules as a function of the number of polyelectrolyte layers is shown in Figure 1b. 8.2-fold maximal enhancement was observed for the sample containing three polyelectrolyte layers (corresponding thickness is 3.3 nm) (Figure 1a).

[1] S. V. Gaponenko, Introduction to Nanophotonics, Cambridge University Press, Cambridge (2010).

[2] D. V. Guzatov et al., “Plasmonic enhancement of molecular fluorescence near silver nanoparticles: theory, modeling, and experiment,” J. Phys. Chem. C 116(19), 10723–10733 (2012)

## EVALUATION OF D AND G RAMAN MODES RATIO FOR THE ANALYSIS OF CARBON NANOTUBE STRUCTURE

Ieva Puodžiūtė and Justinas Čeponkus

Faculty of Physics, Vilnius University, Saulėtekio Ave. 9-III, LT-10222 Vilnius, Lithuania

[iewute.puodzius@gmail.com](mailto:iewute.puodzius@gmail.com)

Carbon nanotubes are very perspective and important materials in the field of physics, chemistry, medicine and material sciences. Scientists still face with a problem to analyse carbon characteristics from their spectra. The goal of this project is to study D and G modes intensity dependence on environment surrounding carbon nanotubes. We studied single-walled carbon nanotubes (SWCNT) and functionalized carbon nanotubes with carboxyl group (COOH) by the means of FT-Raman spectroscopy. FT-Raman with NIR excitation spectroscopy is easy, fast, cheap and precise method to study such complicated structures [1]. In FT-Raman spectrometers Nd:YAG laser (1064 nm) is usually used for the Raman excitation, the photon energy is too low to excite fluorescence. High sensitivity, high speed and possibility to average high number of spectral scans allow to observe even very weak spectral bands in the FT-Raman spectra.

The samples were prepared using “pallet” technique. Carbon materials were mixed with potassium-bromide (KBr) powder in different proportion and mechanical pressure of 10 ton per  $\text{cm}^2$  was applied. Measurements were performed using a FT-Raman spectrometer MultiRAM from “Bruker”. The spectra were measured in range of 3600 to 50  $\text{cm}^{-1}$ .

FT-Raman spectra of single-walled carbon nanotubes with different concentration of nanotubes in KBr pallet are presented in figure 1.

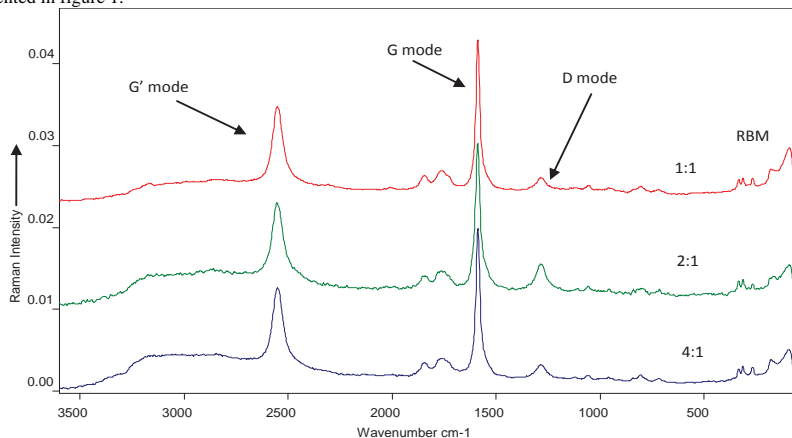


Fig. 1. FT-Raman spectra of SWCNT in KBr: 1:1 – one part of SWCNT and one part of KBr; 2:1 – two parts of SWCNT and one part of KBr; 4:1 – four parts of SWCNT and one part of KBr.

The band at  $1589\text{ cm}^{-1}$  (G mode) seems to be the most important one for characterization of carbon nanotubes. The band localized at  $2551\text{ cm}^{-1}$  (G' mode) also is characteristic for carbon nanotubes and is attributed to the first overtone of  $1589\text{ cm}^{-1}$  band. A low-frequency weak band at  $171\text{ cm}^{-1}$  is attributed to the breathing mode (RBM – radial breathing mode) of nanotubes [1], but it is less suited for identification of carbon structures due to its weakness. The band at  $1290\text{ cm}^{-1}$  (D mode), according to literature, describes the defects of carbon nanotubes [1, 2]. However during our measurements we noticed that this band intensity also depends on other factors.

Our results show that D modes intensity depends on proportion of nanotubes in KBr compound. As it can be seen in the figure 1, the intensity of D band in 2:1 concentration is different from this band intensity in 1:1 and 4:1 spectra. The dependence of D mode intensity from the nanotube to KBr ratio is not linear according to our observations. The intensity of this mode is also dependent from other factors such as moisture from the atmospheric water and possibly others environmental factors. Most likely explanation for such dependency could be that at some concentrations the interaction between the nanotubes itself and nanotubes and KBr powder is minimized due to the size ratios of KBr particles and nanotubes.

[1] T. Belin, F. Epron. Characterization methods of carbon nanotubes: a review, Materials Science and Engineering B, 119 (2005) 105–118.

[2] R.Schonfelder, et al. On the merits of Raman spectroscopy and thermogravimetric analysis to assess carbon nanotubes structural modifications, Applied Physics A, 106 (2012) 843-852.

## INVESTIGATION OF ARTWORKS POLYCHROMY USING PIXE ANALYSIS AND RAMAN SPECTROSCOPY METHODS

Mantas Stankevičius<sup>1</sup>, Mindaugas Brinkus<sup>1</sup>, Valdemaras Aleksa<sup>1</sup>

<sup>1</sup> Department of General Physics and Spectroscopy, Vilnius University, Lithuania  
[mantas.stankevicius@ff.stud.vu.lt](mailto:mantas.stankevicius@ff.stud.vu.lt)

The identification of pigments, ground layers and binders in polychromy of artworks is very important for restoration and conservation. Raman spectroscopy method is a powerful technique in analysis of artifacts and is used widely for more than 30 years [1]. Proton induced X-ray emission (PIXE) analysis is accurate method to investigate element analysis [2]. In this study the samples of Egyptian sarcophagus of the god's Amon singer (Thebes, XI - IX century BC) and 300 years old baptistery were investigated by Raman and PIXE spectroscopic methods (Fig. 1).

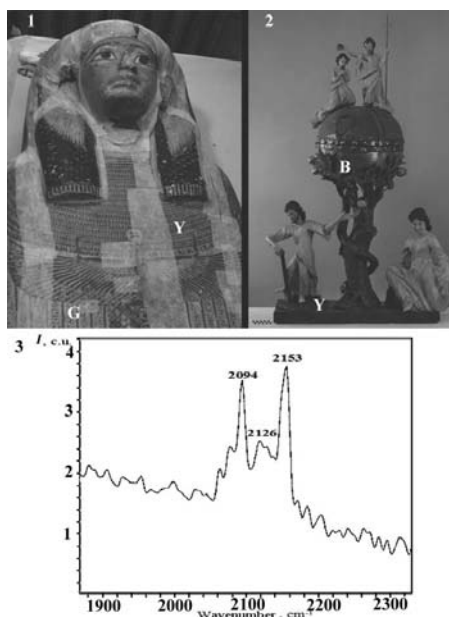


Fig. 1. 1 – Egyptian sarcophagus; 2 – baptistery; 3 – Raman spectra of blue baptistery sample. Letters G, Y, B shows the place from which the green, yellow and blue samples were taken.

The results of sarcophagus green sample PIXE analysis showed that green sample consists of mostly of copper (37%) and calcium (23%). Investigation using Raman spectroscopy revealed that green pigment is a mixture of azurite ( $\text{Cu}_3(\text{CO}_3)_2(\text{OH})_2$ ) and malachite ( $\text{Cu}_2(\text{OH})_2\text{CO}_3$ ). Raman spectra of yellow sample of sarcophagus showed that yellow pigment is an orpiment ( $\text{As}_2\text{S}_3$ ) with impurities of goethite ( $\text{Fe}^{3+}\text{O}(\text{OH})$ ).

Yellow and blue samples of baptistery were investigated using PIXE analysis. Results showed that yellow sample consists mostly of lead (64.1%), sulfur (17.2%) and calcium (13.9%). Blue sample mostly has calcium (87.4%) and iron (5.3%). Raman spectroscopy method showed that yellow pigment is lead white ( $\text{Pb}_3(\text{CO}_3)_2(\text{OH})_2$ ) and blue pigment is Prussian blue ( $\text{Fe}_4[\text{Fe}(\text{CN})_6]_3$ ).

In conclusion, Raman spectroscopy and PIXE analysis combined together are effective methods for identification of pigments, ground layers and binders, but has some shortcomings in ways of sample preparation, which are under consideration in this work.

[1] L. Bonizzoni, S. Bruni, V. Guglielmi, M. Milazzo, O. Neri, Field and laboratory multi-technique analysis of pigments and organic painting media from an Egypt coffin (26th dynasty), *Archeometry* (2010)

[2] I. M. Govil, Proton Induced X-ray Emission - A tool for non-destructive trace element analysis, *Current science* 12: 1542 – 1549 (2006)



## PHOTOPHYSICAL PROCESSES OF ORGANIC INDOLO[3,2-*b*]CARBAZOLE COMPOUNDS

Simona Streckaitė<sup>1</sup>, Renata Karpicz<sup>1</sup>, Saulius Grigalevičius<sup>2</sup>

<sup>1</sup>Institute of Physics, Center for Physical Sciences and Technology, A. Gostauto Ave 11,  
LT-01108 Vilnius, Lithuania

<sup>2</sup>Department of Organic Technology, Kaunas University of Technology, Radvilėnų pl. 19, LT-50254, Kaunas,  
Lithuania

*simona.streckaite@gmail.com*

Interest in organic semiconducting materials has been recently increasing because of their potential applications in electronics. Organic photoactive materials are extremely attractive due to great mechanical properties and low cost of production. However, we are facing a problem combining stability and processability with charge transport properties. Widely investigated effective charge transporting materials are indolo[3,2-*b*]carbazoles.

New class of compounds based on indolo[3,2-*b*]carbazole are being studied as hole-transporting materials. These compounds can be well utilized as hole-transporting layers in organic light emitting diodes (OLEDs) because of their high thermal stability and determinable hole-injecting and transporting properties [1-3].

In our work we present analysis of properties of three new indolo[3,2-*b*]carbazole compounds named as SV100, SV101 and SV106, under names of different connection of benzene functional group. Compounds were investigated as solutions using chloroform solvent and as thin films. Films were made by spin coating technique using polystyrene as matrix material. Sample thickness was about few hundred nanometres.

In solutions fluorescence kinetics decay monoexponential, meanwhile in thin films it consists of two exponential decays. Also a large influence of oxygen and evaporated aluminium electrodes to fluorescence quenching was observed. Optical properties of investigated materials showed no dependence of added electrical field.

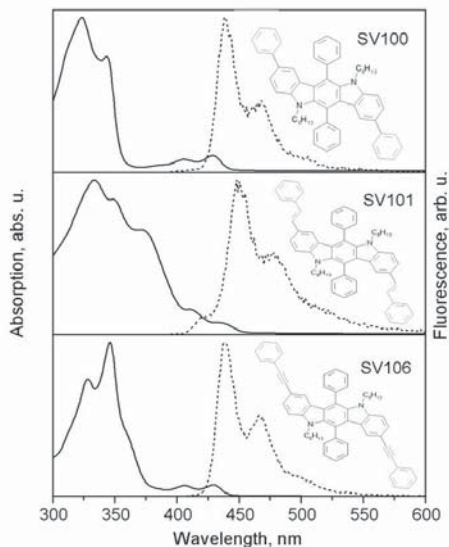


Fig.1. Absorption (solid line) and fluorescence (dash line) spectra of all investigated compounds in dilute chloroform solution.

### Acknowledgements

S. S. acknowledges support by project "Promotion of Student Scientific Activities" (VP1-3.1-SMM-01-V-02-003) from the Research Council of Lithuania. This project is funded by the Republic of Lithuania and European Social Fund under the 2007-2013 Human Resources Development Operational Programme's priority 3.

[1] H. Zhao, X. Tao, F. Wang, Y. Ren, X. Sun, J. Yang, Y. Yan, D. Zou, X. Zhao, M. Jiang, Chem. Phys. Lett., 2007, 439, 132–137.

[2] M. Kirkus, J. V. Grazulevicius, S. Grigalevicius, R. Gu, W. Dehaen, V. Jankauskas, European Polymer Journal, 2008, 45, 410–417.

[3] N. Blouin, A. Michaud, S. Wakim, P. T. Boudreault, M. Leclerc, B. Vercelli, S. Zecchin, G. Zotti, Macromol. Chem. Phys., 2006, 207, 166–174.

## STABILITY AND INTENSITY OF SPECTRAL LINES IN HFEDLS WITH ZINC

Anda Svagere<sup>1</sup>, Rolands Zvejnieks<sup>1</sup>

<sup>1</sup>Institute of Atomic Physics and Spectroscopy, University of Latvia  
[anda.svagere@gmail.com](mailto:anda.svagere@gmail.com)

Covering the spectrum from the vacuum ultraviolet to the infrared, high-frequency electrodeless lamps (HFEDLs), due to their capability to emit high intensity narrow spectral lines, are widely used as emission sources in various experiments such as sensitized fluorescence experiments, measurements of the shifts, broadening of spectral lines, and scientific devices, for example, emission and absorption spectrometers, spectrometers for refractive index measurements and frequency standards. Also because of the lack of electrodes, that can cause impurities, HFEDLs are also very convenient for plasma-surface interaction studies [1].

Main requirements for such light sources are high intensity of spectral lines, long lifetime, emission stability and narrow and not self-absorbed line profiles. Of course, depending on the application, these requirements may vary, so it is necessary to optimize light sources for each particular use.

In this work we present measurements of HFEDLs containing zinc as working element and argon as buffer gas, developed in our laboratory for different analytical devices, particularly, atomic absorption spectrometers. We compared three different types of lamps – lamps filled with zinc with sidearm, zinc lamps without sidearm and lamps filled with zinc and antimony iodine. Our aim was to see how changes in filling and lamp form influence behaviour of zinc and argon spectral lines.

During our research we investigated both intensity changes of spectral lines induced by change of generator voltage and stability of spectral line intensity during several hours of HFEDLs working time.

The emitted light spectra were registered using two different spectrometers - AVANTES AVS-PC2000 plug-in spectrometer with a 2048-element linear CCD-array detector in the wavelength range from 190 till 850 nm and Jobin Yvon SPEX 1000M in the range from 200 till 850 nm.

The results of our measurements showed that in order to achieve higher intensities of zinc spectral lines, lamps without sidearm or with addition of antimony iodine should be chosen. Lack of sidearm also provided better stability of zinc spectral lines.

- 
- [1] A. Skudra, Z. Gavare, N. Zorina, M. Zinge, E. Gavars, R. Poplauskis, A. Svagere, Plasma Temperature and Surface Studies of Argon Hydrogen Containing Low-Temperature Dumbbell form Light Sources, Journal of Materials Science and Engineering B **1**, 439-444(2011)

# SPECTRAL SIGNATURES OF MEDICINE DRUGS IN TERAHERTZ RANGE

Laurynas Tumonis, Rimvydas Venckevičius, Irmantas Kašalynas, Gintaras Valušis

Center for Physical Sciences and Technology, Vilnius, Lithuania

[laurynas.tumonis@ff.stud.vu.lt](mailto:laurynas.tumonis@ff.stud.vu.lt)

Terahertz (THz) imaging and spectroscopy can be applied in various areas including material science, security systems, chemistry, medical industries, etc. The key-feature of THz radiation is ability to penetrate different kind of common materials like clothing, paper, plastic, packaging materials. As many chemical substances, drugs or explosive materials exhibit characteristic spectral THz signatures, it can be used for their identification [1].

In this work we extend such an approach to medicine drugs like *vitamin C* (ascorbic acid) and sedative drugs based on melatonin (*Circadin* and *Stahl nacht*) via Fourier spectra to determine spectral range needed for identification.

The samples were prepared from the *vitamin C*, *Circadin*, and *Stahl nacht* tablets. Each tablet was grinded into the powder with average particles size up to 300  $\mu\text{m}$ . The samples were prepared from powder covered on the adhesive tape. Transmittance spectra of the samples were measured by the vacuum Fourier spectrometer. The transmittance was found by normalizing spectrum of the sample to the empty adhesive tape spectrum. The data were measured with 3  $\text{cm}^{-1}$  spectral resolution in frequency range of 0.9–4.5 THz.

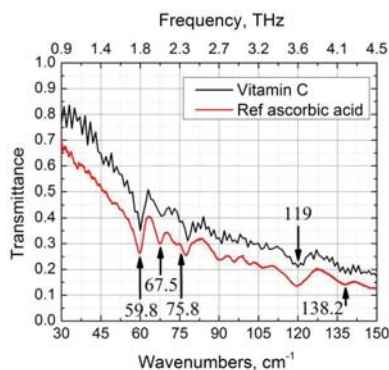


Fig. 1 The transmittance spectra of *vitamin C* and the reference spectra of ascorbic acid taken from database [2].

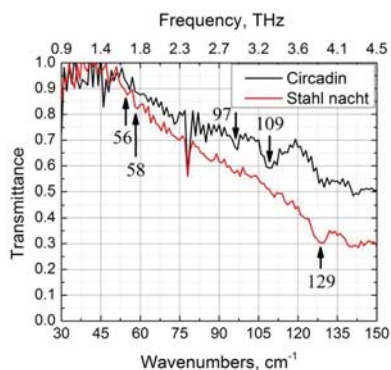


Fig. 2 The transmittance spectrums of sedative drugs (*Circadin* and *Stahl nacht*).

The transmittance of the *vitamin C*, *Circadin*, and *Stahl nacht* powders are shown in Fig. 1 and Fig. 2. Initially, measured transmittance of the *vitamin C* powder was compared with reference spectra of ascorbic acid taken from materials database [2]. We note that the reference sample was prepared differently; the sample powders were compressed in the HDPE matrix. As it is seen from Fig. 1, measured absorption lines in our experiment correspond to the reference data. The transmittance spectra of two sedative drugs, in which major component is melatonin, are shown in Fig. 2. The minima at 56  $\text{cm}^{-1}$ , 58  $\text{cm}^{-1}$ , 97  $\text{cm}^{-1}$ , 109  $\text{cm}^{-1}$  and 129  $\text{cm}^{-1}$  are present in both samples spectrum and these lines can be attributed to the melatonin. Experiment data does not exclude those common excipients or other type additives those could be used in these drugs. We note large transmittance difference between two data which could be also an indicator of different chemical composition as well as material amount. Thus, quantitative material measurement and analysis is possible on medical drugs containing the melatonin. As it is seen, characteristic spectral signatures appears below 4 THz range.

The obtained results allow to infer that transmittance spectra of *vitamin C*, *Circadin* and *Stahl nacht* below 4 THz provides a possibility to distinguish different drugs containing melatonin.

[1] I. Kašalynas, R. Venckevičius, D. Seliuta, I. Grigelionis, G. Valušis, *InGaAs-based bow-tie diode for spectroscopic terahertz imaging*, Journal of Applied Physics **110**, 114505 (2011)

[2] <http://www.riken.jp/THzdatabase/> (ascorbic acid), viewed 2013-02-01

## ANLYSIS OF CHEMICAL CONSTITUENS OF URINARY SEDIMENTS BY MEANS OF SURFACE ENHANCED RAMAN SPECTROSCOPY

Martynas Velička, Milda Pučetaitė, Valdas Šablinskas

Department of General Physics and Spectroscopy, Vilnius University, Saulėtekio Ave. 9-III, LT-10222 Vilnius, Lithuania

[martynas.velicka@ff.stud.vu.lt](mailto:martynas.velicka@ff.stud.vu.lt)

Raman spectroscopy is a commonly used tool for determining the composition of various substances. Unfortunately, the measurements are only effective if the molar concentration of the substance is high enough. Typically, the detection limit is  $1\div 10$  mM. However, the signal of the measurements can be significantly increased by applying the surface enhanced Raman scattering (SERS). In this work, a couple of chemical constituents of urinary sediments: L-Cystine, Urea, were analysed by this method.

Elevated concentrations of urinary sediments indicate a higher risk of formation of renal stones [1]. Identification of sediments can be performed by analysis of their constituents. As the concentration of these constituents is far too small for the conventional Raman spectroscopy, SERS method had to be used to measure their spectra. Two samples of  $10^{-4}$  M and one sample of  $10^{-3}$  M were studied.

Surface enhanced Raman spectroscopy can be applied by using the nanoparticle colloids of gold (Au), silver (Ag) or copper (Cu). In this work silver nanoparticle colloid, prepared by Lee and Meisel method [2], was used. To intensify the aggregation of silver nanoparticles the 0.05 M of sodium chloride (NaCl) was added to the solution of colloid and sample. The spectra of dried samples were measured with Bruker FT-Raman spectrometer "Multiram" and 1064 nm laser was used for the excitation. Conventional Raman and SERS spectra of urea is presented in Fig. 1.

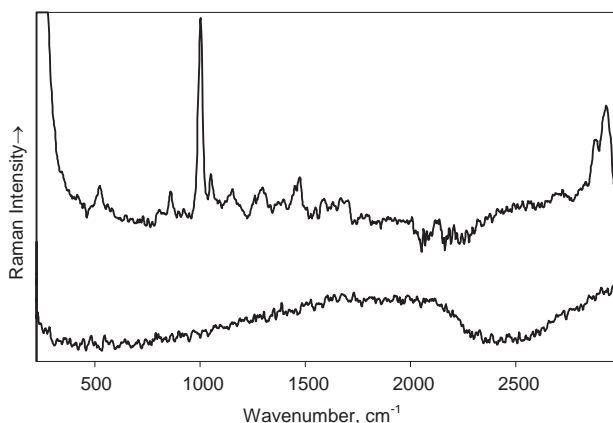


Fig. 1. Raman (bottom) and SERS (top) spectra of urea solution in water ( $c=10^{-3}$  M)

Upon processing the registered spectra it was found that the enhancement factor for urea samples varied from a hundred to a thousand times. This variability of enhancement factor can be explained by the different sizes of the silver nanoparticle aggregates formed in different experiments. This finding calls for further experiments and optimization of the experimental parameters. New SERS experiments with electrochemical cell are intended in the near future.

### Acknowledgements

This work was partly supported by project "Promotion of Student Scientific Activities" (VP1-3.1-ŠMM-01-V-02-003) from the Research Council of Lithuania (M.V.). This project is funded by the Republic of Lithuania and European Social Fund under the 2007-2013 Human Resources Development Operational Programme's priority 3.

[1] S. Tamošiūtė, V. Hendrixson, A. Želvys, R. Tyla, Z. A. Kučinskienė, F. Jankevičius, M. Pučetaitė, V. Jablonskienė, V. Šablinskas, Combined studies of chemical composition of urine sediments and kidney stones by means of infrared microspectroscopy, *Journal of Biomedical Optics* 2(18), (2013)

[2] P. C. Lee and D. Meisel, Adsorption and Surface-Enhanced Raman of Dyes on Silver and Gold Sols', *J. Phys. Chem.* 86, 3391-3395 (1982)

# APPLICATION OF FLUCTUATION ANALYSIS METHOD FOR EVALUATION OF HUMAN CARDIOVASCULAR SYSTEM

Artūras Vyšniauskas, Dovilė Čibiraitė, Sandra Pralgauskaitė, Jonas Matukas

Department of Radiophysics, Vilnius University, Lithuania

[Arturas.Vysniauskas@ff.stud.vu.lt](mailto:Arturas.Vysniauskas@ff.stud.vu.lt)

Nowadays one of the mostly occurring human death causes is disorder of cardiovascular system. Therefore it is actual to find new or improve existing methods of human blood circulation system assessment. Examination of human body requires non-invasive, reliable and very sensitive method which could allow us to recognize the very first indication of a disease. Blood circulation system generates various signals (electric, acoustic) that carry considerable information on the system state. And it is well known that fluctuation of the signal can give valuable information that is unattainable by investigation of averaged values [1]. In this report we present the investigation of fluctuation of human limb impedance.

A new approach in the investigation is analysis of noise characteristics of electrical signals of human body limbs. Voltage fluctuations are measured via two terminals that are attached to a hand (Fig. 1). Voltage fluctuation spectral density is evaluated through comparison with the thermal noise of standard resistor  $R_e$ :

$$S_V = \frac{\overline{V^2} - \overline{V_s^2}}{\overline{V_e^2} - \overline{V_s^2}} 4kT_0 R_e \text{ [V}^2\text{s]}; \quad (1)$$

where  $\overline{V^2}$ ,  $\overline{V_s^2}$  and  $\overline{V_e^2}$  are the investigated object, the measuring system, and the standard resistor thermal noise variances in the narrow frequency band  $\Delta f$ ;  $T_0$  is the absolute temperature of the standard resistor. The experiments are being conducted in Faraday's cage (an enclosure formed by two screens of copper and iron) in order to filter extraneous signals. Due to the fact that investigation results depend on such factors as human age, skin moisture, physical state and environmental conditions, incredibly huge database must be accumulated and carefully analyzed.



Fig. 1. Terminals attached to a hand.

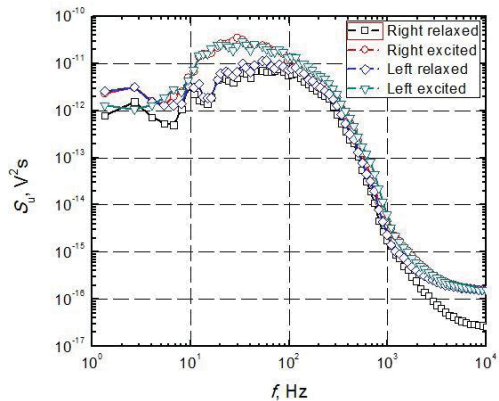


Fig. 2. Spectral density of voltage fluctuations in right and left hands in relaxed and excited states.

In Fig. 2, there is shown spectral density dependencies on frequency of voltage fluctuation in both hands of a person under study at relaxed and excited (after a series of sit-ups) states. It is seen that in excited state noise spectral density is about half of order larger comparing to the relaxed state. It is observed that noise level in relaxed state slightly differs for different persons but noise level increase at excited state is observed for all investigated cases.

These preliminary investigations enable to assume that fluctuation analysis can be employed for a human cardiovascular system assessment. For the further investigations of human blood circulation system there should be evolved the measurement technique that works at very low frequencies concerning the characteristic times of processes in human body.

[1] L. K. J. Vandamme, Noise as a diagnostic tool for quality and reliability of electron devices, IEEE Trans. Electron. Dev. **41** 2176-2187 (1994).

## SELF-MODULATION REGIME STUDIES OF SELENIUM CONTAINING HIGH-FREQUENCY ELECTRODELESS LAMPS

Madara Zinge<sup>1</sup>, Valters Dzelmē<sup>1</sup>

<sup>1</sup>Institute of Atomic Physics and Spectroscopy, University of Latvia, Skulu str. 4, LV-1050, Latvia  
[madara.zinge@gmail.com](mailto:madara.zinge@gmail.com)

Depending on application, requirements for light sources are different and for each particular use light sources have to be optimized. Therefore they must have several important parameters, for example, high intensity of spectral lines, emission stability in time, long life-time etc. High-frequency electrodeless lamps (HFEDL) are widely used as bright radiators of narrow and intense spectral lines in different types of scientific devices, for instance, in atomic absorption spectrometers. Depending on HFEDL filling and operating mode, it is possible to observe the self-modulation regime. For optimization of light sources it is important to understand processes in plasma, including self-modulation mode.

HFEDL under study was filled with Selenium and Argon mixture (pressure 1 Torr). This type of lamp is manufactured at the Institute of Atomic Physics and Spectroscopy, University of Latvia. The spherical lamp vessel with diameter of 1 cm is made of SiO<sub>2</sub> and filled with working element and buffer gas. An inductively coupled discharge is induced by placing lamp in a high frequency generator coil. The frequency of electromagnetic field is about 100 MHz.

The emission spectra of the discharge was registered by means of JobinYvon SPEX 1000M high resolution spectrometer (grating 1200 l·mm<sup>-1</sup>) and charge coupled device matrix detector (2048x512 Thermoelectric Front Illuminated UV Sensitive CCD Detector, Simphony). AVANTES AVS-PC2000 plug-in spectrometer with a 2048-element linear CCD-array detector (wavelength range 190 – 850 nm) was used for intensity stability measurements.

HFEDL was operated at different excitation generator voltage values (21–29V), and the emission spectra changes were analyzed (Fig. 1). In emission spectra of Se + Ar HFEDL bands of different molecules could be observed, for example, OH, C<sub>2</sub>, CN and Se<sub>2</sub>. Previous measurement results show that OH rotational spectra at 310 nm can be successfully used for estimation of gas temperature in HFEDL.

Intensity stability of Se + Ar HFEDL in dependence on excitation generator voltage was measured. These measurements showed that lamp stabilize within 1 – 2 minutes, however at higher values of applied voltage it is possible to observe self-modulation regime (Fig. 1.). The behavior of different atomic lines (Se, Ar) and molecular bands (Se<sub>2</sub>, OH) in self-modulation mode was studied. During the self-modulation regime first we observe intense discharge in buffer gas (argon), then due to the increase of gas temperature, the intensity of Se lines grow rapidly until the discharge goes into its minimum phase. After the cooling period (minimum phase) the discharge in buffer gas starts again. In maximum intensity phase estimated gas temperature is about 1000 K, at applied voltage 29 V.

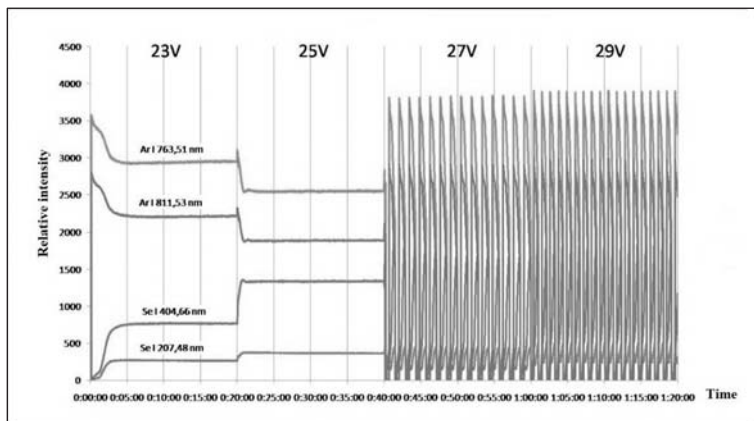


Fig. 1. Intensity stability of Se + Ar HFEDL in dependence on excitation generator voltage.

## SAMPLE TEMPERATURE CONTROLLER

Tomas Žukauskas<sup>1</sup>

<sup>1</sup>Department of Physics, Vilnius University, Lithuania  
[tomas.zukauskas@ff.stud.vu.lt](mailto:tomas.zukauskas@ff.stud.vu.lt)

Automated and accurate sample temperature control is very important for the measurements of electrical properties of solid state materials. Therefore an automated temperature control system is required that can effectively control a small heater with low thermal inertia, accurately measure sample temperature and provide rich functionality for measurement automation and ease integration to other systems. During this work such system was built for use in a broad band impedance spectrometer [1], four electrode impedance spectrometer for investigation of solid ion conductors [2] and other similar measurement systems. Temperature controller was built using standard laboratory equipment and personal computer with MATLAB computing environment.

The hardware part of temperature control system is shown on Fig 1. It consists of a resistive sample heater, a computer controlled Agilent E3634A linear power supply unit, an Amprobe TMD90A digital thermometer with a K type thermocouple together with required hardware interfaces.

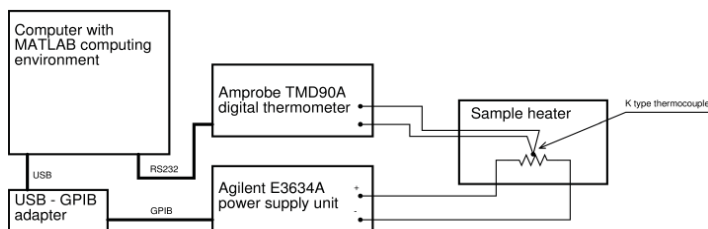


Fig. 1. Block diagram of temperature controller hardware.

The heart of this controller is a software program written in MATLAB programming language. This program controls temperature according to a given curve, allows temperature stabilization and measurement triggering at certain points. It also provides temperature versus time curve monitoring tools.

For temperature control, custom closed-loop PID (proportional-integral-differential)[1] algorithm is used. The PID algorithm coefficients and heater temperature versus voltage relation is determined by automated calibration function. This prevents system instability and provides fast and accurate temperature control without manual system tuning. Some error detection mechanisms are also implemented to ensure safe system operation without constant supervision.

The temperature controller program was designed using object oriented programming paradigm. This program consists of the two hardware dependent classes, the main controller class, and the graphical user interface (GUI) class. The hardware dependent classes provide separate methods for data acquisition from the digital thermometer and power supply unit control, thus separating hardware dependent program code from rest of the program. Main controller class provides methods for external system control from other programs and implements temperature control and calibration algorithms. GUI class provides all required controls and parameter monitoring tools.

This temperature control system can be used for various applications. Program modularity and automated calibration function allows easy adaptation to different hardware. Control accuracy and other limitations mostly depend on the equipment used. Using the above mentioned equipment 0.2K temperature control accuracy was achieved in the temperature range 300K – 1200K. System was stable at lower than 5 K/min rates of temperature change.

- 
- [1] A. Kežionis, E. Kazakevičius, T. Šalkus, A. Orliukas, Broadband high frequency impedance spectrometer with working temperatures up to 1200 K, Solid State Ionics 188, 110-113 (2011)
  - [2] A. Kežionis, P. Butvilas, T. Šalkus, S. Kazlauskas, D. Petrulionis, T. Žukauskas, E. Kazakevičius, and A. F. Orliukas, Four-electrode impedance spectrometer for investigation of solid ion conductors, Rev. Sci. Instrum. 84, 013902 (2013).

# Poster session 2

---

15:30

Thursday

- Semiconductor and condensed matter physics, material sciences
- Functional materials and derivatives, modern technologies



## PHOTOLUMINESCENCE OF InGaN EPITAXIAL LAYERS WITH HIGH INDIUM CONTENT

Justinas Aleknavičius

Semiconductor Physics Department, Vilnius University, Saulėtekio Ave. 9-III, LT-10222 Vilnius, Lithuania  
[ju.aleknavicius@gmail.com](mailto:ju.aleknavicius@gmail.com)

Nitride semiconductors have been widely investigated during the last two decades due to their exceptional material properties. The bandgap of the ternary InGaN compound can be varied from 0.7 eV (InN) to 3.4 eV (GaN), thus it is very attractive for the development of light-emitting diodes (LEDs) and laser diodes (LDs) covering entire visible spectral range. Violet, blue and white InGaN-based LEDs are already successfully commercialized, however, the growth of InGaN layers with high indium content is challenging and faces material quality problems.

In this work, the InGaN epitaxial layers with high indium content were studied using photoluminescence spectroscopy. InN and In-rich InGaN thin films were grown by metalorganic chemical vapor deposition (MOCVD) technique on sapphire substrates. All the samples were grown at Vilnius University Institute of Applied Research.

Four samples with different indium content were compared:  $\text{In}_{0.6}\text{Ga}_{0.4}\text{N}$ ,  $\text{In}_{0.8}\text{Ga}_{0.2}\text{N}$  and two InN epilayers with different background electron concentration. Photoluminescence spectra in the near infrared region were measured using a standard spectroscopic setup, consisting of *Andor Shamrock 303i* spectrometer and *iDus* InGaAs CCD detector array. CW HeNe laser ( $\lambda = 632.8$  nm) was used for PL measurements under low excitation conditions, while Q-switched YAG:Nd laser radiation ( $\lambda = 1064$  nm, pulse duration  $\tau = 10$  ns) was used for high excitation conditions. All the measurements were performed at room temperature.

The PL spectra of all four InGaN epilayers measured at low excitations are shown in Fig. 1. As expected, the PL bands shift to the short-wavelength side, as indium content decreases. This is accompanied by the decrease of PL intensity. This decrease is associated with lower quality of the epitaxial layer resulting in increasing rate of nonradiative carrier recombination. The multiple peaks observed in the structure of the spectra are related to *Fabry-Perot* interference due to PL signal reflection off the substrate. Positions of interference minima and maxima provide a reference for determining thicknesses of each epitaxial layer.

The studies of photoluminescence dynamics at high excitations (up to  $\sim 30$  MW/cm<sup>2</sup>) revealed the strong PL band broadening and peak position blueshift with increasing excitation.

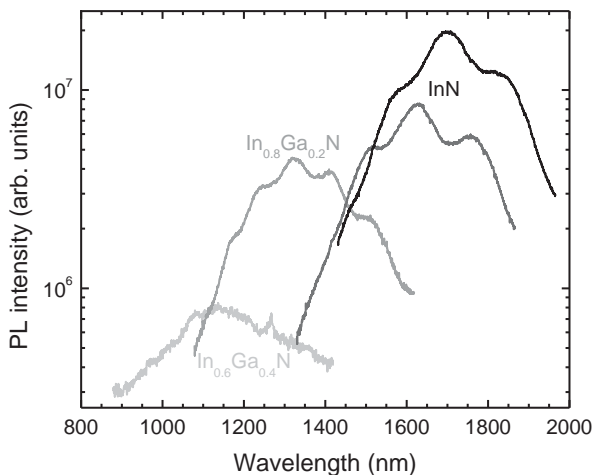


Fig. 1. PL spectra of  $\text{In}_x\text{Ga}_{1-x}\text{N}$  epitaxial layers

# INVESTIGATION OF INTERMEDIATE STAGES OF GAN GROWTH: STRAIN TRANSFORMATIONS FROM INTERFACE TO EPILAYER

Aurina Arnatkevičiūtė

Institute of Applied Research, Vilnius University, Lithuania  
aurina.arnatk@gmail.com

The development of undoped GaN epilayer at gradual stages of growth in the context of strain evolution was investigated by photoluminescence (PL) measurements. A series of samples of thickness from 200 nm to 3.5  $\mu\text{m}$  corresponded to islets and continuous structure of epilayer, respectively. Surface and interface room temperature PL spectra measured under relative low cw excitation ( $1 \text{ W/cm}^2$ ) evidenced quite well the evolution of blue (BL) and yellow (YL) photoluminescence spectra helping us to determine the structural transformations in due the course of growth.

Shift of the bandgap PL to shorter wavelength on either side of the samples ( $\lambda=325 \text{ nm}$ ,  $1 \text{ W/cm}^2$  and  $\lambda=265 \text{ nm}$  and  $0,2 \text{ mW/cm}^2$  excitation) with increasing epilayer thickness was observed (Fig. 1). Variant bandgap PL peak position correspondence to excitation depth demonstrates strain evolution in the epilayer volume. Plausible factors contributing to strain variation for different thick samples are: lattice thermal expansion coefficient mismatch between sapphire substrate and GaN, resulting in a residual compressive strain and coalescence of islets or presence of dopants initiating tensile strain [1-3]. Islets being relative small have perfect crystalline structure and are not affected by strain. Most threading dislocations at this stage would result only from island coalescence originating a tensile strain and redshifted bandgap PL. The observed blueshift, however, appears with sample thickness of  $0.36 \mu\text{m}$  and saturates at  $1.1 \mu\text{m}$ , what indicates rise and dominance of compressive stress in the structure of larger islet or even continuous structure overgrown (Fig. 1). For excitation light  $\lambda=325 \text{ nm}$  and  $\lambda=265 \text{ nm}$  the penetration depth is  $\sim 200 \text{ nm}$  and  $\sim 100 \text{ nm}$ , respectively: the shallower it is, the more relaxed compressive strain at the GaN/sapphire interface is, the longer wavelength is detected (Fig. 1), what correlates well with the conclusion about open site and stress reduction [3,4]. Relative higher energy bandgap PL detected from surface indicates in average higher compressive strain on this side, thus confirming about the more relaxed situation at the interface.

Considering reduction in compressive stress and bandgap narrowing effect, while increasing carrier concentration [5,6], the strain change in continuous structure overgrown samples (Fig. 2) in our case is explained unambiguously. At the start of coalescence islets due to relative high carrier concentration (up to  $n \sim 3.5 \cdot 10^{18} \text{ cm}^{-3}$ ) show red-shifted band-gap PL (Fig. 2): the formation of dislocation-type defects defines reduced compressive strain and more free carriers. In samples with continuous structure overgrown (from  $d \sim 1.1 \mu\text{m}$ ) carrier concentration decreases and band-gap PL shifts to higher energies indicating the origination of compressive strain.

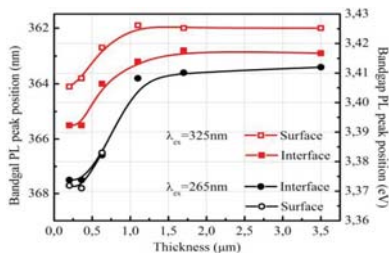


Fig. 1. PL bandgap peak position at  $\lambda=265 \text{ nm}$  and  $\lambda=325 \text{ nm}$  excitation dependence on thickness of undoped GaN samples of different growth. Lines are guides for eyes.

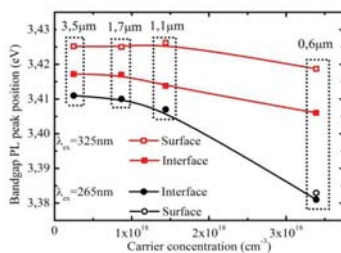


Fig. 2 PL bandgap peak position at  $\lambda=265 \text{ nm}$  and  $\lambda=325 \text{ nm}$  excitation dependence on carrier concentration of overgrown undoped GaN samples of different different growth stage. Lines are guides for eyes.

- [1] A. Krost, A. Dadgar, Schulze, J. Bläsing, G. Strassburger, R. Clos, A. Diez, P. Veit, T. Hempel, *J. Cryst. Growth* **275** 209 (2005).
- [2] J. Xie, S. Mita, L. Hussey, A. Rice, J. Tweedie, LeBeau, R. Collazo Z. Sitar, *Appl. Phys. Lett.* **99** 141916 (2011).
- [3] K. J. Lethy, P. R. Edwards, C. Liu, P. A. Shields, D. W. E. Allsopp R. W. Martin, *Semicond. Sci. Technol.* **27** 085010 (2012).
- [4] F. C. Wang, C. L. Cheng, Y. F. Chen, C. F. Huang, C. C. Yang, *Semicond. Sci. Technol.* **22** 896 (2007).
- [5] I. H. Lee, J. J. Lee, P. Kung, F. J. Sanchez M. Razeghi, *Appl. Phys. Lett.* **74** 102 (1999).
- [6] I. H. Lee, I. C. Choi, C. R. Lee, E. J. Shin, D. Kim, S. K. Noh, S. J. Son, K. Y. Lim H. J. Lee, *J. Appl. Phys.* **83** 5787 (1998).

## DLTS SPECTROSCOPY OF TECHNOLOGICAL AND RADIATION DEFECTS IN Si STRUCTURES

Darius Bajarūnas, Eugenijus Gaubas

Institute of Applied Research. Vilnius University, Saulėtekio av. 9-III, LT-10222 Vilnius, Lithuania  
[darius.bajarunas@ff.stud.vu.lt](mailto:darius.bajarunas@ff.stud.vu.lt)

Silicon detectors for experiments in high luminosity colliders should tolerate high energy hadron irradiations of fluences up to  $10^{16}$  n/cm<sup>2</sup>. However, the intense hadron irradiations induce considerable radiation defect densities that drastically affect the functional parameters of particle detectors, i.e. the leakage current is increased while full depletion voltage and charge collection efficiency are reduced [1]. Also, point defects, especially metallic impurities, detrimentally change performance of solar cells [2]. Therefore, it is important to study the role of technological and radiation induced defects in the deterioration of diodes electrical parameters.

In this work, parameters of deep traps were examined to identify the defects in Magnetic Czochralski (MCz) Si material based particle detectors and solar elements. The solar elements under research were produced by enterprise “Precizika – MTC”. The CERN standard MCz Si pin diodes were irradiated by reactor neutrons using fluences in the range of  $10^{12}$ - $10^{16}$  cm<sup>-2</sup>. Spectra of defects attributed carrier traps have been studied by deep level transient spectroscopy (DLTS) [3] technique and employing a commercial HERA–DLTS System FT 1030 spectrometer. It has been revealed that C-DLTS is not applicable for samples exposed to neutron fluences higher than  $10^{13}$  n/cm<sup>2</sup>. This is due to the fact that complete compensation of shallow dopants by radiation induced traps leads to a fully depleted structure even in the absence of external bias. For samples irradiated with higher fluences, current optical DLTS (I-ODLTS) regime has been applied by employing the first (1064 nm) and the second (532 nm) harmonics of Nd: YAG laser for trap filling by photo-excited carriers. Vacancy related traps were identified in a broad range of temperatures and carbon related defects were observed in the low temperature range in MCz pin diodes. The spectra containing multiple peaks have been analyzed by varying duration of excitation pulses. Analysis of DLTS spectra in “Precizika – MTC” solar elements enabled us to identify the transitional metal impurities, such as Cu and Ni. The range of densities of the technological and radiation defects covering values from  $10^9$  to  $10^{15}$  cm<sup>-3</sup> has been evaluated for the reliable DLTS spectroscopy of Si structures fabricated by different growth technologies. However, this range of trap densities can be covered by combining different measurement regimes as C- and I-ODLTS, installed within HERA–DLTS System FT 1030 spectrometer.

- 
- [1] B. J. Baliga, *Fundamentals of Power Semiconductor Devices*. (Springer Science Business Media, LLC, New York, 2008).
  - [2] Gianluca Colletti, *Impurities in silicon and their impact on solar cell performance*, dissertation, Alkmaar (2011).
  - [3] P. Blood and J.W. Orton, *The Electrical Characterization of Semiconductors: Majority Carriers and Electron States* (Academic Press Inc., San Diego, 1992).

## Behaviour of acoustic beam generated from leaky surface wave upon reflection in YX-LiTaO<sub>3</sub>

Jaroslavas Belovickis, Romualdas Rimeika

Vilnius University, Faculty of Physics, Department of Radiophysics  
jaroslavas.belovickis@ff.stud.vu.lt

The non-specular reflection of a leaky surface acoustic wave radiated beam from the surface of piezoelectric lithium tantalate crystal has been investigated using an acoustoelectric and acousto-optic technique. The Schoch-type beam displacement upon reflection strongly depends on whether the surface is free or metalized. This effect is attributed to the excitation (on the reflecting surface) of the leaky surface wave [1, 2].

The experimental technique is shown in Fig. 1, where interdigital transducers (IDTs) with a period of 40  $\mu\text{m}$  and 20 electrode pairs were deposited on the top surface of the sample. Laser light with a wavelength of 633 nm from the HeNe laser was directed onto the sample surface. The schematics for parallel polarization ( $E_{\parallel}$ ) of the incident laser light is depicted in the case (a) and for the perpendicular ( $E_{\perp}$ ) in the case (b). As a result of anisotropic light diffraction by the leaky surface acoustic wave radiated bulk acoustic wave, the incident light beam was split into transmitted ( $I_t$ ) and diffracted ( $I_d$ ) beams with mutually orthogonal polarizations. Indices  $I_i$  and  $I_r$  denote the incident and reflected light beams, respectively.

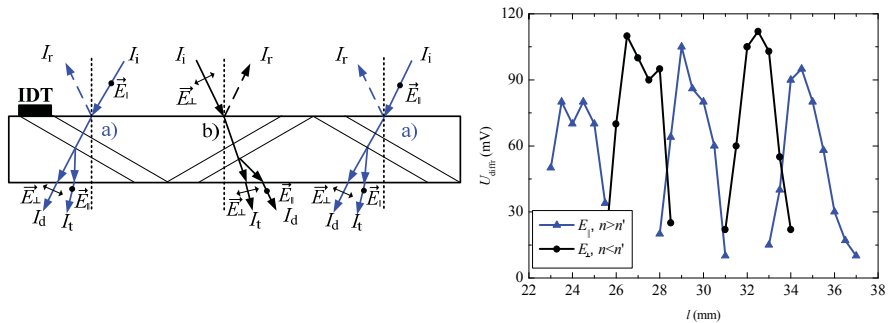


Fig. 1. Configurations of light diffraction for the parallel (a), perpendicular incident light beam polarizations (b) and its dependence of diffracted light signal amplitude on the probing light beam position along the crystal X-axis.

This experiment shows that the acoustic wave reflection from the surface along the substrate X axis is approximately equal for both cases. As seen, the value of the diffracted angle depends on the incident light beam polarization. The extraordinary refractive index for lithium tantalate crystal (2,18) is bigger than the ordinary (2,175). If the phase matching condition is satisfied the peaks of diffracted light signal obtained from the case of a parallel incident light polarization (blue curve) are located closer to the interdigital transducer because of Snell's law. The case of perpendicular light polarization is performed along the reflected BAW from the crystal sample bottom.

A small variation of the diffracted signal amplitude is attributed to negligible attenuation of the bulk acoustic beam along the crystal. This surface wave is a leaky wave; hence, it re-radiates the energy back into the crystal bulk as it travels along the crystal surface. The dependence of diffracted light intensity versus the light beam position yields the acoustic beam intensity distribution along the substrate X axis.

In conclusion, the reflection of leaky surface wave generated acoustic beam from the non-conducting surface of piezoelectric lithium tantalate crystal was investigated. It has been shown that the beam reflected from the free crystal surface is displaced forward as compared to specular reflection. This shift is attributed to excitation of the surface wave and consequent energy re-radiation into the crystal bulk. Such a re-radiation is considerably stronger on the conducting surface leading to the significantly smaller beam shift. The sensitivity of wave reflection to the surface conductivity offers the possibility of implementation of leaky acoustic wave based sensors responding to the changes in surface condition due to various external factors.

[1] R. Rimeika, A. Sereika and D. Čiplys, Appl. Phys. Lett. **98**, 052909 (2011).

[2] R. Rimeika, J. Belovickis and D. Čiplys, Appl. Phys. Lett. **102**, 031601 (2013).

## EPR SPECTROSCOPY OF NEUTRON IRRADIATED STRUCTURES

Paulius Cicėnas, Tomas Čeponis, Eugenijus Gaubas, Vidmantas Kalendra

Department Institute of Applied Research, Vilnius University, Saulėtekio Ave. 9-III, LT-10222 Vilnius, Lithuania  
[paulius.ccs@gmail.com](mailto:paulius.ccs@gmail.com)

High energy radiation interacts with material and creates various types of damage such as ionisation and displacement damage. Thereby different types of defects are introduced. Displacement lattice damage in semiconductor materials makes a significant impact on their electrical properties, through creation of the stable radiation defects, due to which several deep levels in the band -gap appear. Consequently, the important material parameters such as free carrier mobility and density, resistivity  $\rho$  and carrier generation ( $\tau_g$ )/recombination ( $\tau_r$ ) lifetimes are modified by displacement damage [1]. Thus it is extremely important to evaluate the exposed doses correctly.

In this work, the electron spin resonance (ESR/EPR) spectroscopy has been applied to evaluate different type particle irradiation doses by using the alanine sensors. The spallator 25 MeV neutrons irradiated alanine pallets have been examined. EPR spectroscopy is based on absorption of microwave radiation by an unpaired spin electrons within the sample placed in a magnetic field [2]. Moreover, barrier evaluation by linearly increasing voltage (BELIV) technique has been employed to evaluate an impact of deep traps on electrical characteristics of CERN standard Si particle detectors irradiated in the same environment as the alanine sensors. BELIV technique is based on measurements and analysis of barrier capacitance current transients by applying the linearly increasing voltage pulse [3].

It has been shown that EPR signal changes, being proportional to the density of free radicals in the irradiated alanine sensors, correlate well with that of BELIV response components, namely, with generation current increase and barrier capacitance diminishing in CERN standard Si particle detectors. It has been obtained that even small irradiation fluences of either spallator or nuclear reactor neutrons induce a decrease of the effective doping density in the base region of Si particle detectors, made of large resistivity Si materials. This leads to a crucial degradation of the particle detector operational characteristics. EPR spectroscopy appears to be a useful tool to evaluate radiation doses and density of free radicals created by irradiations in the alanine sensors. EPR spectroscopy of irradiated alanine enables one to evaluate the structural arrangement of material modifications containing free radicals.

---

[1] C. Claeys, E. Simoen, *Radiation Effects in Advanced Semiconductor Materials and Devices*, (Springster – Verlag Berlin Heidelberg New York, 2002).

[2] M.Brustolon, E. Giamello, *Electron Paramagnetic Resonance: A Practitioner's Toolkit* (John Wiley & Sons, Inc, USA, 2009).

[3] E. Gaubas, T. Čeponis, J. Kusakovskij, and A. Uleckas. Barrier evaluation by linearly increasing voltage technique applied to Si solar cells and irradiated pin diodes. *ISRN Materials Science* **2012**, Article ID 543790 (2012).

# ELECTRICAL PROPERTIES OF $\text{Li}_{4x}\text{Ti}_{1-x}\text{P}_2\text{O}_7$ ( $x = 0.06, 0.1$ ) COMPOUND CERAMICS

Pranciškus Dobrovolskis, Vilma Venckutė

Department of Physics, Vilnius University, Lithuania  
pranciškus.dobrovolskis@ff.stud.vu.lt

$\text{LiVPO}_7$  and  $\text{TiP}_2\text{O}_7$  are reported to be active cathode materials for applications in lithium secondary batteries.  $\text{TiP}_2\text{O}_7$  belongs to cubic symmetry with the  $\text{Pa}\bar{3}$  space group. Its lattice is built up from corner sharing  $\text{TiO}_6$  octahedra and  $\text{P}_2\text{O}_7$  groups which form large tunnels for migration of lithium cations [1]. The purpose of this work is to investigate electrical properties of  $\text{TiP}_2\text{O}_7$  compound when lithium is initially inserted into the host compound during the synthesis.

The powder of  $\text{Li}_{4x}\text{Ti}_{1-x}\text{P}_2\text{O}_7$  ( $x = 0.06, 0.1$ ) compounds were synthesized by solid state reaction. X-ray diffraction (XRD) analysis shows that these compounds are isostructural with  $\text{TiP}_2\text{O}_7$  compound at room temperature. The results of XRD analysis are presented in Table 1.

Table 1. Summary of XRD analysis results of  $\text{Li}_{4x}\text{Ti}_{1-x}\text{P}_2\text{O}_7$  ( $x = 0.06, 0.1$ ) compounds.

Compound	Lattice parameters $a, \text{\AA}$	$V, \text{\AA}^3$	Symmetry (space gr.)	Formula units Z	Theoretical density $\rho_{\text{XRD}}, \text{g/cm}^3$
$\text{Li}_{0.24}\text{Ti}_{0.94}\text{P}_2\text{O}_7$	23.6247	13186	cubic	108	3.00
$\text{Li}_{0.4}\text{Ti}_{0.9}\text{P}_2\text{O}_7$	23.6245	13185	( $\text{Pa}\bar{3}$ )		2.99

The powders were pressed into pellets. The pellets of compounds with different stoichiometric factor  $x = 0.06$  and  $0.1$  were sintered at 1373 and 1273 K temperature respectively. Two different sintering durations of 1 and 5 hours were chosen. The relative densities of the sintered ceramics were from 74 to 86%.

Electrical properties (dielectric permittivity, tangent losses and electrical conductivity) of the ceramics were investigated by two probe methods in two frequency ranges:  $10 - 2 \cdot 10^6$  Hz and  $10^6 - 3 \cdot 10^9$  Hz [2]. The anomalies of electrical conductivity are observed and lead to the changes of activation energy of electrical conductivity. The temperature dependence of electrical conductivity is showed in Fig.1.

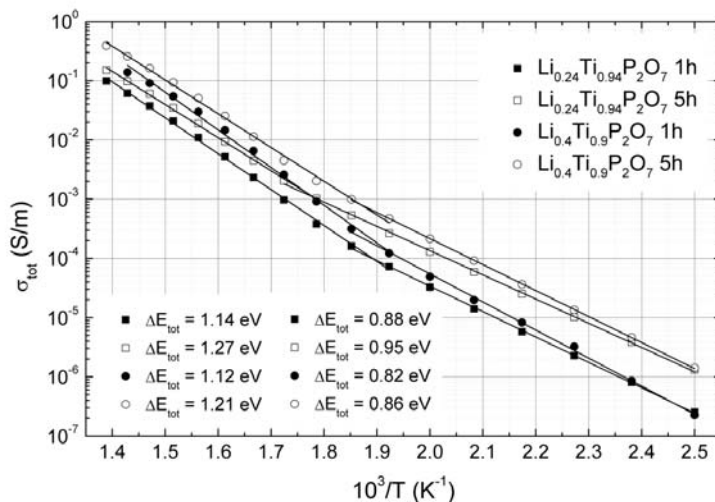


Fig. 1 The electrical conductivity dependence on temperature

- [1] Y. Uebou, S. Okada, M. Egashira, J.-I. Yamaki, Synthesis, structures, and electrochemical characteristics of pyrophosphates, The Reports of Institute of Advanced Material Study, Kyushu University **15** 57-61 (2001).
- [2] A. Kežionis, E. Kazakevičius, T. Šalkus, A. Oriukas, Broadband high frequency impedance spectrometer with working temperatures up to 1200 K, Solid State Ionics **188**, 110-113 (2011).

## MID-INFRARED PHOTOLUMINESCENCE MAPPING OF AlGaInAsSb/GaInAsSb QW EPITAXIAL STRUCTURES FOR NEXT GENERATION TYPE-I GaSb LASER DIODE DEVELOPMENT

Edgaras Dvinelis, Kristijonas Vizbaras, and Augustinas Vizbaras

Brolis Semiconductors UAB, Moletu pl. 73, LT-14259, Vilnius, Lithuania  
[edgaras.dvinelis@brolis-semicon.com](mailto:edgaras.dvinelis@brolis-semicon.com)

Type-I mid-infrared laser diodes based on GaSb have long been a promising material and technology platform for room-temperature laser diodes for the 2-4  $\mu\text{m}$  wavelength range. However, long-wavelength laser diodes required complex materials such as quaternary GaInAsSb or AlGaAsSb and even quinary AlGaInAsSb, which have been reported to be very demanding in terms of epitaxial growth and fabrication technology, in addition to thermal instability, known as the “blue shift” effect and the miscibility gap [1]. In our work, we demonstrate that  $\text{Al}_x\text{Ga}_y\text{In}_{1-x-y}\text{As}_z\text{Sb}_{1-z}$  based materials are in fact very stable and controllable once proper technological conditions are met, and can be applied for type-I laser diode development in the entire 1.8-4.0  $\mu\text{m}$  wavelength range utilizing the intrinsic advantages of the type-I optical transition - high gain and low voltage drop.

The main objective of this work is construction, automatization of photoluminescence (PL) mapping system and characterization of epitaxial layers grown by molecular beam epitaxy (MBE) technique. PL mapping data provides valuable information about transition energy, quality, defect, impurity distribution and homogeneity of epitaxial layer. The data of homogeneity is particularly important for commercial epitaxial layer growth systems because it directly characterizes the compatibility of the active material for large scale production.

PL mapping system which was created in this work can measure and analyze wafers up to 100 mm in diameter in entire 1  $\mu\text{m}$  – 20  $\mu\text{m}$  spectral range. This system uses FTIR spectrometer, Au coated free-space optical setup and stepper motor based precision transition stages. The control and data analysis software was built up using LabView software platform.

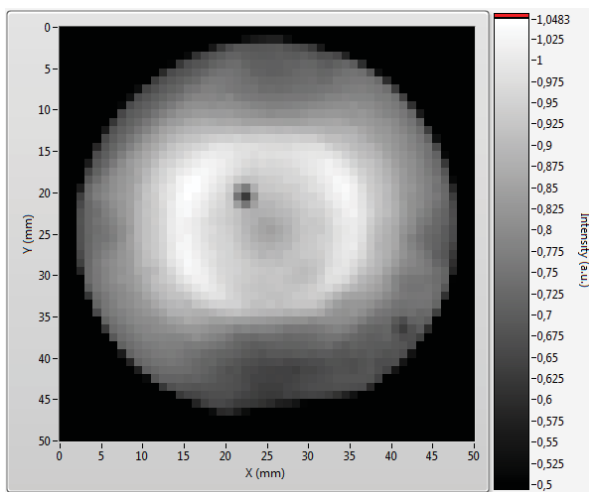


Fig. 1. A room-temperature PL intensity map of GaInAsSb/GaSb single QW structure

In the initial system qualification stage GaSb based bulk and GaInAsSb/AlGaAsSb quantum well structures were investigated. Experimental tests proved system robustness, reliability and performance for the intended application purposes. Numerous AlGaAsSb epitaxial structures were investigated after system qualification stage, for example PL intensity map of GaInAsSb/GaSb single quantum well (QW) structure is shown in Fig. 1. This PL intensity map and data mapping of other PL parameters (wavelength, FWHM) provide us valuable information about homogeneity of the epitaxial layer grown by MBE technique. Our experiments revealed that PL peak wavelength homogeneity across the wafer diameter is superior having less than 0.4% deviation providing great promise for industrial scale applications of the investigated structures.

[1] O.Dier et al., Appl. Phys. Lett., 86, 151120, (2005).

# SPECTROSCOPIC ELLIPSOMETRY OF $\text{GaBi}_x\text{As}_{1-x}$

Adomas Eikevičius, Saulius Tumėnas

Semiconductor optics laboratory, Center for Physical Sciences and Technology, Vilnius, Lithuania  
[a.eikevicius@gmail.com](mailto:a.eikevicius@gmail.com)

Spectroscopic ellipsometry is a leading optical technique for the direct investigation of the dielectric function of solids. Spectroscopic ellipsometry measures the change in polarized light upon light reflection on a sample. When linearly polarized light is reflected by a sample surface, its polarization state changes to an elliptical polarization. Ellipsometry measures two parameters of the polarization,  $\Psi$  and  $\Delta$ , which represent the amplitude ratio  $\Psi$  and the phase difference  $\Delta$  for p- and s-polarized light waves [1]. There are several commercially available spectroscopic ellipsometry instruments, operating at given spectral ranges. However, for detailed studies of optical transitions in semiconductors, the standard specifications usually are not sufficient, one, e.g., needs the wide spectral range, the high spectral resolution and possibility for low-temperature measurements.

In this work we present home-made spectroscopic ellipsometry setup based on rotating analyzer configuration (RAE) and operating in the vertical optical configuration. The principal scheme of the RAE ellipsometer is presented in Figure 1. The key parameters of the RAE ellipsometer are the following: the spectral range 210 – 3000 nm with step of 0.01 nm, the angle of incidence in the range of  $10^\circ - 90^\circ$  with an accuracy of  $0.01^\circ$ , and the  $\sigma_\Psi=0.09^\circ$  and  $\sigma_\Delta=0.16^\circ$  registration precision of the ellipsometric parameters, as determined in straight through configuration.

The spectroscopic ellipsometry setup was used for studies of an optical response of  $\text{GaBi}_x\text{As}_{1-x}$  semiconductor. The ability to tune energy spectrum of GaBiAs through careful control of the alloy composition makes the semiconductor to be a perspective candidate for various optoelectronic applications, such as the long-wavelength emitters and detectors as well as the spintronic-related devices. The  $\text{GaBi}_x\text{As}_{1-x}$  samples were grown in a solid-state MBE system [2] on a low-temperature GaAs buffer layer, deposited on a semi-insulating (100) GaAs substrate. The Bi content varied from 0 (pure GaAs) to 13% ( $x = 0.013$ ). The ellipsometric measurements show that the interband optical transitions at various critical points depend on Bi content. The incorporation of dilute concentration of Bi into GaAs induces a strong reduction of the band gap ( $\sim 60$  meV per  $x = 0.01$ ) and enhances the spin-orbit splitting in accord with previous results [3].

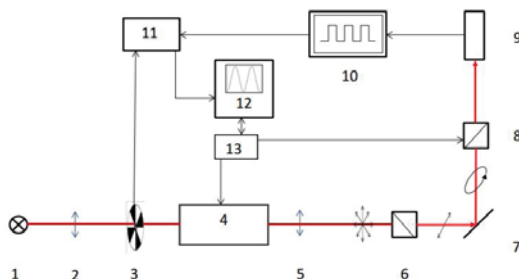


Fig. 1. A scheme of rotating-analyzer ellipsometer RAE, which consists of light source (1), lenses (2, 5), chopper (3), monochromator (4), polarizer (6), sample (7), rotating analyzer (8), detector (9), oscilloscope (10), lock-in amplifier (11), computer (12), and controller (13).

- [1] R.M.A. Azzam, N.M. Bashara, *Ellipsometry and Polarized Light* (Amsterdam: North-Holland, 1977).
- [2] K. Bertulis, A. Krotkus, G. Aleksejenko, V. Pačebutas, R. Adomavičius, G. Molis, S. Marcinkevičius, GaBiAs: A material for optoelectronic terahertz devices, *Appl. Phys. Lett.* **88**, 201112 (2006).
- [3] S. Tumėnas, V. Karpus, K. Bertulis, H. Arwin, Dielectric function and refractive index of  $\text{GaBi}_x\text{As}_{1-x}$  ( $x = 0.035, 0.052, 0.075$ ), *Phys. Status Solidi (C)* **9**, 1633-1635 (2012).



# DIELECTRIC PROPERTIES OF $\text{Ba}_2\text{NdFeNb}_{3,7}\text{Ta}_{0,3}\text{O}_{15}$ SOLID SOLUTION

Dainius Gabrielaitis<sup>1</sup>, Marjorie Albino<sup>2</sup>, Michaël Josse<sup>2</sup>, Martynas Kinka<sup>1</sup>, Vytautas Samulionis<sup>1</sup>, Robertas Grigalaitis<sup>1</sup>, Mario Maglione<sup>2</sup>, Jūras Banys<sup>1</sup>

<sup>1</sup> Faculty of Physics, Vilnius University, Lithuania

<sup>2</sup> CNRS, Université de Bordeaux, ICMCB-CNRS, France  
dainius.gabrielaitis@ff.stud.vu.lt

Tetragonal Tungsten Bronze (TTB) structural family attracted much attention in recent years. It is one of the largest oxygen octahedral ferroelectric families next to the ferroelectric perovskites [1]. Three types of open channels that develop within its octahedral framework give rise to its unique properties. More open crystalline network makes TTB a more flexible material. A wide range of substitutions available in TTB framework enables scientists to synthesize many different compounds. This feature makes it a better candidate (as compared to perovskites) in search of relaxors, ferroelectrics and even multiferroics.

$\text{Ba}_2\text{NdFeNb}_{3,7}\text{Ta}_{0,3}\text{O}_{15}$  ceramic under investigation here belongs to TTB structural family. Dielectric measurements of complex permittivity upon heating and cooling were performed. During measurements temperature rate was maintained around 1K/min. Silver paste was applied to the specimens for better contacts. For measurements at lower frequencies (20 Hz - 1 MHz) capacitance bridge method was used. 1 MHz - 3GHz results were obtained with coaxial line and "Agilent" vector network analyser. Waveguides and scalar network analysers by "Elmika" were used for the measurements in 8 GHz - 37 GHz frequency range.

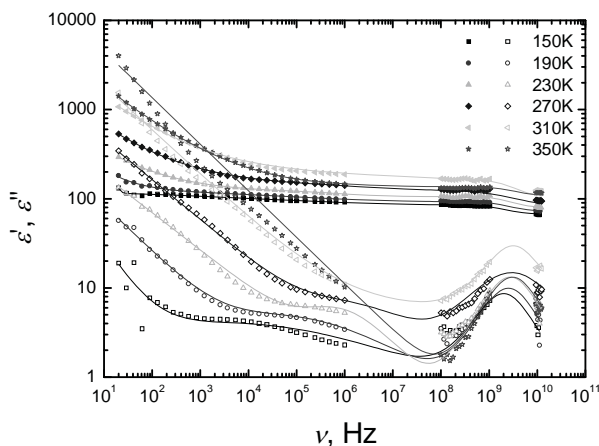


Fig.1 Frequency dependence of complex dielectric permittivity upon heating. Solid lines show approximation with Cole-Cole equation.

Obtained results show ferroelectric phase transition at 315 K while heating. On cooling a huge shift of permittivity maxima is observed. Permittivity dispersion at lower temperatures indicates appearance of a second phase. Wide hysteresis loop ranging over 50 K is also seen. Such wide hysteresis loop is unusual however similar results were reported for  $\text{Ba}_2\text{NdFeNb}_4\text{O}_{15}$  compound [2]. The main interest is to find explanation for observed behaviour upon heating and cooling which could be done by examining frequency dependence of complex permittivity (Fig. 1). It clearly shows two separate, temperature dependent processes. Approximation with Cole-Cole equation and obtained parameters will be used to explain undergoing processes.

[1]. R. Guo, H. T. Evans, A. S. Bhalla, *Crystal Structure Analysis of Ferroelectric Tetragonal Tungsten Bronze  $\text{Pb}_{0.59}\text{Ba}_{0.40}\text{Nb}_{2.03}\text{O}_6$* , *Applications of Ferroelectrics*, 241 - 244 vol 1, 1996.

[2]. J. Banys, S. Bagdzevicius, M. Kinka, V. Samulionis, R. Grigalaitis, E. Castel, M. Josse, M. Maglione. *Dielectric Studies Of  $\text{Ba}_2\text{Pr}_2\text{Nd}_{1-3}\text{FeNb}_4\text{O}_{15}$  Ceramics*, *Applications of Ferroelectrics (ISAF/PFM)*, International Symposium on Piezoresponse Force Microscopy and Nano scale Phenomena in Polar Materials, 2011.

## PROPERTIES OF LANTHANUM, NIOBIUM, MANGANESE DOPED BARIUM TITANATE CERAMICS PRODUCED FROM NANOPOWDERS

Viktorija Jankauskaitė<sup>1</sup>, Robertas Grigalaitis<sup>1</sup>, Jūras Banys<sup>1</sup>, Mirjana Vijatović Petrović<sup>2</sup>,  
Jelena Bobić<sup>2</sup>, Biljana Stojanović<sup>2</sup>

<sup>1</sup>Faculty of Physics, Vilnius University, Sauletekio al. 9/3, Vilnius, Lithuania

<sup>2</sup>Institute for Multidisciplinary Research, Belgrade University, Kneza Višeslava 1, Belgrade, Serbia  
[viktorija.jankauskaite@ff.stud.vu.lt](mailto:viktorija.jankauskaite@ff.stud.vu.lt)

Barium titanate ( $\text{BaTiO}_3$ ) is the first ferroelectric ceramics and a good candidate for a variety of applications due to its excellent dielectric, ferroelectric and piezoelectric properties [1]. Doping of  $\text{BaTiO}_3$  with ions having a similar ionic radius could lead to structure and microstructure changes and furthermore modification of dielectric and ferroelectric properties. The possibility of easy substitution is enabled due to the capability of the perovskite structure to host different sized ions in the  $\text{BaTiO}_3$  lattice. Experimental process was given in detail in previous reports [2]. Doped barium titanate has found wide application in semiconductors, PTC thermistors, ultrasonic transducers and piezoelectric devices.

The dielectric properties of  $\text{BaTiO}_3$  with 0.3 mol% La and 0.05 mol% Mn (BTLM) and  $\text{BaTiO}_3$  with 0.8 mol% Nb and 0.1 mol% Mn (BTNM) were investigated in a broad frequency (20 Hz – 1 GHz) and temperature (100 K – 500 K) range. The investigations showed that the temperature dependence of complex dielectric permittivity is similar to pure barium titanate, however all temperatures of phase transitions differ in both materials.

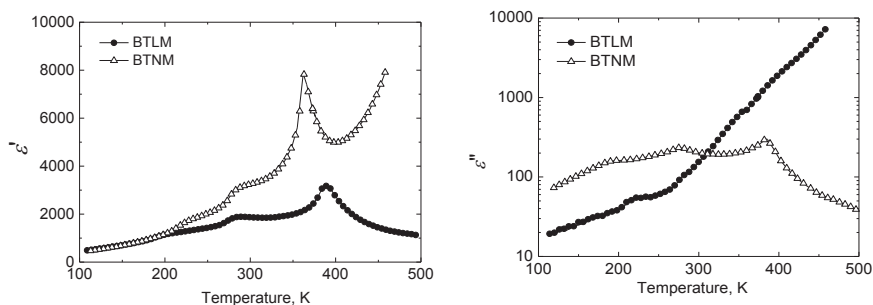


Figure 1. Temperature dependences of complex dielectric permittivity of  $\text{BaTiO}_3$  doped 0.3% La, 0.05% Mn (BTLM) and  $\text{BaTiO}_3$  doped 0.8% Nb, 0.1% Mn (BTNM) at frequency 2.6 kHz.

### References

- [1] Vijatović M.M., Bobić J.D., Stojanović B.D., *History and challenges of barium titanate* **155**, 1-5 (2008).
- [2] Stojanovic B.D., Zaghet M.A., Foschini C.R., Varela J.A., *Ferroelectrics* **270**, 1-10(2002).

# Investigation of thermally stimulated conductivity and photoconductivity spectra in TlBr

Vytautas Janonis

Semiconductor Physics Department and Institute of Applied Research, Vilnius University, Saulėtekio Ave. 9-III, LT-10222, Vilnius, Lithuania  
[Vytautas.Janonis@ff.stud.vu.lt](mailto:Vytautas.Janonis@ff.stud.vu.lt)

Thallium bromide is a promising material, in the production of low noise, high resolution X- and  $\gamma$ - ray detectors, which could work at room temperature. Main essential properties of thallium bromide are its wide band gap (2.68 eV), high density (7.56 g/cm<sup>3</sup>) and high atomic numbers (Tl: 81 and Br: 35) [1,2]. These properties ensure high photon stopping efficiency, which is required for a good quality detector. Main problems in using TlBr detectors are associated with the required very high quality of material [3], also by the degradation which is caused by the process of ionic conductivity in the crystal [1]. Moreover, thallium bromide is hygroscopic, and Tl is toxic, therefore cannot be left in a room environment [3].

The aim of this research was to investigate photoelectrical properties of thallium bromide sample. Dark and photocurrent dependencies were investigated at different temperatures from 80 to 300 K. The photoconductivity spectra were measured at different temperatures.

After investigating current-voltage (IV) characteristics at different temperatures, their ohmic behavior was confirmed, therefore it was stated that influence of contact potential barriers was negligible.

Temperature dependencies of the dark current and photocurrent upon band to band light excitation were measured. Close to the room temperature the value of the thermal charge generation energy of 1,022 eV was identified from the dark current measurements. When measuring photocurrent, effect of the thermal quenching of photoconductivity was observed between 110 and 190 K.

Thermally stimulated currents (TSC) were measured in the dark and after exciting the crystal for 5, 20 and 50 minutes with light at its photoconductivity maximum, so the energy levels would be filled. Increase in current was observed between 100 and 200 K. No obvious maxima were observed, therefore it was stated that TSC was caused not by one, but by several dispersed energy levels, which will be investigated during further research.

From photoconductivity spectra two defect levels with photoionisation energies at 2.2 and 1.8 eV were identified. Furthermore increase in photocurrent with decreasing the temperature was observed.

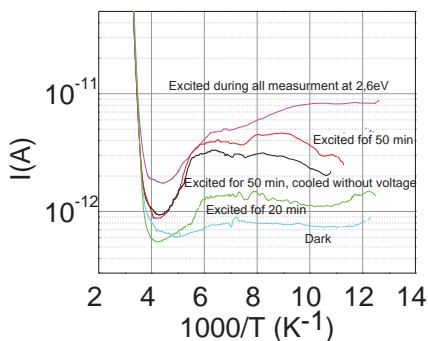


Fig. 1. Dependence of the thermally stimulated current on temperature.

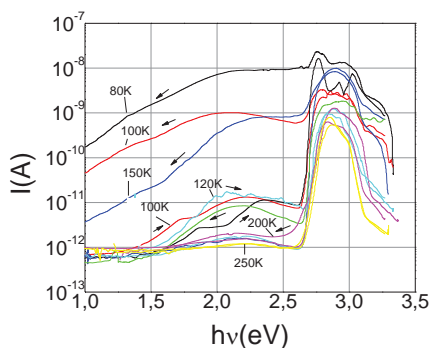


Fig. 2. Photoconductivity spectra.

- [1] V. Kažukauskas, A. Ziminskij, N. Vainorius, V. Gostilo, M. Shorohov and V. Bozhko. Long-Lasting Current Transient Phenomena in TlBr, Proceedings of the 14th International Symposium Ultrafast Phenomena in Semiconductors, Vilnius 2010.
- [2] J. Vaitkus, J. Banys, V. Gostilo, S. Zatuloka, A. Mekys, J. Storasta, A. Zindulis. Influence of electronic and ionic processes on electrical properties of TlBr crystals. Nucl. Instr. Meth. Phys. Res. A, 546, pp. 188–191, 2005.
- [3] Vasilij Kozlov *TlBr raw material purification, crystal growth, annealing, detector fabrication and characterisation for gamma-ray detector applications*. Academic dissertation 2010.

## RECOMBINATION CHARACTERISTICS DEPENDENT ON TECHNOLOGICAL REGIMES OF GaN AND DIAMOND FORMATION

Arnoldas Jasiūnas, Eugenijus Gaubas

Institute of Applied Research, Vilnius University, Saulėtekio Ave. 9-III, LT-10222 Vilnius, Lithuania  
[arnoldasj@gmail.com](mailto:arnoldasj@gmail.com)

Si based devices are reaching their theoretical limits because of recent achievements in material science, thus, wide band gap semiconductors gain more attention in modern semiconductor device industry. Considering their superior electric, thermal characteristics and also mechanical stability such wide band gap semiconductors as diamond and GaN are promising candidates to be used for optoelectronics as well as fabrication of high power and high frequency devices [1]. Also, their radiation hardness makes them perspective to be used as a material in future high-luminosity particle colliders and desirable for radiation detectors [2, 3]. However, the impact of the formation technological regimes to quality and defect density of grown samples is not ascertained. Moreover, attempts to manufacture diamond pn junctions encounter the issues related to a lack of shallow dopants.

The lifetime of excess charge carriers is one of the major sample material parameters. Study of the dynamics of non-equilibrium charge carriers through the radiative and non-radiative (via the defect states in the band gap) recombination channels enables ones to characterize the samples under test and to optimize their formation regimes. In this work, charge carrier dynamics is evaluated by the non-invasive contactless microwave probed photoconductivity transient technique (MW-PC) combined with the confocal microscopy of sample surfaces. Additionally, the electron spin resonance (ESR/EPR) spectroscopy is employed in this research in order to determine the main defects and their types in the diamond samples, based on the analysis of defects ascribed structure symmetry and spin densities.

Excess carrier decay transients have been investigated in metal-organic chemical vapour deposition (MOCVD) grown undoped GaN epi-layers on sapphire substrates with different growth temperatures (900-1100 °C) in the reactor chamber. Also these measurements were carried out on the high-pressure high-temperature (HPHT) grown diamond single crystals, cut into 245-280  $\mu\text{m}$  thick samples oriented perpendicularly to  $\{100\}$  direction.

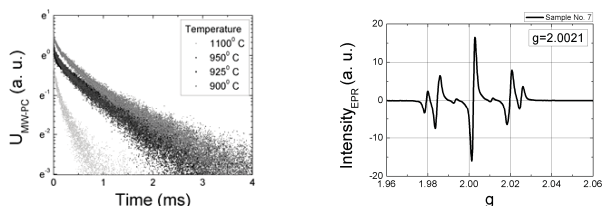


Fig. 1. Asymptotic relaxation of MW-PC in GaN samples (a) and an EPR spectrum of the nitrogen contaminated diamond sample (b).

It has been revealed that in GaN recorded transients show a two-componential decay shape. Initial fast component of the MW-PC transients is ascribed to carrier decay through radiative recombination processes in crystalline material while the asymptotic stretched-exponent relaxation can be associated with the carrier transport within the dislocation net at the micro-crystal boundaries. MW-PC transient studies of the HPHT grown diamond samples have shown rather short recombination lifetimes. The single substitutional nitrogen atom in the diamond crystal lattice site has been identified as the main extrinsic crystallographic defect evaluated by comparing the acquired EPR spectra with those given in literature [4]. Considering both the data of the MW-PC transients and of confocal microscopy, the correlation between radiative, non-radiative recombination probabilities and concentration of various defects introduced during formation of the diamond single crystal can be evaluated. Variations of the excess charge carrier lifetime and intensities of photoluminescence spectral bands, respectively to a position of the sample in the diamond single crystal and the in-plane position of the measurement in the sample correlate well with the type and density of nitrogen defects identified.

- 
- [1] S. Koziumi, K. Watanabe, M. Hasegawa, H. Kanda, Ultraviolet Emission from a Diamond pn Junction, *Science* **292** (6), 1899-1901 (2001).  
[2] A. J. Blue, *New materials and processes for radiation detection*, doctoral dissertation (2005).  
[3] J. Grant, A. Blue, J. Vaitkus, E. Gaubas et al., GaN as a radiation hard particle detector, *Nucl. Instr. and Meth.* **576**, 60-65 (2007).  
[4] W. V. Smith, P. P. Sorokin, I. L. Gelles, G. J. Lasher, Electron-Spin Resonance of Nitrogen Donors in Diamond, *Physical Review* **115** (6), 1546-1553 (1959).

## ALKYL CHAIN LENGTH EFFECT ON THE FLUORESCENCE PROPERTIES OF TRIPHENYLAMINE DERIVATIVES

J. Jovaišaitė<sup>1</sup>, S. Raišys<sup>1</sup>, K. Kazlauskas<sup>1</sup>, R. Reghu<sup>2</sup>, J. V. Gražulevičius<sup>2</sup>, S. Juršėnas

<sup>1</sup>Institute of Applied Research, Vilnius University, Saulėtekio 9-III, LT-10222 Vilnius, Lithuania

<sup>2</sup>Department of Organic Chemistry, Kaunas University of Technology, Radvilėnų 19, LT-50254 Kaunas, Lithuania  
[justina.jovaisaite@ff.stud.vu.lt](mailto:justina.jovaisaite@ff.stud.vu.lt)

Triphenylamine (TPA) derivatives have been widely investigated for almost two decades because of their excellent thermal and electrochemical stability, electron donating ability and optoelectronic properties.[1] Inherently twisted molecular structure of the TPA derivatives allows formation of the functional amorphous layers by various techniques, such as solution casting or vacuum evaporation. Owing to their superior charge transport and good emission properties the compounds are considered as multifunctional for organic light emitting diode (OLED) application.

The current work covers optical studies of new TPA derivatives containing alkyl chains of different length. Influence of the alkyl chain length on the fluorescence properties of TPA compounds is investigated in dilute tetrahydrofuran (THF) solutions as well as in neat solid films. Additionally, the properties of the TPA-based nanoaggregates formed in aqueous solutions by precipitation method were assessed. Various characterization techniques such as absorption and fluorescence spectroscopy, fluorescence quantum yield and fluorescence lifetime were employed in determining optical properties of the TPA derivatives and nanoaggregates.

The obtained results indicated that different alkyl chain length has almost no effect on the optical properties of the TPA derivatives in dilute solutions, where intermolecular interactions are absent. In contrast, fluorescence and absorption spectra, quantum yields and lifetimes of the solid films of the TPA derivatives were significantly influenced by different alkyl chain length signifying importance of molecule packing. Large intermolecular separation, and thus, reduced intermolecular interaction for the compounds bearing long alkyl chains ( $-C_{12}H_{25}$  and  $-C_{10}H_{21}$ ) allowed maintaining optical properties similar to those found in solution. Estimated fluorescence quantum yields for these derivatives in solid films were about twice as low (~33%) as compared to those in solutions, whereas the quantum yields for the compounds having short alkyl groups were reduced down to an order of magnitude (~4%). Similarly, the stronger red shift and larger lifetime shortening were obtained for the TPA derivatives with shorter alkyl groups. The fluorescence properties of the TPA nanoaggregates were found to be almost the same as those of the neat solid films. However, nanoaggregates exhibited by a factor of two higher fluorescence quantum yields. Importantly, the nanoaggregates composed of the TPA molecules with the longest ( $-C_{12}H_{25}$ ) chains had the same quantum yield as that in solution. These results suggest that long alkyl chains are capable of inhibiting concentration quenching due to the increased intermolecular separation.

The results also indicate the TPA derivatives under study possess multifunctional properties, which might be very attractive for OLED applications.

---

[1] Haijian Xia, Jiating He, Bin Xu, Shanpeng Wen, Yaowen Li, Wenjing Tian, *A facile convergent procedure for the preparation of triphenylamine-based dendrimers with truxene cores*, Tetrahedron 64, 5736–5742 (2008)

# THIN DIELECTRIC FILM LOADING EFFECT ON PLASMONS EXCITATION IN PERFORATED METAL FILMS

Vaiva Kaveckytė, Irmantas Kašalynas

Center for Physical Sciences and Technology, A. Goštauto 11, LT-01108 Vilnius, Lithuania

[Vaiva.Kaveckyte@ff.stud.vu.lt](mailto:Vaiva.Kaveckyte@ff.stud.vu.lt), [irmantak@ktl.mii.lt](mailto:irmantak@ktl.mii.lt)

Plasmon related phenomena have been used in the wide range of fields from biosensing to optoelectronics. Opaque metal films with periodically arranged subwavelength size holes demonstrate strongly enhanced light transmission and act as optical filters at certain wavelengths. Change of the dielectric medium near perforated metal film shifts the resonant transmittance peak, which originates due to the surface plasmons excitation by incident light. It was observed that the transmission spectrum of the perforated film depends on the aperture shape and size indicating that localized plasmons excitation must be also considered [1]. In this work we investigate the transmission spectra of the resonant metallic filters in terahertz frequency range. The effect of thin dielectric film loaded on the filter was studied in particular. Results were interpreted in terms of surface and localized plasmons excitation in perforated metal films.

The resonant band-pass filter (see Fig. 1) was fabricated of 30  $\mu\text{m}$  thick free-standing stainless steel film by laser ablation [2]. Cross-shaped apertures had dimensions of 102.3  $\mu\text{m}$  in length, 31.3  $\mu\text{m}$  in width and were spaced with the period of 145.5  $\mu\text{m}$  in area of 1x1  $\text{cm}^2$  equidistantly. The spectra were measured at the incidence angle  $\theta = 10^\circ$  by vacuumed Fourier spectrometer. Two (12 and 50  $\mu\text{m}$  thickness) polyethylene beam splitters were used to cover the frequency range of 14-248  $\text{cm}^{-1}$ . Data was acquired with the resolution of 0.7  $\text{cm}^{-1}$ . For each transmission and reflection spectrum there were measured ten interferograms which were averaged before applying Fourier transform. Obtained spectra were approximated by Lorentz function. Statistical errors of experiment did not exceed 15%.

The transmission spectrum of the sample is shown in Fig. 2. Transmission through the apertures at resonant frequency exceeded 60% of the incident light. The frequency of the peak was measured at  $f_0 = 1.612$  THz and it was dependent on arm length of the cross aperture. Since surface plasmons are confined to the metal-dielectric interface, the change of air medium with any other dielectric should modify the filter performance. For this reason, a 30  $\mu\text{m}$  thickness polyethylene film with  $n = 1.55$  refractive index was attached to the back side of the THz filter (see inset, Fig. 1). This resulted in the transmittance peak red-shift by  $\Delta f_b = 0.029$  THz. A smaller than expected peak red-shift was attributed to small thickness of the dielectric film [3] and weak surface waves excitation in comparison with localized ones [1]. However, attachment of the same dielectric film to the front side of the resonant filter red-shifted the transmittance peak by  $\Delta f_f = 0.121$  THz. Larger change in spectrum was result of the polished front side of the metal film permitting stronger surface waves generation along metal-dielectric interface.

In conclusion, the transmittance spectra of the resonant THz filter loaded with different dielectrics were measured by the Fourier spectrometer. The localized plasmons excitation dominated the transmittance spectrum of the perforated metal film with and without an additional 30  $\mu\text{m}$  thickness dielectric layer. Only dielectric film loading on polished THz filter surface side enabled efficient surface plasmons excitation measured as a large transmittance peak red-shift.

The author V. K. acknowledges support from the Research Council of Lithuania through the student research grant in 2012.

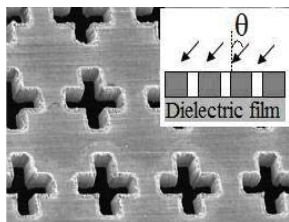


Fig. 1. SEM image of the band-pass filter [2]. Inset: Scheme of dielectric film attached to the back side of the sample in accordance to the incident light geometry.

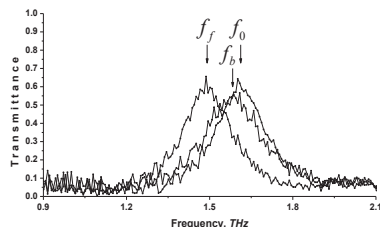


Fig. 2. The transmittance peak of the bare resonant THz filter ( $f_0$ ) and with attached polyethylene film to the back side ( $f_b$ ) and polished front side ( $f_f$ ).

- [1] F. Miyamaru, M. W. Takeda, Coupling between localized resonance and excitation of surface waves in metal hole arrays, *Physical Review B* **79**, 153405 (2009).
- [2] B. Voisiat, A. Biciunas, I. Kasalynas, G. Raciukaitis, Band-pass filters for THz spectral range fabricated by laser ablation, *Applied Physics A* **104**, 953–958 (2011).
- [3] M. Tanaka, F. Miyamaru, M. Hangyo, Effect of thin dielectric layer on terahertz transmission characteristics for metal hole arrays, *Optics Letters* **30**, 1210–1212 (2005).

# Modelling Electrical Characteristics of Bow-tie Diodes

Deividas Kovalenkovas, Tadas Malinauskas

Institute of Applied Research, Vilnius University, Lithuania  
deividas.kovalenkovas@ff.stud.vu.lt

Terahertz (THz) radiation is frequency range between microwave and far infrared of the electromagnetic radiation spectrum. THz radiation can propagate through many dielectric materials, such as clothing and common packaging substances so it is possible to use it for non-destructive and non-ionizing way of imaging and spectroscopy [1]. It could be successfully used in security applications, particularly for explosive, chemical and biological agents detection. In order to inspect agents high sensitivity detectors such as bow-tie detectors must be developed. Bow-tie diode is suitable for sensing of electromagnetic radiation over a broad, 10 GHz–2.52 THz, frequency range at room temperature [2]. The bow-tie diode consists of trapezoidal shape n-doped semiconductor, with metal contacts connected to short and long edges. The device operation is based on non-uniform electron heating due to its asymmetric geometry.

Although bow-tie diode performance was demonstrated experimentally, some of its operation mechanisms still lack a theoretical explanation. So in this work we analysed bow-tie diode electrical characteristics. The device current-voltage characteristics, the spatial distributions of electrical field, carrier density and electron temperature were simulated using TCAD Synopsys semiconductor device modelling software. To account for hot electron effects hydrodynamic transport model [3] was used. Current density in this model was calculated using this equation:

$$J_n = k\mu_n \nabla(n \cdot T_n) + en\mu_n E$$

Simulation results showed asymmetry of I-V characteristic, i.e. that reverse current is smaller than forward current (fig.1). This due to the fact that, electric field distributes in a wider area of the device when reverse bias is applied (fig. 2), so electron mobility is decreased in a wider area too. This means that electric resistance is larger when reverse bias is applied.

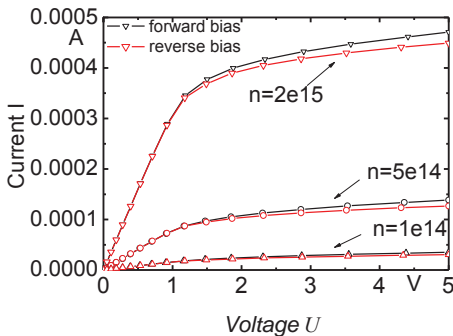


Fig. 1. Modelled current-voltage characteristics.

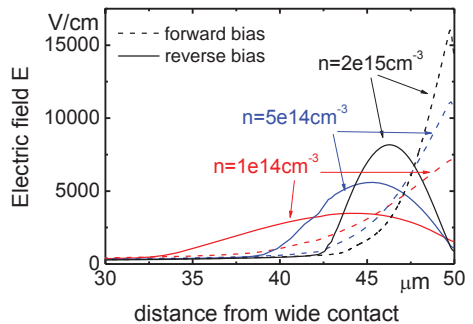


Fig. 2. Distribution of amplitude of electric field.

[1] I. Kašalynas, R. Venckevičius, D. Seliuta, I. Grigelionis, and G. Valušis, "InGaAs-based bow-tie diode for spectroscopic terahertz imaging," *J. Appl. Phys.*, vol. 110, no. 11, pp. 114505-1–114505-6, Dec. 2011.

[2] D. Seliuta, I. Kašalynas, V. Tamošiūnas, S. Balakauskas, Z. Martūnas, S. Ašmontas, G. Valušis, A. Lisauskas, H. G. Roskos, and K. Köhler, *Electron. Lett.* 42, 825 (2006).

[3] Sentaurus Device User Guide, Version C-2009.06, June 2009

## **THE INFLUENCE OF LOCALIZED STATES ON THE OPTICAL PROPERTIES OF SEMICONDUCTORS**

Oleg Kravcov<sup>1</sup>

<sup>1</sup>Faculty of Physics, Vilnius University, Lithuania  
Oleg.Kravcov@ff.stud.vu.lt

An anomalous “S and W-shaped” temperature dependence of photoluminescence (PL) peak position in InGaN and MgZnO layers have been simulated by calculating energy spectrum of excitons. Using the Gaussian distribution model for localized states and changing basic function parameters was analyzed the influence on the optical properties of semiconductors.

Simulated dependence was analyzed and compared with experimental results.



## CHARACTERIZATION OF X-RAY INDUCED ROOM TEMPERATURE UNSTABLE RADICALS IN SUCROSE

Jevgenij Kusakovskij<sup>1</sup>, Freddy Callens<sup>2</sup>, Henk Vrielinck<sup>2</sup>, Eugenijus Gaubas<sup>1</sup>

<sup>1</sup>Institute of Applied Research, Vilnius University, Sauletekio av. 9-III, LT-10222 Vilnius, Lithuania

<sup>2</sup>EMR research group, Dept. Solid State Sciences, Ghent University, Krijgslaan 281-S1, B-9000 Gent, Belgium

[Jevgenij.Kusakovskij@tmi.vu.lt](mailto:Jevgenij.Kusakovskij@tmi.vu.lt)

In carbohydrates, high energy radiation creates radicals, these are molecules or molecular fragments with unpaired electrons. Free radicals are usually highly reactive and unstable. Direct products of radiation interaction can go through many transformations before acquiring a relatively stable conformation. This leads to structural alterations on the molecular level that in turn can change the functionality of a molecule and have a potential to cause serious health issues in living organisms. In the solid state, these radicals can be stable (trapped) at room temperature. Studies and characterization of radicals are thus in demand in radiation chemistry and in radiation dosimetry fields. Sucrose is particularly interesting from the perspective of radiation chemistry as a model system for DNA radiation damage studies because it bears resemblance to DNA components and the crystalline state is presumed to mimic the tight packing of DNA in chromosomes. From the standpoint of dosimetry, the widespread of sucrose and stability of its radicals at ambient temperature make it a feasible nuclear emergency dosimeter. Additionally, sucrose radicals are important for characterization of irradiated foodstuffs.

In this work, the U1 and U2 radicals in single crystal sucrose, that have limited stability at room temperature [1], have been studied using electron paramagnetic resonance (EPR) and electron-nuclear double resonance (ENDOR) spectroscopy. Measurements in three planes were performed in Q-band (34 GHz) at 50 K. The rotation planes are determined by fitting the angular variations of ENDOR ( $m_S = -1/2$ ) transitions associated with largest hyperfine couplings (HFC) of the truly stable radicals T1, T2 and T3 [2-4]. Four HFC tensors of largest proton couplings of U1 and U2 have been determined and compared to high-level DFT calculation results. Contributions of individual radicals to the EPR spectrum at crystallographic orientations have been resolved by comparing simulated EPR spectra to measured ENDOR-induced EPR spectra.

- 
- [1] H. Vrielinck, H. De Cooman, Y. Karakirova, N. D. Yordanov, and F. Callens, Early-stage evolution of the epr spectrum of crystalline sucrose at room temperature after high-dose x irradiation, *Radiation Research* **172**, 226-233 (2009).
- [2] H. De Cooman, E. Pauwels, H. Vrielinck, A. Dimitrova, N. D. Yordanov, E. Sagstuen, M. Waroquier and F. Callens, Radiation-induced defects in sucrose single crystals, revisited: A combined electron magnetic resonance and density functional theory study, *Spectrochim. Acta A* **69**, 1372-1383 (2008).
- [3] H. De Cooman, E. Pauwels, H. Vrielinck, E. Sagstuen, F. Callens and M. Waroquier, Identification and Conformational Study of Stable Radiation-Induced Defects in Sucrose Single Crystals using Density Functional Theory Calculations of Electron Magnetic Resonance Parameters, *J. Phys. Chem. B* **112**, 7298-7307 (2008).
- [4] H. De Cooman, E. Pauwels, H. Vrielinck, E. Sagstuen, S. Van Doorslaer, F. Callens, and M. Waroquier, ENDOR and HYSORE analysis and DFT-assisted identification of the third major stable radical in sucrose single crystals X-irradiated at room temperature, *Phys. Chem. Chem. Phys.* **11**, 1105-1114 (2009).

# MODELING OF GEOMETRICAL EFFECTS ON SHALLOW DONOR STATES IN MOS-STRUCTURES

Elena Levchuk<sup>1</sup>, Leonid Makarenko<sup>1</sup>, Olga Lavrova<sup>1</sup>

<sup>1</sup> Department of Applied Mathematics and Computer Science, Belarusian State University, Independence Ave. 4, 220030 Minsk, Belarus  
[fpm.levchukEA@bsu.by](mailto:fpm.levchukEA@bsu.by)

The manipulation of donor electron wave functions by the electric field near an interface between two materials can be considered as a basic element for the development of quantum informatics devices. This problem was investigated earlier in works [1-4] using variational methods. In the given work main characteristics of such a system with electric field applied by a disc-shaped gate are studied using finite element method (FEM) and variational method.

One of the most important characteristics describing the given system is a critical potential ( $\Phi_{oc}$ ) – the gate potential which corresponds to the electron transferring from the donor to the gate. The main aim of this work is to study effects of different geometrical parameters on the critical potential.

The problem is formulated as follows: the area  $z > 0$  is filled with a semiconductor and a thin disc-shaped gate of a diameter  $d$  and potential  $\Phi_0$  is situated on the plane  $z = 0$ . The center of the gate is positioned at the origin. A donor is located at the distance  $z_0$  from the semiconductor interface.

To calculate the electron wave function  $\psi$  and energy  $E$  the following eigenvalue problem should be solved:

$$(\hat{T} + \hat{V}_D + \hat{V}_{D'} + \hat{V}_{im} + \hat{V}_G)\psi = E\psi, \quad \rho > 0, z > 0, \quad (1)$$

$$\psi|_{z=0} = 0, \quad \psi \xrightarrow{\rho \rightarrow \infty} 0, \quad \psi \xrightarrow{z \rightarrow \infty} 0. \quad (2)$$

where  $\hat{T}$  – the kinetic energy operator,  $\hat{V}_D$ ,  $\hat{V}_{D'}$ ,  $\hat{V}_{im}$  – the interaction between the electron and the donor, the donor image and electron image respectively,  $\hat{V}_G$  describes the potential landscape in the semiconductor due to the gate.

The problem (1) – (2) has been solved using finite element method and Ritz method with the following trial function:

$$\psi_\Sigma = C_G \psi_G + C_D \psi_D, \quad (3)$$

where the term  $\psi_D = Nz \exp(-\sqrt{(z-z_0)^2 + \rho^2})$ , and  $\psi_G = C_1 z \exp(-\alpha_1 \rho^2 - \beta_1 z^2) + C_2 z \exp(-\alpha_2 \rho^2 - \beta_2 z^2)$  (we consider  $\langle \psi_i | \psi_i \rangle = 1$ ,  $i = D, G$ ). The ground ( $E_0$ ) and first excited ( $E_1$ ) state energies, calculated with the trial function (3) and FEM, for different values of the gate potential are represented in figure 1.

The value of the critical potential ( $\Phi_{oc}$ ) can be calculated in two ways. Firstly,  $\Phi_{oc}$  corresponds to the point of minimum distance between the curves, describing the dependences of the ground and first excited state energies on the gate potential. Secondly, the critical potential can be found as the point where  $C_G/C_D = 1$  for both ground and first excited states (the inset of figure 1).

Using this two methods of evaluating the critical potential we have studied the effect of varying several geometrical parameters (donor depth, gate diameter) on the value of  $\Phi_{oc}$ . It was found that these parameters strongly influence on the critical potential, and the dependence of  $\Phi_{oc}$  on  $d$  is not monotonous.

An anticrossing behavior, demonstrated by the ground and first excited state energies, was also observed for higher excited states.

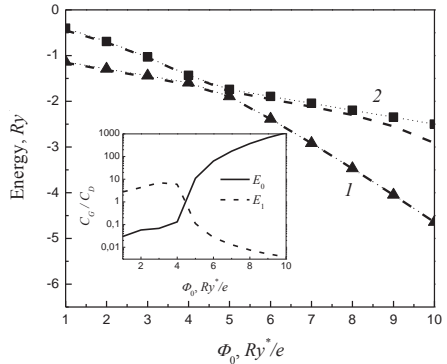


Fig. 1. Ground (curves 1) and first excited (curves 2) state energy for different gate potentials,  $d = 4$ ,  $z_0 = 8$ . Dashed lines represent the values, calculated with FEM, and markers – the values, calculated with the trial function (3). The inset shows the value of  $C_G/C_D$  for different values of the gate potential: solid curve corresponds to the ground state and dashed curve corresponds to the first excited state.

[1] G.D.J. Smit, et al, *Phys. Rev.* **B68**, 193302 (2003).

[2] L.M. Kettle, et al, *Phys. Rev.* **B68**, 075317 (2003).

[3] M.J. Calderon, et al, *Phys. Rev. Lett.* **96**, 096802 (2006).

[4] Y.L. Hao, et al, *Phys. Rev.* **B80**, 035329 (2009).

## SPATIALLY RESOLVED LUMINESCENCE IN LGSO:Ce CRYSTALS

M. Mackoit

Semiconductor Physics Department and Institute of Applied Research, Vilnius University, Sauletekio al. 9 III, Vilnius, LT-10222, Lithuania

[mazena.mackoit@ff.stud.vu.lt](mailto:mazena.mackoit@ff.stud.vu.lt)

Oxide single crystals based on rare-earth silicates are known scintillators used in devices of medical diagnostics, scientific experiments on high-energy physics, particle physics and other applications. Mixed oxyorthosilicate crystals have been obtained in the last two decades. The enhancement of light yield in mixed crystals is a key issue for a range of applications. The improvement of light yield in LGSO:Ce might be produced by formation of Lu- and Gd-enriched regions. This short-range inhomogeneity might lead to formation of potential barriers limiting diffusion of thermalized uncorrelated carriers.

Confocal microscopy was used to study the spatial distribution of luminescence characteristics in LGSO:Ce crystals. CW laser diode ( $\lambda = 405$  nm) was used for excitation. The objective with numerical aperture  $NA = 0.55$  ensured the lateral resolution of 400 nm and axial resolution of 1600 nm.

The spatial distributions of luminescence parameters are strongly influenced by surface morphology. Deeper in the crystal, the LGSO:Ce and LSO:Ce luminescence spectra consist of one broad band peaked at  $\sim 510$  nm. In LSO:Ce crystals, luminescence band position gradually shifts to longer wavelength with increasing distance from the surface. A detailed analysis of the spectra shows that the shift is accompanied by a decrease in intensity of the spectral component peaked at  $\sim 470$  nm. Meanwhile, in LGSO:Ce crystals, spatial inhomogeneities ( $\sim 1$  to  $3 \mu\text{m}$  in diameter) are observed in the band position images. Comparison of the spectra from areas with different band position reveals a strong variation in intensity at  $\sim 470$  nm. Also, another spectral component peaked at  $\sim 600$  nm was observed to have a strongly inhomogeneous spatial distribution.

The results show that the luminescence spectrum of LGSO:Ce consists of subbands, which are associated with CeO7 and CeO6 polyhedra. The intensity ratio of these subbands depends on activator distribution between these polyhedra, which, in turn, is influenced by Lu/Gd ratio in the crystal. With addition of Gd<sup>3+</sup> with bigger ionic radius, the quantity of Ce<sup>3+</sup> in six fold polyhedra increases due to loosening of crystal lattice. Therefore, it can be assumed that the spatial inhomogeneity of the spectral component ( $>550$  nm) of LGSO:Ce reflect fluctuations in Lu/Gd ratio across the crystal.

# ANTENNA-COUPLED InGaAs “BOW-TIE” DIODE DESIGNS FOR TERAHERTZ DETECTION

Karolis Madeikis<sup>1,2</sup>, Linas Minkevičius<sup>1</sup>, Gintaras Valušis<sup>1,2</sup>

<sup>1</sup> Semiconductor Physics Institute of Center for Physical Sciences and Technology,  
A. Goštauto str. 11, LT-01108, Vilnius, Lithuania

<sup>2</sup> Vilnius University Faculty of Physics, Saulėtekio al. 9, bldg. III, LT-10222 Vilnius, Lithuania

[karolismadeikis@gmail.com](mailto:karolismadeikis@gmail.com)

Application of terahertz (THz) waves for security, medical diagnostic and imaging needs [1] remains the main stimulus to develop compact and sensitive THz detectors which would operate at room temperature. This work is dedicated to theoretical analysis and optimization of InGaAs “bow-tie” diodes [2].

Simulations, using 3D finite-difference time-domain method, [3] were used to calculate a distribution of electromagnetic field amplitude ratio in an active zone of the detector plane. Typical simulation area is shown in Fig. 1. Black cuboid edges show simulation area size. It was considered that planar antennas were made of ideal conductor on InP substrate which dielectric permittivity is  $\varepsilon=12.61$ . The plane on the left (Fig. 1) shows the entrance of THz frequency wave and the grey cuboid on the right denotes InP substrate. Plane wave propagates along  $x$  coordinate direction.

Two types of structures were studied. The first one was log-periodic antenna presented in Fig. 2. It has a log-periodic circular-toothed structure with tooth and bow angles of  $\alpha$  and  $\beta$ . The ratio of the radial sizes of successive teeth is  $(R_{n+1}/R_n) = 0.5$ , while the size ratio of the tooth and anti-tooth –  $(r_n/R_n) = \sqrt{2}$ . The next structure was the log-periodic antenna coupled with a “bow-tie” diode in its center.

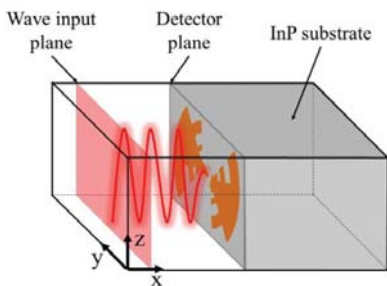


Fig. 1. Simulation area. The plane on the left – THz wave entrance and the grey cuboid on the right depicts InP substrate, detector plane shows its position in modeling space.

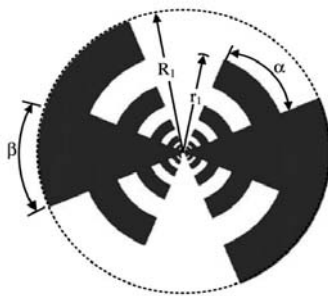


Fig. 2. Log-periodic antenna and parameters which define its shape.

Influence of geometrical properties for antennas performance and resonance frequency were determined. It is demonstrated that log-periodic antenna coupled with a “bow-tie” diode at 0.3 THz exhibits sensitivity nearly one order of magnitude higher in comparison with conventional bow-tie diodes.

## ACKNOWLEDGEMENT

This work was supported by Research Council of Lithuania (grant MIP-093/2012).

- [1] John F Federici, Brian Schulkin, Feng Huang, Dale Gary, Robert Barat, Filipe Oliveira and David Zimdars, THz imaging and sensing for security applications—explosives, weapons and drugs, *Semicond. Sci. Technol.* **20** (7), 266-280 (2005).
- [2] L. Minkevičius, V. Tamošiūnas, I. Kašalynas, D. Selinta, G. Valušis, A. Lisauskas, S. Boppel, H. G. Roskos and K. Köhler “Terahertz heterodyne imaging with InGaAs-based bow-tie sensors”, *Appl. Phys. Lett.* **99** (13), 131101 (2011).
- [3] Linas Minkevičius, Imantas Kašalynas, Dalius Seliuta, Vincas Tamošiūnas, Gintaras Valušis, Frequency-dependent properties of InGaAs bow-tie detectors in terahertz frequency range, *Lithuanian Journal of Physics* **50** (2), 173-180 (2010).

## FORMATION AND OPTICAL CHARACTERIZATION OF NANOAGGREGATES FORMED BY TRIPLET OLED EMITTERS

Rita Merzlikovaitė, Saulius Antanas Juršėnas

Institute of Applied Research, Vilnius University, Lithuania  
rita.merzlikovaitė@ff.stud.vu.lt

Classic studies of organic luminescence are generally conducted in the solution state. However, the conclusions drawn from the dilute solution data cannot commonly be extended to the concentrated solutions, because many organic luminophores show very different light-emitting behaviors in dilute and concentrated solutions. For example, luminescence is often quenched in high concentrations. This effect is called aggregation-caused quenching (ACQ) and considered detrimental from the viewpoint of technological applications as solid state materials are usually used. This is why luminogenic materials with attributes of aggregation-induced emission (AIE), an opposite effect to ACQ, have attracted much interest since the debut of the concept in 2001. AIE effect allows actively utilizing the aggregation process, instead of working against it [1]. Almost all organic luminophores are singlet emitters. Since luminophores fluoresce, its' electroluminescence quantum yield can only be as high as 25%. Therefore it is of great interest to study triplet organic emitters because these emitters could enable efficiencies quadruple that of fluorescent materials [2,3].

Nanoaggregates formed from triplet emitters were studied in this work. Precipitation technique was used to form phosphorescent organic nanoaggregates from four different organometallic iridium compounds (Fig. 1). Precipitation technique is based on three simple steps. Firstly, the solution with THF is prepared, and then different volume fractions of distilled water are injected into the solution under vigorous stirring. Since the luminophores dissolve in THF but are hydrophobic while THF is soluble in water, aggregates start to form in the solution after the percentage of water reaches a certain value. Nanoaggregates were also formed using 1,4-dioxane and acetonitrile mixture as organic solvent and ethanol instead of water. Nanoaggregates were characterized by measuring photoluminescence of both solutions and evaporated layers of solutions. Pictures of nanoaggregates were taken by using fluorescence microscopy and scanning electron microscope (SEM) (Fig. 2).

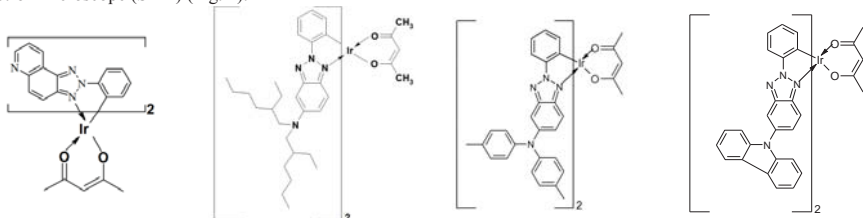


Fig. 1. Molecular structure of the organometallic iridium complexes V-422, V-447, V-669, V-686, respectively.

Results have shown that different H type, J type and amorphous aggregates form depending on the structure of the molecule. It was shown that the type of solvent mixture, that was used to form aggregates, influences final shape and size of the aggregate.

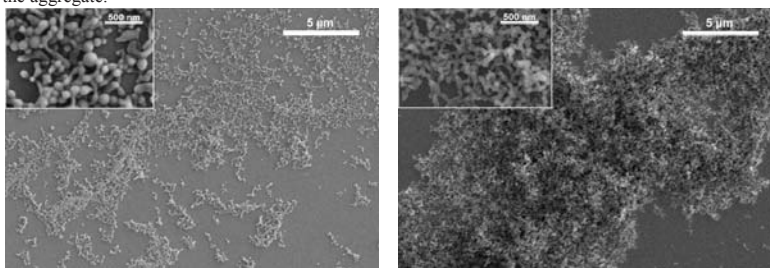


Fig. 2. SEM images of nanoaggregates formed from organometallic iridium compounds V-669 and V-686 in THF/H<sub>2</sub>O solution.

[1] Y. Hong, J. W. Y. Lam, B. Z. Tang, Aggregation-induced emission, Chem. Soc. Rev. **40**, 5361–5388 (2011).

[2] H. Yersin, W. J. Finkenzeller, *Highly Efficient OLEDs with Phosphorescent Materials*, (Wiley-VCH, Weinheim, 2008).

[3] K. A. Franz, W. G. Kehr, A. Siggel, J. Wiczorek, W. Adam, Ullmann's Encyclopedia of Industrial Chemistry (Wiley-VCH, Weinheim, 2002).

## DLTS SPECTROSCOPY ON Ge DOPED Si DIODES

Dovilė Meškauskaitė, Eugenijus Gaubas

Institute of Applied Research, Vilnius University, Saulėtekio Ave. 9-III, LT-10222 Vilnius, Lithuania  
[dovime@gmail.com](mailto:dovime@gmail.com)

Dependence of the device electrical characteristics on fluence is essential in evaluation of the functionality of high-energy particle detectors under high fluence irradiation conditions. Ge doped during Czochralski pulling of the silicon crystals can be a beneficial technique for impurity engineering, enabling to improve properties of Si wafers and devices [1], [2]. DLTS (deep level transient spectroscopy) is widely used method for studying deep level defects in semiconductors. DLTS method is used for the measurement of a deep-level activation energy, the concentration of the defects and the capture cross section. C-DLTS is based on measurements of the capacitance transient signals resulting from relaxation processes, following the abrupt changes of bias voltage and temperature [3].

In this work two sets of n-type Cz grown Si diodes have been investigated, some of them with Ge doping concentrations of about  $10^{19} \text{ cm}^{-3}$ . Samples were irradiated by penetrative electrons with fluences ranging from  $10^{14}$  to  $10^{16} \text{ cm}^{-2}$ . In order to investigate thermal donor formation, heat treatment at  $450^\circ \text{C}$  was performed for 0.5 – 2h. The impact of germanium doping on diode characteristics and on thermal donor formation was analyzed by means of capacitance-voltage (C-V), current-voltage (I-V) and capacitance-deep level transient spectroscopy (C-DLTS) measurements.

The DLTS spectra enabled us to identify the radiation defects. It has been observed, that electrons beam irradiation produced different charge states of vacancy-oxygen and divacancy defects in Ge doped and undoped samples. Germanium is an isovalent impurity in Si at substitutional sites, being electrically non-active, but therefore, Ge atoms can cause the increase of internal stresses when incorporated into Si lattice [2]. The relaxation of the inner stresses is determined by interactions of vacancies with the Ge atoms, thus forming complexes of Ge-V or Ge-O-V. Germanium and vacancy interaction also leads to an increase of the V-O defects production. It was found that concentration of divacancy defects in double-logarithmic scale show a linear increase with irradiation fluence, in Ge doped and undoped samples. Analysis of the DLTS spectra also showed that large fluences ( $10^{16} \text{ cm}^{-2}$ ) initiate formation of vacancy-phosphorus complexes (this defect often called E-centre or V-P). Also, it has been established profiles of distribution of deep traps density in depth of the base region.

Study of annealed at  $450^\circ \text{C}$  samples showed that concentration of thermal donors (TD) increases with enhancement of annealing time. It has been obtained that impurities of Ge lead to a increase of the efficiency of formation of TD relatively to the undoped samples. It can be explained by formation of by Ge stable complexes with oxygen and vacancies, which reduces the oxygen migration and formation of oxygen clusters [4].

---

[1] Xuegong Yu, et al., Intrinsic gettering in germanium-doped Czochralski crystal silicon crystals, *Journal of Crystal Growth* 250, 359–363 (2003).

[2] J. Chen, D. Yang, Influence of germanium doping on the mechanical strength of Czochralski silicon wafers, *J. Appl. Phys.* 103, 123521 (2008).

[3] D. V. Lang, "Deep-level transient spectroscopy: A new method to characterize traps in semiconductors," in *Journal of Applied Physics*, vol. 45, pp. 3023-3032, (1974).

[4] H. Li, D. Yang, The effect of germanium doping on oxygen donors in Czochralski-grown silicon, *J. Phys.: Condens. Matter* 16 5745–5750 (2004).

## **SURFACE PLASMON ENHANCED PHOTOLUMINESCENCE OF InGaN/GaN QUANTUM WELLS**

Eimantas Mikolajūnas

Semiconductor Physics Department, Vilnius University, Saulėtekio Ave. 9-III, LT-10222 Vilnius, Lithuania.  
[e.mikolajunas@gmail.com](mailto:e.mikolajunas@gmail.com)

The development of high-efficiency semiconductor light emitting diodes (LEDs) is of great interest for a wide range of applications including solid-state lighting. InGaN alloys are particularly attractive as they can be used to cover the entire visible spectrum by tuning their composition. At the same time, however, their internal quantum efficiency for light emission strongly decreases with increasing In content, leading to limited luminescence yields at wavelengths in the green spectral region and beyond. As a result, several techniques for light-emission efficiency enhancement are currently being investigated in conjunction with InGaN materials, one of them is the use of surface plasmon polaritons supported by metallic nanostructures.

In this work, photoluminescence (PL) of InGaN multiple quantum well (MQW) samples, covered by two different Ag nanoparticles arrangements, is studied. One of the samples had a periodic Ag nanoparticles arrangement with 190 nm period. The other sample had a random arrangement with a large separation between neighboring Ag nanoparticles. InGaN MQW structures were grown by MOCVD technique on sapphire substrate and Ag particles were deposited on top of the surfaces with the technique of polystyrene nanosphere lithography.

Spatial PL distribution of InGaN structures was studied using confocal microscopy. Objective of high numerical aperture (NA=0.9) ensured spatial resolution of ~250 nm. PL spectra were measured under steady-state condition using continuous wave He-Cd laser emitting at  $\lambda = 442$  nm. To analyze the distribution of Ag nanoparticles on the samples, atomic force microscopy was used.

The study revealed that PL enhancement depends on the metal nanoparticles arrangement and it is possible to evaluate impact of one metal nanoparticle on enhancement of photoluminescence. In case of the periodic structure of Ag nanoparticles PL enhancement can be increased for at least 2.7 times, in comparison with non-periodic structure. This observation highlights the importance of properly designing of Ag nanoparticles array on InGaN alloys for optimal light-emission efficiency enhancement.

## DLTS INVESTIGATION OF Mn-IMPLANTED Ge

Grigorij Muliuk<sup>1</sup>, Johan Lauwaert<sup>2</sup>, Henk Vrielinck<sup>2</sup>

<sup>1</sup> Vilnius University, Faculty of Physics, Saulėtekio al. 9. III, Vilnius, Lithuania

<sup>2</sup> Ghent University, Faculty of Sciences, Solid State Sciences dep., Krijgslaan 281 S1, Gent, Belgium  
[grigorij.muliuk@ff.stud.vu.lt](mailto:grigorij.muliuk@ff.stud.vu.lt)

First experimental studies of metal impurity levels in semiconductor germanium (Ge) began from 1950s using resistivity and Hall effect measurements. Later when deep-level transient spectroscopy (DLTS) was introduced it became a preferential technique to study the behavior of trap levels in the semiconductor [1].

The aim of this work is to characterize the levels that manganese (Mn - a transition metal in the 3<sup>rd</sup> series) introduces in germanium. This material is highly applicable for the ferromagnetic semiconductor researches for over 10 years [2].

This work concerns *n*-type Ge implanted with Mn transition metal samples with the dose of  $5 \cdot 10^{13}$  atoms/cm<sup>2</sup>. After implantation the dopant ions are concentrated in a layer close to the surface, thus, in order to disperse the dopant and to make it active an additional thermal annealing on 500°C was performed. Expected free carrier concentration is  $N_s = 2 \cdot 10^{14}$  cm<sup>-3</sup>.

DLTS measurements for the sample of 30 minutes annealing with selected reverse bias  $V_R = -1V$  is presented in Fig. 1 (1 curve). One can clearly see a peak in the 112K temperature. From Arrhenius analysis obtained activation energy is  $E_t = 0.18$  eV. This result is close to the literature value from previously reported resistivity measurement for the Mn implanted Ge ( $E_V + 0.16$  eV). However, it has relation with the hole capture in the valence band [3]. Moreover, experimentally we measured  $N_t = 2.96 \cdot 10^{16}$  cm<sup>-3</sup>. A value is also confirmed using Hall-Van der Pauw measurements. This is two orders of magnitude higher than the expected result. Furthermore, high  $N_t$  affect reverse capacitance ( $C_R$ ) which is also high and yields the 10<sup>-3</sup>F order of magnitude.

Fig. 1 (2 curve) shows the DLTS spectrum measured on a smaller sample at a larger  $V_R = -5V$ , and a correspondingly larger electrical field. One can see that amplitude of the peak at the lower temperature region decreased what can be explained by the decrease of reverse capacitance ( $C_R$  at -5V is lower than at -1V). Moreover, comparing with the previous measurement the amplitude at higher temperature range emerged and it is more suitable for analysis.

Another effect that can be observed comparing measurements from Fig. 1 is that the peak at 112K (1 curve) shifted to the lower temperatures (96K, 2 curve). This means that trap energy decreases when applied electric field increases. This can be explained by the Poole-Frenkel effect as applied negative voltage creates an electrical field that lowers the potential barrier and because of this, less energy is required to thermally emit carriers. This can only happen if traps are attractive for majority carriers, thus positively charged. Hence, we would have to conclude that the levels we observe have donor characteristic. This does not correspond with the double-acceptor levels that literature suggests for Mn [3].

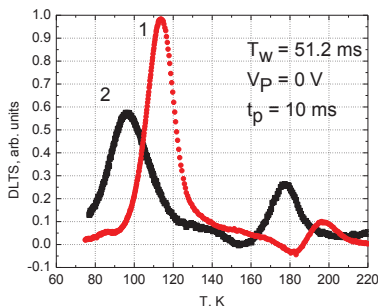


Fig. 1. DLTS measurements for Ge-Mn sample: 1 – measured on  $V_R = -1V$ ; 2 – measured on  $V_R = -5V$

[1] J. Lauwaert, J. Vanhellefont, E. Simoen, H. Vrielinck, P. Clauws. *J. Appl. Phys.* **111**, 113713, (2012).

[2] M. Jamet, T. Devillers, I-S. Yu, A. Barski, P. Bayle-Guillemaud. *Int. J. of Nanotechnology.* **7**, 575 - 590, (2010).

[3] H.H. Woodbury and W.W. Tyler. *Phys. Rev.* **100**, 659, (1955).



## Optical study of excitation-dependent recombination processes in various (In,Ga)N structures

K. Gelžinytė, K. Nomeika

Institute of Applied Research and Faculty of Physics, Vilnius University

[Kristina.Gelzinyte@ff.stud.vu.lt](mailto:Kristina.Gelzinyte@ff.stud.vu.lt), [Kazimieras.Nomeika@ff.stud.vu.lt](mailto:Kazimieras.Nomeika@ff.stud.vu.lt)

Determination of the exact pathways of non-equilibrium carrier recombination in (In,Ga)N remains an open topic despite the intensive studies carried out during the last decade. This interest is strongly based on the non-radiative losses appearing in the light emitting diodes (LEDs) at high carrier densities. The origin of these losses is not established yet; several possible culprits have been named [1]. Main difficulty in disclosing non-linear recombination processes arises from the fact that most studies are being carried on the electrically-driven multilayered LED structures and using time-integrated methods. On the other hand, optical pump-probe methods allow monitoring of excess carrier density in a direct way with good temporal and spectral resolution.

In this work, we present a study of non-equilibrium carrier recombination and diffusion in various (In,Ga)N structures using light-induced transient gratings (LITG) [2], differential transmission (DT) and two-color pump-probe (PP) techniques. We compare carrier dynamics in three MOCVD grown samples: (i) 50-nm thick  $\text{In}_{0.13}\text{Ga}_{0.87}\text{N}$ ; (ii) MQW structure consisting of 12 periods  $\text{In}_{0.108}\text{Ga}_{0.892}\text{N}$  QWs and  $\text{In}_{0.05}\text{Ga}_{0.95}\text{N}$  barriers, both of 5.5 nm thickness; (iii) stair-case LED structure consisting of 6-periods of  $\text{In}_{0.2}\text{Ga}_{0.8}\text{N}/\text{In}_{0.01}\text{Ga}_{0.99}\text{N}$  QWs having  $\sim 3$  nm well width. All samples were studied within 80-700 K temperature and  $\sim 3 \times 10^{18} - 10^{20} \text{ cm}^{-3}$  carrier density ranges. We recorded the PP and LITG transients for both resonant and non-resonant excitation and were able to estimate accurately the density of photo-excited carriers by precise measurement of laser beam size and energy. This allowed the well-based numerical analysis of the transients using so-called ABC model.

We demonstrate that the density of photo-excited carriers is limited due to stimulated emission (Fig. 1 (a)) and/or absorption bleaching in all the structures, which restrains the possible influence of non-radiative Auger type recombination at room and low temperatures; however, it's influence becomes more feasible at elevated temperatures. Band to band recombination was found to be the main non-linear recombination process at moderate to high carrier densities. On the other hand, the linear recombination term was shown to increase with carrier density, which was attributed to density activated non-radiative recombination. In addition, we demonstrate that structure of an (In,Ga)N plays an important role in carrier recombination.

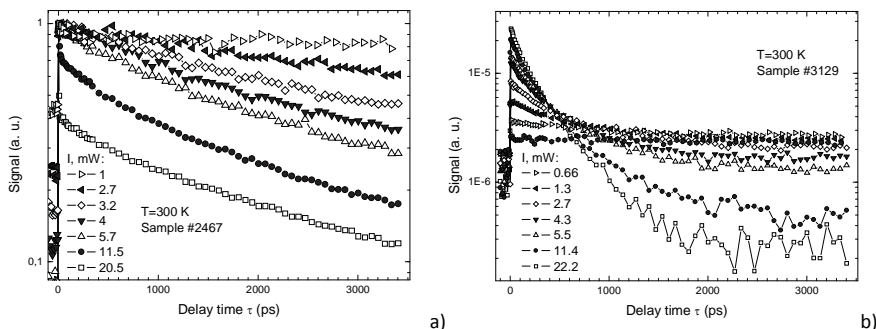


Fig. 1. Kinetics acquired from the pump-probe experiment in different samples.

[1] Ü. L. Özgür, Proc. SPIE **98**,1180 (2010).

[2] G. Juška, J. Petrulis, Light-Induced Transient Gratings in Semiconductors: A Nondestructive Optical Technique for the Characterization of Materials for Electronics, Physics of Advanced Materials, Winter School (2008).

# INVESTIGATION OF CARRIER DYNAMICS IN (Al,Ga)N LAYERS BY LIGHT INDUCED TRANSIENT GRATING TECHNIQUE

Žydrūnas Podlipskas

*Department of Semiconductor Optoelectronics, Institute of Applied Research, Vilnius University,*

*Saulėtekio Avenue 9-3, Vilnius 10222, Lithuania*

[Zydrunas.Podlipskas@ff.stud.vu.lt](mailto:Zydrunas.Podlipskas@ff.stud.vu.lt)

The recent sharp progress of III-nitride based devices caused a growing interest in aluminum-rich AlGaIn layers and quantum well structures growing technology, optical and electrical properties. It is difficult to grow and characterize high Al mole fraction  $\text{Al}_x\text{Ga}_{1-x}\text{N}$  compounds, due to inevitably forming dislocations [1] during the growing process and significantly wider energy gap compared to GaN [2], but the latter ternary materials are irreplaceable in deep ultraviolet applications. After research group of IPR (Institute of Applied Research) started to grow AlGaIn layers using MOCVD technique, it has become necessary to characterize the later layers for further quality improvement of the compounds. In this work I investigated nonequilibrium carrier dynamics in various aluminum content AlGaIn layers and their dependencies on growing conditions.

This study was performed using optical Transient Gratings (TG) experimental technique. In the studies I used picosecond pump-probe setup, designed to measure light-induced refractive index ( $\Delta n$ ) change dynamics over a wide excitation energy ( $0,05 - 1 \text{ mJ/cm}^2$ ) range. Nonequilibrium carrier lifetime and diffusion coefficient were determined from the diffraction signal kinetics.

In this study, 15 AlGaIn layers with different molar concentrations of Al (17, 22, 41%) were grown by Metalorganic Chemical Vapour Deposition (MOCVD) on sapphire ( $\text{Al}_2\text{O}_3$ ) substrates under different ammonia ( $\text{NH}_3$ ) flows, and were excited with short-wavelength (263 nm) coherent light beams.

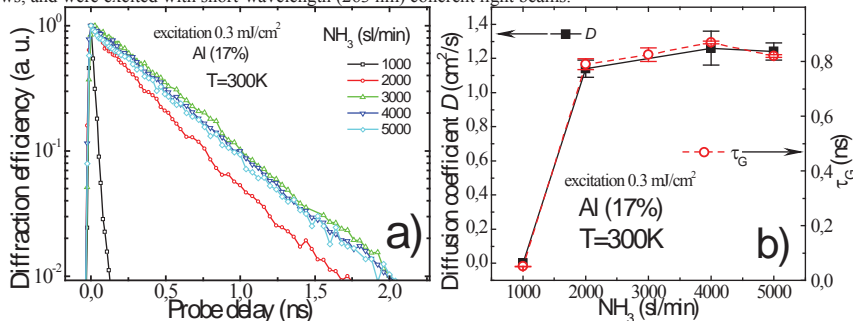


Fig. 1. a) Diffraction efficiency kinetics for AlGaIn layers, grown under various  $\text{NH}_3$  flows; b) diffusion coefficient  $D$  and nonequilibrium carrier lifetime  $\tau_G$  dependencies on  $\text{NH}_3$  flow.

TG measurements showed that decay transients of TG signal are exponential for low Al content (17 and 22%) AlGaIn layers (Fig. 1. a)), and reflects linear free carrier recombination through defective levels (Shockley-Read-Hall recombination). Whereas for high Al molar concentration (41%) AlGaIn compounds research revealed additional physical mechanisms, that are influenced by the chaotic structure of the samples: square bimolecular recombination and/or localized carriers delocalisation. The latter processes contribution to the kinetics non-linearity will be determined from the PL and temperature TG measurements.

The estimated lifetime of free carriers at the same  $\text{NH}_3$  flow significantly decreases with increasing Al content (from 790 to 420 ps). Determined AlGaIn layers free carrier lifetime dependencies from ammonia flow revealed a general regularity for the compounds series of different Al content – flow Increase leads to a significant layer quality improvement (recombination time increases from 41 to 685 ps for 22% AlGaIn layers, while  $\text{NH}_3$  flow varies within 500 –2500 sl/min range). The latter dependencies have nonequilibrium carrier lifetime maximum or saturation at different  $\text{NH}_3$  flow values for different Al content layers, and strongly correlate with the diffusion coefficients (Fig. 1. b)). Estimated nonequilibrium carrier lifetime ( $\tau_R$ ) and diffusion coefficient ( $D$ ) increases with  $J$ . After further PL and TG measurements and confirmed assumption of strong localization influence to carriers dynamics, the latter dependencies could be interpreted as defective states saturation and the excitation activated diffusion models.

**Acknowledgment.** This work was partly supported by the Lithuanian Science Council Student Research Fellowship Award (Ž.P.).

[1] R. S. Qhalid Fareed et al., Migration enhanced MOCVD buffers, phys. stat. sol. (c) 2, No. 7 (2005).

[2] Pelá et al., Accurate band gaps of AlGaIn, InGaIn, and AlInN alloys calculations based on LDA-1/2 approach, Appl. Phys. Lett. **98**, 151907 (2011)

## Hall and magnetoresistivity measurements in fast electron irradiated silicon

V. Rumbauskas, A. Mekys, J. V. Vaitkus

<sup>1</sup> Vilnius university, Institute of Applied Reserch, Saulėtekio av. 9, Vilnius, Lithuania  
[vytautas.rumbauskas@ff.vu.lt](mailto:vytautas.rumbauskas@ff.vu.lt)

A set of silicon samples have been irradiated by 6 MeV electrons with doses from 1 to 5 ( $\times 10^{16}$ ) e/cm<sup>2</sup>. The influence of irradiation to electrical parameters has been tested by Hall and magnetoresistivity measurement techniques. Both measurements revealed carrier mobility of different values, which were attributed to different physical processes of the carrier transport.

Hall and magnetoresistivity effects come in parallel as valuable for carrier transport characterization. In principal the both methods reveal carrier mobility directly and including conductivity measurements the carrier density may be found. The main disadvantage of these techniques is the lack of knowledge of such called Hall and magnetoresistivity factors [1], which introduce discrepancy. Also the geometry of the sample under investigation is very important because it introduces another discrepancy as well. Another crucial parameter for these methods is the homogeneity of the material. And here is the main difference between the mentioned methods as they are differently sensitive to the less controllable parameter – homogeneity. It was already shown how the irradiation with fast neutrons changes Hall and magnetoresistivity effects in silicon [2-3]. There the Hall mobility lowers significantly with the dose because the irradiation created large clusters of the point defects, which simply screen the Hall voltage at the contacts. At the same measurement the magnetoresistant mobility changes only slightly with the dose because the magnetoresistivity effect is proportional not to the absolute value of the resistivity but to its relative change in the presence of magnetic field. This enables with the help of the magnetoresistant effect to extract information from the conductive parts of the material, which is less affected by the irradiation and a kind of average information is extracted about the same material with the help of Hall effect. In this work we apply the both mentioned measurement techniques simultaneously for the silicon samples irradiated by fast electrons (6MeV) to show the difference of the measurements revealed characteristics and discuss the ability for further application.

---

[1] P. Blood, J.W. Orton, The Electrical Characterization of semiconductors: Majority Carriers and Electron States, Philips Reserch Laboratories, Redhill, Surrey RH15HA, UK, (1992).

[2] R. H. Bube, Investigation of hall and photo-hall effects in inhomogeneous materials, Appl. Phys. Lett. 13, 136 (1968).

[3] A. Medešis, J. Visackas, Determination of the physical parameters of polycrystalline materials from Hall and Seebeck effects., Lith. J. Phys. 15, 260-264 (1975).

## BROADBAND DIELECTRIC INVESTIGATION OF BARIUM TITANATE AND NICKEL-ZINC FERRITE COMPOSITE CERAMICS

Aurimas Sakanas<sup>1</sup>, Robertas Grigalaitis<sup>1</sup>, Jūras Banys<sup>1</sup>, Liliana Mitoseriu<sup>2</sup>, Vincenzo Buscaglia<sup>3</sup>, Paolo Nanni<sup>4</sup>

<sup>1</sup> Faculty of Physics, Vilnius University, Lithuania

<sup>2</sup> Faculty of Physics, University "Al. I. Cuza", Romania

<sup>3</sup> Institute of Energetics & Interphases IENI-CNR, Italy

<sup>4</sup> Department of Chemical & Process Engineering, University of Genoa, Italy  
aurimas.sakanas@ff.vu.lt

Ferroelectric barium titanate and nickel-zinc ferrite composite ceramics belong to a multifunctional materials group called multiferroics. Multiferroic materials, exhibiting more than one ferroic property (ferromagnetism, ferroelectricity, ferroelasticity) in a single phase has drawn a wide scientific and technological attention in the present years for the fundamental research and due to the variety of possible practical applications. One of the most promising candidates is barium titanate and nickel zinc ferrite composite.

$x\text{BaTiO}_3-(1-x)\text{Ni}_{0.5}\text{Zn}_{0.5}\text{Fe}_2\text{O}_4$  composite ceramics with  $x=0.5, 0.6$  and  $0.7$  molar ratios were successfully prepared by the co-precipitation method, and from the X-ray diffraction patterns obtained the presence of only the perovskite BT and spinel NZF phases was confirmed [1].

Although dielectric properties of this material were already investigated, the results up to only megahertz frequencies were presented [2, 3]. Here we demonstrate the results of the broadband dielectric spectroscopy in the 20 Hz to 50 GHz frequency range.

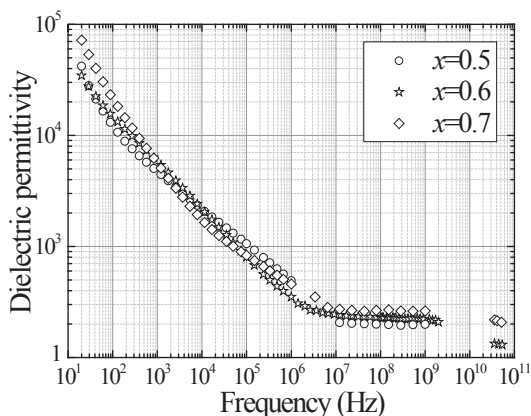


Fig. 1. Frequency dependence of the real part of dielectric permittivity at 500 K for  $x\text{BaTiO}_3-(1-x)\text{Ni}_{0.5}\text{Zn}_{0.5}\text{Fe}_2\text{O}_4$  composites with different  $x$ .

The real part of dielectric spectra of the composite ceramics (Fig. 1) manifests conductivity contribution up to a few megahertz frequencies followed by a relaxation process. Such conductivity behavior must be primarily due to ferrite phase of the composite and it is likely to be related to the Maxwell-Wagner polarization mechanism [4, 5]. At high enough frequencies, where the conductivity contribution is remarkably reduced, diminished permittivity with the increasing concentration of nickel-zinc ferrite can be observed.

- 
- [1] A. Testino, L. Mitoseriu, V. Buscaglia et al., Preparation of multiferroic composites of  $\text{BaTiO}_3\text{-Ni}_{0.5}\text{Zn}_{0.5}\text{Fe}_2\text{O}_4$  ceramics, *Journal of the European Ceramic Society* **26**, 3031-3036 (2006).
- [2] L. Mitoseriu, V. Buscaglia, Intrinsic/extrinsic interplay contributions to the functional properties of ferroelectric-magnetic composites, *Phase Transitions* **79**, 1095-1121 (2006).
- [3] L. P. Curecheriu, M. T. Buscaglia, V. Buscaglia et al., Functional properties of  $\text{BaTiO}_3\text{-Ni}_{0.5}\text{Zn}_{0.5}\text{Fe}_2\text{O}_4$  magnetoelectric ceramics prepared from powders with core-shell structure, *Journal of Applied Physics* **107**, 104106-1-11 (2010).
- [4] Z. Yu, C. Ang, Maxwell-Wagner polarization in ceramic composites  $\text{BaTiO}_3\text{-(Ni}_{0.3}\text{Zn}_{0.7})\text{Fe}_2\text{O}_4$ , *Journal of Applied Physics* **91**, 794-797 (2002).
- [5] F. Kremer, A. Schönhal, *Broadband Dielectric Spectroscopy* (Springer-Verlag, Berlin Heidelberg New York, 2002).

# INVESTIGATION OF THE IMPACT OF Au NANOPARTICLES ON THE ELECTRICAL AND CHARGE TRANSPORT PROPERTIES OF a-Si:H SOLAR CELLS

ANDRIUS SAKAVICIUS

Department of Semiconductor Physics, Faculty of Physics and Institute of Applied Research, Vilnius University,  
Saulėtekio Ave. 9 III, LT-10222 Vilnius, Lithuania  
[Andrius.Sakavicius@ff.stud.vu.lt](mailto:Andrius.Sakavicius@ff.stud.vu.lt)

Due to their low fabrication cost, pin-type hydrogenated amorphous silicon solar cells (a-Si:H SCs) are potential renewable solar energy sources. However, the device efficiency of a-Si:H SCs is still lower than that of poly-Si SCs. One method of improving device performances in a-Si:H SCs is to insert a transition metal oxide, such as tungsten oxide ( $\text{WO}_3$ ) between a textured fluorine-tin oxide (FTO) glass and a p-type Si layer as an adjusted p-type electrode. The  $\text{WO}_3$  layer increases carrier collection due to the band alignment between neighbouring layers in a-Si:H SCs and provides a large shunt resistance, which reduces carrier recombination at the interface [1].

In our investigations a double layer of gold nano particles (Au-NPs) and amorphous tungsten oxide ( $\text{a-WO}_3$ ) was employed as a buffer layer on textured fluorine-tin oxide (FTO) glass in pin-type hydrogenated amorphous silicon solar cells (a-Si:H SCs), see Fig.1. Au-NPs of 10 nm size were spin coated and a- $\text{WO}_3$  layer was thermally evaporated between Au-NPs on a FTO glass and hydrogenated amorphous p-type Si layer. a-Si:H SCs with a double buffer layer showed higher efficiency of 7% improvement, 8.059% from a value of 7.530%, and increased current density of 8.3% improvement,  $14.212 \text{ mA/cm}^2$  from a value of  $13.120 \text{ mA/cm}^2$ , originating from the enhancement of electrical interface contact and bandgap alignment, as well as the slight absorption and surface plasmon resonance effect due to Au-NPs on textured FTO glass.

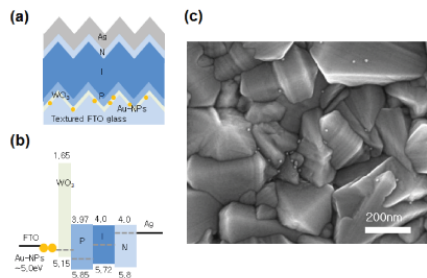


Fig. 1. (a) Schematic device structure and (b) band diagram of solar cells with various buffer layers, including a Au-NP/ $\text{WO}_3$  double buffer layer, (c) UHR FE-SEM image of spin-coated (2000 rpm) Au-NPs (10 nm) on textured FTO glass. [1].

I-V characteristics and temperature dependencies of electrical dark and photo-conductivity of each structure were measured in the temperature range from 340 K down to 100K. Schottky barrier model was used to evaluate physical properties and characteristic parameters.

Carrier mobility measurements were performed by the CELIV (Charge Extraction by Linearly Increasing Voltage) method [2]. The voltage which is proportional to the current flowing through the sample was measured on the load resistor by oscilloscope. Another channel of the oscilloscope was used to measure the output signal of the generator. Carrier mobility was calculated from current kinetics according to the following expression:

$$\mu = \frac{d^2}{At^2_{\max}(1 + 0.36 \frac{\Delta j}{j(0)})} \quad (1)$$

- 
- [1] K. S. Yook, Hydrogenated Amorphous Silicon Thin Film Solar Cells Using a Hybrid Buffer Layer of Gold Nanoparticle and Tungsten Oxide Thin Film *Solid State Lett.* **1**, 42-44 2012.  
 [2] G. Juska, K. Arlauskas, and M. Viliunas, Extraction Current Transients: New Method of Study of Charge Transport in Microcrystalline Silicon, *Phys. Rev. Lett.* **84**, 49464949 2000.

# OPTICAL AND ELECTRICAL CHARACTERIZATION OF VACUUM DEPOSITED THIN ORGANIC LAYERS

Ramūnas Songaila<sup>1</sup>, Saulius Tumėnas<sup>2</sup>

<sup>1</sup> Department of Solid State Electronics, Faculty of Physics, Vilnius University, Lithuania

<sup>2</sup> Semiconductor physics laboratory, Center for Physical Sciences and Technology, Lithuania  
[ramunas.songaila@gmail.com](mailto:ramunas.songaila@gmail.com)

We present results of investigation of the effect of molecular orientation, which affects the charge transport characteristics of vacuum deposited organic amorphous films. The electrical and optical properties of the thin films based on derivatives of diphenylethenyl substituted triphenylamines (TPA) were investigated (structural chemical formulas are presented in Figure 1). The samples for optical and electrical measurements were prepared using vacuum deposition on glass and on ITO/glass substrates, respectively, in a vacuum of  $7 \cdot 10^{-3}$  Pa at the evaporation rate 1.3 nm/s. The spectroscopic ellipsometry measurements were performed using a fast spectroscopic ellipsometer RC2 (J. A. Woollam Co., Inc.) in the 0.73 – 6 eV spectral range at seven different angles of incidence in the  $45^\circ - 75^\circ$  interval in steps of  $5^\circ$ . At each incidence angle, experimental ellipsometric parameters  $\Psi$  and  $\Delta$  were simultaneously recorded. The values of  $\Psi$  and  $\Delta$  did not change by rotating the samples, indicating that films had no in-plane anisotropy. An analysis of the data was carried out using the software CompleteEASE (J. A. Woollam Co., Inc.), which can perform a batch analysis of all data for all incident angles and wavelengths. The dielectric function of the system was extracted by the b-spline [1] mean square error (MSE) [2] technique. The spectra of optical parameters determined satisfy the Kramers–Kronig relations.

The experimental ellipsometric parameters of the organic films first of all were simulated using an isotropic model. The simulation yielded satisfactory results of MSE = 3 for the TPA films V-609 and V-645, which have single  $\text{CH}_3$  unit attached. However, an isotropic model failed to simulate (MSE = 24.3) experimental data of the V-606 and V-646 films, which don't have  $\text{CH}_3$  groups. The attempts to simulate ellipsometric parameters with complicated models of a non-uniform refractive index within the film and assuming the interface layer in-between the substrate and TPA layer have not compensated the deviation. The ellipsometric parameters of the V-606 and V-646 films could be well simulated only by a uniaxial anisotropic model. Good agreement between simulated and experimental parameters using uniaxial anisotropic model was proved by small MSE value of 3.2. The analysis reveals anisotropy in the V-606 and V-646 films. The deduced anisotropic refractive indices of organic layer V-646 are presented in Figure 2.

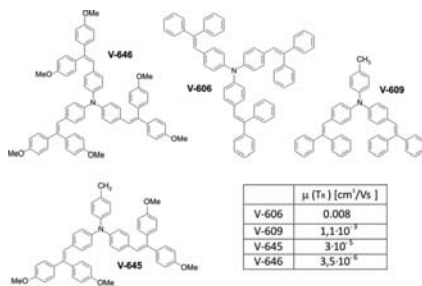


Fig. 1 Molecular structures of TPA studied (inset presents the hole mobilities)

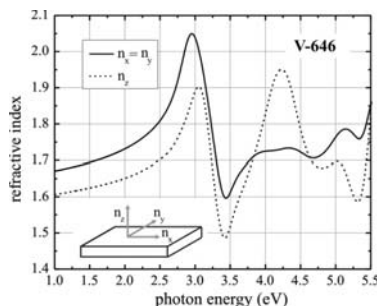


Fig. 2 Ordinary ( $n_x$ , solid line) and extraordinary ( $n_z$ , dashed line) refractive indices of V-646 TPA

We investigated the effect of the horizontal molecular orientation on the hole mobility by performing time-of-flight (TOF) measurements. Inset in Figure 1 shows the measured TOF mobilities of holes in the TPA films deposited on polycrystalline ITO/glass substrate. The highest mobility, of  $0.8 \cdot 10^{-2} \text{ cm}^2/\text{Vs}$ , was estimated in the V-606 layers, what, we assume, is first of all due to horizontal molecular orientation in the amorphous film. If the V-606 layer is modified by changing one of its functional groups with the  $\text{CH}_3$  attachment (V-609), the hole mobility decreases by 7 times and the deposited layer becomes isotropic. When V-606 is modified by attachments of MeO groups (V-645 and V-646), the horizontal molecular orientation manifests itself in optical spectra only in V-646 layers, however the hole mobility decrease by ca. 2000 times.

[1] B. Johs and J. S. Hale, Dielectric function representation by B-splines, *Phys. Status Solidi A* **205**, 715 (2008)

[2] G. E. Jellison, Jr., Data analysis for spectroscopic ellipsometry, *Thin Solid Films* **234**, 416 (1993).

## INVESTIGATION OF GREEN PHOTOLUMINESCENCE FROM CdZnO/ZnO AND InGaN/GaN MULTIPLE QUANTUM WELLS

Marius Stasiūnas<sup>1</sup>, Mindaugas Karaliūnas<sup>2</sup>

<sup>1</sup>Semiconductor Physics Department, Vilnius University, Saulėtekio Ave. 9-III, LT-10222 Vilnius, Lithuania

<sup>2</sup>Institute of Applied Physics, Vilnius University, Saulėtekio Ave. 9-III, LT-10222 Vilnius, Lithuania

[marstas@gmail.com](mailto:marstas@gmail.com)

Qualitative analysis of quantum structures designed for applications in light emitting diode (LED) fabrication is crucial for the development of more efficient samples through finding the best combination of technological steps involved in their epitaxial growth process. Photoluminescence (PL) measurements helps to qualify properties of light emitted from particular sample. Direct band gap semiconductive materials like ZnO and GaN along with their ternary alloys with Cd and In respectively, are widely investigated these days partly because of lack of efficient and high-brightness green LEDs that could be used in full-color displays or even in solid state lighting as a substitute for phosphor-based white LEDs.

Temperature-dependent PL results of 4 samples were investigated in this work. CdZnO/ZnO LEDs (2 samples) had active regions with 3 and 10 periods of CdZnO well layers separated with ZnO barriers. n-ZnO capping layer and the active region were grown using molecular beam epitaxy (MBE), whereas metalorganic chemical vapor deposition (MOCVD) was used for growing p-GaN buffer and u-GaN template layers. Active regions of other 2 samples consisted of 5 periods of InGaN/GaN multiple quantum wells (MQWs) sandwiched between p-AlGaN (top) and n-GaN (bottom) buffer layers atop u-GaN template. Both buffer/template layers and active regions of these samples were grown using MOCVD. One of them also had an MBE-grown p-GaN capping layer. All mentioned samples were fabricated on a c-plane sapphire substrate in the Institute of Photonics and Optoelectronics of National Taiwan University.

Photoexcitation of the sample was performed using selective and non-selective excitation sources. Under selective excitation conditions, violet laser diode (LD) with  $\lambda_{\text{exc}} = 403$  nm was employed, whereas continuous wave He-Cd laser ( $\lambda_{\text{exc}} = 325$  nm) was used for non-selective excitation. The laser spot diameter was estimated to be around 250  $\mu\text{m}$  on the surface of the sample. PL signal was dispersed using a monochromator (Jobin Yvon HRD-1) with holographic diffraction gratings, having 1200 grooves/mm, and registered using a photomultiplier tube (Hamamatsu R1463P). Cooling of the samples was performed utilizing a closed-circuit He cryostat, which allows the temperature of the sample to be changed in the interval from 8 K to 300 K. Samples' temperature was stabilized with the help of a proportional-integral-derivative controller.

Effects like carrier localization, thermal quenching, line broadening and differences between selective and non-selective excitation were analyzed by carrying out the temperature dependencies of spectral peak position, intensity and linewidth of the peak originating from quantum well regions of samples. If compared with CdZnO/ZnO samples, InGaN/GaN MQWs exhibited more pronounced blueshift of spectral peak position on temperature. While this type of dependency can be considered as a fingerprint of carrier localization in quantum wells, it is convenient to use the density-of-states Gaussian band-tail model [1] to describe it qualitatively. Recombination mechanisms in InGaN/GaN MQWs can be attributed to the emission from localized band-tail states originating from quantum dot-like and phase-separated indium-rich regions in the wells. This carrier localization formed in the plane of the layers suppresses lateral carrier diffusion, thereby reducing the probability of carriers entering nonradiative recombination centers [2].

Internal quantum efficiencies (IQE) at room temperature were calculated from PL results after assumption that 8 K spectra reflects radiative recombination from MQWs. Values of IQE (300 K) varied from ~6 % to ~14 % for different samples and were a few percent larger for InGaN/GaN MQWs in comparison with CdZnO/ZnO samples, which indicates poorer CdZnO wells structural quality.

Also, approximate values of Cd and In contents in  $\text{Cd}_x\text{Zn}_{1-x}\text{O}$  and  $\text{In}_y\text{Ga}_{1-y}\text{N}$  alloys were calculated using relationship between band gap energies of constituent compounds and their molar fractions in ternary alloys (Vegard's law). For samples discussed in this work, Cd and In contents in MQWs were estimated to be around 15 % and ~25 % respectively. Mismatches between lattices of the constituents causes higher dislocation densities, which, in hand, intensifies the non-radiative recombination of excitons. Anyway, high Cd and In content is necessary in order to achieve green light emission from MQWs as ZnO and GaN are wide band gap semiconductors.

[1] Petr G. Eliseev, Marek Osinski, Jinhyun Lee, Tomoya Sugahara, Shiro Sakai, Journal of Electronic Materials **29**, 332-340 (2000).

[2] Jiunn-Chyi Lee, Temperature dependence of the spontaneous emission mechanisms of localized-state heterosystem, Optica Applicata **41** No. 4, 911 (2011).

## FORMATION HYDROGEN-RELATED DONOR IN THE EPITAXIAL SILICON IMPLANTED WITH PROTONS

Svekla A.R.

Belarusian State University, Department of Physics, Nezavisimosti Avenue 4, 220030 Minsk, Belarus

svekla.alina@gmail.com

Shallow donors are known to be formed in epitaxial silicon implanted with hydrogen ions and subjected to subsequent annealing in the temperature range 200-500 °C. Introduction in silicon implanted with hydrogen ions and subjected to subsequent annealing both shallow and deep centres were observed by C-V and DLTS methods in the present research. C-V-measurements were carried out at frequency of 1 MHz and at low temperature (80-90 K), when emission rate of electron from deep traps was less enough then measuring frequency.

It was established, that irradiation of Schottky diodes (Pd -Si) results in increase of the depletion layer width (Fig.1.), in consequence of advantage introduction of large densities of E-centres ( $E_c-0.45$  eV). A-center ( $E_c-0.17$  eV) and VOH defect ( $E_c-0.32$  eV) concentrations were insignificant ( $<1 \cdot 10^{13} \text{ cm}^{-3}$ ) in same time.

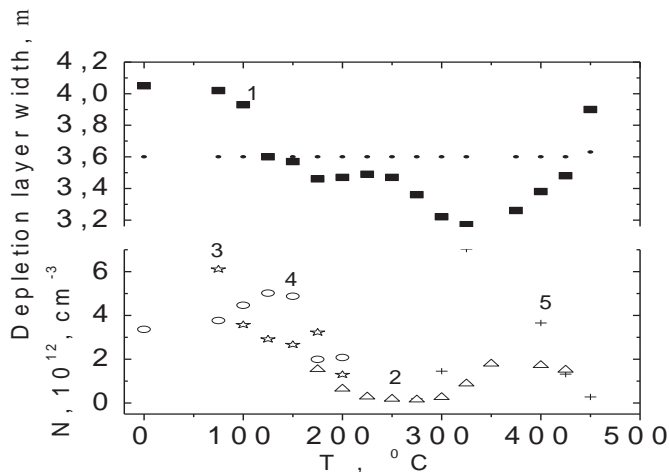


Fig.1. Depletion layer (1) and defects (205) upon 20-min isochronal annealing.

The depletion layer width becomes lower then pre-implantation value in the annealing temperatures above 200 °C. It indicates on the formation of shallow donors. Maximum donor concentration reaches at the  $T=350$  °C. Their increasing at the range temperature of 250-350 °C correlates with introduction of the deep level defect ( $E_c-0.21$  eV). Further increasing of the annealing temperature was accompanied by decreasing both electron and  $E_c-0.21$  eV trap concentration. At the  $T=450$  °C free carrier concentration decreases below then pre-implantation value, and simultaneously anomalous peak in the DLTS appears. This peak corresponds to trap with level of  $E_v+0.31$  eV.

The nature of the deep traps with  $E_c-0.21$  and  $E_v+0.31$  eV levels and their role in the shallow hydrogen-related donor formation were discussed.



## ANALYSIS OF PARAMETRIC LIGHT GENERATION IN 1500 nm REGION

Ignas Abromavičius<sup>1,2</sup>, Valerijus Smilgevičius<sup>1</sup>

<sup>1</sup> Vilnius University Department of Quantum Electronics and Laser Research Center, Saulėtekio avenue 10 (first floor), LT-10223 Vilnius, Lithuania

<sup>2</sup> Vilnius University faculty of physics, Saulėtekio avenue 9, bld. III, LT-10222 Vilnius, Lithuania  
[abromavicius@gmail.com](mailto:abromavicius@gmail.com)

One of the main problems in laser physics is tuning of laser radiation frequency. There are many ways developed to do that (e.g. second and higher harmonic generation, Brillouin and Raman scattering, free electron lasers and parametric light generation and amplification). The purpose of this work was to construct parametric light generator pumped by 1064 nm laser beam and effectively generate signal beam in 1500 nm region. Then amplify the signal and analyze its properties.

Most of the recent works in this area use 532 nm laser beam as pump source, e.g. [1] achieved broad tunability from 750 nm to 1040 nm. But we chose 1064 nm pump beam, which allowed us to achieve signal beam in 1500 nm region where light radiation is less harmful for human eye. The experiment was divided into two steps: first – constructing standing wave OPG (*optical parametric generator*); second – using traveling wave OPA (*optical parametric amplifier*) to amplify the signal wave.

In first part we constructed half confocal OPG with resonator length of 22 mm using a 20 mm KTP crystal. Signal wavelength was 1573 nm and energy exchanging efficiency was 20,09 % (with pumping power of 400 mW). The spectral distribution of OPG in visible light region is shown in Fig. 1. We also analyzed maximum efficiency's and generation threshold's dependency from resonator length. The results are presented in Fig. 2.

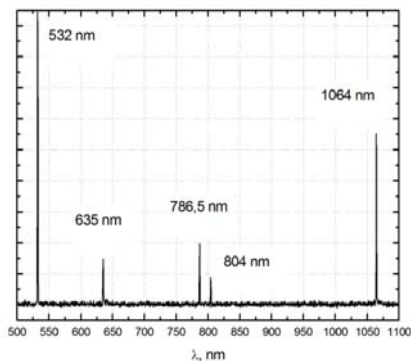


Fig. 1. The spectral distribution of OPG.

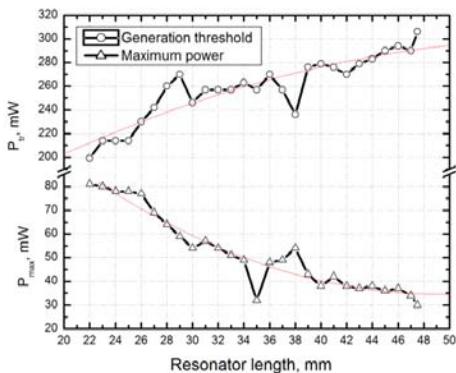


Fig. 2. Maximum efficiency's and generation threshold's dependency from resonator length.

Second part of the experiment used traveling wave OPA to amplify current signal. Achieved energy conversion ratio was 34 % (representing amplification from 25 mW to 110 mW, with pump power of 270 mW). The resulting beam was high power and ready for further analysis or usage.

For further development of this experiment using the same system we will construct OPG pumped by multiple pump waves (similar as described in [2], [3] and [4]) and instead of ordinary KTP crystal we will use periodically-poled PPKTP crystal (as described in [5]).

- [1] M. Yamanaka, N. Srinivasan, H. Kiriya, Y. Izawa, S. Nakai, All-Solid-State Tunable KTP Optical Parametric Oscillator Amplifier System, Journal of the Korean Physical Society, Vol. 33, No. 3, 244-250 (1998).
- [2] V. Smilgevičius, A. Stabinis, Two-beam pumped travelling-wave optical parametric generator, Optics Communications 103, 69-74 (1993).
- [3] D. Kezys, M. Gecevičius, A. Piskarskas, V. Pyragaitė, V. Smilgevičius, A. Stabinis, Multibeam pumping of OPA by Radiation of Fiber Amplifiers, Lithuanian Journal of Physics, Vol. 51, No. 2, 137-142 (2011).
- [4] A. Dubietis, R. Danielius, G. Tamošauskas, A. Piskarskas, Combining effect in a multiple-beam-pumped optical parametric amplifier, Optical Society of America, Vol. 15, No. 3, (1998).
- [5] M. Tiitonen, V. Pasiskevičius, F. Laurell, Spectral and spatial limiting in an idler-resonant PPKTP optical parametric oscillator, Optics Communications 250, 207-211 (2005).

## INVESTIGATION OF Cu(In,Ga)Se<sub>2</sub> LAYER PROPERTIES BY MEANS OF FOURIER SPECTROSCOPY

Martynas Šoliūnas<sup>1,2</sup>, Saulius Balakauskas<sup>1</sup>, Vincas Tamošiūnas<sup>1,2</sup>

<sup>1</sup> Center for Physical Sciences and Technology, A. Goštauto 11, LT-01108 Vilnius, Lithuania

<sup>2</sup> Faculty of Physics, Vilnius University, Saulėtekio al. 9, Bldg. III, LT-10222 Vilnius, Lithuania  
[mart.soliunas@gmail.com](mailto:mart.soliunas@gmail.com)

Cooper indium gallium diselenide (Cu(In,Ga)Se<sub>2</sub>) thin-film solar cells are one of the most likely candidates to replace most popular silicon solar cells in the future. Characterization of Cu(In,Ga)Se<sub>2</sub> absorbers helps to improve their efficiency and other parameters, and can be done by several methods. In this work, application of FTIR (Fourier Transform Infrared Spectroscopy) for the investigation of Cu(In,Ga)Se<sub>2</sub> thin films is presented.

Thin film solar cells Cu(In,Ga)Se<sub>2</sub> absorber samples were prepared by depositing about 1 μm thick CIGS layer. This was done by magnetron sputtering technique with Alcatel SCM 650 magnetron sputtering device using quaternary CIGS target (Pioneer Materials, 20 cm diameter, 6,35 mm thickness, composition: Cu – 22,8 %, In – 20 %, Ga – 7 %, Se – 50,2 %). Polished soda lime glass was used as substrate. For sample CIGS-A, substrate first was covered with approx. 1 μm Mo layer, deposited from the second target in the same equipment. Afterwards, 700 nm thick CIGS layer was deposited and was annealed at about 540°C temperature. For sample CIGS-B, 920 nm thick CIGS layer was grown directly on the glass. Process parameters were the same, as in a case of other samples [1], with confirmed CIGS crystalline structure from measurements using XRD (x-ray diffraction), SEM (scanning electron microscopy) and Raman spectroscopy techniques.

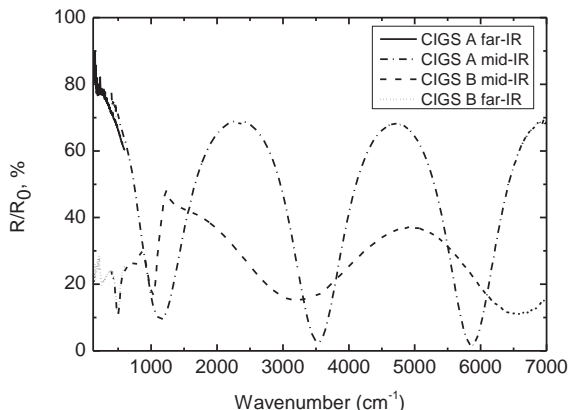


Fig. 1. FTIR spectra of samples CIGS-A and CIGS-B.

FTIR measurements were performed using Nicolet 8700 FT-IR spectrometer. Measurement results are presented in Fig. 1. Several main features should be mentioned. First, clear Fabry-Perot interference indicates, that CIGS layer is transparent within the entire IR range. With more precise measurements of refractive index, this feature can be applied for thickness control. Second, increased reflectivity feature, first observed in [1] is less pronounced at 200 cm<sup>-1</sup>, probably due to less perfect crystalline structure. Also, reflectivity difference in far-IR range can be attributed to transparency of the CIGS layer and different reflection coefficients of glass and molybdenum layer.

M. Šoliūnas would like to acknowledge the support by project "Promotion of Student Scientific Activities" (VP1-3.1-ŠMM-01-V-02-003) from the Research Council of Lithuania. Samples were prepared within project VP1-3.1-ŠMM-08-K-01-009, that is partly supported by the National Programme "An improvement of the skills of researchers", launched by the Lithuanian Ministry of Education and Science.

[1] L. Minkevičius, S. Balakauskas, M. Šoliūnas, R. Suzanovičienė, J. Uzėla, G. Molis, R. Juškėnas, A. Selskis, G. Niaura, G. Valušis, V. Tamošiūnas, Far infrared spectroscopy and imaging of Cu(In,Ga)Se<sub>2</sub> layers (submitted).

# MECHANISMS OF OPTICAL GAIN IN ZnO CRYSTALS

V. Tumas<sup>1</sup>, E. Kuokštis<sup>1</sup>, M. Karaliūnas<sup>1</sup>, E. Anisimovas<sup>2</sup>

<sup>1</sup> *Department of Semiconductors Physics, Vilnius University, Sauletekio Ave. 9-III, LT-10222 Vilnius*

[vytautas.tumas@ff.stud.vu.lt](mailto:vytautas.tumas@ff.stud.vu.lt)

<sup>2</sup> *Department of Theoretical Physics, Vilnius University, Sauletekio Ave. 9-III, LT-10222 Vilnius*

Zinc oxide (ZnO) is a promising material for modern optoelectronics. Recently interest in investigation of ZnO and ZnO-based structures increased essentially due to achievements in growing technology of high quality of quantum-size structures along with unique electrical, optical and crystal structure properties of ZnO itself. It is important not only for industry, medicine and other industries, including novel optoelectronic devices, but for fundamental investigation, too. The oneness of ZnO among other semiconductors is due to large direct energy gap, which ranges from 3.44 to 3.38 eV in temperature interval from 0 to 300 K, and unusually large (60 meV) exciton binding energy. These properties make ZnO a promising material for optoelectronics and are almost ideal for LEDs and laser diodes operating in the blue and near ultraviolet spectra region.

In this paper, various interactions of particles responsible for optical properties of material are taken into consideration.

Usually, inelastic interactions of excitons are very important for optical properties including luminescence mechanisms in highly excited crystal, when colliding excitons annihilate eradiating photons and break down into pairs of electrons and holes, or moves to higher kinetic energy and/or higher excited states. These interactions can be also very important analyzing optical gain.

In first figure are shown optical gain spectra for four different excitonic interactions: a)  $(E_{1s}^K, E_{1s}^{K'}) \rightarrow (\hbar\omega, e-h)$ , b)  $(E_{1s}^K, E_{2s, 2p}^{K'}) \rightarrow (\hbar\omega, e-h)$ , c)  $(E_{1s}^K, E_{1s}^{K'}) \rightarrow (\hbar\omega, E_{2s, 2p}^{K''})$  and d)  $(E_{1s}^K, E_{1s}^{K'}) \rightarrow (\hbar\omega, E_{1s}^{K''})$ .

Also in this work is calculated optical gain spectra for electron – hole plasma at different temperatures and at different excitation rates (Fig. 2).

## HIGH POWER LIGHT EMITTING DIODES AS SOURCES FOR NOVEL SOLAR SIMULATORS

Andrius Vaitkūnas<sup>1</sup>, Algirdas Novičkovas<sup>1</sup>, Algirdas Mekys<sup>1</sup>, Vincas Tamošiūnas<sup>1,2</sup>

<sup>1</sup> Faculty of Physics, Vilnius University, Saulėtekio al. 9, Bldg. III, LT-10222 Vilnius, Lithuania

<sup>2</sup> Center for Physical Sciences and Technology, A. Goštauto 11, LT-01108 Vilnius, Lithuania  
[andrius.v92@gmail.com](mailto:andrius.v92@gmail.com)

Solar simulators are devices providing illumination, which similar to the natural sunlight in standardized conditions. Their purpose is to provide a possibility of controllable indoor test for evaluation of solar cells and modules. Most usually, so-called AM1.5 conditions for the Solar spectrum are simulated. Several types of light sources are used for solar simulators. For examples, xenon arc lamps are the most common source today due to a reasonably good match of the spectrum. However, a quite complex optical system is required to ensure an even illumination at the test plane, which leads also to low energy efficiency of test systems. Quartz tungsten halogen (QTH) lamps offer an alternative; however, their lower color temperature leads to difficulties in filtering out the excessive long wavelength components. Recently, 1.5 W light emitting diodes (LEDs) were already applied to simulate solar radiation with 90% of the required by the standard intensity [1]. In addition, hybrid LED and halogen lamp source with B class spectral match was also demonstrated [2].

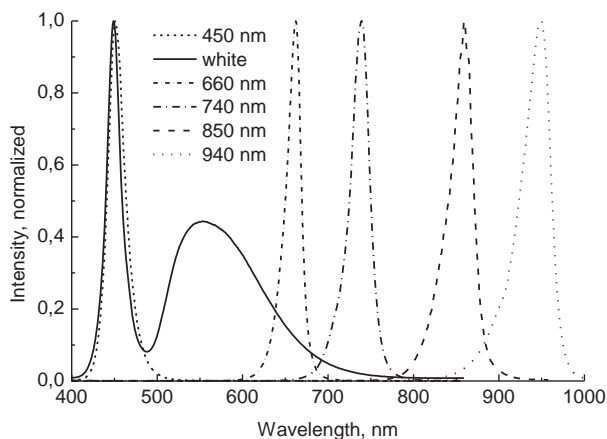


Fig. 1. Emission spectra of investigated light emitting diodes.

In this contribution, we report on the evaluation of high power LEDs for application in solar simulators. Distributions of radiant flux were investigated at various distances using motorized 2D stage and test photodiode with Thorlabs power meter. Six types of light emitting diodes were investigated. Majority of radiated power was provided by cool white Bridgelux LEDs of approx. 10 W of electrical power. These LEDs can provide (see Fig. 1) all the required [3] radiation in 500 – 600 nm spectral range and contribute most of the required optical power for 400 – 500 nm range. The remainder is provided by 3 W Luxeon royal blue LEDs. Ledengin LZ4 10 W LEDs served as light sources in 600 – 700 nm and 700 – 800 nm ranges, while Osram IR LEDs were employed in 800 – 900 nm and 900 – 1100 nm ranges.

Research was supported by the Research Council of Lithuania (Grant No. MIP-099/2012). A. Vaitkūnas would also like to acknowledge the support by project "Promotion of Student Scientific Activities" (VP1-3.1-ŠMM-01-V-02-003) from the Research Council of Lithuania.

[1] S.H. Jang, M.W. Shin, Current Applied Physics 10 (2010) S537–S539.

[2] M. Bliss et al. Solar Energy Materials & Solar Cells 93 (2009) 825–830.

[3] International Electrotechnical Commission standard IEC 60904-9 Ed. 2.0.

## TEMPERATURE AND FLUENCE DEPENDENT VARIATIONS OF STUDY OF CARRIER LIFETIME VARIATIONS IN Si STRUCTURES

Arūnas Velickā, Tomas Čeponis, Eugenijus Gaubas

Institute of Applied Research, Vilnius University, Sauletekio Ave. 9-III, LT-10222 Vilnius, Lithuania  
[Arunas.Velicka@ff.stud.vu.lt](mailto:Arunas.Velicka@ff.stud.vu.lt)

Temperature and fluence dependent variations of excess carrier lifetime and generation current in Si (silicon) device structures can be a powerful tool for evaluation radiation defects density and spectral signatures [1-3].

In this work, study of excess carrier lifetime dependences on fluence of reactor neutrons and accelerated protons has been performed on n- and p- type conductivity Si material wafers. The experimental measurements of carrier lifetimes were implemented by using a microwave-probed photoconductivity transient technique (MW-PCD) [1] and employing VUTEG-5-AIDA and VUTEG-SA10 instruments. These instruments were designed and fabricated at VU (Vilnius University) for fast and non-invasive measurements of dose dependent changes of radiation defect densities. These defect densities are evaluated through the linear relation between carrier lifetime and reciprocal trap density. Also, measurements of the temperature dependent excess carrier lifetime variations were carried out on MCZ n-type Si neutron irradiated and annealed samples (Fig. 1).

Temperature dependent variations of generation current have been performed by using pulsed BELIV (Barrier evaluation by linearly increasing voltage) technique on Si solar cells and neutron irradiated Si pin diodes to perform spectral evaluations of the prevailing deep traps (Fig. 2).

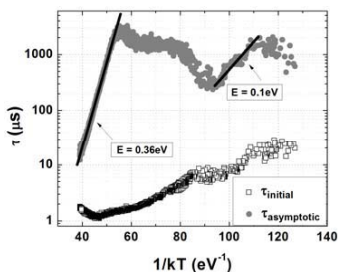


Fig. 1. Excess carrier lifetime temperature dependence of  $10^{14} \text{ cm}^{-2}$  neutron fluence irradiated Si wafer.

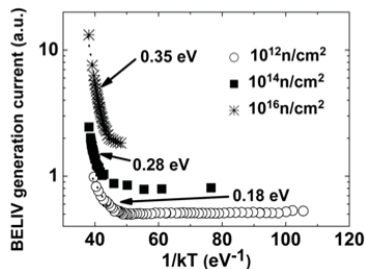


Fig. 2. BELIV generation current temperature variations of  $10^{12}$ ,  $10^{14}$  and  $10^{16} \text{ cm}^{-2}$  neutron fluence irradiated PIN diodes.

[1] S.Rein. Lifetime spectroscopy: a method of defect characterization in silicon for photovoltaic applications. Springer, 1 edition (2005).

[2] E. Gaubas, T. Čeponis, V. Kalendra, J. Kusakovskij, and A. Uleckas. Barrier evaluation by linearly increasing voltage technique applied on Si structures. ISRN Materials Science, 543790, 2012.

[3] E. Gaubas, V. Kalendra, T. Čeponis, A. Uleckas, A. Tekorius, J. Vaitkus and A. Velickā. Study of deep level characteristics in the neutrons irradiated Si structures by combining pulsed and steady-state spectroscopy techniques. 14th international workshop on radiation imaging detectors, 2012.

## ELECTRORESISTANCE OF NANOSTRUCTURED MANGANITE FILMS

Laura Žurauskaitė<sup>1,2</sup>, Saulius Balevičius<sup>1</sup><sup>1</sup>Department of Material Sciences and Electrical Engineering, Center for Physical Sciences and Technology, Lithuania<sup>2</sup>Department of Physics, Vilnius University, Lithuania

zurauskaitė.laura@gmail.com

The electromagnetic pulse (EMP) generated in free space by natural or artificial electromagnetic pulse sources, such as lighting, nuclear EMP or Directed Energy Weapons, can induce high power over-currents in electronic equipment and damage its active electrical components [1]. In order to protect electronic circuits to withstand short EMP, fast fault current limiters are required. Switches based on gas discharge plasma limiters, varistors, and other protectors are slow due to large intrinsic capacitance and their response time is limited to microseconds [2]. Taking into account that EMP pulses are bipolar, the design of symmetrical protectors is of great importance. It was demonstrated [3,4] that thin films of perovskite manganites can be used for fast fault current limiter applications.

In this work, the effects of strong electric fields on the resistivity of thin nanostructured La-Ca(Sr)-Mn-O films, deposited on lucalox substrates by a MOCVD technique with thicknesses of 350 nm were investigated at 5-290 K temperature range in a closed cycle helium gas cryo-cooler by using electrical pulses with pulse lengths of 5 ns, and amplitudes up to 500 V.

It was obtained that nanostructured La-Ca(Sr)-Mn-O films exhibit negative electroresistance (ER) phenomenon at applied strong electric field. The ER was defined by the formula:  $ER = 100\% [R(E) - R(0)] / R(0)$ , where  $R(E)$  and  $R(0)$  are resistances of the film at high and low electric field, respectively. The influence of film chemical composition was analyzed in order to determine the optimal conditions for the design of protectors operating at low temperatures (liquid nitrogen) as well as room temperature. The electroresistance measured at electric fields with amplitudes up to 90 kV/cm for the La-Sr-Mn-O films and 35 kV/cm for the La-Ca-Mn-O films is presented in Fig. 1. One can see that absolute values of ER increase with the electric field strength. The highest ER values were obtained at temperatures, equal or lower than metal-insulator transition temperature  $T_m$  of the films: 200 K for the La-Ca-Mn-O films and 230 K for the La-Sr-Mn-O films. Such electroresistance effect is related to the existence of grain boundaries in the nanostructured films and in most cases this can be explained by inelastic charge carrier tunneling [5]. The most evident difference between the La-Ca-Mn-O and La-Sr-Mn-O films is the strength of the electric field at which the same ER is achieved. For the La-Ca-Mn-O films, this field is 1.7–2 times lower. The threshold field at which the resistance decreases was also lower for films doped with Ca: 0.8 kV/cm at 80 K, 1.1 kV/cm at 290 K, while for the La-Sr-Mn-O film, this was 2.5 kV/cm and 9 kV/cm, respectively.

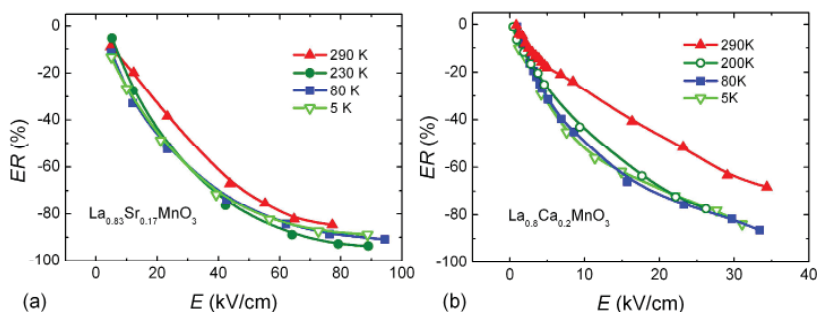


Fig. 1. Electroresistance of La-Sr-Mn-O (a) and La-Ca-Mn-O (b) films.

The losses  $L(E)$  in the transmission line induced by the manganite films were investigated when connecting the samples in parallel to a transmission line. It was demonstrated that using manganite films doped with Ca it is possible to obtain better limiting characteristics at lower threshold electric field values: for La-Ca-Mn-O films the  $L \approx 4$  dB when  $E = 25$  kV/cm, while for La-Sr-Mn-O films the same losses were obtained at 90 kV/cm.

[1] Developing Threats: Electro-Magnetic Pulses (EMP), The House of Commons, Defense Committee, London, 2012.

[2] M. A. Weimer, L. F. Hakim, D. M. King, X. Liang, A. W. Weimer, S. M. George, P. Li and M. D. Groner, Ultrafast metal-insulator varistors based on tunable  $Al_2O_3$  tunnel junctions, Appl. Phys. Lett. **92**, 164101-1-3 (2008).[3] N. Žurauskienė, Thin manganite films for fast fault current limiter applications, Thin Solid Films **515**, 576–579 (2006).[4] S. Balevičius, N. Žurauskienė, V. Stankevič, S. Keršulis, A. Abrutis, V. Plauškaitienė and L. L. Altgilbers, Fast protector against EMP using thin epitaxial and polycrystalline manganite films, IEEE Electr. Device Lett. **32**, 551–553 (2011).[5] M. Ziese, Grain-boundary magnetoresistance in manganites: Spin-polarized inelastic tunneling through a spin-glass-like barrier, Phys. Rev. B **60**, R738-R741 (1999).

## SINTERING OF GADOLINIUM DOPED CERIA CERAMICS AND THEIR ELECTRICAL PROPERTIES

Audronė Žemaitytė, Saulius Kazlauskas

Faculty of Physics, Vilnius University, Saulėtekio 9, LT-10222 Vilnius, Lithuania  
*audrone.zemaityte@gmail.com*

Challenges exist in the solid oxide fuel cell (SOFC) research area due to their high operating temperatures, which results in the degradation of SOFC components, material compatibility issues and etc [1]. In this paper we present sintering conditions and electrical properties in a wide frequency and temperature range of  $\text{Ce}_{0.9}\text{Gd}_{0.1}\text{O}_{1.95}$  (10GDC) and  $\text{Ce}_{0.8}\text{Gd}_{0.2}\text{O}_{1.9}$  (20GDC).

One problem concerning ceria-based electrolytes is that conventional sintering to full density requires temperatures exceeding 1570K. Rather high grain growth rates at those temperatures result in large grains and therefore poor mechanical stability [2]. In order to obtain ceramics with small grains and high stability, powders with a high surface area were used for sintering. Powders for solid electrolyte ceramics were shaped by uniaxial cold pressing at 300MPa. Ceramics were sintered in air atmosphere for 1h, sintering temperatures of 10GDC and 20GDC ceramics were 1373, 1473, 1573, 1673 and 1773 K. Sintered ceramics were studied by impedance spectroscopy method in a wide frequency range 10 Hz – 3 GHz at temperatures up to 700K in air. For the measurements of complex specific ionic conductivity ( $\sigma$ ) and complex specific impedance ( $\rho$ ) 2-electrode and 4-electrode methods were used.

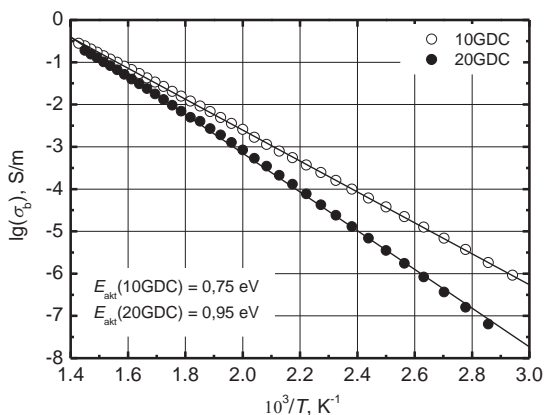


Fig. 1. Temperature dependences of bulk conductivities of 10GDC and 20GDC ceramics.

Temperature dependences of  $\sigma_b$  investigated ceramics are shown in Arrhenius plots. 10GDC ceramics shows a 0.28 S/m bulk ionic conductivity at 700 K. 20GDC ceramics shows a 0.19 S/m ionic conductivity at the same temperature. For ceramic compounds 10GDC and 20GDC relative density greater than 94% was achieved.

All investigated ceramics showed results which are appropriate for successful operation as an electrolyte in intermediate temperature SOFCs.

[1] B.C.H. Steele and A. Heinzel, Materials for fuel-cell technologies, Nature 414, 345-352 (2001).

[2] Y.C. Zhou, R.J. Philips, and J.A. Switzer, Electrochemical synthesis and sintering of nanocrystalline cerium(IV) oxide powders, J. Am. Ceram. Soc. 78(4), 981-985 (1995).

## Fabrication and investigation of NASICON-type solid electrolytes

Loreta Žukauskaitė<sup>1</sup>, Maud Barre<sup>2</sup>

<sup>1</sup> Faculty of physics, Vilnius University, Lithuania

<sup>2</sup> Institut de Recherche en Ingénierie Moléculaire et Matériaux Fonctionnels, Université du Maine, France  
[loreta.zukauskaite@stud.fv.vu.lt](mailto:loreta.zukauskaite@stud.fv.vu.lt)

NASICON materials have been extensively studied because of the high conductivity shown by some compositions and significant potential applications in electrochemical devices. [1,2]. The NASICON structure has a negatively charged 3D-framework, of general formula  $M_2X_3O_{12}$ , where the  $Na^+$  cations reside in fully or partially-occupied sites. The framework is built of  $XO_4$  tetrahedra linked by corners to  $MO_6$  octahedra. In general, the properties of the NASICON-type  $Na^+$  ion conductor compounds strongly depend upon the chemical stoichiometry, the crystal structure and unit cell parameters, that, at the same time, depend on the ionic radii of the cations located in octahedral (M) and tetrahedral (X) sites.[3] We have chosen the  $Na_{1.3}X_{1.7}Al_{0.3}(PO_4)_3$  ( $X=Ti, Zr$ ) and  $Li_{0.65}Na_{0.65}Ti_{1.7}Al_{0.3}(PO_4)_3$  series because of the low cost of the elements, high conductivity and stability with aqueous solutions.

In the present work, the pure materials have been prepared by solid state reaction and by a Pechini-type method. The XRD patterns of the calcinated powders were recorded in order to refine the crystal structures. Thermogravimetric data were recorded in order to follow the chemical reactions. The morphology of the samples was examined by Scanning Electron and Transmission Electron Microscopes (Fig. 1). The stability of NASICON powder in contact with water and humidity in ambient air was confirmed by using flame photometry and FTIR respectively. The sintering parameters were optimized on the basis of dilatometric data. The investigation of the electrical properties were performed in the frequency ranges ( $10^{-3}$ – $10^9$ ) Hz by low frequency and microwave impedance spectrometers in order to determine the influence of grain size on electrical properties.

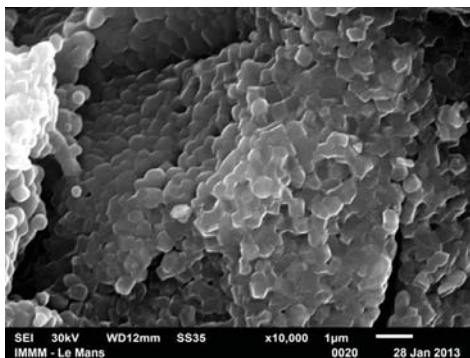


Fig. 1. SEM image of  $Na_{1.3}Ti_{1.7}Al_{0.3}(PO_4)_3$  pellet floc sintered at 850°C

[1] H.Y.-P. Hong, Mater. Res. Bull. 11 (1976) 173.

[2] H. Aono, E. Sugimoto, Y. Sadaoka, N. Imanaka, G. Adach, J. Electrochem. Soc. 140 (1993) 1827 - 1832

[3] P. Maldonado-Manso, M. A. G. Aranda, S. Bruque, J. Sanz, E. R. Losilla, Solid State Ionics 176 (2005) 1613 - 1625



# DIELECTRIC PROPERTIES OF NANOGRAIN BSPT CARAMICS

Sergejus Balčiūnas<sup>1</sup>, Maksim Ivanov<sup>1</sup>, H.Amorin<sup>2</sup>, A. Castro<sup>2</sup>, M. Algueró<sup>2</sup>, Jūras Banyš<sup>1</sup>

<sup>1</sup>Faculty of Physics, Vilnius University, Sauletekio 9/3 817k., LT10222 Vilnius, Lithuania

<sup>2</sup>Instituto de Ciencia de Materiales de Madrid, CSIC, Cantoblanco, 28049 Madrid, Spain  
sergejus.balciunas@gmail.com

Ferroelectric materials are of high interest for both researchers and engineers due to their remarkable properties. Their switchable electric polarization [1] is ideal for use in devices for memory storage and integrated microelectronics. Advanced devices tend to nanoscale, that raises necessity to research new cheaper and more durable materials.

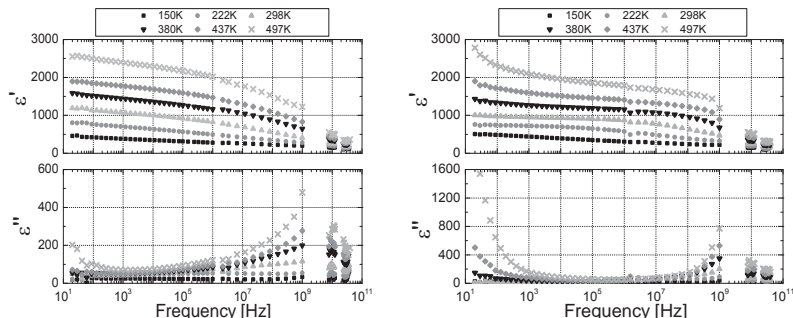


Fig.1 Frequency dependence of real (top) and imaginary (bottom) parts of dielectric permittivity for BSPT 1.6  $\mu\text{m}$  grain size ceramics produced in WC milling media (left) and Stainless steel milling media (right).

BSPT ( $x\text{BiScO}_3-(1-x)\text{PbTiO}_3$ )  $x=0.36$  and  $0.375$  ceramics with micron, submicron and nanoscale grains were produced from nanocrystalline powders obtained by mechanosynthesis [2] in different milling media. In figure 1 we can see that ceramics made with stainless steel milling media have higher dielectric permittivity at low frequencies compared to ones produced with WC milling media. WC-milled ceramics also exhibit a more narrow dispersion region, however dielectric permittivity decreases more rapidly at high frequencies ( $10^6$ - $10^9$  Hz) in this case. Both ceramics have similar dielectric properties in microwave region (10 – 40 GHz).

[1] C. H. Ahn, K. M. Rabe, J.M. Triscone, *Science* 23 January, 2004, Vol. 303 No. 5657 pp. 488-491

[2] M T. Hungria, H. Amorin, M. Alguero, A. Castro, *Scripta Materialia*, 2011, No.64, 97-100

## CARBAZOLE AND FLUORENE DERIVATIVES FOR OPTOELECTRONIC APPLICATIONS

Paulius Baronas<sup>1</sup>, Saulius Juršėnas<sup>2</sup>, Karolis Kazlauskas<sup>2</sup>, Austra Tomkeviciene<sup>3</sup>, Juozas Vidas Grazulevicius<sup>3</sup>

<sup>1</sup> Vilnius University, Saulėtekio al. 9-III, LT-10222 Vilnius, Lithuania

<sup>2</sup> Institute of Applied Research, Vilnius University, Saulėtekio al. 9-III, LT-10222 Vilnius, Lithuania

<sup>3</sup> Department of Organic Technology, Kaunas University of Technology, Radvilėnu pl. 19, LT-50254 Kaunas, Lithuania

*Paulius.Baronas@ff.stud.vu.lt*

Carbazole and fluorene are perspective materials for application in organic blue light - emitting diodes (OLED) considering their high fluorescence quantum emission efficiency and good electrical properties. By combining carbazole and fluorene elements, larger multifunctional molecular compounds with better optical and electronic properties could be produced. Moreover, the thermal stability and glassy state durability of these organic molecules were found to be significantly improved upon incorporation of a carbazole and fluorene moiety in the structure [1].

In this work photophysical properties of a set of tetrameric carbazole and fluorene derivatives (Fig. 1 AM-114, AM-124, AM-138) were investigated. Their optical properties were compared with trimeric and dimeric compounds of similar molecular structure.

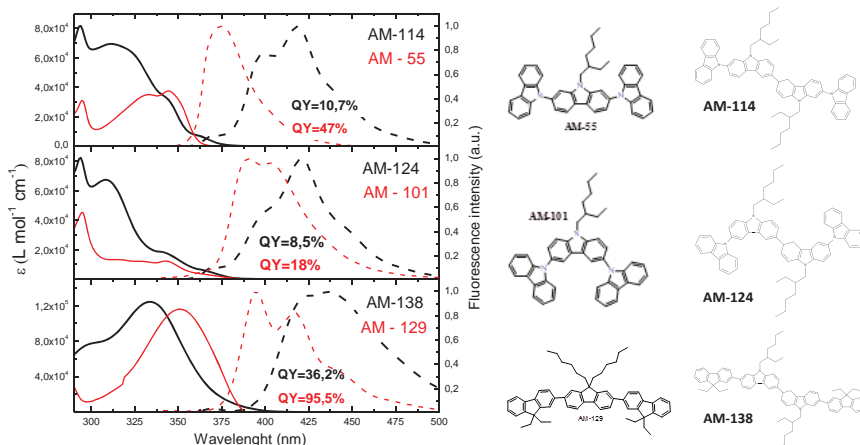


**Fig. 1.** Absorption and fluorescence spectra of trimeric and tetrameric carbazole – fluorene compounds dissolved in tetrahydrofuran solvent. Fluorescence quantum yields are indicated.

Spectroscopic analysis of novel carbazole and fluorene derivatives showed that elongated  $\pi$ -electron conjugation caused significant red shift of absorbance and fluorescence bands compared to trimeric compounds (Fig. 1). Fluorescence quantum yield (QY) was found to be lower (from 8% to 40%) for tetrameric compounds in dilute solutions. Comparable fluorescence spectra and low QY values could be influenced by emission from central 3,3'-bicarbazole structure. However introduction of fluorene moiety enhanced QY both in dilute solution and solid state. A reduction of QY in thin films (from 1.8 % to 8 %) was observed due to close molecular packing.

Relatively high fluorescence decay times ( $\tau_{AM-114}=6.5$  ns,  $\tau_{AM-124}=6.8$  ns,  $\tau_{AM-129}=5.21$  ns) and low fluorescence quantum yields resulted in higher non-radiative recombination rate in respect of radiative rate. Fluorescence decay transients in the solid state exhibited the non – exponential behavior implying the existence of few molecular conformation states in excited state.

Although tetrameric carbazole and fluorene molecules did not exhibit fine optical properties for application as blue-light emitter, strong excitonic coupling in solid state shows tight molecular packing and, thus possibility to use the materials as charge transfer layers. This is in line with pronounced hole mobility values of  $10^{-3}$  cm<sup>2</sup>/Vs obtained by xerographic time-of-flight technique.

[1] Van Dijken, A.; Bastiaansen, J. J. A. M.; Kikken, N. M. M.; Langeveld, B. M. W.; Rothe, C.; Monkman, A.; Bach, I.; Stossel, P.; Brunner, K. J. Am. Chem. Soc., 126, 7718–7727 (2004).

## TRANSISTOR BASED TERAHERTZ SENSORS NOISE CHARACTERISATION

Marek Burakevič<sup>1</sup>, Mantas Ragauskas<sup>1,2</sup>, Jonas Matukas<sup>1</sup>, Gintaras Valušis<sup>2</sup>

<sup>1</sup>Department of Radiophysics, Vilnius university, Lithuania

<sup>2</sup>Center for Physical Sciences and Technology, Lithuania

[marek.burakevic@ff.stud.vu.lt](mailto:marek.burakevic@ff.stud.vu.lt)

Recent tendencies in imaging research show an active interest in terahertz (THz) radiation. Ability of THz radiation to propagate through clothing or common packaging materials makes it perfect for purposes of security. One of the key points in implementing THz imaging systems is having sensitive and reliable sensors, that are capable of working at room temperatures. At the moment, three main types of sensors are used: so called bow-tie diodes, that use electrons heated in non-uniform electric field, microbolometers and field-effect transistors with two-dimensional electron gas (2DEG)

Transistor approach was found to be an effective solution for detection of radiation [1]. Detection mechanism relies on 2DEG under the gate of transistor. Under certain conditions it acts similarly to shallow water and has resonant properties. What is even more useful – detection frequency depends on working parameters of transistor. By changing parameters one can change its mode as it can work either as a wide, either as a narrow spectrum detector.

Investigation of noise characteristics under varying parameters (like temperature) allows to determine certain processes inside of the sensor as well as to reveal the main sources of fluctuations [2].

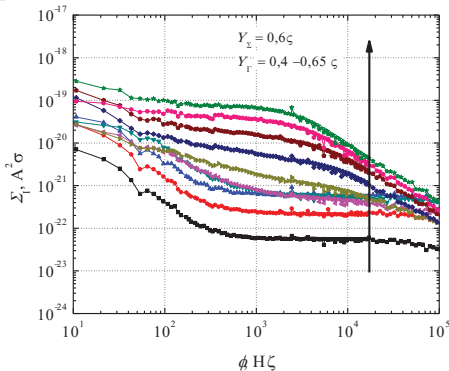


Fig. 1 Spectral density of current fluctuations at room temperature.

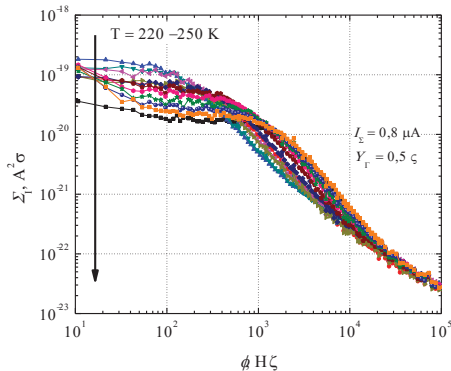


Fig. 2 Spectral density of current fluctuations at various temperatures

Matrix of 5x10 transistors with varying channel lengths and widths was investigated. Even at room temperature Lorentzian type spectra prevailed typical 1/f type spectra for all measured examples (Fig. 1). Changing lattice temperature, while maintaining constant current (Fig. 2) yielded activation energies of approximately 0.2 eV. These results allow to assume, that noise is generated by generation and recombination processes in the defects of the structure

[1] [A. Laisauskas, S. Boppel, H. G. Roskos, J. Matukas, V. Palenskis, L. Minkevičius, G. Valušis, P. Haring Bolivar, *Terahertz responsivity enhancement and low-frequency noise study in silicon CMOS detectors using a drain current bias*, IEEE issue of **ICNF2011**: 21st International Conference on Noise and Fluctuations, June 12-16, 2011, Toronto, Canada, P. 301-304.]

[2] [O. Klimenko, W. Knap, B. Iniguez, D. Coquillat, Y. A. Mityagin, F. Teppe, N. Dyakonova, H. Videlier, D. But, F. Lime, J. Marczewski, and K. Kucharski, *Temperature enhancement of terahertz responsivity of plasma field effect transistors*, J. Appl. Phys. **112**, 014506 (2012)]

## HYBRID ORGANIC-INORGANIC X-RAY SENSITIVE LAYER FORMATION AND INVESTIGATION OF ELECTRICAL PROPERTIES

Rokas Dobužinskas, Kęstutis Arlauskas, Andrius Poškus

<sup>1</sup> Department of Solid State Electronics, Physics Faculty, Vilnius University, Saulėtekio Ave. 9-III, LT-10222 Vilnius, Lithuania  
ramblerlt@gmail.com

Organic semiconductors have recently been used as the transduction material in X-ray detectors. However, these devices have quite low sensitivity because of low attenuation coefficient of thin organic layer. We tried overcome this problem by introducing dense high atomic number (Z) particles, which may increase X-ray attenuation, into organic hole transport material [1].

The ability for a certain material to attenuate X-rays is called the attenuation quantum efficiency (QE) and can be expressed by equation [2]:

$$QE = (1 - e^{-\frac{\mu}{\rho} \rho x}) 100\%$$

Here  $\mu/\rho$  is the mass attenuation coefficient, obtained from a photon attenuation database [3], and  $\rho$  and  $x$  are the density and thickness of the material, respectively.

Into hexaryldiamine (HADA) the various concentrations of ZnCdS ( $Z_{Cd} = 48$ ) were added to form X-ray sensitive layers by thermal fusion. Optimal fusion temperature of HADA is estimated 210 °C.

The X-ray photocurrent measurements of the devices were completed using 8 keV  $K_{\alpha}$  X-rays from a copper target (PHYWE Instruments). In 2kV/cm electric field the 42 pA, 102 pA and 188 pA photocurrents have been measured for pure, 25% and 50% ZnCdS concentration layers respectively. The signal-to-noise ratio is defined by the ratio between the corrected X-ray photocurrent and the dark current. Best result 80 dB was obtained for layer with 25% of ZnCdS. For pure and 50% ZnCdS layers it varied between 10 and 20 dB.

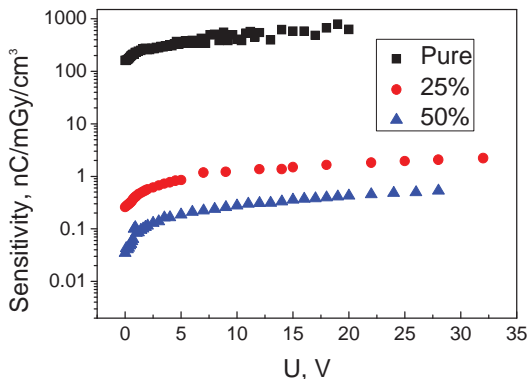


Fig. 1. Various ZnCdS concentration layers sensitivity dependence on applied voltage

According to XCOM model [3] quantum efficiency for various concentration layers are respectively 0.4%, 21%, 48% for pure (■), 25% (●), 50% (▲) layers. Although photocurrent of higher concentration layer is higher the effect for sensitivity is opposite.

[1] A. Poškus. Atomo fizika ir branduolio fizikos eksperimentiniai metodai, Vilniaus universitetas, 2008, 109.

[2] A. Intaniwet et al, Heavy metallic oxide nanoparticles for enhanced sensitivity in semiconducting polymer x-ray detectors, Nanotechnology 23, Maejo University, Thailand, 2012, 2.

[3] Berger M J, Hubbell J H, Seltzer S M, Chang et al, 2011 XCOM: Photon Cross Sections Database, National Institute of Standards and Technology, USA, Standard Reference Database 8 (XGAM) <http://physics.nist.gov/PhysRefData/Xcom/Text/XCOM.html>.

# MULTICOLOUR LED CLUSTERS FOR PHOTOBIOLOGICALLY FRIENDLY SOLID-STATE LIGHTING

Paulius Eidikas<sup>1</sup>, Andrius Petrušis<sup>1</sup>

<sup>1</sup> Institute of Applied Research, Vilnius University, Lithuania  
[paulius.eidikas@ff.stud.vu.lt](mailto:paulius.eidikas@ff.stud.vu.lt)

Recently, light containing short-wavelength components became an object of debate due to the discovery of retinal intrinsically photosensitive ganglion cells that are sensitive to blue light. Blue-enriched white light is claimed to disrupt circadian rhythms and pose health issues even at low illuminance [1]. However in night-time conditions, the relevant luminances fall in the range of mesopic vision, where the luminous efficacy of blue-rich light sources increases with reducing adaptation luminance due to the shifting of the spectral sensitivity of vision to shorter wavelengths. This requires the optimization of the spectral power distributions (SPDs) of mesopic and photopic light sources.

Circadian action factor (1) (CAF) is a solid parameter for evaluating different light sources [2]. While linking CAF to the Kruithof curve [3], photobiologically friendly lighting can be achieved.

$$a_c = K_c / K = K_{c0} \frac{\int_{380nm}^{780nm} C(\lambda) S(\lambda) d\lambda}{K_0 \int_{380nm}^{780nm} V(\lambda) S(\lambda) d\lambda} \quad (1)$$

In this work a comparison of the CAF of trichromatic light-emitting diode (LED) clusters having different correlated colour temperatures (CCTs) and common lamps is discussed. It was shown, that CAF can be varied up to 10 times using trichromatic clusters composed of the commercial LEDs (fig. 1).

Based on an optimization [2], a prototype of an optimal dichromatic solid-state lamp with extra-low colour temperature for street lighting was demonstrated. It consisted of a 20 phosphor conversion amber (597 nm) and 2 direct emission royal blue (455 nm) light emitting diodes with CCT at 1855 K.

Reaction time and Farnsworth-Munsell (F-M) 100 hue tests were performed comparing high pressure sodium (HPS) and extra-low CCT dichromatic (“firelight”) lamp. It was shown up to 10% shorter reaction time and 20% improved F-M test score with “Firelight” lamp at mezopic 0,3 cd/m<sup>2</sup> luminance.

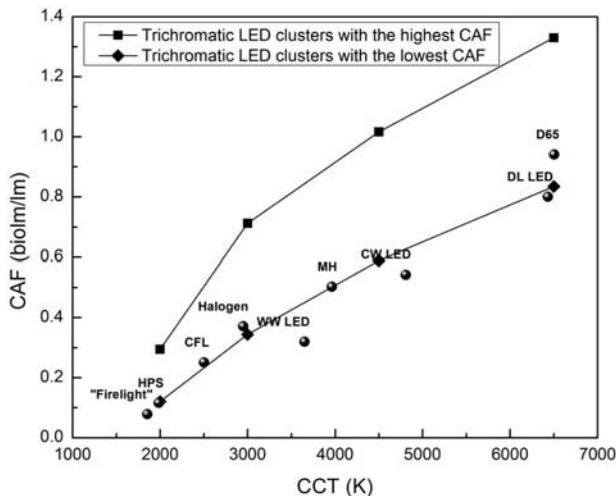


Fig. 1. Photopic CAF dependence on different light sources and CCT.

[1] D. Lang, Blue enhanced light sources opportunities and risks, Proc. SPIE 8278, 827803 (2012).

[2] A. Žukauskas, R. Vaitiekuskas and P. Vitta, Optimization of solid-state lamps form photobiologically friendly mesopic lighting, Appl. Optics 51 (35), 8423-8432 (2012).

[3] A. Kruithof, Tubular Luminescence Lamps for General Illumination, Philips Technical Review 6 (3): 65–96 (1941).

# DIAMOND SYNTHESIS USING PLASMA CHEMICAL VAPOUR DEPOSITION METHOD ON DIFFERENT SUBSTRATE MATERIALS

Eriks Elksnis<sup>1</sup>, Atis Skudra<sup>2</sup>, Arturs Viksna<sup>1</sup>

<sup>1</sup>Faculty of Chemistry, University of Latvia

<sup>2</sup>Institute of Atomic Physics and Spectroscopy, University of Latvia

[elksn@inbox.lv](mailto:elksn@inbox.lv)

Our work is concerned with the preparation, investigation and optimisation of low pressure DC plasma chemical vapour deposition systems for diamond synthesis on different substrate materials. A variety of chemical vapour deposition (CVD) methods have been developed over the last years to obtain layer of diamond at low pressure. These methods have led to many applications taking advantage of the exceptional properties of a diamond. However, their properties have to be improved and operational costs reduced.

In this work we used low power (60W and 120W) DC plasma discharge systems in order to deposit rare modification of nanostructural „cauliflower-like”, triangulary faceted and cubic high-quality diamond films and [polycrystalline](#) particles from hydrocarbon–hydrogen gas mixtures at low pressure on tungsten, molybdenum and nickel substrates. (Fig. 1a., 1b., 1c.).

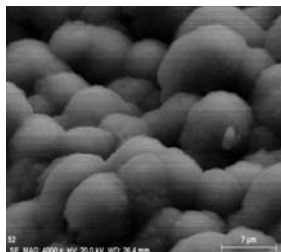


Fig. 1a Image of our „cauliflower-like” diamond coating on tungsten

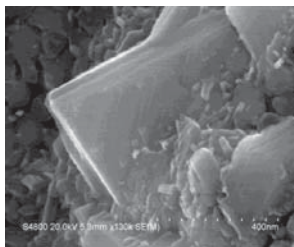


Fig. 1b Image of our „cubic” diamond polycrystalline particle on molybdenum

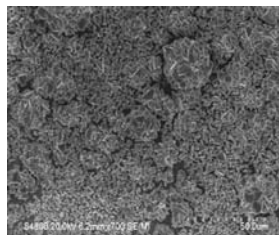


Fig. 1c Image of our „triangulary faceted” diamond coating on nickel

Discharge was operated for 40 - 100 hours, during whom diamond synthesis products on substrate were made. Analysis of tungsten, molybdenum and nickel substrate surfaces were performed by SEM-EDX and data showed that main component of the coating is carbon. There were also oxygen pollution traces.

The work was partly supported by;

1) National Research Program in Materials Science Project #1 Multifunctional materials.

## BROADBAND DIELECTRIC SPECTROSCOPY AND ULTRASONIC INVESTIGATIONS OF COMPOSITES OF POLY( $\epsilon$ -CAPROLACTONE) AND $\text{Mo}_6\text{S}_3\text{I}_6$ NANOWIRES

Džiugas Jablonskas<sup>1</sup>, Austė Kuprevičiūtė<sup>1</sup>, Šarūnas Svirskas<sup>1</sup>, Vytautas Samulionis<sup>1</sup>,  
Jūras Banys<sup>1</sup> and Tonny McNally<sup>2</sup>

<sup>1</sup>Vilnius University, Faculty of physics, Saulėtekio av. 9, III b., LT-10222 Vilnius, Lithuania

<sup>2</sup>School of Mechanical and Aerospace Engineering, Queen's University Belfast, BT9 5AH, UK

[dziugas.jablonskas@ff.stud.vu.lt](mailto:dziugas.jablonskas@ff.stud.vu.lt)

$\text{Mo}_6\text{S}_3\text{I}_6$  (MoSI) nanowires have excellent conductivity and are good alternative to carbon nanotubes as functional one dimensional (1D) nanofiller for polymeric materials used in electrostatic discharge, EMI shielding, flexible electronic substrate and electrode applications [1].

A Poly( $\epsilon$ -caprolactone) (PCL) is one of the most commonly used polymers in biomedical applications, mainly because it is biodegradable and non-toxic. Chemical formula of PCL is  $[[\text{CH}_2]_5\text{COO}]_n$ , where  $n \approx 300$ . It is A2-type polymer, it consists of monomers, which contain dipoles of carboxyl group, which are separated by non-polar methyl group. Dielectric spectroscopy of PCL has shown three relaxation processes, which are noted  $\alpha$ ,  $\beta$  and  $\gamma$ .  $\alpha$  relaxation resides in lower frequencies and it is the dielectric manifestation of the cooperative motions that occur at the dynamic glass transition temperature.  $\beta$  and  $\gamma$  relaxations, which resides in higher frequencies, are related with more localized dipole motions of polymer [2].

Some structural and mechanical characteristics of PCL- $x\%$ MoSI composite were investigated earlier and presented in [1]. However, there are very little data about dielectric properties of PCL- $x\%$ MoSI composite. Thus, the aim of this report is to present the results of dielectric spectroscopy of PCL- $x\%$ MoSI composites.

Also, the temperature dependencies of longitudinal ultrasonic velocity and attenuation in PCL- $x\%$ MoSI composites will be presented. The influence of nanowires in composite on ultrasonic properties will be discussed.

---

[1] S. J. Chin, P. Hornsby, D. Vengust, D. Mihailovič, J. Mitra, P. Dawson, T. McNally, Pol. Adv. Tech., vol. 23(2), pp. 149-160 (2010).

[2] V. Sencadas, M. Grima, E. Laredo, M. C. Pérez Y., A. Bello J. Chem. Phys. Vol. 114 (14) pp. 6417-6425 (2001).

## CHARACTERISTIC WIDTH OF THE MAGNETIC FIELD DRIVEN MICRO-CONVECTION IN THE HELE-SHAW CELL

Guntars Kitenbergs<sup>1,2</sup>, Kaspars Ērglis<sup>1</sup>, Oksana Petrichenko<sup>1</sup>, Andrei Tatulchenkov<sup>1</sup>, Fahrettin Gökhan Ergin<sup>3</sup>, Bo Beltoft Watz<sup>3</sup>, Regine Perzynski<sup>2</sup>, Andrejs Cēbers<sup>1</sup>

<sup>1</sup> Lab MMLL, Department of Theoretical Physics, University of Latvia, Riga, Latvia

<sup>2</sup> Lab PECSA, UMR 7195, UPMC, Paris, France

<sup>3</sup> Dantec Dynamics A/S, Skovlunde, Denmark

[guntars.kitenbergs@lu.lv](mailto:guntars.kitenbergs@lu.lv)

Magnetic field driven micro-convection draws attention both from the theoretical point of view and as a possible technique for mixing enhancement at micro scale. An experimental study is done by observing mixing of water based magnetic fluid ( $\gamma\text{-Fe}_2\text{O}_3$ ) and water in a Hele-Shaw cell with a micro-PIV (Particle Image Velocimetry) setup, described in [1]. Here we continue the investigation of this mixing phenomenon, particularly focusing on the characteristic width of the patterns that are time and magnetic field dependent. These peculiar fingering patterns (Fig. 1) emerge due to the ponderomotive forces of the self-magnetic field of a magnetic fluid under the action of a vertical homogeneous magnetic field.

To find the characteristic width we use concentration fields that are calculated from the acquired images using Beer-Lambert law and vorticity fields that are obtained by using micro-PIV technique with special image processing algorithms [2]. We post-process the concentration and vorticity fields in various ways (FFT, profile analysis, etc.) due to the high complexity of the pattern, especially for high magnetic fields, when finger splitting and merging are observed. As a result, the dynamics of the characteristic width over time for different magnetic fields is found (Fig. 2). Clear time dependence can be observed, in particular for greater field values. The obtained results are discussed and compared with numerical simulations.

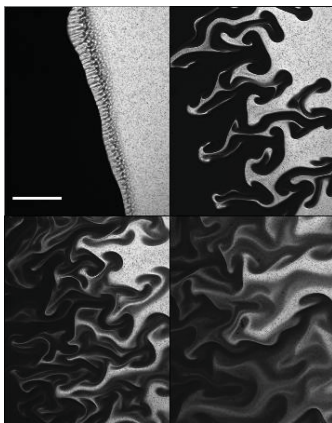


Fig. 1. Development of the fingering pattern of magnetic micro-convection ( $B=42$  G,  $t=0.8$  s). Scale bar is  $200\ \mu\text{m}$ .

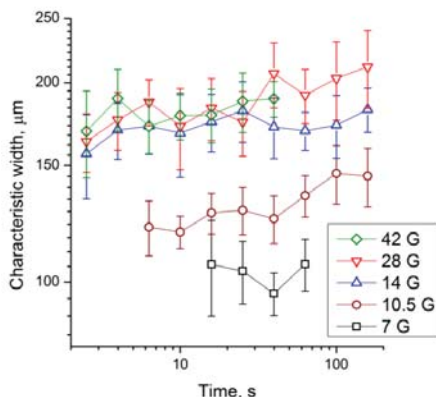


Fig. 2. Characteristic width dependence on time at different magnetic fields obtained by profile analysis.

[1] K. Ērglis, A. Tatulchenkov, G. Kitenbergs et al., Magnetic Field Driven Micro-Convection in the Hele-Shaw Cell, *J. Fluid Mech.* **714**, 612-633 (2013).

[2] F.G. Ergin, B.B. Watz, K. Ērglis & A. Cēbers, Poor-Contrast Particle Image Processing in Micro-Scale Mixing, *ASME Conf. Proc.*, 649 (2010).

[3] C. Derec, P. Boltenhagen, S. Neveu & J.-C. Bacri, Magnetic instability between miscible fluids in a Hele-Shaw cell, *Magnetohydrodynamics*, **44**(2), 135-142 (2008)



## NEW ASYMMETRIC ANTHRACENE DERIVATIVES FOR OPTOELECTRONIC APPLICATIONS

Regimantas Komskis<sup>1</sup>, Tomas Serevičius<sup>1</sup>, Povilas Adomėnas<sup>2</sup>, Ona Adomėnienė<sup>2</sup>, Renaldas Rimkus<sup>2</sup>, Vyintas Jankauskas<sup>3</sup>, Karolis Kazlauskas<sup>1</sup> and Saulius Juršėnas<sup>1</sup>

<sup>1</sup>Institute of Applied Research, Vilnius University, Saulėtekio al. 9-III, LT-10222 Vilnius, Lithuania

<sup>2</sup>UAB „Tikslioji Sintezė“ (Ltd), Kalvarijų g. 201E, LT-03225 Vilnius, Lithuania

<sup>3</sup>Department of Solid State Electronics, Vilnius University, Saulėtekio al. 9-III, LT-10222 Vilnius, Lithuania  
[regimantas.komskis@gmail.com](mailto:regimantas.komskis@gmail.com)

Anthracene derivatives with various substituents at different positions are in a great interest of today's science as a promising emissive material for blue organic light – emitting devices (OLED) [1]. Materials show high emission efficiency, colour purity and stability [2]. However, like other organic compounds, anthracene derivatives tend to crystallize in thin films and strongly deteriorate colour purity and efficiency of OLED device. Additionally, for inexpensive and efficient production of anthracene – based OLED devices it is necessary to improve solubility of these compounds in common solvents. A key of importance is to investigate the impact of substituents on optical and electrical properties of anthracene derivatives.

In this work optical properties of a set of asymmetric 3 – phenylanthracene derivatives with bulk phenyl, naphthyl, biphenyl, carbazole and benzoanthracene moieties at 9<sup>th</sup> and 10<sup>th</sup> positions of molecule were investigated. In addition to this, a newly designed 9H-carbazole and condensed system with two anthracene fragments, connected with additional heteroatom (NOP) (Fig. 1) was also optically characterised

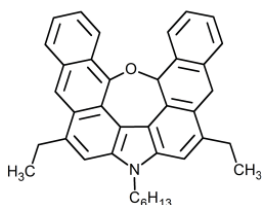


Fig. 1. NOP compound

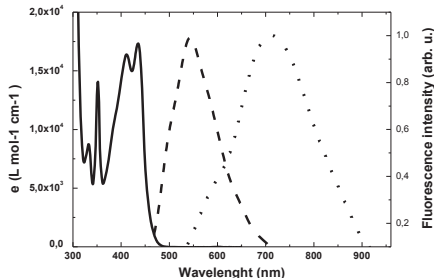


Fig. 2. Absorption and fluorescence spectra of NOP compound. Solid line – absorption spectrum in dilute solution; dashed and dotted – fluorescence intensity in dilute solution and thin film respectively.

Asymmetric anthracene derivatives with substituents at 9<sup>th</sup>, 3<sup>rd</sup> and 9<sup>th</sup>, 10<sup>th</sup> and 3<sup>rd</sup> positions show absorption and fluorescence peaks at 397/422 nm and 406/435 nm, respectively. Additionally phenyl substitute in 3rd position extends  $\pi$ -conjugated electron system. As the result, red shift in absorption and fluorescence is observed in comparison with unsubstituted anthracene. Anthracene derivatives with the bulk substitutes in 9th and 10th positions showed slightly increased fluorescence quantum efficiency (up to 48.6%) in comparison with derivatives substituted at 9<sup>th</sup> and 3<sup>rd</sup> positions (up to 42.6%) due to a faster radiative decay rate. Investigation of fluorescence QY in polystyrene matrix showed, that bulk substitutes in 9<sup>th</sup> and 10<sup>th</sup> position of anthracene disrupt planar geometry and fluorescence QY in thin film is up 13.2%. The investigation of radiative and non-radiative relaxation pathways reveals constant fluorescence non-radiative decay times, which implies a minor impact on intersystem crossing due to phenyl substitute introduced into 3<sup>rd</sup> position.

The detailed spectroscopic analysis of NOP compound demonstrated twofold absorption in dilute solution (Fig. 2). Vibronic series in absorption spectra at 411 nm and 435 nm which are also typical to unsubstituted anthracene derivatives and several narrow carbazole-specific bands (at 240 nm) were observed. Redshifted absorption spectra indicates extended  $\pi$ -conjugated electron system and planar geometry of the molecule. NOP compound demonstrates strong absorbance ( $17325 \text{ l mol}^{-1} \text{ cm}^{-1}$ ) and large Stokes shift of fluorescence of about 106 nm. A 173 nm redshift of the thin film fluorescence peak evidence eximer formation in the solid state. Nonexponential decay in dilute solution and thin films also confirms intermolecular interaction and competing exciton radiative relaxation and diffusion processes.

[1] M. Ananth Reddy, G. Malleshm. Synthesis and characterization of novel 2,5-diphenyl-1,3,4-oxadiazole derivatives of anthracene and its application as electron transporting blue emitters in OLEDs, *Synthetic Metals* 161, 869–880, (2011).

[2] Jong-Kwan Bin, Jong-In Hong. Efficient blue organic light-emitting diode using anthracene-derived emitters based on polycyclic aromatic hydrocarbons, *Organic Electronics* 12, 802–808, (2011).

## DIELECTRIC SPECTROSCOPY OF MEDIUM GRAPHITE LOADED EPOXY RESIN COMPOSITES

Ieva Kranauskaitė<sup>1</sup>, Jan Macutkevič<sup>1</sup>, Jūras Banys<sup>1</sup>, Alain Celzard<sup>2</sup>, Stefano Bellucci<sup>3</sup>

<sup>1</sup>Faculty of Physics, Vilnius University, Lithuania

<sup>2</sup>IJL – UMR CNRS 7198 AND LERMAB – ENSTIB, <sup>3</sup>INFN-Laboratori Nazionali di Frascati

[ieva.kranauskaite@ff.stud.vu.lt](mailto:ieva.kranauskaite@ff.stud.vu.lt)

Polymer composites with various carbon inclusions, like single- or multi- walled carbon nanotubes, carbon black, graphite or graphene are interesting for fundamental research and very attractive for various applications due to possibility to manipulate composite properties at nanoscale. The value of dielectric permittivity and electrical conductivity of these composites could be very high close to percolation threshold. However, despite of lot of publications is a lack of deep understanding relation between carbon filler microscopic properties and composite dielectric properties [1].

The aim of this work was to investigate dielectric properties of epoxy resin filled with graphite flakes inclusions namely medium graphite (diameter of the graphite flakes are  $d = 500 - 750 \mu\text{m}$ ). The concentration of graphite inclusions was from 0.25 to 2.0 wt. %.

Dielectric investigations were performed in frequency range from 20 Hz to 1 MHz, while the temperature interval was from 10 K to 450 K measuring loss tangent and capacity with LCR meter (HP – 4284A). At temperatures close to room temperature the dielectric dispersion is observed. At higher temperatures electrical conductivity appears.

---

[1] W. Bauhofer, J. Z. Kovacs, *Composite Science and Technology* 69, 1486 (2009).

# SELF-ASSEMBLY OF FLUORESCENT NANOAGGREGATES BASED ON 1,4-DIVINYLBENZENE DERIVATIVES

Gediminas Kreiza<sup>1</sup>, Karolis Kazlauskas<sup>1</sup>, Arūnas Miasojedovas<sup>1</sup>, Eglė Arbačiauskienė<sup>2</sup>, Aurimas Bieliauskas<sup>2</sup>, Algirdas Šačkus<sup>2</sup> Saulius Juršėnas<sup>1</sup>

<sup>1</sup>Institute of Applied Research, Vilnius University, Saulėtekio 9-III, LT-10222 Vilnius, Lithuania

<sup>2</sup>Department of Organic Chemistry, Kaunas University of Technology, Radvilėnų 19, LT-50254 Kaunas, Lithuania  
[gediminas.kreiza@ff.vu.lt](mailto:gediminas.kreiza@ff.vu.lt)

Fluorescent organic nano- and microstructures exhibiting the so-called aggregation-induced emission (AIE) phenomenon have recently attracted much attention because of their potential use in optoelectronic devices, such as OLEDs, lasers or sensing systems [1]. Self-assembly of molecules into aggregates in polymer matrix by exposure to organic solvent vapor or by thermal treatment is promising for technological application, e.g. for vapor or temperature sensing kits as it can result not only in enhanced emission but also in a strong blue or red shift of the fluorescence spectra [2].

In this work, fluorescent aggregates based on novel divinylbenzene derivatives with cyano groups were formed directly in a polymer film using thermal treatment and vapor exposure. The aggregates were examined in regard to their morphology and optical properties by various methods such as fluorescence microscopy, spectroscopy and time correlated single photon counting. Additionally, the amplified spontaneous emission (ASE) of the divinylbenzene derivatives dispersed in polymer matrix was observed and ASE threshold values were determined. These derivatives were also used to form fluorescent organic nanoparticles (FONs) by a reprecipitation method in aqueous solution. Isolated molecules in a dilute solution showed very low fluorescence quantum efficiency (0.5%), but upon addition of more than 50% of water volume fraction highly fluorescent (QY=70%) nanoparticles were formed.

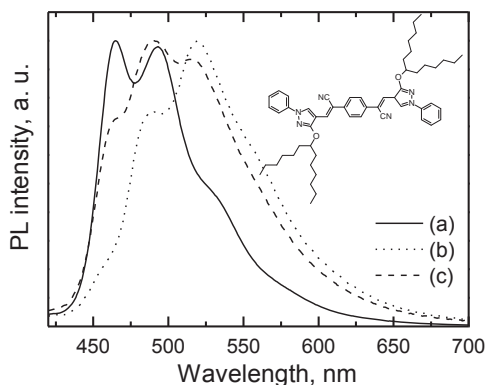


Fig. 1. Normalized fluorescence spectra of polystyrene film doped with a 10% mass fraction of 1,4-divinylbenzene derivative: (a) – untreated film, (b) – the film exposed to THF vapor for 2 minutes, (c) – the film annealed at 110 °C for 2 hours. Inset shows chemical structure of divinylbenzene derivative.

The ability to control the aggregation process by exploiting various end-groups of cyano-substituted divinylbenzene derivatives was demonstrated. The untreated polymer films containing isolated molecules exhibited blue emission, but after the vapor- or temperature-induced aggregation a red shift of the fluorescence spectra was observed due to the specific molecular arrangement in the aggregates (Fig. 1). The latter result shows promise for the divinylbenzene-doped polymer films in sensing applications.

[1] Y. Hong, J. W. Y. Lam and B. Z. Tang, Aggregation-induced emission, Chem. Soc. Rev. 40, 5361–5388 (2011).

[2] B. K. An, S. K. Kwon, and S. Y. Park, Photopatterned arrays of fluorescent organic nanoparticles, Angew. Chem. 119, 2024–2028 (2007).

## 20 mol. % $\text{Gd}_2\text{O}_3$ doped $\text{CeO}_2$ solid electrolyte electronic conductivity dependance on oxygen activity

Dalius Petrulionis<sup>1</sup>, Odile Bohnke<sup>2</sup>

<sup>1</sup> Faculty of physics, Vilnius University, Lithuania

<sup>2</sup> Institut de Recherche en Ingénierie Moléculaire et Matériaux Fonctionnels, Université du Maine, France  
dalius.petrulionis@stud.ff.vu.lt

Solid oxide fuel cells are an attractive power generation technology thanks to their extremely high efficiency, fuel flexibility and low environmental impact. Despite these advantages, operating temperatures in excess of 800 °C are required to achieve efficient operation in current commercial products due to the use of doped  $\text{ZrO}_2$  based electrolytes. This necessitates the use of expensive sealant and structural materials for manufacture of fuel cell stacks, making the final product too expensive for widespread adoption. Current research in the area is mainly concerned with fuel cell operating temperature reduction to the intermediate range of 600 °C to 800 °C, which can be achieved using various doped  $\text{CeO}_2$  based electrolytes. Disadvantages of these materials include higher electronic conductivities, as compared to doped  $\text{ZrO}_2$ , and the ability to be significantly reduced in the conditions present on the anode side of the fuel cell, making the material unusable as an electrolyte. In this work we present a study of 20 mol. %  $\text{Gd}_2\text{O}_3$  doped  $\text{CeO}_2$  (GDC) electronic conductivity as it depends on oxygen activity over a temperature range of 600 °C to 750 °C.

The measurements were carried out using a modified Hebb-Wagner method, based on the analysis of steady state polarization curves around an ion-blocking microcontact. [1] Due to a slight deviation from stoichiometry present in the oxide, oxygen activity at the blocking electrode can be controlled by applying different DC voltages across the measurement cell. The oxygen activity at the other side of the pellet must be held constant by a reversible electrode, which is conductive to both, oxygen ions and electrons. To ensure fully blocking behavior of the microelectrode, the measurements were carried out in dry  $\text{N}_2$  atmosphere using Platinum as the electrode material. The sample and electrode interface was encapsulated using a glass-based sealant. A 1:1 charge ratio mix of  $\text{CuO}$  and  $\text{Cu}_2\text{O}$  was pressed into pellets and sintered in inert atmosphere to be used as a reversible electrode and known oxygen activity reference.

The solid electrolyte pellets were prepared from commercial (Fuel Cell Materials) GDC nanopowder (grain size < 10 nm) with a surface area of 220  $\text{m}^2/\text{g}$ . X-ray diffraction and thermogravimetry was performed on the powder to determine the presence of impurities. The powder was heat treated to remove any adsorbed water, as well as other unwanted volatile compounds, before being isostatically pressed at 5000 bar and sintered at 1400 °C for 1h, losing its nanoscale character.

Electronic conductivity results at 750 °C, typical of the material at all temperatures, are shown in the figure below.

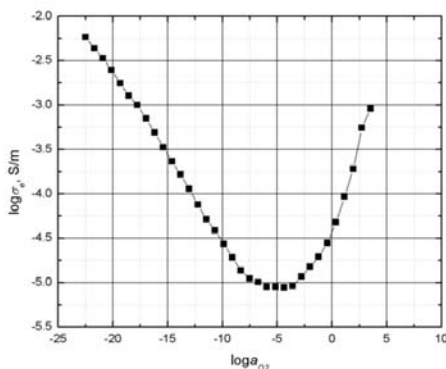


Fig. 1. Electronic conductivity of GDC at 750 °C as it depends on oxygen activity. Oxygen gas with a partial pressure of 1.013 bar is taken as activity standard.

Two distinct regions in the graph are visible, corresponding to electron conductivity at low oxygen activities and hole conductivity in the high oxygen activity range. The electrolytic domain, where no significant electronic transport is possible lies in the intermediate oxygen activity range, leading to the conclusion that this material is best suitable for use as an electrolyte in single-chamber SOFCs, which operate at intermediate oxygen partial pressures, and as a component of multi-phase metal-ceramic electrodes for conventional fuel cells, where electronic conductivity is desirable.

[1] S. Lubke, H.-D. Wiemhofer, Electronic conductivity of Gd-doped ceria with additional Pr-doping, Solid State Ionics 117, 229-243 (1999).

# Poster session 3

---

15:00  
Friday

- Astrophysics and astronomy
- Biophysics, medical and environmental physics
- Chemistry and chemical physics
  - Interdisciplinary
  - Theoretical physics

## High-resolution spectroscopy of star BS17569-0011

Artis Aberfelds<sup>1</sup>, Laimonis Zacs<sup>2</sup>

<sup>1</sup> Faculty of Physics and Mathematics, University of Latvia, Latvia

<sup>2</sup>Laboratory of Astrospectroscopy, Laser Centre of the University of Latvia, Latvia

During this scientific work high-resolution absorption spectrum analysis of the star BS17569-0011 was performed. Available data classifies it as a metal-poor older generation star with anomalous spectral energy distribution. Extracted data also shows systemic radial velocity, atmospheric effective temperature, surface gravity, microturbulent velocity and abundances of five chemical elements. Star's spectrum analysis identified intense TiO lines and Balmer H $\alpha$  line emission. Atmospheric parameters are typical of red giants,  $T_{eff} = 4250$  K,  $\log(g) = 1.0$  (cgs),  $v = 3.0$  km / s. Abundance of iron atoms in the current star's atmosphere is about 16 times lower than in the Solar atmosphere. Element abundances formed neutron capture processes are relatively high, about 10 times higher. The data shows that the BS17569-0011 belongs to the Galactic halo population and red giant branch evolution phase.

## Oxygen abundances in the Oldest Galactic Populations

K. Adelbergytė<sup>1</sup>, A. Kučinskas<sup>2,3</sup>, V. Dobrovolskas<sup>2</sup>

<sup>1</sup> Vilnius University, Faculty of Physics, Vilnius, Lithuania

<sup>2</sup> Vilnius University Astronomical Observatory, Vilnius, Lithuania

<sup>3</sup> Institute of Theoretical Physics and Astronomy of Vilnius University, Vilnius, Lithuania  
[karolina.adelbergyte@gmail.com](mailto:karolina.adelbergyte@gmail.com)

Oxygen is the third most abundant element in the universe after H and He and is the main product of Type II SNe. It is believed that oxygen is immediately released into the interstellar medium after these massive stars are formed.

Further progress in the study of the chemical evolution of galaxies requires progressively more accurate determinations of element abundances in stars of various ages and metallicities. A particularly widely addressed issue for the last decade has been oxygen abundances in metal-poor stars. The firm knowledge of oxygen abundances in the oldest Galactic populations may therefore provide important observational constraints, allowing to discriminate between different scenarios of the Galactic chemical evolution. However, up to date its measurements remain rather scarce and imprecise due to only very few spectral lines available for investigation.

In this work we used infrared OH lines to determine the oxygen abundance by fitting the spectrum synthesis calculations to the infrared OH lines. Observations were obtained with CRIRES high-resolution spectrograph at the 8.2 m telescope of ESO (VLT, Chile). Three metal-poor ( $[\text{Fe}/\text{H}] \sim -3$  dex) halo stars were observed: HD122653, HD186478 and BD-18 5550. The derived oxygen to iron abundances ratios vary from  $[\text{O}/\text{Fe}] = 0.92$  dex to 1.09 dex. We found a correlation between the oxygen and iron abundances, the most oxygen-abundant stars being most rich in iron.

# PREDICTING ASYMMETRIES AND SHIFTS OF SPECTRAL LINES IN THE METAL-POOR RED GIANT HD 122563

Jonas Klevas<sup>1</sup>, Arūnas Kučinskas<sup>1,2</sup>, Hans-Günter Ludwig<sup>3</sup>, Piercarlo Bonifacio<sup>4</sup>, Mathias Steffen<sup>5</sup>,  
Dainius Prakapavičius<sup>1</sup>

<sup>1</sup>Vilnius University Institute of Theoretical Physics and Astronomy, Goštauto 12, Vilnius LT-01108, Lithuania

<sup>2</sup>Vilnius University Astronomical Observatory, Čiurlionio 29, Vilnius LT-03100, Lithuania

<sup>3</sup>ZAH Landessternwarte Königstuhl, D-69117 Heidelberg, Germany

<sup>4</sup>GEPi, Observatoire de Paris, CNRS, Université Paris Diderot, Place Jules Janssen, 92190 Meudon, France

<sup>5</sup>Leibniz-Institut für Astrophysik Potsdam, An der Sternwarte 16, D-14482 Potsdam, Germany

[jonas.klevas@tfai.vu.lt](mailto:jonas.klevas@tfai.vu.lt)

Convection is active in late-type stellar atmospheres and introduces velocity fields, which causes spectral line shifts and asymmetries in the observed spectrum. Convective energy transfer is a common phenomenon in the atmospheres of low-mass stars. Amongst the directly observable consequences related with the convective velocity fields are Doppler-shifts and asymmetries of various spectral lines, that can be detected in stellar spectra of sufficiently high spectral resolution and signal-to-noise ratio. Although such line shifts and asymmetries are routinely observed in the Sun for more than 30 years now, predicting them with a reasonable accuracy became possible only recently with the advances in three-dimensional (3D) hydrodynamical stellar atmosphere models. The comparison of the observed and theoretical spectral line asymmetries and line shifts may therefore provide important insights about the role of convection in the spectral line formation, and may allow to constrain theoretical models by identifying which properties of the model atmospheres are still not realistic enough to stand the test of observations.

Studies of the spectral line Doppler-shifts and asymmetries have been done so far for only a few types of stars (including the Sun, Procyon, several M dwarfs and a metal-poor red giant). In this study we therefore extended the previous work by studying shifts and asymmetries of neutral iron (Fe I) lines in the metal-poor red giant HD 122563. For this purpose we used high quality ( $R = \lambda/\Delta\lambda = 115000$ ,  $S/N \approx 310$ ) archival HARPS spectrum covering the visible wavelength range ( $\sim 400 - 700$  nm). 3D hydrodynamical CO<sup>5</sup>BOLD stellar model atmospheres were used to synthesize theoretical profiles of the Fe I lines studied in the HARPS spectrum. We further calculated coreshifts<sup>1</sup> and bisectors<sup>2</sup> of the observed and theoretical Fe I lines, in order to make a comparison of theoretical predictions with the observed data.

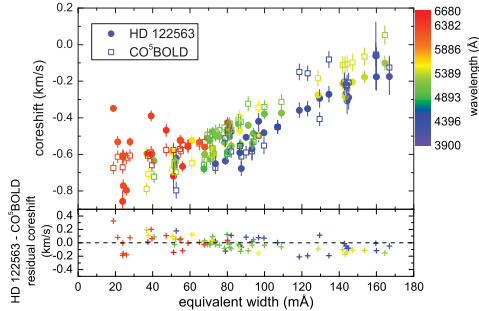


Fig. 1. Top panel: observed and theoretical coreshifts of Fe I lines plotted versus line equivalent width (line strength). Errors are at  $1\sigma$  level. Bottom panel: observed minus theoretical residual coreshifts plotted versus  $W$ .

One important result of our study is that both observed and theoretical coreshifts depend on the spectral line strength, so that the coreshifts are largest in case of weakest spectral lines. Theoretical models also predict the dependence of coreshifts on wavelength, slight hints for which can be seen in the observed data too. Generally, theoretically predicted coreshifts agree well the observed ones, although there are hints that model predictions are somewhat worse in case of the weakest and strongest Fe I lines. Observed and computed line bisectors seem to agree well too, except that models tend to predict slightly larger blueshifts for the weakest lines ( $\sim 0.1$  km/s).

The obtained results therefore suggest that current 3D hydrodynamical model atmospheres can reproduce the interior structures of a metal-poor red giant HD 122563 sufficiently well. At the same time, refinement of the models is still needed in order to reliably predict asymmetries and shifts of the weakest and strongest Fe I lines. Nevertheless, the very fact that 3D hydrodynamical stellar model atmosphere models are capable of successfully reproducing the observed spectral line asymmetries and shifts may open up entirely new ways to study the interior structures of stellar atmospheres.

<sup>1</sup>Coreshift is the Doppler shift of the deepest point in the line profile.

<sup>2</sup>Bisector is a line constructed from the midpoints of horizontal lines connecting the line wings.



## SILICON ABUNDANCE IN THE ATMOSPHERES OF RED GIANT STARS OF GALACTIC GLOBULAR CLUSTER 47 TUCANAE

Edgaras Kolomiecias<sup>1</sup>, Arūnas Kučinskas<sup>2</sup>

<sup>1</sup>Faculty of Physics, Vilnius University, Lithuania

<sup>2</sup>Institute of Theoretical Physics and Astronomy, Vilnius University, Lithuania  
[reaggas@yahoo.com](mailto:reaggas@yahoo.com)

Research done during the past decade has shown that stars in Galactic globular clusters do not all have the same age and they do not share the same chemical composition. This suggests that globular clusters may consist of two (or more) generations of stars, with the second generation born from the material enriched by the ejecta of the most massive stars, and/or asymptotic giant branch stars. It therefore seems that the early stages of cluster formation were in fact more complex than previously thought: supernova explosions, winds from massive first-generation stars could have created expanding bubbles of gas and shock fronts which could have triggered further star formation episodes. Many of these events should have left behind their characteristic imprints in the chemical composition of the second-generation globular cluster stars. Some of these signatures can therefore be found in stellar spectra, by analyzing spectral features that belong to light elements, such as oxygen, sodium, magnesium, aluminum and silicon. Such studies may allow to better understand chemical evolution of Galactic globular clusters and to tell more about their stellar populations.

In this study we have determined the abundance of silicon in the atmospheres of red giant stars of Galactic globular cluster 47 Tucanae (47 Tuc). The analysis was based on the spectra of 49 stars that were obtained with GIRAFFE spectrograph mounted on the VLT telescope at the European Southern Observatory in Chile. This is so far the largest sample of red giant stars analyzed in this cluster for the silicon abundance. Two spectral lines of neutral silicon were used, with their central wavelengths located at 614.2483 and 615.5134 nm. Line equivalent widths were measured using DECH20T package, by fitting a Gaussian profile to the observed spectral line. Stellar model atmospheres were computed using ATLAS9 code and were further employed to derive silicon abundances with WIDTH9 package.

The mean silicon abundance obtained for a sample of 49 red giants in 47 Tuc,  $[\text{Si}/\text{Fe}] = +0.19 \pm 0.09$ , agrees well with the silicon abundances obtained in stars of 47 Tuc by other authors:  $[\text{Si}/\text{Fe}] = +0.37 \pm 0.23$  [1],  $[\text{Si}/\text{Fe}] = +0.22 \pm 0.01$  [2], and  $[\text{Si}/\text{Fe}] = +0.30 \pm 0.10$  [3]. Star-to-star scatter of silicon abundances obtained in this study is small ( $< \pm 0.1$  dex), which means that both first and second generation stars in this cluster do have very similar silicon abundances. This, in turn, may mean that objects that enriched second generation stars did not synthesize significant fraction of silicon in their interiors, and therefore the derived silicon abundance should be very similar to that of primordial matter from which the cluster has formed. On the other hand, unaltered silicon abundance in the second generation stars may suggest that the first generation polluters were stars of the lower mass, i.e., those in which the core temperatures did not reach those needed for the Al-Si thermonuclear cycle to take place. This may rule out the hypothesis that the polluters could have been massive stars, leaving asymptotic giant branch stars the only possible polluter candidates.

---

[1] Alves-Brito A., Barbuy B., 2004, IAU222, 549.

[2] McWilliam, A., Bernstein, R.A. 2008, ApJ 684, 326 .

[3] Carretta, E., Gratton, R. G., Lucatello, S., Bragaglia, A., & Bonifacio, P. 2005, A&A 433, 597.

# STAR FORMATION HISTORY OF THE DWARF IRREGULAR GALAXY LEO A

Rokas Naujalis<sup>1</sup>, Rima Stonkutė<sup>2</sup>

<sup>1</sup> Faculty of Physics, Vilnius University, Lithuania

<sup>2</sup> Center for Physical Sciences and Technology, Lithuania

[rokasni@yahoo.com](mailto:rokasni@yahoo.com)

Dwarf irregular galaxy Leo A is one of the most isolated galaxies in the Local Group. Lack of any neighbors means that this galaxy evolved naturally. Its metallicity is very low  $Z = 0.0005$  [1], and ~80% of its baryonic mass still remains in the gas phase [2]. Study of this type objects can help us better understand processes and dynamics governing the evolution of galaxies. Previous studies of Leo A star formation history (SFH) covered large timescales [3, 4] and were unable to achieve high time resolution. In order to improve time resolution, SFH was derived only for the last 300 million years (Myr) using blue loop (BL) and main sequence (MS) stars.

Observation data from Subaru SuprimeCam (50% completeness limit  $I \sim 24$  mag) and Hubble ACS (50% completeness limit  $I \sim 28$  mag) and isochrones of  $Z = 0.0004$  [5] were used. Salpeter IMF in the mass range from 0.5 to 100  $M_{\odot}$  was used for population modeling. Both the BL and MS methods complement each other. The MS method works well for youngest ages, however, for older ages (because of different age stellar population overlap in the color-magnitude diagram) it is difficult to apply it reliably. In Fig. 1 three MS older age data points are located much lower than those derived from BL stars, and were excluded from further analysis. The BL method on the other hand is not reliable at younger ages (< 50 Myr) because there are too few stars that could be used to compute the star formation rate (SFR).

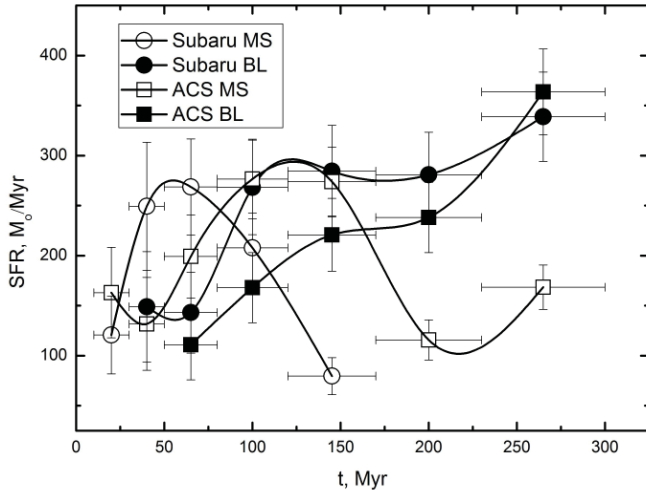


**Fig. 1.** Leo A star formation history during the last 300 Myr. Circles indicate Subaru SuprimeCam data while squares indicate Hubble ACS data. Empty symbols indicate SFH derived using the main sequence stars and filled symbols indicate SFH derived using the blue loop stars.

The results (Fig. 1) show that SFR in Leo A galaxy has steadily declined from ~350  $M_{\odot}/\text{Myr}$  at the age of 300 Myr to ~150  $M_{\odot}/\text{Myr}$  at 30 Myr. These results are in good agreement with previous determinations [3, 6].

The significantly different distribution of the MS stars (younger than 170 Myr) and the BL stars (younger than 300 Myr) in the galaxy was demonstrated. This discovery permits evaluation of the velocity of star forming regions in the Leo A galaxy.

[1] van Zee L., Skillman E. D. & Haynes M. P. 2006, ApJ, 637, 239

[2] Young, L. M., & Lo, K. Y. 1996, ApJ, 462, 203

[3] Cole, A. A., et al. 2007, ApJ, 659, L17

[4] Schulte-Ladbeck, R., et al. 2002, AJ, 124, 896

[5] Girardi, L., et al. 2002, A&A, 391, 195

[6] Hunter D. A. & Elmegreen B. G. 2004, AJ, 128, 2170

## CREATING AN ATMOSPHERIC REFRACTIVE INDEX MAP OF LITHUANIA

Edvinas Brilius<sup>1</sup>, Stasys Tamošiūnas<sup>2</sup>

<sup>1</sup> Faculty of Physics, Vilnius University, Lithuania

<sup>2</sup> Institute of Applied Research, Vilnius University, Lithuania  
[edvinas.brilius@gmail.com](mailto:edvinas.brilius@gmail.com)

The speed at which electromagnetic waves travel through vacuum is constant, and equal to  $3 \times 10^8$  ms<sup>-1</sup>. However Earth's atmosphere is not vacuum, it is composed out of a gas mixture, where 78 % is nitrogen, 21 % is oxygen, 0.9 % is argon, 0.03 % is carbon dioxide. These gases slightly changes radio wave propagation through atmosphere, which in turn can affect their transmission quality from the transmitter to receiver. Radio wave propagated through the earth's atmosphere encounters variations in the atmospheric refractivity index along its trajectory that causes the ray path to become curved. At standard atmosphere conditions near the earth's surface, the radio refractive index,  $N$ , has a value of approximately 1.0003 [1]. The atmospheric radio refractive index  $n$  can be calculated using Eq. (1):

$$n = 1 + N \times 10^{-6} \quad (1)$$

Radio refractivity is used to simplify the values and make them more manageable. The refractivity is a dimensionless parameter, expressed by:

$$N = A \left( p + B \times \frac{p_v}{T} \right) \div T \quad (1)$$

Where  $p$  is atmospheric pressure (hPa),  $p_v$  is water vapor pressure, and  $T$  is absolute temperature.  $A = 77,6$  K/hPa and  $B = 4810$  K. For frequencies up to 100 GHz, the error is less than 0.5%.

We propose a model on how to calculate atmospheric refractive index in any location on the map (Fig. 1). Only locations coordinates, height above sea level and temperature must be known. Some locations are used as a reference points for the model. These locations are Vilnius, Kaunas, Klaipėda, Panevėžys, Šiauliai, Kybartai, Pagėgiai, Telšiai, Utena and Alytus, where metrological data about temperature, relative air humidity and atmospheric pressure is measured a few times a day. These parameters are used to calculate radio wave refractivity in these locations.



Fig. 1. Marked area on the map, where proposed model can be used.

Refractivity values in the location on the map other than the reference points, according to the proposed model, can be calculated directly from known refractivity values in the mentioned cities or from other metrological data. This makes the proposed model very flexible and more accurate.

By testing and analyzing the model few conclusions are made. First – the use of relative humidity monthly averages can sometimes lead to wrong refractive index values. Second – model is capable of calculating radio refractive index with good accuracy, when primary weather parameters are correct.

[1] R.L. freeman , *Radio System Design for telecommunications*, 3rd edition. New York: Wiley-Interscience, John Wiley&Sons, Inc., 2007. P 2-33.

## MODIFIED SUBSTRATE SPECIFICITY OF CYP7B1 R486C MUTANT – A POSSIBLE REASON FOR SPASTIC PARAPLEGIA TYPE 5

Yaroslav Dichenko<sup>1</sup>, Aleksei Yantsevich<sup>1</sup>, Sergei Usanov<sup>1</sup>

<sup>1</sup> Institute of Bioorganic Chemistry, National Academy of Sciences, Republic of Belarus  
dichenko@iboch.bas-net.by

Human cytochrome P450 CYP7B1 (CYP7B1) is a 506 amino acid microsomal enzyme participating in hydroxylation of a number of steroids [1]. This protein plays crucial role in different metabolic processes: bile acids biosynthesis [2], neurosteroid metabolism [3], regulation of immunoglobulin production [4] and metabolism of estrogen receptor ligands [5]. The mRNA expression of human CYP7B1 is tissue-specific with main localization in kidneys and brain [1]. Dysfunction of CYP7B1 is associated with a number of genetic disorders such as liver failure in children and neuropathy in adults [1]. Eight different mutations in **cyp7b1** gene are related with one of such neuropathies – spastic paraplegia type 5 – autosomal recessive disorder characterized by lower limb spasticity and weakness [1]. Molecular reason of this pathology still remains unclear.

Sequence analysis show that Arg486 amino acid residue is conserved in CYP7 family and located in the substrate recognition site (SRS). Examination of CYP7B1 model, build by us with CYP7A1 (PDB ID: 3DAX) as a template, showed that R486C mutation localized near the active center of the enzyme. So our hypothesis is that this mutation with changes of substrate specificity and activity of the enzyme.

In order to understand molecular background of the disorder, we constructed an expression system, expressed and purified recombinant R486C mutant of CYP7B1 (R486C). The content of native form of R486C in final preparation was more than 90%. Expression level of R486C in the same expression system as for wild type CYP7B1 (WT) was significantly lower. Good expression level was achieved only in the presence of substrate (dehydroepiandrosterone (DHEA)) in culture medium. The explanation of the fact is possible stabilization of structure by ligand binding in the enzyme active site.

Examination of ligand binding properties of R486C and comparison with the results obtained for wild type enzyme showed modified affinity of R486C for neurosteroids.  $K_d$  of R486C with DHEA is two times higher than for WT. R486C did not bind pregnenolone and 21-hydroxypregnenolone. Also we found that R486C has modified affinity for different androstane derivatives.

So R486C mutation leads to substrate specificity alteration and decrease in structure stability.

Other mutant forms of CYP7B1 are under investigation. Further comparative study of normal and mutated human enzyme will help to understand the influence of enzyme mutations on the development of mentioned disorders.

---

[1] A.R. Stiles, J.G. McDonald, D.R. Bauman, D.W. Russell, CYP7B1: one cytochrome P450, two human genetic diseases, and multiple physiological functions, *J. Biol. Chem.* **284**(42), 28485-28489 (2009).

[2] J.Y. Chiang, Regulation of bile acid synthesis, *Front. Biosci.* **3**, 176-193 (1998).

[3] S. Steckelbroeck, M. Watzka, D. Lutjohann et al, Characterization of the dehydroepiandrosterone (DHEA) metabolism via oxysterol 7 $\alpha$ -hydroxylase and 17-ketosteroid reductase activity in the human brain, *J. Neurochem.* **83**(3), 713-726 (2002).

[4] D.R. Bauman, A.D. Bitmansour, J.G. McDonald et al, 25-Hydroxycholesterol secreted by macrophages in response to Toll-like receptor activation suppresses immunoglobulin A production, *Proc. Natl. Acad. Sci. USA* **106**(39), 16764-16769 (2009).

[5] Y. Omoto et al, Early onset of puberty and early ovarian failure in CYP7B1 knockout mice, *Proc. Natl. Acad. Sci. USA* **102**(8), 2814-2819 (2005).

## THE DYNAMICS OF FEMORAL HEAD BLOOD FLOW AFTER A FEMORAL NECK FRACTURE

Vilmaras Gėgžna<sup>1,2</sup>, Jaunius Kurtinaitis<sup>3,4</sup>, Andrius Brazaitis<sup>3,4</sup>, Narūnas Porvaneckas<sup>3,4</sup>

<sup>1</sup> Institute of Applied Research, Vilnius University, Lithuania

<sup>2</sup> Faculty of Natural Sciences, Vilnius University, Lithuania

<sup>3</sup> Republican Vilnius University Hospital, Vilnius University, Lithuania

<sup>4</sup> Faculty of Medicine, Vilnius University, Lithuania

*Vilmaras.Gegzna@tmi.vu.lt*

The aim of the study was to determine blood flow dynamics in femoral head after a femoral neck fracture using dynamic magnetic resonance imaging.

42 patients diagnosed with a femoral neck fracture who underwent dynamic magnetic resonance imaging procedure within 24 hours after trauma were included in the study. Relative enhancement ratio was calculated for the affected femoral head.

Before the measurements a catheter inserted into subcutaneous vein in the area of elbow was connected to contrast injection pump that was synchronized with MRI (magnet resonance imaging) machine “Siemens MAGNETOM Symphony” (1.5 T, “Tim System”, Erlangen, Germany). 0.2mg of the contrast material “Magnegita” per 1 kg body mass was injected at rate of 3 ml/s. Scanning procedure started with “T2 trufi ax” and “pd fs cor” modes to identify the locations of femoral heads. Then “f3D\_vibe\_MEAS” scanning mode was turned on. Scanning slice thickness was 3 mm. Scanning procedure was repeated at time periods from 0:00 to 6:24 minutes at intervals of 32seconds.

The obtained data was normalized and classified to 3 groups in accordance with AO fracture classification system (31-B1, 31-B2, 31-B3). Each data set was divided into 3 spatial sections of femoral head: the front section (the first third of the head), middle section (the second third of the head), and the rear section (the last third of the head). Then values of the same class patients were averaged. The averages were fitted with model, described with equation 1.

$$I = I_0 + \Delta I \left( 1 - e^{-\frac{t}{\tau}} \right) \quad (1)$$

where  $I$  is the MRI signal intensity in arbitrary units (a.u.),  $t$  – time in minutes,  $\tau$  – a signal intensity increase rate in minutes<sup>-1</sup>,  $I_0$  – signal intensity at  $t = 0$ ,  $\Delta I$  – difference between  $I_0$  and asymptotic maximum intensity  $I_{\max}$ .

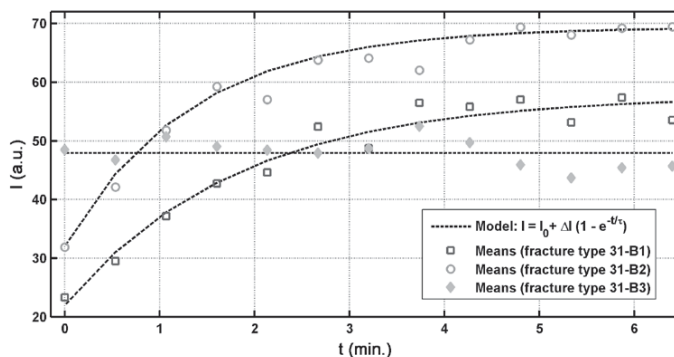


Fig. 1. Experimental data and the fitted model of blood flow dynamics at the rear part of femoral head.

Figure 1 illustrates the results of fitting procedure. The chosen model was fitted well to class “31-B1” and “31-B2” averages’ data ( $r^2 > 0.95$ ) while linear dependence  $I = I_0$  (i.e.  $\Delta I = 0$ ) was the best fit for class “31-B3”.

Our previous study [1] showed that the most significant statistical differences using normalized values of signal intensity were found comparing the data from rear part of femoral head. However, a more detailed analysis is needed to confirm suitability of fitting coefficients ( $I_0$ ,  $\Delta I$  and  $\tau$ ) to discriminate between the classes statistically.

[1] J. Kurtinaitis et al. Femoral head blood flow after femoral neck fracture. Dynamic magnetic resonance imaging volumetric measurements [article in Lithuanian]. Medicinos teorija ir praktika 19(4.2), 705–709(2013).

# MITOCHONDRIAL INVOLVMENT IN ASCORBATE-INDUCED CALCIUM IONS RELEASE INTO CYTOSOL OF HEP-2C CELLS

Elena N. Golubeva<sup>1</sup>

<sup>1</sup> Department of Physics, Belarusian State University, Republic of Belarus  
golubeva.ln.87@gmail.com

Nowadays ascorbic acid is considered as a promising anticancer therapeutic agent. Ascorbic acid at pharmacological (millimolar) concentrations is ascertained to induce cancer cell death, however its mechanism of action still being undiscovered. Previously in our experiments ascorbic acid has been shown to induce calcium ions release from intracellular calcium stores into cytosol of human larynx carcinoma cells HEP-2c [1]. But whether this ascorbate-induced calcium ions release is associated with  $\text{Ca}^{2+}$  efflux from endoplasmic reticulum or from cancer cells mitochondria due to the mitochondrial permeability transition pore opening providing an initial stage of apoptosis is still obscure.

In this study mechanism of calcium ions release, induced by ascorbic acid (5 mM), into cytosol of human larynx carcinoma cells HEP-2c from intracellular calcium stores was investigated. There are two possible intracellular calcium stores (mitochondria and endoplasmic reticulum), which can be responsible for ascorbate-induced calcium ions release. In order to reveal involvement of endoplasmic reticulum in the ascorbate-mediated process mentioned above N-ethylmaleimide (NEM, thiol-alkylating agent) was used. It is established that NEM at low (20–200  $\mu\text{M}$ ) concentrations induces  $\text{Ca}^{2+}$  release from skeletal sarcoplasmic reticulum vesicles inhibiting  $\text{Ca}^{2+}$ -ATPases [2]. In our experiments NEM (50  $\mu\text{M}$ ) also elicits cytosolic calcium ions concentration increase ( $27 \pm 6$  nM) in HEP-2c cells without any influence on the magnitude of ascorbate-induced cytosolic calcium ions release. Moreover addition of NEM after ascorbic acid treatment of cells leads to the same cytosolic calcium ions concentration increase as in experiments without ascorbic acid pretreatment indicating that NEM-induced and ascorbate-induced  $\text{Ca}^{2+}$  release into cellular cytosol is associated with depletion of different intracellular calcium stores. These results permit to assume that ascorbate-induced  $\text{Ca}^{2+}$  release occurs due to transient mitochondrial permeability transition pore (MPTP) opening. Using fluorescent dye JC-1 (serves for measurements of changes in mitochondrial membrane potential) ascorbic acid is shown to induce loss of mitochondrial membrane potential and mitochondrial redistribution in the cytoplasm of HEP-2c cells (Fig. 1). This consequence is in agreement with the proposal of ascorbate-induced  $\text{Ca}^{2+}$  release into HEP-2c cells cytosol from mitochondria as  $\text{Ca}^{2+}$  efflux during transient MPTP opening is accompanied by depolarization of the inner mitochondrial membrane [3].

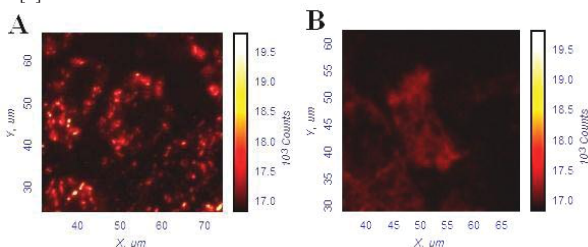


Fig. 1. Image of mitochondrial distribution and mitochondrial membrane potential in HEP-2c cells. A – cells in control, B – cells preloaded with ascorbic acid (5 mM).

However HEP-2c cells treatment with 5  $\mu\text{M}$  of cyclosporine A (CsA, inhibitor of permeability transition pore opening) has no effect on  $\text{Ca}^{2+}$  release induced by 5 mM of ascorbic acid into cytosol. Magnitude of the increase of cytosolic  $\text{Ca}^{2+}$  concentration caused by ascorbic acid treatment (5 mM) is not altered in HEP-2c cells treated with 5  $\mu\text{M}$  of CsA for 24 h either. The results obtained indicate that whether ascorbate-induced calcium ions release into cancer cells cytosol occurs due to MPTP opening, mechanism of MPTP formation is CsA-insensitive as described in [4]. To sum up, derived data provide evidence that  $\text{Ca}^{2+}$  release induced by ascorbic acid arises from transient calcium ions efflux from HEP-2c cells mitochondria leaving behind several issues opened for further investigations.

- [1] G. Martinovich, E. Golubeva et al., Redox Regulation of Calcium Signaling in Cancer Cells by Ascorbic Acid Involving the Mitochondrial Electron Transport Chain, *J Biophys*, doi:10.1155/2012/921653 (2012).
- [2] E. V. Menshikova et al., Low N-Ethylmaleimide Concentrations Activate Ryanodine Receptors by a Reversible Interaction, Not an Alkylation of Critical Thiols *The journal of biological chemistry*, **275**, 36775–36780 (2000).
- [3] T. B. Levine, A. B. Levine, *Metabolic Syndrome and Cardiovascular Disease* (ISBN: 978-1-4051-9575-1, 2012).
- [4] M. Saitome, H. Katoh et al., Transient opening of mitochondrial permeability transition pore by reactive oxygen species protects myocardium from ischemia-reperfusion injury, *Am J Physiol Heart Circ Physiol*, **296**, H1125-H1132 (2009).

# THE RESPONSE OF A PURE BACTERIAL CULTURE TO THE EFFECT OF ANTIMICROBIAL AGENTS EMPLOYING A LEAKY MODE DIFFRACTION GRATING WAVEGUIDE SENSOR

Tadas Juknius<sup>1</sup>, Tomas Tamulevičius<sup>2,3</sup>, Ieva Gražulevičiūtė<sup>3</sup>, Dainius Virganavičius<sup>2</sup>, Irena Klimienė<sup>1</sup>, Algimantas Petras Matusevičius<sup>1</sup>, Sigitas Tamulevičius<sup>2,3</sup>

<sup>1</sup> Veterinary academy, Lithuanian University of Health Sciences, Lithuania

<sup>2</sup> Institute of Materials Science, Kaunas University of Technology, Lithuania

<sup>3</sup> Physics Department, Kaunas University of Technology, Lithuania

TadasJuknius@inbox.lt, Tomas.Tamulevicius@ktu.lt

The aim of this study is to investigate the response of a pure bacterial culture (*Staphylococcus aureus*) placed in broth and saline solutions (0.9 %) to the effect of antibiotics (*benzylpenicillinum* and *gentamicinum*) employing a custom built motorized angular white polarized light reflectance measurement stand and a leaky mode diffraction grating sensor chip. Common microbiology tests used for the evaluation of the effectiveness of antimicrobial agents are time consuming while the suggested method provides results in real time. Therefore it is important for pharmaceutical applications.

Various types of evanescent field sensors are widely used in the fields of biology and chemistry, due to their sensitivity and rapid real time detection. Evanescent field probing techniques are based on variations of real or imaginary part of refractive index of the analyte. Such variations cause a certain spectral response (shift in the amplitude or peak position of the reflectance spectrum). Most of these devices are sensitive only in a 100-200 nm range from the interface (restricted by the evanescent field penetration depth), thus the measurements are made by functionalizing the sensor surface with a layer of (bio)active substance. On the other hand, waveguide sensors that exhibit leaky modes are reported to have higher evanescent field penetration depths, therefore they are able to measure processes further away from the interface with greater precision and sensitivity and without the need of activation layer [1].

In this work a sub-wavelength (428 nm) period sinusoidal relief sensor chip was used to monitor the effect of antimicrobial agents. It was fabricated in a diamond like carbon film employing holographic lithography and dry etching [2]. The leaky modes are supported in the waveguide due to periodic modulation and asymmetry of the structure. The sensor chip was mounted in a thermostated measurement cell (20 °C). Reflectance measurements of TM polarization at 14° angle of incidence were performed employing custom built motorized angular reflectance measurement stand and CCD spectrometer ( $\lambda=360\text{--}780\text{ nm}$ ) [2]. The analyte was confined within measurement cell and fractions of a milliliter of antibiotics were injected at fixed time intervals. The changes in peak position (see Fig. 1.) and amplitude of the reflectance spectrum were monitored over time.

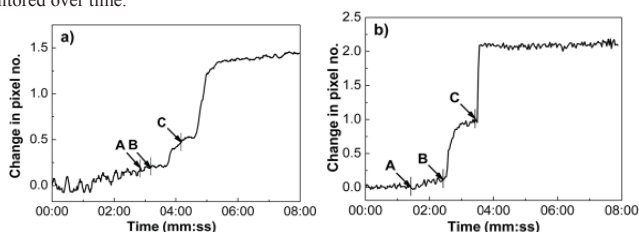


Fig. 1. The change in the pixel number corresponds to the shift of peak position in the reflectance spectrum of *S. aureus* ( $1200 \cdot 10^6$  cells/mL) saline solution (0.9 %) treated with *benzylpenicillinum* (a) and *gentamicinum* (b). A, B, C marks the injections of 0.2 ml (100 000 VV/ml) of *benzylpenicillinum* or 0.2 ml (5 mg/ml) of *gentamicinum* to 1.5 ml bacteria solution respectively.

As demonstrated in Fig. 1 the first injection of antibacterial agent causes minimal change in the spectral response of the solution while further injections are followed by a visible change of the peak position in reflectance spectrum. This corresponds to variations in the refractive index of the analyte media due to bacteria eradication by antibiotics. After the third injection all bacteria lysis in the solution may have occurred. This was valid for both antibacterial agents. The eradication of bacteria has been proved by microbiology tests.

[1] M. Zourob *et al.*, The development of a metal clad leaky waveguide sensor for the detection of particles, *Sensors and Actuators B*, 90, 296–307 (2003)

[2] T. Tamulevičius *et al.*, Application of holographic sub-wavelength diffraction gratings for monitoring of kinetics of bioprocesses, *Applied Surface Science*, 258, 9292–9296 (2012).

## THE KINETIC MODEL OF NEUROTRANSMITTER RELEASE FROM PRESYNAPTIC BOUTON

Maryna Hliatseвич, Pavel Bulai

Department of Biophysics, Physics Faculty, Belarusian State University, Belarus  
gletseвич.marina@gmail.com

Modeling synaptic transmission promises to provide bright insights into information processing in human brain. One of the main steps of synaptic transmission is neurotransmitter release from presynaptic terminal into synaptic cleft. The objective of our research work is to elaborate mathematical model for Markov chain which describes crucial reactions of neurotransmitter release (NR).

NR is caused by calcium concentration changes upon action potential arrival [1]. The sensor molecule providing the linkage between calcium ions influx and synaptic vesicle exocytosis is thought to be a synaptotagmin (ST) – the protein which has 5 sites for  $\text{Ca}^{2+}$  binding and is located on synaptic vesicle membrane [2]. After binding with calcium ions it promotes formation of SNARE (derived from ‘soluble NSF attachment receptor’) complexes that cause exocytosis. If we assume binding sites of ST to be equal and independent, then we can introduce rate constants for calcium binding and dissociation from site ( $\alpha$  and  $\beta$ ) and describe the kinetic of calcium binding to the one site by the following equation:

$$\frac{dm}{dt} = \alpha[\text{Ca}^{2+}]m - \beta(1 - m) \quad (1)$$

where  $m$  stands for the part of the bond sites. If we regard the total number of ST molecules to be equal  $Z$ , then number of complexes  $\text{ST-Ca}_5$  could be termed as  $Zm^5$ .

After binding calcium ions ST initiates SNARE complex formation. This process could correspond to  $\text{Ca}^{2+}$ -independent isomerization step introduced by authors of [1], and is described by reaction



where  $\text{ST-Ca}_5^*$  is formed SNARE complex and  $\gamma, \delta$  are rate constants of forward and backward reaction.

Let us consider presynaptic bouton. It contains  $N$  synaptic vesicles that one could divide into four types: docked at the plasmatic membrane, primed (prepared for NR by SNARE complex), released and inactivated [3]. Let us denote  $D, P, R$  and  $I$  as the fraction of  $N$  for corresponding vesicle types. If we assume that there are  $n$  ST molecules on each docked vesicle and  $l$  formed SNARE complexes are needed for exocytosis initiation, then the total number of ST molecules in bouton is derived as  $nDN$  and transition between states of vesicle could be described as



$$I = 1 - D - R - P$$

Using mass action law one could describe the processes depicted in Eq. (1)-(3) with the help of following system of ordinary differential equations:

$$\begin{aligned} \frac{d(\text{ST-Ca}_5)}{dt} &= -\gamma(\text{ST-Ca}_5) + \delta(\text{ST-Ca}_5)^* = -\gamma nDNm^5 + \delta(\text{ST-Ca}_5)^* \\ \frac{d(\text{ST-Ca}_5)^*}{dt} &= -\frac{d(\text{ST-Ca}_5)}{dt} \\ \frac{dD}{dt} &= -k_1 D \cdot (\text{ST-Ca}_5)^* + k_2 P + \frac{I}{\tau_{rec}} \\ \frac{dP}{dt} &= -(k_3 + k_2)P + k_1 D \cdot (\text{ST-Ca}_5)^* \\ \frac{dR}{dt} &= k_3 P - \frac{R}{\tau_{inact}} \end{aligned} \quad (4)$$

where  $k_1, k_2, k_3$  are rate constants of corresponding reactions,  $\tau_{rec}$  and  $\tau_{inact}$  are the time constants of vesicle inactivation and recovery, respectively [4].

The novelty of our work consists in elaboration of the first deterministic model which accounts for calcium binding to ST, SNARE complex formation and transitions between states of synaptic vesicles. Some parameters ( $N, D, l, n, k_3, \gamma, \delta$ ) are provided in literature, but others should be fitted accordingly to the experimental results.

[1] J. H. Bollmann, B. Sakmann, J. G. Borst, Calcium sensitivity of glutamate release in a calyx-type terminal, *Science* **289-5481**, 953-957 (2000).

[2] E.R.Chapman, Synaptotagmin: a  $\text{Ca}^{2+}$  sensor that triggers exocytosis? *Nat. Rev. Mol. Cell Biol.* **3-7**, 498-508 (2002).

[3] T. C. Sudhov, The synaptic vesicle cycle, *Annu. Rev. Neurosci.* **27**, 509–547 (2004).

[4] S.G.Tewari, K.K. Majumdar, A mathematical model of the tripartite synapse: astrocyte-induced synaptic plasticity, *J. of Biol.Phys.* **38-3**, 465-496 (2012).



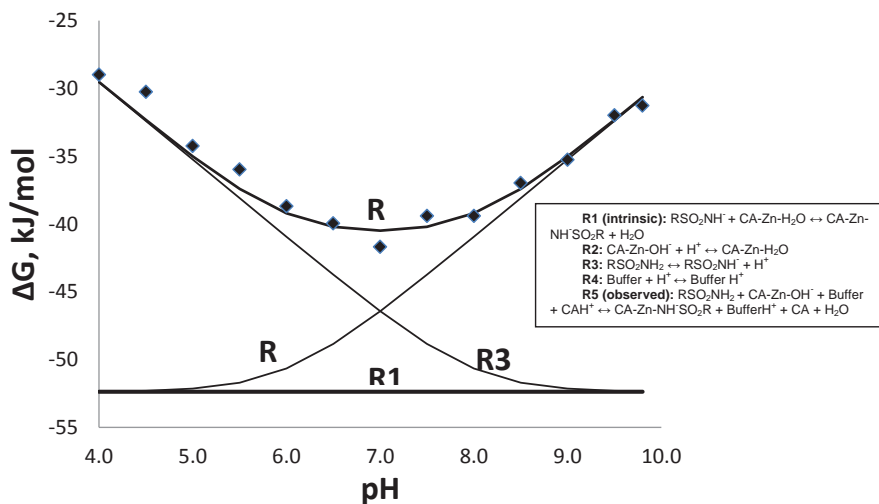
# THERMODYNAMICS OF ETHOZZOLAMIDE BINDING TO RECOMBINANT HUMAN CARBONIC ANHYDRASE (CA) VI

Justina Kazokaitė, Daumantas Matulis

Department of Biothermodynamics and Drug Design, Institute of Biotechnology, Vilnius University, Lithuania  
[kazokaite@ibt.lt](mailto:kazokaite@ibt.lt)

Carbonic anhydrases catalyze the reversible hydration of carbon dioxide to bicarbonate and participate in diverse physiological processes. In humans, 12 CA isoforms possess catalytic activity. They differ from each other in tissue localization and cellular distribution. CAVI is the only secreted isoenzyme of human CA family. It has common roles of CAs as pH regulation in saliva, antireflux defense and has a protective effect in stomach and oesophagus. Gene comparison tells that CAVI is closely related to the two membrane associated isoenzymes CAIV and CAIX. CAIV is a drug target for several pathologies, including glaucoma (together with CAII and CAXII), retinitis pigmentosa and stroke [1]. CAIX is a marker for hypoxic tumors. This association links CAVI with certain cancers which might be associated with salivary glands [2]. CA isoforms are therapeutic targets for inhibition to treat diseases. Sulfonamide-based compounds, such as ethoxzolamide (EZA), appear to be effective in inhibiting CAs. However, it is important to find isoform-selective compounds.

In this work, EZA binding to CAVI was analyzed by fluorescent thermal shift assay (TSA). TSA is a rapid screening method for the identification of binders and requires low amounts of protein. CA inhibitor binding is linked to several protonation–deprotonation reactions. These linked reactions strongly affect the observed thermodynamic parameters of binding and often do not correlate with the intrinsic parameters. Only the intrinsic parameters should be used for compound structure–activity relationship analysis [3].



The dependencies of the observed Gibbs free energies of EZA binding ( $\Delta G$ ) on pH.

- [1] Simone G et al. Multiple Binding Modes of Inhibitors to Carbonic Anhydrase: How to Design Specific Drug Targeting 15 Different Isoforms? Chem Rev. 2012; 112: 4421-68
- [2] Sly W et al. Structure, function and applications of carbonic anhydrase isoenzymes. Bioorg Med Chem. 2012
- [3] Matulis D et al. Characterization of human carbonic anhydrase XII stability and inhibitor binding. Bioorg Med Chem. 2012

## REDOX-REGULATION OF FUNCTIONAL AND MORPHOLOGICAL CHARACTERISTICS OF CELLS 293, PRODUCING CHI3L1 PROTEIN

Julia Kirpich, Nina Krylova, Elena Golubeva, Tatsiana Kulahava

Department of Biophysics, Faculty of Physics, Belarusian State University, Belarus  
[juliakirpich@gmail.com](mailto:juliakirpich@gmail.com)

Nowadays many proteins serve as biomarkers of cell and tissue pathologies. Among them is chitinase – 3 like protein 1 (CHI3L1, YKL-40, HC-gp39, human cartilage glycoprotein 39). Expression of CHI3L1 is associated with conditions of increased matrix turnover and tissue remodeling [1]. This protein is assigned the role of molecular marker of inflammation, carcinogenesis, and related events. CHI3L1 is rarely detected in serum of healthy people. Many types of cancer cells produce CHI3L1 (glial, breast, colorectal, lung, kidney, pancreas, ovary, prostate, uterine cell carcinoma, osteosarcoma, oligodendrogliomas, glioblastoma and tumors of embryonic cells). The CHI3L1 gene is among the highly upregulated genes in glioblastoma, papillary thyroid carcinoma, and in extracellular myxoid chondrosarcoma [1,2,3,4]. Some inflammatory diseases are also accompanied by excessive CHI3L1 production (rheumatoid or osteoarthritis) [5]. But the functions of this protein in cancer and inflammation have not been revealed yet. So the purpose of our study was to detect how CHI3L1 intracellular production influences the unique redox and morphological properties of cancer cells. We studied hydrogen peroxide utilization rate, cell antioxidant status by measuring the amount of one of the main cell reduction equivalents – glutathione. Moreover, considering functional activity of CHI3L1 could give a cell some structural peculiarities, we decided to study mitochondrial distribution in cells.

Two cell lines (Human Embryonic Kidney 293 cells): the 293 cells, stably transfected with «empty» vector pcDNA3.1 (293\_pcDNA) and the 293 cells, stably expressing CHI3L1 (293\_CHI3L1) were kindly provided by Dr. V. Kavsan (IMBG, Ukraine) [1]. These cell lines were different only with the presence or absence of CHI3L1. Comparing experimental data on the two cell lines using fluorescent analysis we established the role of this protein in functional activity of cells.

Measuring fluorescence of cell-permeate probe 2',7'-dichlorodihydrofluorescein diacetate (H<sub>2</sub>DCFDA) in cells exposed to hydrogen peroxide we calculated the constant of hydrogen peroxide utilization which appeared to be  $(1,6 \pm 0,5) \cdot 10^3 \text{ s}^{-1}$  for 293\_pcDNA cells and  $(4,3 \pm 0,6) \cdot 10^3 \text{ s}^{-1}$  for 293\_CHI3L1 cells. Therefore, the constant of hydrogen peroxide utilization is 2.7-fold higher for 293\_CHI3L1 cells. The level of reduced glutathione was also estimated. It was established that 293\_CHI3L1 cells had 2-fold increased level of reduced glutathione as compared with 293\_pcDNA cells. These results showed that cells producing CHI3L1 possessed better antioxidant system that provided them with resistance to oxidative stress.

To reveal structural peculiarities of selected cell lines fluorescent dye JC-1 for mitochondria membrane potential detection was used. Thus mitochondria were visualized and mitochondria membrane potential was evaluated by taking the ratio of integral intensities around 590 nm (J-aggregates) and 530 nm (monomer form) [6]. It was established that the integral intensity of JC-1 fluorescence (590 nm) was higher in 293\_CHI3L1 cells twice as large as in 293\_pcDNA cells. Evaluating fluorescent images of cells it was shown that in 293\_CHI3L1 cells the number of active mitochondria was greater than in 293\_pcDNA cells. Therefore, these data gave evidence that CHI3L1 intracellular production influenced mitochondria activity and localization.

To summarize, CHI3L1 intracellular production causes reduced glutathione level increase, oxidative stress (hydrogen peroxide) resistance, mitochondria activity enhancement, and enlarged mitochondria number.

- 
- [1] O. V. Balynska et al., Characterization of new cell line stably expressing CHI3L1 oncogene, ISSN 0233–7657, Biopolymers and Cell. 2011. Vol. 27. N 4. P. 285–290
- [2] K. Eurich et al., Potential role of chitinase 3-like-1 in inflammation-associated carcinogenic changes of epithelial cells, World J Gastroenterology. – 2009. – No 15 (42). – P. 5249-5259.
- [3] P.A. Areshkov et al., Chitinase 3-like protein 2 (CHI3L2, YKL-39) activates phosphorylation of extracellular signal-regulated kinases ERK1/ERK2 in human embryonic kidney (HEK293) and human glioblastoma (U87 MG) cells, Cytology and Genetics. – 2010. – V. 44. – No. 1. – P. 1-6.
- [4] M. Ringsholt et al., YKL-40 protein expression in normal adult human tissues - an immunohistochemical study, J. Molecular Histology. – 2007. – V. 38. – P. 33-43
- [5] A. D. Recklies et al., The chitinase 3-like protein human cartilage glycoprotein 39 (HC-gp39) stimulates proliferation of human connective-tissue cells and activates both extracellular signal-regulated kinase- and protein kinase B-mediated signalling pathways, Biochem J. 2002 July 1.
- [6] E. Simeonova et al., Monitoring the mitochondrial transmembrane potential with the JC-1 fluorochrome in programmed cell death during mesophyll leaf senescence, Protoplasma (2004) 223: 143–153

# THE INVESTIGATION OF BLACK CARBON IN AEROSOL PARTICLES AND IDENTIFICATION OF ITS ORIGIN

Julija Pauraitė<sup>1</sup> and Vidmantas Ulevičius<sup>2</sup>

<sup>1</sup> Faculty of Physics, Vilnius University, Sauletekio Ave 9, build. 3, LT-10222 Vilnius, Lithuania

<sup>2</sup> Institute of Physics, Center for Physical Sciences and Technology, Savanoriu ave. 231, LT-02300 Vilnius, Lithuania  
[julijapauraitė@yahoo.com](mailto:julijapauraitė@yahoo.com)

The influence of aerosols particles on health and climate are not yet completely examined. It is known that aerosols have significant influence on climate change. Some of them have ability to cool down the atmosphere, while others absorb sun radiation and increase temperature. Aerosols containing black carbon (BC) represents second category. BC is prevailing in every common background but higher concentrations can be observed in urban environment.

Continuous measurements of black carbon (BC) aerosols mass concentration were performed at a background site Preila from September to December, 2012 period. This was used to characterize BC temporal variation of mass concentration over the East Baltic region. An aethalometer was deployed at the site and provided real-time, continuous measurements of the BC mass concentrations. Measured light attenuation was converted to BC mass. The optical transmission of carbonaceous aerosol particles was measured sequentially at seven wavelengths  $\lambda$  (0.37, 0.45, 0.52, 0.59, 0.66, 0.88 and 0.95  $\mu\text{m}$ ). The BC mass concentration measured at the 0.88  $\mu\text{m}$  wavelength is considered to represent BC in the atmosphere as at this wavelength.

It was obtained and compared concentrations of BC of different seasons. To obtain higher accuracy, this included corrections of concentration, attenuation and other optical properties. Also, the calculation of Ångström exponent was performed. This exponent is usually used to describe the dependency of the aerosol optical thickness, or aerosol extinction coefficient on wavelength. Ångström exponent enabled identification of BC source. This is the reason of it significant importance in optical methods.

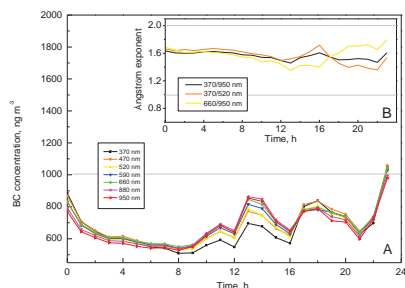


Fig.1. Time series of: (A) BC mass concentration, (B) the light Ångström exponent of absorption coefficient during 17<sup>th</sup> of September, 2012

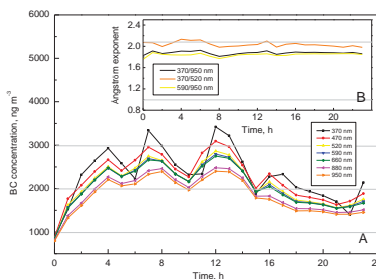


Fig.2. Time series of: (A) BC mass concentration, (B) the light Ångström exponent of absorption coefficient during 14<sup>th</sup> of December, 2012

Analysis of the data revealed that during warm season concentrations and Ångström exponent values were low and varied in the range from 100 to 2000  $\text{ng m}^{-3}$  of BC and exponent from 1.2 to 1.7 (fig. 1), while during cold season concentrations (from 1000 to 5000  $\text{ng m}^{-3}$ ) and Ångström exponent values (from 1.6 to 2.1) were markedly higher (fig. 2). This difference in Ångström exponent indicates that aerosols from diesel fuel burning predominate in summer and biomass burning has higher influence during winter.

[1] S. Byčienienė, V. Ulevičius, S. Kecorius, Characteristics of black carbon aerosol mass concentration over the East Baltic region from two-years measurements, Environmental Monitoring c0em00480d (2011).

## ELECTROPHORETIC STUDY OF COMPLEXING BETWEEN DNA AND CARBOXYLATED CARBON NANOTUBES

Nadya Pleshko<sup>1</sup>, Vladimir Krot<sup>1</sup>

<sup>1</sup>Department of Physics, Belarusian State University, Belarus

[nadyavp@tut.by](mailto:nadyavp@tut.by)

Carbon nanotubes (CNTs) exhibit a unique combination of excellent mechanical, electrical, and electrochemical properties which stimulate ever increasing interest in the application of CNTs as components in biosensors. The initial stage for the development of the DNA-containing biosensors is linking of a molecule of nucleic acid to the surface of CNT.

The interaction of native DNA (nDNA) and denaturated DNA (dDNA) with CNT was estimated by electrophoretic separation of the products from the DNA-CNT interaction (Fig. 1). DNA was revealed with the help of coloring by ethidium bromide; CNT was exhibited in gel as dark areas without an additional coloring. The ethidium bromide dye, being linked to DNA, is fluorescent in the UV spectral region, whereas linking to the DNA-CNT complex leads to lower fluorescence intensity of the dye due to fluorescence quenching as CNT is a universal quencher for different fluorophors [1].

Analysis of the electrophorograms for nDNA and dDNA complexes with CNT demonstrates that the fluorescence intensity at track 5 (Fig.1) is lower than that at track 3. Based on the data obtained, it is supposed that the complexation efficiency of CNT with dDNA is higher than that with nDNA.

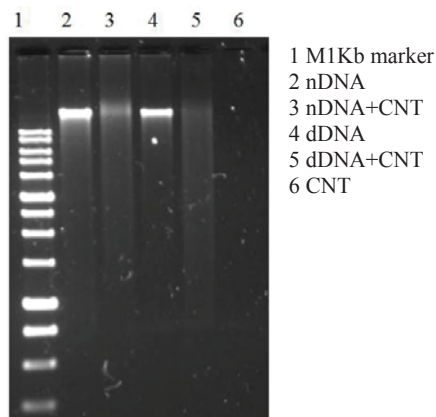


Fig. 1. Electrophoresis of the products from the DNA-CNT interaction in 1% agarose gel.

[1] Zhi Zhu, Ronghua Yang et al., Single-walled carbon nanotube as an effective quencher, Anal Bioanal Chem 396, 73-83 (2010).

## ACTIVATION OF BOVINE SERUM ALBUMIN-GOLD NANOCLOUDERS VIA TWO PHOTON EXCITATION

Deividas Sabonis<sup>1</sup>, Ričardas Rotomskis<sup>1,2</sup>

<sup>1</sup>Laboratory of Biomedical Physics, Institute of Oncology, Vilnius University, Baublio 3B, LT-08406, Vilnius

<sup>2</sup>Biophotonics group of Laser Research Center, Vilnius University, Saulėtekio 9, c.3, LT-10222, Vilnius

[Sabonis.Deividas@gmail.com](mailto:Sabonis.Deividas@gmail.com)

Near infrared two-photon excitation has been a research focus since it became evident that deeper penetration in tissues for imaging and sensitization applications is only accessible within the spectral therapeutic window of 700-1200 nm. The interest in nanoparticles has increased rapidly because of the specific characteristics useful for imaging and treatment of various oncological diseases and cancer. However photophysical properties upon two-photon excitation (TPE) of nanoparticles are yet poorly investigated (Fig. 1).

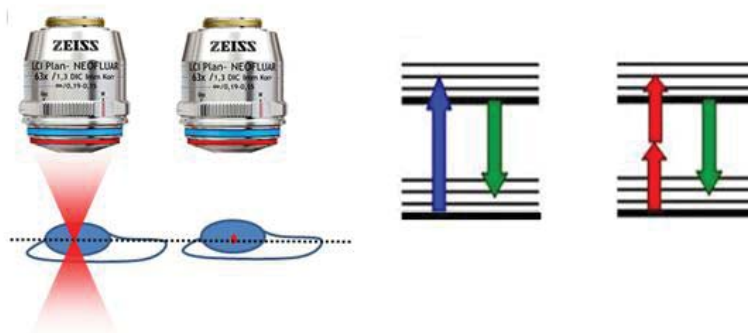


**Fig.1.** Comparison of one and two photon excitation

Experiments were carried out on bovine serum albumin (BSA) coated-gold nanoclusters (Au NCs) (synthesized from HAuCl<sub>4</sub> (Sigma-Aldrich, Germany)). TPE of samples was performed by using laser system PHAROS (1030 nm, 280 fs, Light Conversion, Lithuania). Two-photon absorption (TPA) cross sections were evaluated by a comparative method with rhodamine B as reference compound [1].

Photoluminescence spectrum measured upon TPE of BSA-Au NCs exhibited intensive band at 665 nm. TPA cross sections of these nanoparticles were compared with the conventional fluorescent organic molecules. Our results confirm that BSA-Au NCs have high enough TPA cross sections compared to organic dyes and therefore can be used as potential two-photon absorbing agents in cancer diagnostics and therapy.

[1] Makarov, N.S., M. Drobizhev, and A. Rebane, Two-photon absorption standards in the 550-1600 nm excitation wavelength range. *Optics Express*, 2008. 16(6): p. 4029-4047.

# ELECTROMAGNETIC PULSE INTERACTION WITH A HUMAN SKIN TAKING INTO ACCOUNT PERMITTIVITY DISPERSION

Olga Simachova

Department of Theoretical Radio Physics, V.N.Karazin Kharkiv National University, Ukraine  
o.n.simachova@gmail.com

The video pulse interaction with the dielectric flat-layered structure that models a human skin taking into account dispersion by the Debye formula is considered in this paper. The results are calculated temporal reflected, absorbed and transmitted fields characteristics; also parts of reflected and transmitted energy are determined.

The electromagnetic pulse with a flat front  $F_{in}(\xi)$  falls from a free space with the angle  $\theta$  on the flat layered structure consisted of the layer with the dielectric constants  $\varepsilon_1, \mu_1$  that lies on the dielectric half-space with  $\varepsilon_f, \mu_f$  (Fig.1).

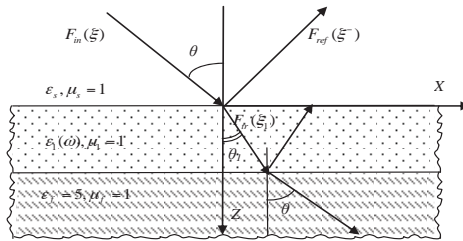


**Figure 1.** Problem statement.

The incident pulse temporal form is  $F_{in}(\xi) = A_0 e^{-\frac{\xi^2}{2a^2}}$ , where  $A_0$  - an amplitude,  $2a$  - a duration.

The permittivity of the layer is complex and described by the Debye approximation, that is the most satisfied for biological media [1]:

$$\varepsilon = \varepsilon_\infty + \frac{\varepsilon_0 - \varepsilon_\infty}{1 + i\omega\tau} \quad (1)$$

Taking into consideration secondary reflections into the layer the result reflected field can be written as

$$F_{ref}^{(n)}(\xi^-) = \frac{A_0 a}{\sqrt{2\pi}} \int_{-\infty}^{\infty} e^{-\frac{\omega^2 a^2}{2}} e^{i\omega\xi^-} (V(\omega, \theta) + \sum_{n=2}^{\infty} R(\omega, \theta) \cdot R_-(\omega, \theta_1) \cdot V_-^{n-2}(\omega, \theta_1) \cdot V_1^{n-1}(\omega, \theta_1)) d\omega \quad (2)$$

and the transmitted field

$$F_{tr}^{(n)}(\xi_1) = \frac{A_0 a}{\sqrt{2\pi}} \int_{-\infty}^{\infty} e^{-\frac{\omega^2 a^2}{2}} e^{i\omega\xi_1(\omega)} \times \sum_{n=2}^{\infty} R(\omega, \theta) \cdot R_1(\omega, \theta_1) \cdot V_-^{n-1}(\omega, \theta_1) \cdot V_1^{n-1}(\omega, \theta_1) d\omega. \quad (3)$$

The program for the temporal distribution calculation of the transmitted and reflected signals for the dielectric layer taking into account the permittivity dispersion was created. The problem was solved in a time domain for arbitrary shape and duration of the incident pulse signal. The results for the transmitted field dependence on incidence angle, dispersion of transmission coefficients and specific absorption rate calculation are presented.

[1] Ø. G. Martinsen, S. Grimnes S., H. P. Shwan, Interface phenomena and dielectric properties of biological tissues, Encyclopedia of Surface and Colloid Science, 2643-2652 (2002).

## FLUOROMETRIC INVESTIGATION OF AU-BSA-99TC MULTIMODAL IMAGING TRACER

Ernestas Svirbutavičius<sup>1</sup>, Marius Stalnionis<sup>1,2</sup>, Marija Matulionytė<sup>1,2</sup>

<sup>1</sup> Laboratory of Biomedical Physics, Institute of Oncology, Vilnius University, Baublio 3B, LT-08406, Vilnius

<sup>2</sup> Biophotonics Group of Laser Research Center, Faculty of Physics, Vilnius University, Sauletekio 9, Bldg. 3, Vilnius LT-10222, Lithuania  
[svirbutavicius@gmail.com](mailto:svirbutavicius@gmail.com)

Medical imaging techniques have great importance to the course of the cancer treatment process. One of the imaging methods is Nuclear Medicine, where radioactive materials such as Technetium-99m (99mTc) are used. However, this method has low resolution and the image can be recorded only on the screen.

In cases where the boundaries of the object have to be determined more precisely, fluorescing materials can be used, for their better resolution and ability to directly visualize of the object [1]. Fluorescent nanoparticles (NP) are of great scientific interest at the moment, for they can be bound to biomolecular structures and delivered to the selected targets. Radioactive metals such as 99mTc can be used for labeling these NPs allowing to apply dual imaging modalities. This combination would give the opportunity to use dual imaging of structures and help surgeons visualize the tumor.

In this research dual imaging NPs were synthesized using photoluminescent gold bovine serum albumin nanoclusters (Au-BSA NC) and “cold” Technetium-99 (99Tc). Au-BSA nanoclusters were synthesized using tetrachlorauric acid (HauCl<sub>4</sub>), BSA and sodium hydroxide (NaOH) as a reducing agent [2]. Synthesis of Au-BSA-99Tc NP was carried out using 1 ml of 99Tc, 1 ml of Au-BSA ( $3.6 \cdot 10^{-7}$  mol/ml), 0.5 ml SnCl<sub>2</sub> (0.4 mg/ml); Saline (0.9% NaCl). The content of the SnCl<sub>2</sub> in Au-BSA-99Tc solution varied. To make stannous solution, 4 mg of SnCl<sub>2</sub> were diluted with 10 ml of Saline. Synthesis was done by mixing Au-BSA with the stannous solution and then adding 99Tc [2].

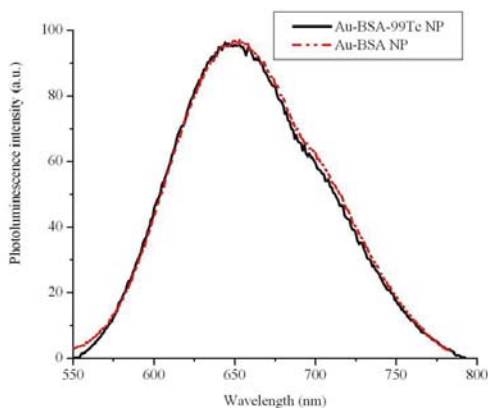


Fig. 1. Photoluminescence spectra of Au-BSA NP and Au-BSA-99Tc NP.

To evaluate the photoluminescence properties of synthesized Au-BSA-99Tc compound spectrophotometric analysis were performed. “Varian Cary 50” spectrophotometer and quartz cells were used to evaluate the fluorescence. The excitation wavelength was set to 470 nm. Photoluminescence spectra showed that the optical properties of the synthesised compound remained the same: the photopeak of Au-BSA NPs and the peak of Au-BSA-99Tc NPs are observed the same wavelength (650 nm) (Fig.1). The spectroscopic findings allowed to draw the conclusion that the additional components do not cause the suppression of the photoluminescence of Au-BSA NP. Thus, allow to conclude that the Au-BSA NP structure and properties remain unchanged. Hence, there is a possibility of using our synthesized compound for dual imaging studies, but other properties such as stability of compound and the effect of Au-BSA concentration changes should be investigated.

[1] A. Azhdarinia et al., Dual-Labeling Strategies for Nuclear and Fluorescence Molecular Imaging: A Review and Analysis, *Molecular Imaging and Biology* 14, 261-276, (2012).

[2] J. Xie et al., Protein-Directed Synthesis of Highly Fluorescent Gold Nanoclusters, *Journal of the American Chemical Society*, 131, 888-889, (2009).

[3] Y. Wang et al., On-Site Preparation of Technetium-99m Labeled Human Serum Albumin for Clinical Application, *Tohoku Journal of Experimental Medicine*, 211, 379-385, (2007).

# INVESTIGATIONS OF LUMINESCENCE OF SINGLET OXYGEN GENERATED BY THE QUANTUM DOT–SENSITIZER COMPLEX

Gediminas Špogis<sup>1,2</sup>.

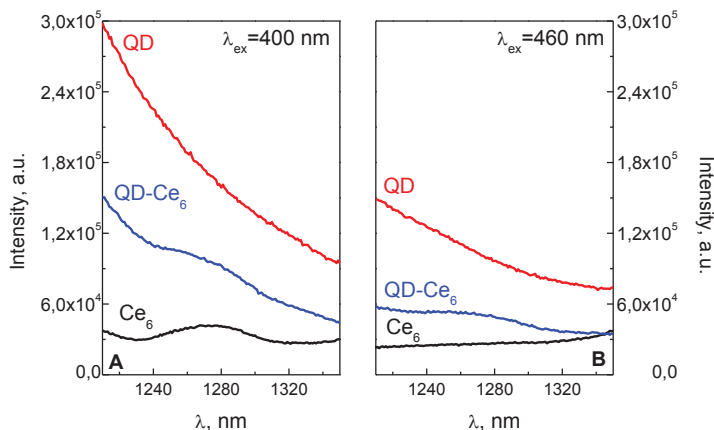
<sup>1</sup>Faculty of Physics, Vilnius University, Saulėtekio Ave. 9-III, LT-10222 Vilnius, Lithuania

<sup>2</sup>Institute of Oncology, Vilnius University, Baublio 3b, LT-08406 Vilnius, Lithuania

[Gediminas.Spogis@gmail.com](mailto:Gediminas.Spogis@gmail.com)

Quantum dots (QDs) are extensively studied as promising materials for applications in various fields of medicine. QDs, also named luminescent semiconductor nanocrystals, are known for their unique photophysical properties, such as narrow size-dependent photoluminescence (PL) spectra, broad absorption spectra with large extinction coefficients, high PL quantum yields, exclusive photostability and ability to functionalize QD surface. It was suggested, that QDs could be used as energy donors for conventional photosensitizers (PS) in photodynamic therapy of cancer (PDT) – a treatment that uses light activatable drug and light of appropriate wavelength to damage cancer cells [1]. Singlet oxygen (<sup>1</sup>O<sub>2</sub>) is the main reactive intermediate involved in cancer cell killing during PDT. Thus, investigations of <sup>1</sup>O<sub>2</sub> generated by QD-PS complexes are important in order QDs could be used in PDT.

In this work we studied the production of <sup>1</sup>O<sub>2</sub> generated by CdSe/ZnS QDs (625 nm) and chlorin e<sub>6</sub> (Ce<sub>6</sub>) PS complex QD-Ce<sub>6</sub> in heavy water (D<sub>2</sub>O) solution. The formation of <sup>1</sup>O<sub>2</sub> was measured by detecting <sup>1</sup>O<sub>2</sub> luminescence at 1270 nm using near-infrared photomultiplier tube, cooled with liquid nitrogen. The samples were irradiated by continuous light source at 400 and 460 nm. The absorption of Ce<sub>6</sub> at 460 nm is minimal, therefore <sup>1</sup>O<sub>2</sub> production by QD-Ce<sub>6</sub> occurs only due to resonant energy transfer (FRET) from QD to bound Ce<sub>6</sub>. The results when the samples were irradiated at 400 nm, where Ce<sub>6</sub> absorption is much higher, are also presented for comparison.



1 Fig. Spectral properties of QD, Ce<sub>6</sub> and complex QD-Ce<sub>6</sub> in D<sub>2</sub>O in <sup>1</sup>O<sub>2</sub> luminescence spectral range when samples are irradiated by light of different wavelengths (A – λ<sub>EX</sub>=400 nm, B – λ<sub>EX</sub>=460 nm).

The variations in spectra of QD, Ce<sub>6</sub> and QD-Ce<sub>6</sub> in D<sub>2</sub>O indicated that QD and Ce<sub>6</sub> forms a complex in D<sub>2</sub>O [2]. The spectral properties of QD, Ce<sub>6</sub> and QD-Ce<sub>6</sub> in D<sub>2</sub>O in spectral range of <sup>1</sup>O<sub>2</sub> luminescence, when the samples are irradiated at different wavelengths, are presented in fig. 1. The illumination of Ce<sub>6</sub> at 400 nm as well as QD-Ce<sub>6</sub> at both 400 nm and 460 nm resulted in a pronounced, though not intense, <sup>1</sup>O<sub>2</sub> luminescence signal at 1270 nm, indicating that <sup>1</sup>O<sub>2</sub> is produced. No <sup>1</sup>O<sub>2</sub> luminescence signal was detected in QD D<sub>2</sub>O solutions when illuminating the samples at 400 nm and 460 nm, nor in Ce<sub>6</sub> D<sub>2</sub>O solution, irradiated by 460 nm light, resulting in no <sup>1</sup>O<sub>2</sub> in solutions.

Based on the experimental results we conclude, that QD-Ce<sub>6</sub> complex is able to generate <sup>1</sup>O<sub>2</sub>. The production of <sup>1</sup>O<sub>2</sub> occurs because of the resonant energy transfer from light absorbing QD to bound Ce<sub>6</sub> molecules. Thus, QDs could be potentially used in PDT resulting in a more effective treatment.

[1] Samia, A.C.S., Chen, X., Burda, C. Semiconductor Quantum Dots for Photodynamic Therapy. *Journal of The American Chemical Society* **125**(51), 15736-15737 (2003).

[2] Valančiūnaitė, J., Rotomskis, R. Quantum dots as energy donors for photosensitizers: perspectives for photodynamic therapy of cancer. *SPIE Proceedings* **7376**(1), (2010).



***AhR* gene methylation and protein expression in different malignancy gliomas**  
Indrė Valiulytė<sup>1,2</sup>, Mykolas Mikučiūnas<sup>1,3</sup>, Paulina Vaitkienė<sup>1</sup>, Daina Skiriutė<sup>1</sup>, Arūnas Kazlauskas<sup>1</sup>

1. Laboratory of Neurooncology and Genetics, Institute of Neuroscience, Kaunas Academy of Medicine, Lithuanian University of Health Sciences, Eiveniu str. 4, Kaunas, LT 50009, Lithuania;
2. Department of Biochemistry and Biotechnologies, The Faculty of Natural Sciences, Vytautas Magnus University, Kaunas, Lithuania. Vileikos str. 8, LT-44404 Kaunas; [IndreValiulyte@gmail.com](mailto:IndreValiulyte@gmail.com)
3. The Faculty of Medicine, Lithuanian University of Health Sciences, Kaunas, Lithuania. A. Mickevičiaus str.9.

**Abstract:**

Glioblastoma is highly aggressive primary brain tumor with strongly variable patient survival. The *AhR* gene methylation is one of several potential epigenetic prognostic markers in glioblastoma. *AhR* gene expression is involved in many critical life processes (e.g. cell type-specific differentiation, cell division, apoptosis).

The objective of this study was to investigate *AhR* gene methylation and protein expression in human brain tumor – glioma.

**Methods:** Were investigated 73 patients with different grade gliomas: grade I- 8 samples, grade II – 8, grade III - 8 and grade IV (Glioblastoma) – 48 samples. Tumor DNA was extracted from 25-40mg of frozen tissue and the methylation status of *AhR* gene promoter was determined by bisulfite treatment of DNA. *AhR* gene methylation was performed by using methylation specific polymerase chain reaction (MS-PCR) method. MS- PCR products were separated by electrophoresis on 2% agarose gels with ethidium bromide and visualized under UV illumination. Western blot was used to determine the AhR expression in gliomas.

**Results:** 37.5% of all patients had *AhR* gene methylation. In different malignancy grade gliomas *AhR* gene promoter methylation frequencies were varied. Glioblastomas demonstrated AhR promoter methylation in 25/48 (52.1%). All of grade I (0/8) and grade III (0/8) gliomas have not showed *AhR* promoter methylation. *AhR* promoter methylation was observed in 25% (2/8) of grade II gliomas. AhR protein expression was different between glioma malignancy grades.

**In conclusion:** *AhR* gene methylation is related with glioma malignancy. *AhR* gene methylation may be involved in gliomagenesis process and might be one of the potential epigenetic prognostic markers in glioblastoma.

**Acknowledgement.** This research was funded by a grant (No. LIG-11/2012) from the Research Council of Lithuania.

## MULTICURVE RESOLUTION ALGORITHM AND ARTIFICIAL NEURAL NETWORKS APPLIED FOR ANALYSIS OF INTERVERTEBRAL DISC TISSUE AUTOFLUORESCENCE

Vilmantas Gėgžna<sup>1,2</sup>, Darius Varanius<sup>1,2</sup>, Gunaras Terbetas<sup>3,4</sup>, Aurelija Vaitkuvienė<sup>1</sup>, Juozas Vidmantis Vaitkus<sup>1,5</sup>

<sup>1</sup> Institute of Applied Research, Vilnius University, Lithuania

<sup>2</sup> Faculty of Natural Sciences, Vilnius University, Lithuania

<sup>3</sup> Republican Vilnius University Hospital, Vilnius University, Lithuania

<sup>4</sup> Faculty of Medicine, Vilnius University, Lithuania

<sup>5</sup> Faculty of Physics, Vilnius University, Lithuania

*Darius.Varanius@tmi.vu.lt*

**Background.** There is very little knowledge in scientific literature about methods to classify intervertebral disc tissues in real time. This work is dedicated towards this purpose.

**Materials and methods.** During intervertebral disc hernia operation in Republican Vilnius University Hospital pieces of intervertebral disc tissue were removed as part of conventional procedure. Optical properties of these samples were investigated using fluorescence spectroscopy method using no artificial or additional fluorophores. 1085 fluorescence spectra were registered from specimens of intervertebral disc hernia tissues. These specimens were classified to 3 medical groups according to localization of tissue (D – specimen from inner part of a disc, S – free sequester, P – herniation from subligamentous space). The fluorescence was excited using 355nm radiation of a microlaser STA-01-TH (Standa, Ltd.).

**Analysis.** Registered spectra were normalized to maxim peak value. Noise of fluorescence signal was reduced using the smoothing procedure. Next, spectra analysis followed. There was made an assumption, that the whole fluorescence spectrum of a specimen is a sum of fluorescence spectra of several fluorescent materials (fluorophores) that the sample is consisted of. The real spectra of these materials are unknown. Thus the registered spectra were decomposed to smaller spectra, called the components, using multi curve resolution (MCR) alternating least square (ALS) algorithm [1],[2]. Each spectrum was described by the intensities of all extracted components. These intensities were used to train an artificial network (ANN) to identify spectra of medical (D, S, P) groups.

**Results.** During this analysis more than 75% of spectra were identified correctly as belonging to appropriate medical group.

**Conclusion.** Combination of spectra decomposition to components using MCR-ALS algorithm and implementation of an ANN seems a promising direction for analysis of intervertebral disc hernia fluorescence spectra.

---

[1] Y. B. Monakhova, S. A. Astakhov, et al. Methods of the decomposition of spectra of various origin in the analysis of complex mixtures. Journal of Analytical Chemistry 66(4), 351-362 (2011).

[2] J. Jaumot, R. Gargallo, et al. A graphical user-friendly interface for MCR-ALS: a new tool for multivariate curve resolution in MATLAB. Chemometrics and Intelligent Laboratory Systems 76(1), 101-110 (2005).

# INTERDIGITAL CAPACITIVE SENSOR FOR CELLULAR MONOLAYER FUNCTIONAL STATE ANALYSIS

Nina Krylova<sup>1</sup>, Nikita Vasilyeu<sup>1</sup>

<sup>1</sup> Department of Biophysics, Physics Faculty, Belarusian State University, Belarus  
rfklmn@mail.ru

Bioimpedance spectroscopy methods with using interdigital capacitive sensors are perspective for non-invasive analysis in biomedical applications, for example in pre-clinical drug development [1]. They can provide information on functional, electric and proliferative activity of cells [2]. Nowadays capacitive sensors are utilized in studying of toxicity of pharmaceutical drugs [3]. However, the using techniques are based on detection of cells quantity in a sample demand long periods. They are not allow to register the early functional changes arising in cells at their stimulation or disruption. Thus, the purpose of present work is to develop an express method for registration of functional and electric activity of cells using interdigital capacitive sensors.

The sensor's biosensitive dielectric nanostructured coat containing cerium ions and multiwall carbon nanotubes modified by carboxyl groups was created by Langmuir–Blodgett technology. Cellular monolayers were formed on a sensor's surface at growing of C6 rat glioma cells. The registration of frequency and capacity characteristics of the sensor was carried out by means of the impedance analysis using electro-physical measuring device based on the pulse arranged RC-oscillator.

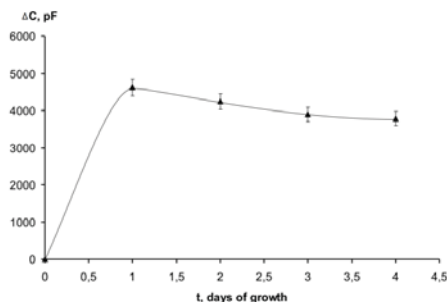


Fig. 1. Increment of sensor's capacity in medium with cells relative to sensor's capacity in medium without cells depending on growth interval.

As shown in the Fig.1, addition of cell suspension in the medium leads to increment of sensor's capacity by increasing the concentration of ions (cells can be considered as macroions). The formation of a continuous cellular monolayer is observed on the second day of cell growth and is accompanied by electric-field shielding effect (EFSE), revealing as sensor capacity (C) decrease. The degree of EFSE is gradually rising on 3 and 4 days with increase of cellular monolayer density. However, the degree of EFSE depends on a content of medium used and increases in following sequence:  $C(0,15 \text{ mol/l NaCl}) < C(0,15 \text{ mol/l NaCl with } 2,5 \text{ mmol/l CaCl}_2) < C(\text{Erla medium without } 2,5 \text{ mmol/l CaCl}_2 (\text{pH}=7,4)) < C(\text{Erla medium}) < C(\text{minimal Egla medium})$ . We proposed that such dependence is associated with changes in value of membrane potential, which characterizes the electric activity of cells.

The functional activity of cells can be estimated based on metabolic activity at their stimulation. In [4] it has been shown by means of chemiluminescent analysis that stimulation of glioma cells at menadione addition leads to production of superoxide anions in extracellular medium. We registered an increase of C at menadione action on glioma cells. General view of the kinetic dependence  $C(t)$  is consistent to the corresponding dependence obtained by the chemiluminescent analysis.

Thus, the developing bioimpedance spectroscopy method with using interdigital capacitive sensors allows to receive information on degree of cellular monolayer formation, metabolic and electric activity of cells.

[1] Beate Klösgen, Christine Rügenapp, Bernhard Gleich, Bioimpedance Spectroscopy, Systems Biology **2**, 241-271 (2011)

[2] G. N. Semenkov, V. V. Hrushevsky, H. V. Krylova, N. G. Krylova, T. A. Kulahava, I. V. Lipnevich, T. I. Orekhovskaya, G. N. Shulitsky, Monitoring of Blood Phagocyte Functional State by Cyclic Dielectric Spectroscopy, NPSC **14**, 295-299 (2011)

[3] Lee, R.; Kim, P.H.; Choi, J.W.; Oh-Joon, K.; Kim, K.; Kim, D.; Yun, C.-O.; Yoo, K.-H. Capacitance-based real time monitoring of receptor mediated endocytosis. Biosens. Bioelectron. **25**, 1325-1332 (2010)

[4] T.A. Kulahava, G.N. Semenkov, Z.B. Kvacheva, W. Krol, E. Szliszka, A. Grzybowski, Z.P. Czuba, S.N. Cherenkevich, Modification of redox processes in astroglial cells induced by microbial and viral infections, Med. Sci. Monit. **16**, HY11-HY17, (2010)

## USABILITY OF PSYCHOPHYSICAL EXPERIMENT SCHEME IN COLOUR VISION DEFICIENCY CHARACTERIZATION

Brigita Zutere<sup>1</sup>, Kaiva Luse<sup>1</sup>

<sup>1</sup> Department of Optometry and Vision science,  
University of Latvia  
[brigita.zutere@gmail.com](mailto:brigita.zutere@gmail.com)

### Aim

It is important to diagnose colour vision deficiency as early as possible, because colour vision deficiency can influence the choice of future profession and our visual perception in general. The aim of research is to find weather the test made in University of Latvia by K. Luse, M. Ozolinsh, S. Fomins and A. Gutmane is appropriate for the detection and characterization of red-green colour vision deficiency.

### Methods

Lately there have been developed several new colour vision deficiency screening and diagnostic tests, but it is important to check if specificity and sensitivity of the test agree with the standards already used in practice. **Sensitivity** [1] is the proportion of truly diseased persons in the screened population who are identified as diseased by the screening test. In our case we used, *Richmond HRR (4th edition)* test as golden standard:

$$\text{sensitivity} = \frac{\text{number of participants who fail in HRR test}}{\text{number of participants who fail in HRR test} + \text{number of participants who fail in HRR test but does not fail in the new test}}$$

Whereas **specificity** [1] is the proportion of participants *without* the disease who have low scores on the screening

$$\text{specificity} = \frac{\text{number of participants who does not fail in HRR test}}{\text{number of participants who does not fail in HRR test} + \text{number of participants who fail in HRR test but does not fail in the new test}}$$

test:

For Richmond HRR test sensitivity and specificity become 0.98 and 1.0, respectively, when the fail criterion is three or more errors. [2]

### Results

671 children were examined in 5 Latvian schools – 359 female and 321 male, with the average age of 12.6 years. The results show that 20 participants have red-green confusion which is 3.87% from all the examined students: the colour deficiency was found in case of 1 girl and 19 boys, which is respectively 0.40% and 7.09%. Findings are similar to colour vision prevalence in Caucasian population by other authors.

Specificity of the test is 0.977 and sensitivity – 1.0, so it means that this new test is appropriate for red-green colour vision deficiency characterization. Early study suggests that the performance of the new test was similar to Richmond HRR, but at the same time it is cheaper and easier to make, so it could be a good opportunity how to make large population researches, for example in schools.

### Acknowledgment

This research is done with a support of European Social Fund project “Support for doctorate studies in University of Latvia”, authors are thankful to ERAF project.

---

[1] Data Analysis. Calculus is Statistics: Sensitivity and Specificity, USA: NCSSM Statistics Leadership Institute, 1999. 3 p. [Viewed: 20.01.2013.]

[2] Cole, B. L., Lian, K. Y., Lakkis, C. *The new Richmond HRR pseudoisochromatic test for colour vision is better than the Ishihara test*, Department of Optometry and Vision Sciences, The University of Melbourne, Vic, Australia, 2006

## SPECTRAL AND STRUCTURAL CHARACTERISTICS OF THE METHANOL DIMER IN THE GAS PHASE.

Alexandr Bedulin, George <sup>\*</sup>Pitsevich

Belarusian State University, Minsk, Belarus

[alexandr.bedulin@gmail.com](mailto:alexandr.bedulin@gmail.com)

The interest to rotational and vibrational-rotational spectra of hydrogen bonded complexes drastically increased in recent years. Few works appears on rotational spectra of methanol dimer [1,2] which note a decrease of barriers to methyl tops internal rotation upon complex formation. Interest in H- bonding of the metanol dimer is due to the fact that it is among the simplest organic molecules, which could exhibits hydrogen bonding, and like (H<sub>2</sub>O)<sub>2</sub> it also exhibits multidimensi-onal tunneling splittings of torsion-rotational states. However, no articles in literature was found in which the theoretical study of spectral and structural characteristics of the methanol dimer in the gas phase has been performed. The optimized geometry of methnol dimer (Fig.1) was found using quantum mechanical package GAUSSIAN 09.

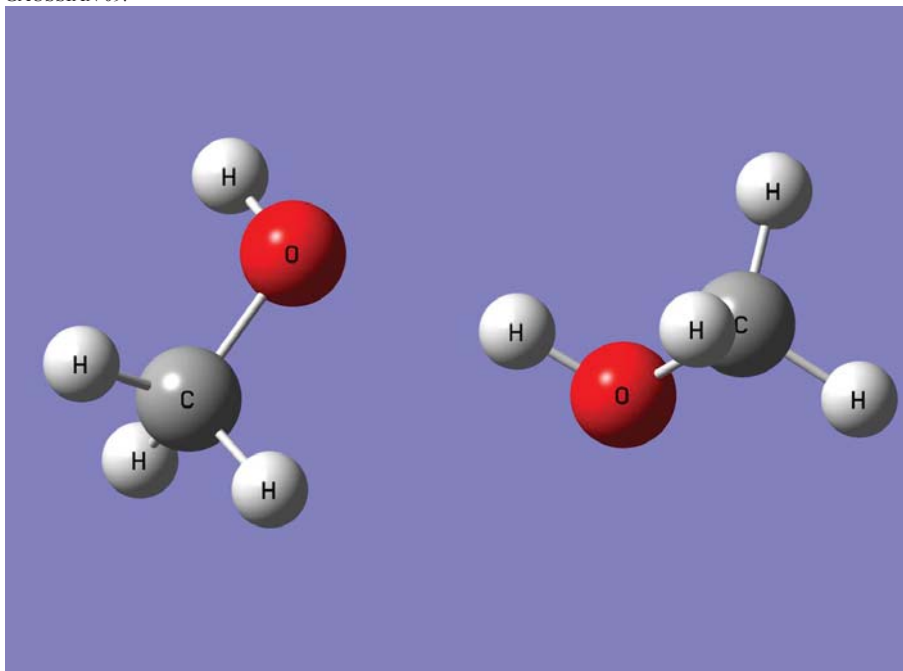


Fig.1 Optimized geometry of the free methnol dimer.

Then IR spectrum of dimer was calculated in harmonic and anharmonic approximation. It was found that frequencies of donor and acceptor hydroxil stretchig vibrations in dimer are 3500.4 and 3654.9 cm<sup>-1</sup>. The rotational constants in ground vibrational state were calculated too: A<sub>00</sub>=16805.593 MHz; B<sub>00</sub>=2212.790 MHz; C<sub>00</sub>=2183.509 MHz. It is in reasonable agreement with experimental data [2]: A<sub>00</sub>=14310.171 MHz; B<sub>00</sub>=2281.006 MHz. The vibration-rotation interection constants were calculated for metanol dimer. It was found that for  $\nu_{OH}$  vibration this constants are negative but not too high as it was expected [3]. The barriers to methyl tops internal rotation were calculated and its values in good agreement with experiment data [1,2].

[1] F.J.Lovas,S.P.Belov,M.Yu.Tretyakov,W.Stahl,R.D.Suenram, J.Mol.Spectr., v.170, p.478-492 (1995).

[2] F.J.Lovas,H.Hartwig, J.Mol.Spectr., v.185, p.98-109 (1995).

[3] J.C.Lassegues,J.Lascombe in Vibrational Spectra and Structure v.11 edited by J.R.Durig, Elsevier Science Limited, p.93 (1982).

## The Transformation of the Central Force Fields to the Natural Coordinates Representation.

A.S.Bogush, Pitseovich G.A.

Belarusian State University, Minsk, Belarus  
[Andynew.by@mail.ru](mailto:Andynew.by@mail.ru)

Despite the fact, that the central force fields (CFF) model after modification to Urey-Bradley force field (UBFF) was forgotten, it was revived after it was used in the calculations of the vibrational spectra of molecules in a such quantum chemistry package as HyperChem. In the literature have accumulated extensive data on these fields for polyatomic molecules. As well known [1] in the CFF only stretching types of coordinates are used. In addition to usual stretching coordinates describing a variation in the length of a chemical bond the stretching coordinates describing a variations of non- bonded interatomic distances are used. Therefore, direct comparison of the CFF and the most widely used general valence force field (GVFF), that used set of natural coordinates, impossible. Let us consider the conversion of the CFF to the GVFF using a set of natural vibrational coordinates. For definiteness, assume that the two sets of coordinates do not contain the redundant coordinates. We denote the column of the vibrational coordinates used to

describe the CFF are:  $\begin{Bmatrix} \mathbf{x} \\ \mathbf{q} \end{Bmatrix}$ , where  $\mathbf{x}$  - part of the coordinates, which is not included in the set of natural coordinates,  $\mathbf{q}$  -

the part of natural coordinates. So, potential energy can be express as:  $2U = \begin{Bmatrix} \mathbf{x} \\ \mathbf{q} \end{Bmatrix}^T \mathbf{L} \begin{Bmatrix} \mathbf{x} \\ \mathbf{q} \end{Bmatrix}$ , where  $\mathbf{L}$ -force constant

matrix,  $\begin{Bmatrix} \mathbf{x} \\ \mathbf{q} \end{Bmatrix}^T$  -row matrix of coordinates. Next, complete the set of coordinates as follows:  $\begin{Bmatrix} \mathbf{x} \\ \mathbf{q} \\ \mathbf{l} \end{Bmatrix}$  - where  $\mathbf{l}$ - is set of

coordinates to complement the  $\mathbf{q}$  set to the full set of independent coordinates. Using approach [2] one can find matrix

a:  $\begin{Bmatrix} \mathbf{x} \\ \mathbf{q} \end{Bmatrix} = \mathbf{a} \begin{Bmatrix} \mathbf{q} \\ \mathbf{l} \end{Bmatrix}$  to express  $\mathbf{x}$  part of coordinates through set of independent coordinates. Further, it is not difficult to

obtain the relations:  $\begin{Bmatrix} \mathbf{x} \\ \mathbf{q} \end{Bmatrix} = \mathbf{A} \begin{Bmatrix} \mathbf{q} \\ \mathbf{l} \end{Bmatrix}$  and  $\begin{Bmatrix} \mathbf{x} \\ \mathbf{q} \end{Bmatrix}^T = \begin{Bmatrix} \mathbf{q} \\ \mathbf{l} \end{Bmatrix}^T \mathbf{A}^T$ . So for potential energy we get:

$$2U = \begin{Bmatrix} \mathbf{x} \\ \mathbf{q} \end{Bmatrix}^T \mathbf{L} \begin{Bmatrix} \mathbf{x} \\ \mathbf{q} \end{Bmatrix} = \begin{Bmatrix} \mathbf{q} \\ \mathbf{l} \end{Bmatrix}^T \mathbf{A}^T \mathbf{L} \mathbf{A} \begin{Bmatrix} \mathbf{q} \\ \mathbf{l} \end{Bmatrix}$$

Since using set of natural coordinates we have  $2U = \begin{Bmatrix} \mathbf{q} \\ \mathbf{l} \end{Bmatrix}^T \mathbf{K} \begin{Bmatrix} \mathbf{q} \\ \mathbf{l} \end{Bmatrix}$  where  $\mathbf{K}$  is force constant matrix for GVFF. So we

can get:  $\mathbf{K} = \mathbf{A}^T \mathbf{L} \mathbf{A}$ . This approach was tasted on hydrogen peroxide molecule.

---

1.S.Califano Vibrational States John Wiley & Sons, London, New York, Sydney, Toronto 1976

2.G.A.Pitsevich,A.E.Malevich American Journal of Chemistry 2012, v.2, p.24-27.

# TRANSFER OF GRAPHENE OXIDE COATINGS ONTO POLYETHYLENE TEREPHTHALATE SUBSTRATE: A SIMPLEX OPTIMIZATION STUDY

Justina Dakševič<sup>1</sup>, Jurgis Barkauskas<sup>1</sup>

<sup>1</sup>Department of General and Inorganic Chemistry, Vilnius University,  
Naugarduko 24, LT – 03225 Vilnius, Lithuania

[Justina.daksevic@chf.stud.vu.lt](mailto:Justina.daksevic@chf.stud.vu.lt)

Graphene is a single layer of carbon atoms bound through  $sp^2$  bonds forming a hexagonal two-dimensional crystal lattice. It has a very high electron mobility at room temperature, with values of up to  $200,000 \text{ cm}^2 \text{ V}^{-1} \text{ s}^{-1}$ . This form of carbon is the strongest material ever known, theoretically perfect graphene sheet is about 100 times stronger than steel. Graphene has high optical transparency of 97.7 %, high thermal conductivity of up to  $5000 \text{ W m}^{-1} \text{ K}^{-1}$ , extremely high theoretical specific surface area of  $2630 \text{ m}^2/\text{g}$  and is not permeable to gas. Graphene due to its outstanding thermal, mechanical and electrical properties is employed in nanoelectronics, biotechnology, sensing, nanofiltration, etc. [1]. One of the most promising applications of graphene-based materials is their use as transparent, conductive thin films. For this purpose they must be transferred onto arbitrary insulating substrates. Initially, graphene coatings can be produced by micro-mechanical exfoliation of graphite, epitaxial growth, chemical vapor deposition on metal substrates such as Ni and Cu. Precursors most commonly used to produce graphene coatings are graphene oxide (GO) films [2].

GO has a layered structure similar to that of graphite, however, the basal plane of carbon atoms in graphene oxide is densely decorated with hydroxyl, epoxy, carbonyl and carboxyl groups. Presence of functional groups not only expands the interlayer distance but also improves the hydrophilic properties and dispersibility of GO. GO dispersions are used to produce GO films by spin-coating, dip-coating, spraying, vacuum filtration, Langmuir-Blodgett methods [3-4].

In the laboratory GO was synthesized by a Hummer's method [5] from graphite using  $\text{NaNO}_3$ ,  $\text{H}_2\text{SO}_4$  and  $\text{KMnO}_4$ . Obtained brown powder was dried and used for the fabrication of GO coatings onto polycarbonate substrate [6]. Simultaneously, nanocomposite coatings composed of GO and Congo red (CR) and exfoliated GO have been fabricated using the same protocol. Obtained coatings were dried at room temperature, cut-off from cylinder and transferred onto the transparent polyethylene terephthalate (PET) substrate by heating and pressing. Simplex-optimization for three most significant factors (temperature, thickness of the interlayer and thickness of the coating) was performed. Experiments were carried out using combinatorial approach. Libraries were prepared on the basis of previous tests for optimization using a Plackett-Burman experimental design and examined by different methods (optical microscopy, SEM, contact angle measuring, electrical conductivity and adhesion testing). Optimal conditions for transfer of GO coating were found as follows: temperature –  $185^\circ\text{C}$ , thickness of GO coating –  $500 \text{ nm}$  and thickness of the interlayer –  $0.80 \mu\text{m}$ .

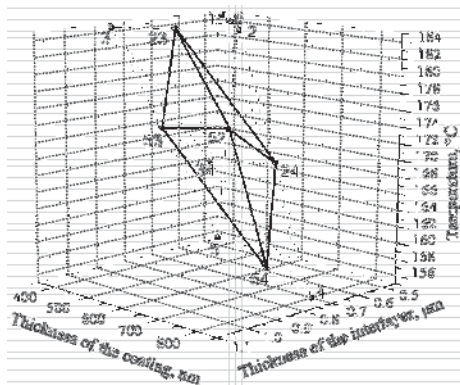


Fig. 1. Simplex optimization of GO transfer onto PET substrate.

- [1] V. Singh, D. Joung, Lei Zhai, S. Das, S. I. Khondaker, S. Seal, Graphene based materials: Past, present and future, *Progress in Materials Science* **56**, 1178–1271 (2011).
- [2] I. V. Zolotukhin, I. M. Golev, A. V. Nefedov and A. V. Uskov, *Graphenes: Methods of Production and Application, Inorganic Materials: Applied Research* **2**, 91–96 (2011).
- [3] D. R. Dreyer, S. Park, C. W. Bielawski, R. S. Ruoff, The chemistry of graphene oxide, *Chem Soc Rev* **39**, 228 (2010).
- [4] F. Chen, S. Liu, J. Shen et al., Ethanol-Assisted Graphene Oxide-Based Thin Film Formation at Pentane Water Interface, *Langmuir* **27**, 9174–9181 (2011).
- [5] W. S. Hummers, R. E. Offeman, Preparation of Graphitic Oxide, *J. Am. Chem. Soc.* **80**, 1339 (1958).
- [6] J. Barkauskas, J. Dakševič, R. Juškėnas, R. Mažeikienė, G. Niaura, G. Račiukaitis, A. Selskis, I. Stankevičienė, R. Trusovas, Nanocomposite films, and coatings produced by interaction between graphite oxide and Congo red, *Journal of Materials Science* **47**, 5852–5860 (2012).

## SOL-GEL SYNTHESIS AND CHARACTERIZATION OF $\text{Ca}_{1-2x}\text{M}_x\text{RE}_x\text{MoO}_4$ ( $\text{M} = \text{Li, Na, K, Rb AND Cs}$ ; $\text{RE} = \text{Eu, Gd, Sm and Tb}$ ) POWDERS

Gytasutas Janulevičius<sup>1</sup>, Artūras Žalga<sup>1</sup>

<sup>1</sup>Department of Inorganic Chemistry, Vilnius University, Lithuania  
[gytasutas.janulevicius@chf.stud.vu.lt](mailto:gytasutas.janulevicius@chf.stud.vu.lt)

Nowadays, considerable research attention has been devoted to trivalent lanthanide ions as luminescence centers due to the rapid development of diode lasers. Especially, phosphors excited by vacuum ultraviolet light have drawn a great amount of attention with their application in plasma display panels, and mercury-free fluorescent lamps. Besides, the search for stable, inorganic rare-earth-based red phosphor with high absorption in the near-UV/blue spectral region is an attractive and challenging research task. Moreover, nano- or micrometersized inorganic compounds activated by rare-earth ions have received much attention due to a wide application in luminescence devices, such as cathode ray tubes, field emissive display, and plasma display panels. Such applications are highly dependent on the basic factors that govern the luminescence. For instance, particle size and morphology are primarily responsible for the luminescent properties and the device performance of  $\text{Ln}^{3+}$ -doped phosphors. For practical applications, phosphors with spherical morphology of a fine size (0.5–4  $\mu\text{m}$ ), which could be obtained only at relatively low temperatures, may offer dual advantages over other morphologies in that they achieve high packing densities and minimize the light scattering [1].

The optical properties of trivalent rare-earth ions either in tungstates or in molybdates with scheelite ( $\text{CaWO}_4$ ) or powellite ( $\text{CaMoO}_4$ ) structures, respectively, have been widely investigated in the last several years. Many different preparation techniques, such as traditional solid-state reactions, combustion, Czochralski method, solvothermal processes, microwave irradiation, spray pyrolysis, the facile microemulsion mediated hydrothermal process, electrochemical, sonochemical, and sol-gel synthesis are successfully used for the synthesis of different inorganic ceramic materials. Among these different synthesis routes, the solution-based synthetic methods play a crucial role in the design and production of fine ceramics and have been successful in overcoming many of the limitation of the traditional solid-state, high-temperature methods. The use of solution chemistry can eliminate major problems, such as long diffusion paths, impurities, and agglomeration, and result in products with improved homogeneity [2].

In the past few decades, many researchers have carried out the studies on the formation of metal complexes with organic ligands. Furthermore, the metal complexes with organic ligands have been used for the preparation of ceramics and metal oxide thin films by sol-gel process, using metal nitrates, chlorides, and acetates as starting materials. Besides, metal salts are very useful, inexpensive, and very easy to handle in comparison to metal alkoxides, and hence they are good alternatives for the conversion to oxides by thermal decomposition. They can be dissolved in many kinds of organic solvents in which metal complexes are formed. From this point of view, the wet synthesis route called an aqueous sol-gel method, is really attractive and compared to other techniques, as it has the advantages of a good control of the starting materials and of the processing parameters, a high purity of the raw materials, and the low temperature of the process. A good homogeneity of the product could be achieved by control of the stoichiometry of the starting solution [3].

In order to explain and better understand the possible thermal decomposition behaviour of precursors and crystallization process of the sol-gel materials, the thermal analysis (TG/DSC) of the as-prepared Ca-Mo-O nitrate-tartrate gel was performed. Besides, we report the synthesis of powellite-type  $\text{Ca}_{1-2x}\text{M}_x\text{RE}_x\text{MoO}_4$  compound substituted with  $\text{RE}^{3+}$  ions ( $\text{RE} = \text{Sm, Eu, Gd and Tb}$ ) and alkaline metals ( $\text{M} = \text{Li, Na, K, Rb and Cs}$ ) by aqueous sol-gel synthesis route with tartaric acid as a complexing agent. Also, the crystal phase analysis of synthesized compounds by X-ray diffraction (XRD) analysis was performed and surface morphology of annealed samples at different temperatures using scanning electron microscopy (SEM) was estimated.

**Acknowledgements** The study was funded from the European Community's Social Foundation under grant agreement no. VP1-3.1-ŠMM-08-K-01-004/KS-120000-1756.

- 
- [1] A. Žalga, Z. Moravec, J. Pinkas, A. Kareiva, On the sol-gel preparation of different tungstates and molybdates. *J Therm Anal Calorim* 2011, 105, 3-11.
- [2] K. Tonsuaadu, A. Žalga, A. Beganskiene, A. Kareiva, Thermoanalytical study of the YSZ precursors prepared by aqueous sol-gel synthesis route. *J Therm Anal Calorim* 2012, 110, 77-83.
- [3] A. Žalga, R. Sazinas, E. Garskaite, A. Kareiva, T. Bareika, G. Tamulaitis, R. Juskenas, R. Ramanauskas, R.: Sol-gel synthesis of  $\text{RE}^{3+}$ -activated  $\text{CaWO}_4$  phosphores. *Chemija* 2009, 20, 169-174.



## FABRICATION OF METAL NANO-ISLANDS AND DETERMINATION OF THEIR PLASMONIC RESONANCE FOR GAN APPLICATIONS

Agnė Kalpakovaitė<sup>1</sup>, Tomas Grinys<sup>2</sup>

<sup>1</sup> Faculty of Physics, Vilnius University, Saulėtekio av. 9, 10222 Vilnius, Lithuania

<sup>1,2</sup> Institute of Applied Research, Vilnius University, Saulėtekio av. 10, 10223 Vilnius, Lithuania

[Agne.Kalpakovaitė@ff.stud.vu.lt](mailto:Agne.Kalpakovaitė@ff.stud.vu.lt)

Nanometer scale self-organized metal islands have a number of applications. They can be used in medicine to kill cancer cells selectively. Another field of application is optoelectronics [1-2]. At the interface between conductive particles and insulator or semiconductor the excitation of collective electrons, known as surface plasmons (SP), can be observed. The internal quantum efficiency of light emitting diode (LED) can be enhanced by coupling between dipoles in quantum wells (QW) and SPs. Experimentally the coupling can be observed by measuring transmittance spectra. At SP resonance frequency the intense light absorption is observed. The resonance frequency as well as wavelength of SPs can be tuned with change in the matter and diameter of metal nanoparticles. This allows obtaining an electromagnetic field enhancement in the wide range of energies.

The nano-islands were prepared by depositing Au and Ag metal thin films of different thicknesses on undoped GaN/sapphire templates. GaN on sapphire was grown by metal organic chemical vapor deposition (MOCVD) technique. Afterwards samples were annealed at different temperatures by rapid thermal annealing (RTA). As the optical response of fabricated samples strongly depends on size and density of nano-islands, it is important to investigate the influence of various technological parameters: such as thickness of deposited metal layer, annealing temperature or time. In this work transmittance spectra were measured to determine the SP resonance. Fig. 1 shows transmittance spectra of samples with Ag and Au nano-islands on the surface. The absorption peaks were observed at 464 nm and 550 nm for Ag and Au samples respectively. Fig. 2 shows scanning electron microscopy (SEM) images of prepared samples. According to SEM image statistical analysis the size of nano-islands has an exponential distribution with the average mean diameter less than 50 nm.

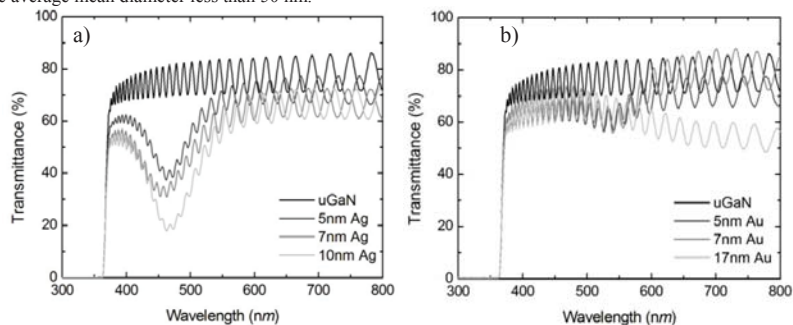


Fig. 1. Transmittance spectra of samples after annealing for 10 min: a) Ag layers at 750°C, b) Au layers at 800°C.

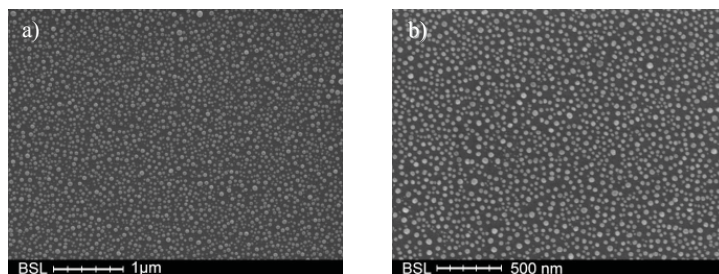


Fig. 2. SEM images of samples after annealing for 10 min: a) 10 nm Ag layer, b) 7 nm Au layer.

[1] M.K. Kwon, J.Y. Kim, et al., Surface-Plasmon-Enhanced Light Emitting Diodes, *Adv. Mater.* 20, 1253 (2008).

[2] J.H. Sung, J.S. Yang, et al., Enhancement of electroluminescence in GaN-based light-emitting diodes by metallic nanoparticles, *Appl. Phys. Lett.* 96, 261105 (2010).

## THE INFLUENCE OF SOLVATION EFFECTS IN THE STRUCTURE AND POTENTIAL ENERGY SURFACE OF THE PYRIDINE N-OXIDE/TRICHLOROACETIC ACID COMPLEX

Helen Khrol<sup>1</sup>, George \*Pitsevich<sup>1</sup>, Alex Malevich<sup>1</sup>, Valdas Sablinskas<sup>2</sup>, Vitautas Balevicius<sup>2</sup>

<sup>1</sup>Belarusian State University, Minsk, Belarus

<sup>2</sup>Vilnius University, Vilnius, Lithuania

[alexandr.bedulin@gmail.com](mailto:alexandr.bedulin@gmail.com)

Multidimensional potential surface determines the structure and spectral characteristics of molecular systems. In case of formation of a hydrogen bond the special interest represented the potential surfaces associated with the movement of the hydroxyl hydrogen atom of the donor molecule. Equilibrium position of the hydrogen atom in the hydrogen bridges are often very mobile and can be changed under the influence of the environment. In this study we investigated the effect of solvent on the spectroscopic and structural parameters of the pyridine n-oxide/trichloroacetic acid complex. For a free complex, as well as for the complex in chloroform, acetonitrile and water were calculated equilibrium geometrical parameters, and the characteristics of the IR spectra. According to the calculations, surrounded by solvent molecules hydrogen bridge length in the complex decreases. Stretching vibration of the hydroxyl group exposed to significant red shift. A more detailed comparative analysis of changes in the shape of the potential surface was performed for free complex and the complex in acetonitrile. Fig. 1 shows the potential curves related to the stretching vibrations of OH groups in the free complex and Fig. 2 - in the complex in acetonitrile.

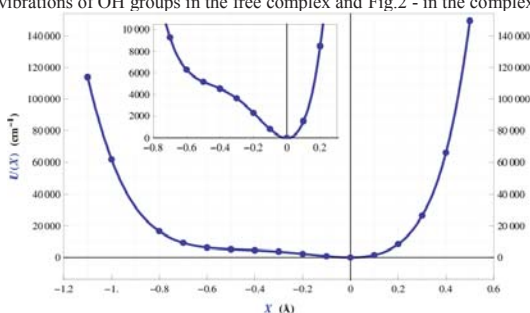


Fig.1. Potential energy of the free complex as a function of the hydrogen atom displacement along X axis.

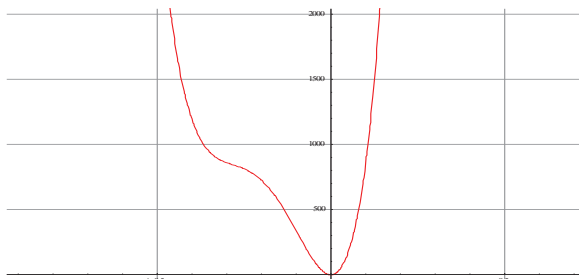


Fig.2 Potential energy of the complex in acetonitrile as a function of the hydrogen atom displacement along X axis.

For the free complex the depth of the potential well for the free complex is about 4000 cm<sup>-1</sup>. In the complex, dissolved in acetonitrile, the well depth is reduced to 800 cm<sup>-1</sup> (Fig.2). There is in addition the shift of the global minimum to the center of the hydrogen bridge. As can be seen from Fig. 1, on the right of the minimum the slope of the potential curve is comparable to the usual covalent chemical bonds. However, on the left, down to the displacement of the order of 0.6 Å, the slope of the potential curve is much smaller than in the case of ordinary chemical bonds. Here the attraction of the oxygen donor offset the attraction of the acceptor oxygen. Only since the deviation of 0.8 Å the potential energy begins to increase sharply as the attraction of the acceptor oxygen is replaced by repulsion.

## NMR MONITORING OF HYDROGEN – DEUTERIUM EXCHANGE IN IONIC SOLUTIONS

Vytautas Klimavičius

Department of General Physics and Spectroscopy, Vilnius University, Lithuania  
vytautas.klim@gmail.com

These days NMR is one of the most powerful techniques for studying hydrogen - deuterium (H/D) exchange reactions and other phenomenon in modern materials [1]. Ionic liquids (ILs) or room temperature ionic liquids (RTILs) are a class of the materials which have a property of H/D exchange reactions. RTILs are novel materials which sometimes are called molten salts. RTILs have numerous of interesting features which might be applied in industry and research. All this is achieved by changing anion and cation subsystems [2].

In this research two RTILs were investigated (1-decyl-3-methylimidazolium bromide  $[C_{10}mim][Br]$  and 1-decyl-3-methylimidazolium chloride  $[C_{10}mim][Cl]$  (Fig. 1)). There where two different concentrations (0.01 and 0.4 mol. fr.) with heavy water ( $D_2O$ ) and both RTILs prepared. Just after sample preparation  $^1H$  and  $^{13}C$  NMR spectra were

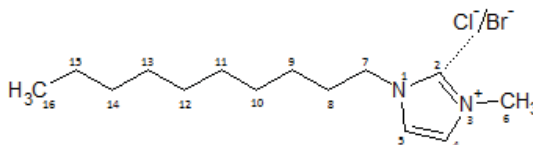


Fig. 1. 1-decyl-3-methylimidazolium chloride/bromide  $[C_{10}mim][Cl/Br]$  molecule with atoms numbering.

recorded and then repeatedly more spectra with exact time intervals were recorded. H/D exchange reactions were monitored by analysing  $^1H$  and  $^{13}C$  NMR spectra (integral intensity, chemical shift, multiplicity, etc.). It was identified that H/D exchange occurs in samples with concentration of 0.01 mole fraction of RTIL in  $D_2O$ . The proton in the hydrogen bridge with anion  $C-H \cdots Cl/Br^-$  is replaced by deuterium. Its spectral line in  $^1H$  NMR spectra vanishes with time.  $^{13}C$  NMR spectra indicated H/D exchange when  $C-H \cdots Cl/Br^-$  carbons spectral line changes from singlet to triplet. It happened because a pulse sequence of  $^{13}C - ^1H$  homodecoupling was employed while  $^2H$  ( $I=1$ ) was not decoupled at all. As a monitoring parameter for H/D exchange a ratio of an integral intensity of H2 proton with its and H16 protons integral intensities ( $I(H2)/(I(H2)+I(H16))$ ) was chosen. In sample with  $[C_{10}mim][Br]$  H/D reaction took 8 - 10 hours, when in  $[C_{10}mim][Cl]$  even after 48 days of waiting time H/D reaction was not fully finished. From  $^{13}C$  spectra it was assigned secondary isotopic effects for C2, C4, C5, C6, C7 carbons when  $C-H \cdots Cl/Br^-$  proton is changed with deuterium, a difference of chemical shift  $\delta_H - \delta_D$  vary from 0.25 ppm to 0.02 ppm, respectively to the distance to H2. No H/D exchange reactions were noticed in samples of 0.4 mole fraction of RTIL. However in the samples containing  $[C_{10}mim][Cl]$  all spectral lines appeared to be like in the solid state NMR. This observation can be explained by the fact that RTILs with certain water content form a ionogel phase which is solid. This phenomenon will be investigated in future using solid state NMR technique.

All this experimental data gives valuable information about RTILs and stimulates to create theoretical models. What is more, it motivates for new research projects which might give impressive results.

[1] S. Ohta, A. Shimizu, Y. Imai, H. Abe, N. Hatano, Y. Yoshimura, Open Journal of Physical Chemistry 1, 70-76 (2011).

[2] T. J. S. Schubert, M. Smiglak, T. Beyersdorff, B. Iliev, F. Stomke, Ionic Liquids Today 1-10, December (2010).

## QUANTUM CHEMICAL PREDICTIONS OF THE H-1 NMR SPECTRA OF 1-DECYL-3-METHYL-IMIDAZOLIUM IN THE LIQUID PHASES

Dovilė Lengvinaitė, Kęstutis Aidas

Dept. of General Physics and Spectroscopy, Faculty of Physics, Vilnius University, Lithuania

[dovile.lengvinaite@ff.stud.vu.lt](mailto:dovile.lengvinaite@ff.stud.vu.lt)

Nuclear magnetic resonance spectroscopy, most commonly known as NMR spectroscopy, can provide detailed information about the structure, dynamics, reaction state, and chemical environment of molecules. Differences between isotropic values of nuclear magnetic shielding tensors, the so-called chemical shifts, are most common observables in the NMR spectroscopy. Experimentally, a curious behavior of the H-1 NMR spectra of 1-decyl-3-methyl-imidazolium ([DMim]) molecule (Fig. 1) - a popular cationic component of imidazolium based ionic liquids – dissolved in solvents of varying polarity was recorded: the increasing shielding of the proton at the 2<sup>nd</sup> position of the imidazolium ring was observed with the rising polarity of the solvent [1]. In this study, we are trying to calculate the H-1 NMR spectrum of [DMim] molecule in different solvents using density functional theory (DFT) methods as well as polarizable continuum model (PCM) to account for solvent effects. In order to be selected reliable DFT functional and basis set, we have performed a series of test calculations using different DFT methods and basis sets, and compared the results to the corresponding high-level *ab initio* predictions. Tryout system was 1,3-dimethyl-imidazolium cation. In this presentation, we will compare calculated and experimental H-1 NMR spectra of [DMim] molecule in solvents of varying polarity and we will assess the suitability of the adopted approach to predict H-1 NMR spectra of ionic liquids.

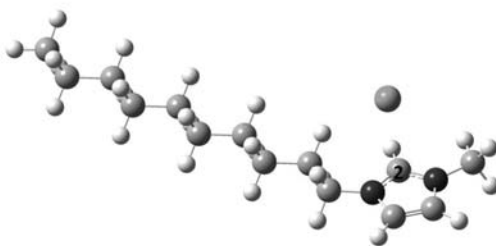


Fig 1. Structure of the 1-decyl-3-methyl-imidazolium chloride ionic pair.

---

[1] V. Balevicius, Z. Gdaniec, K. Aidas, J. Tamuliene, NMR and Quantum Chemistry Study of Mesoscopic Effects in Ionic Liquids, *J. Phys. Chem. A* **2010**, *114*, 5365-5371

## AMYLOID-LIKE FIBRIL ELONGATION FOLLOWS MICHAELIS-MENTEN KINETICS

Katažyna Milto, Vytautas Smirmovas

Department of Biothermodynamics and Drug Design, Vilnius University Institute of Biotechnology, Vilnius, Lithuania  
[milto@ibt.lt](mailto:milto@ibt.lt)

The assembly of proteins into amyloid-like fibrils has been studied extensively. A key to control protein aggregation is understanding its mechanism. The "nucleation-elongation" model has been suggested to explain fibril formation [1]. First of all, the nucleus must occur, but once it is formed the elongation process starts. The process of elongation has been noticed to be similar to an enzymatic reaction [2]. In this case the formed nucleus acts as an enzyme while monomers and/or oligomers act as substrate. Though, due to the complexity of amyloid-like aggregation, the degree of similarity is not clear.

We tried to design experimental conditions in the way to ensure the only process going in our test tube during the measurement is fibril elongation via attaching monomers to fibril ends. In this case we can schematically describe the process as  $F + M \rightleftharpoons FM \rightarrow F$ , where F stands for fibril end, M – monomer, and FM is short-living complex, which exists from the time monomer attaches to the fibril and until it's completely incorporated. It reflects the enzymatic reaction scheme thus we were able to apply the Michaelis-Menten equation to fit fibril elongation kinetics (Fig. 1).

Excellent correlation with experimental data ( $r^2_{adj} > 0,999$ ) and proposed model supports the possibility to describe the fibril elongation process as Michaelis-Menten kinetics event.

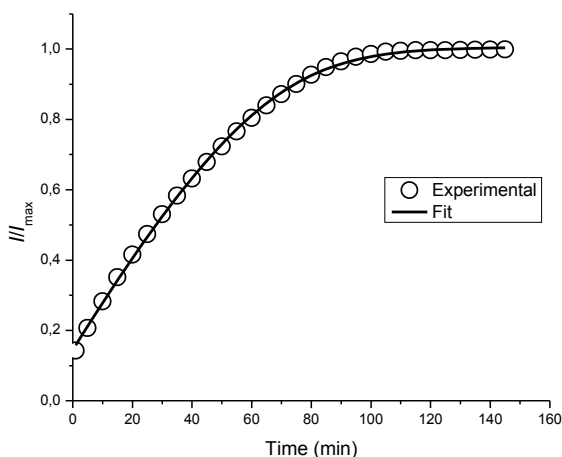


Fig. 1. Elongation kinetics of human insulin fibrils (experimental data of Thioflavin T fluorescence assay).

[1] F. Chiti, C.M. Dobson, Protein misfolding, functional amyloid, and human disease, *Annu Rev Biochem.* **75**, 333-66 (2006).

[2] T. Scheibel, J. Bloom, S. L. Lindquist, The elongation of yeast prion fibers involves separable steps of association and conversion, *PNAS* **101**, 2287-92 (2004).

## DRAG FORCE STUDY OF THE HEXAFLUOROPHOSPHATE SOLUTION LAYER PROPERTIES AT GOLD ELECTRODE SURFACE

Arūnas Pulmanas, Vytautas Daujotis

Department of General and Inorganic Chemistry, Vilnius University, LT-01513 Vilnius, Lithuania  
[arunas.pulmanas@chf.stud.vu.lt](mailto:arunas.pulmanas@chf.stud.vu.lt)

Reduction of water flow friction by applying electric potential to the pipe wall [1] can contribute to the ability to actively manipulate a wall-bounded liquid flow field to effect a desired change. This effect has been tested in two Norwegian hydroelectric power stations [2]. However, the mechanism of this effect is not clear yet.

Computer controlled fluid circulation system for measuring the drag force of the body, whose electrode potential can be controlled independently, was built. By using this technique the potential dependence of the drag force on a gold coated sphere was measured in a stream of 0.01 M sodium hexafluorophosphate (98%, Sigma-Aldrich) solution prepared in distilled water. Hexafluorophosphate was chosen in order to compare the results, obtained in present work, with those obtained by using piezoelectric sensor [3]. The averaged drag force values were assigned to the flow velocities and potential intervals, at which they were measured. Then the drag coefficients were calculated for the sphere via Eq. (1) and were corrected for the wall effect [4].

$$C_D = 8F_D / (\pi \rho v^2 d^2) \quad (1)$$

The LOESS (local smoothing technique with tri-cube weighting and polynomial regression) procedure was used to smooth the drag force data as a function of the potential. The Loess fits for gold coated sphere drag versus potential are shown in Fig. 1. The sampling proportion was chosen to be 0.4 since this produced a good tradeoff between noisy undersmoothing and oversmoothing which misses some of the peak-and-valley details in the data.

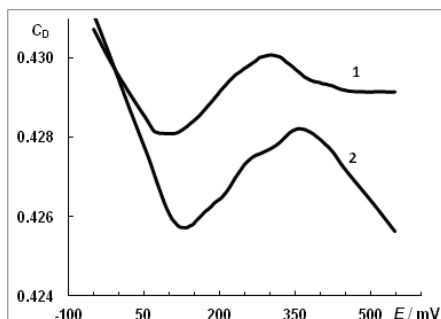


Fig. 1. LOESS fits (sampling proportion 0.4 and polynomial degree 1) for gold coated sphere drag vs. potential at settling velocity  $\sim 0.177$  m/s: 1 - 5 potential cycles,  $dE/dt = 0.5$  mV/s (2769 drag force coefficients); 2 - 6 potential cycles,  $dE/dt = 0.4$  mV/s (4157 drag force coefficients).

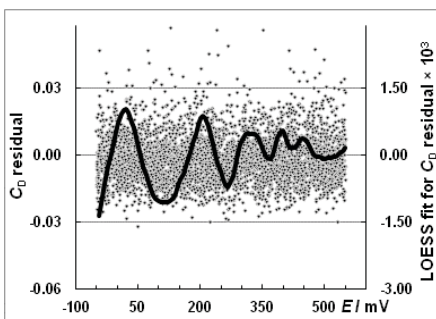


Fig. 2. Scatter plot (dots) of drag coefficient residuals and their LOESS fits (solid line, sampling proportion 0.2 and polynomial degree 1) vs. potential for LOESS fit 2 in Fig. 1.

To gain insight in goodness of LOESS fits in Fig. 1, the residuals of these fits are plotted versus the potential (Fig. 2), where again the LOESS smoothing technique is used to smooth the drag coefficient residuals as a function of potential. The character of interfacial viscosity change with potential is similar to the potential dependence of drag coefficient (Fig. 1) and correlates with the dependence of interfacial viscosity on the potential, which was obtained by using dual-quartz resonator (two resonators with differently textured surfaces in a monolithic sensor).

The results obtained increase the ability to actively manipulate a wall-bounded liquid flow field to effect a desired change what is of great technological importance.

[1] M. Waskaas, *US Patent No US 6,334,957* (2002).

[2] M. Waskaas, V. Daujotis, K. E. Wolden, R. Raudonis, D. Plausinaitis, *Russ. J. Electrochem.* **44**, 609 (2008).

[3] V. Daujotis, D. Plausinaitis, M. Waskaas, R. Raudonis, *9th Spring Meeting of the ISE*, May 8 to 11, 2011, Turku, Finland.

[4] R. Clift, J.R. Grace, M. E. Weber, *Bubbles, drops and particles*, Academic Press, New York, 1978.

## SYNTHESIS OF PHOSPHORYLATED ISOINDOLINONE DERIVATIVES

Piotr Zagórski<sup>1</sup>, Andrzej Józwiak<sup>1</sup>, Dariusz Cał<sup>2</sup>, Mieczysław W. Płotka<sup>1</sup>

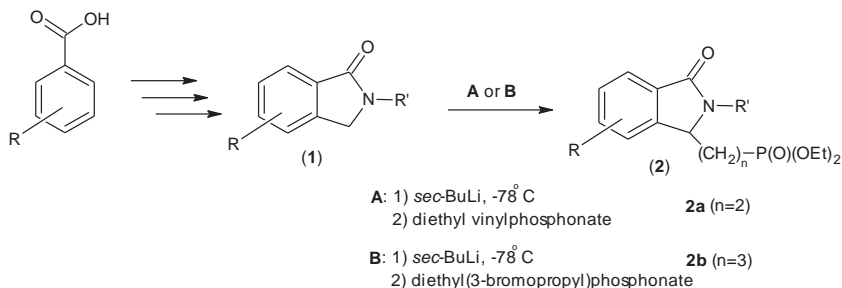
<sup>1</sup> Department of Organic Chemistry, University of Łódź, Faculty of Chemistry, Poland

<sup>2</sup> Department of Organic and Applied Chemistry, University of Łódź, Faculty of Chemistry, Poland  
zagorek@op.pl

Isoindolinone building block is present in many natural alkaloids like Lennoxamine<sup>[1]</sup>. There are other synthetic drugs that contain isoindolinones moiety, for example Pagoclone<sup>[2]</sup>. In recent years a lot of attention has been paid to the synthesis of phosphorylated isoindolinone derivatives<sup>[3-8]</sup>.

Our research aim is to enrich a modest library of new phosphonic acids and esters containing an isoindolinone structure.

A key step in the synthesis is lithiation of isoindolinone (**1**) using *sec*-buthyllithium in tetrahydrofuran followed by a reaction of the generated lithiated species with diethyl vinylphosphonate (for products **2a**) or diethyl (3-bromopropyl)phosphonate (for products **2b**).



[1] Fuchs J. R.; Funk, R. L. *Organic Letters* **2001**, 3, 3923–3925.

[2] Stuk T. L.; Assink B. K.; Erdman D. T.; Fedij V.; Jennings S. M.; Lassig J. A.; Smith R. J.; *Organic Process Research & Development* **2003**, 7, 851–855.

[3] Viveros-Ceballos, J. L.; Ordonez, M.; Cativiela, C. *Tetrahedron: Asymmetry*, **2011**, 22, 1479-1484.

[4] Couture, A.; Dienau, E.; Woisel, P.; Grandclaudeon, P. *Synthesis*, **1997**, 12, 1439-1445.

[5] Kachkovskiy, G. O.; Kolodiazhnyi, O. I. *Phosphorus, Sulfur and Silicon and the Related Elements*, **2010**, 185, 2441-2448.

[6] Ordonez, M.; Tibhe, G. D.; Zamudio-Medina, A.; Viveros-Ceballos, J. L. *Synthesis*, **2012**, 44, 569-574

[7] Kachkovskiy, G. O.; Kolodiazhnyi, O. I. *Phosphorus, Sulfur and Silicon and the Related Elements*, **2009**, 184, 890-907.

[8] Claeys, D. D.; Stevens, C. V.; Roman, Bart I.; Van De Caveye P.; Waroquier, M.; Van Speybroeck, V. *Organic and Biomolecular Chemistry*, **2010**, 8, 3644-3654.

# MODELING A CARBON NANOTUBE BASED DETECTOR OF MODULATED TERAHERTZ RADIATION

Anton Yermalovich

Department of Micro- and Nanoelectronics, Belarusian State University of Informatics and Radioelectronics, Belarus  
[Anton.Yermalovich@gmail.com](mailto:Anton.Yermalovich@gmail.com)

Due to recent success in development and visualization of nanosized clusters and other metallic nanoparticles, a new branch of nanooptics and nanotechnology quickly develops — nanoplasmonics. The most important feature of nanoplasmonic devices is the combination of strong electromagnetic oscillation localization combined with high frequencies of these oscillations, which in turn leads to a gigantic amplification of local optical and electromagnetic fields [1]. The localized plasmons parameters depend on the shape of the nanoparticles, which allows to fine-tune their resonance system to effectively interact with light and other quantum systems (quantum dots, molecules) [2].

Some of the possible applications of these effects are highly effective tunable fluorophores and nanosized light sources, as well as surface plasmon amplification by simulated emission of radiation. It is also possible to create micro-mechanical oscillators (Fig. 1), using highly conducting microcantilevers and carbon nanotubes as mechanically floating gates [3]. Such devices are shown to exhibit not only mechanical resonance, but also resonance at frequencies of plasma oscillations.

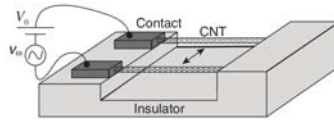


Fig. 1. General view of device under consideration

In detectors, such as the one presented above, it is possible to induce a parametric balance if the amplitude of the input signal exceeds some threshold value. When this happens, low frequency mechanical vibrations are induced in the resonator, even in the absence of the carrier frequency modulation [4]. Presenting the plasma and mechanical distributions of the resonators as lumped parameters, it is possible to write out a set of equations for associated resonators, the solution of which will allow to evaluate the threshold value of the input signal: Eq. (1):

$$\begin{cases} y + \gamma_m y + \omega_m^2 y = -\frac{2\eta\rho}{M_c d} \\ \rho + \gamma_e \rho + \omega_e^2 (1 + \zeta \frac{v_{te}\rho}{v_0} \frac{y}{d}) \rho = \frac{4}{\pi} \omega_e^2 C_l \delta \varphi(t) \end{cases} \quad (1)$$

This work is an attempt to estimate the threshold amplitude of the AC input signal, exceeding which results in self-induced mechanical oscillations.

- 
- [1] D. J. Bergman, M. I. Stockman, Surface Plasmon Amplification by Stimulated Emission of Radiation: Quantum Generation of Coherent Surface Plasmons in Nanosystems, *Phys. Rev. Lett.* 90 027402 (2003)
  - [2] D. V. Guzato, V. V. Klimov, Radiative decay engineering by triaxial nanoellipsoids, *Chem. Phys. Lett.* 412 341 (2005).
  - [3] M. I. Dyakonov, M. S. Shur, Shallow water analogy for a ballistic field effect transistor: New mechanism of plasma wave generation by dc current, *Phys. Rev. Lett.* 71 2465 (1993).
  - [4] Viacheslav Semenenko, and Victor Ryzhii, Detection of Modulated Terahertz Radiation Using Combined Plasma and Mechanical Resonances in Double-Carbon-Nanotube Device, *Applied Physics Express* 4 075101 (2011).



# INTRINSIC THERMODYNAMICS OF BENZENESULFONAMIDES BINDING TO HUMAN CARBONIC ANHYDRASES

Miglė Kišonaitė, Asta Zubrienė, Daumantas Matulis

Department of Biothermodynamics and Drug Design, Vilnius University Institute of Biotechnology, Vilnius, Lithuania

[kisonaite@ibt.lt](mailto:kisonaite@ibt.lt)

Carbonic anhydrases (CAs, EC 4.2.1.1) are ubiquitous metalloenzymes, taking part in many essential functions in human organism. CAs catalyse a simple physiological reaction: the conversion of  $\text{CO}_2$  to the bicarbonate ion and protons ( $\text{CO}_2 + \text{H}_2\text{O} \leftrightarrow \text{HCO}_3^- + \text{H}^+$ ) [1]. Humans have 12 active CA isoforms widespread in many tissues and organs. Their activity and distribution in cells are different. Many of the CA isozymes are important therapeutic targets to treat a range of disorders including glaucoma, obesity, epilepsy and cancer [2]. A well-known class of CA inhibitors is sulfonamides. Although, a wide range of sulfonamide inhibitors have been developed, most of them lack selectivity to different CA isozymes. Today there are at least 30 inhibitors used in the biomedical applications, however none of them is selective for specific isozyme. That is why searching for novel specific inhibitors of human CA is an attractive strategy to create new pharmacological tools. The structure – activity relationships (SAR) of designed inhibitors require detailed thermodynamic characterization of the binding reaction [3]. Only intrinsic parameters could be used in the rational design and SAR of the novel inhibitors.

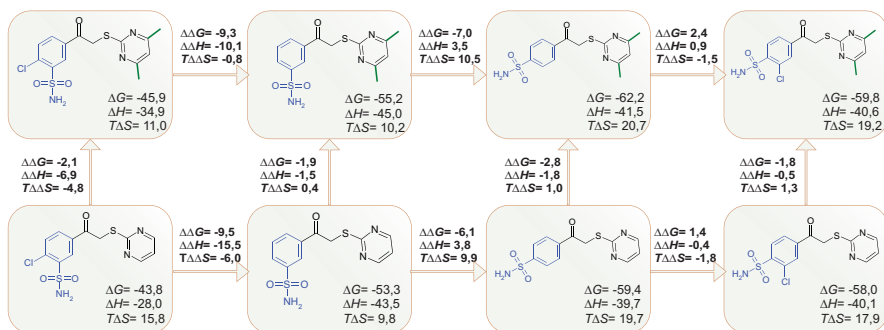


Fig. 1. Intrinsic parameters of inhibitor binding to CA I.

Intrinsic binding parameters for [(2-pyrimidinylthio)acetyl]benzenesulfonamides binding to recombinant human CA I, CA II, CA VII, CA XII, CA XIII isozymes were determined. Gibbs free energy, enthalpy and entropy were measured using thermal shift assay (TSA) and isothermal titration calorimetry (ITC). Determination of the inhibitor binding thermodynamics enables correct analysis of SAR and rational design of novel CA inhibitors.

- [1] V. Alterio, A. Di Fiore, K. D'Ambrosio, C. T. Supuran, G. De Simone, Multiple binding modes of inhibitors to carbonic anhydrases: how to design specific drugs targeting 15 different isoforms? *Chem Rev*, 112(8):4421–4468 (2012).
- [2] C. T. Supuran, Carbonic anhydrases: novel therapeutic applications for inhibitors and activators, *Nature Reviews*, 7, 168-181 (2008).
- [3] L. Baranauskienė, D. Matulis, Intrinsic thermodynamics of ethoxzolamide inhibitor binding to human carbonic anhydrase XIII, *BMC Biophysics*, 5:12 (2012).

## INTELLIGENT STREET LIGHTING

Lukas Matijošaitis<sup>1</sup>, Laurynas Dabašinskas<sup>1</sup>, Arūnas Tuzikas<sup>1</sup>

<sup>1</sup> Institute of Applied Research, Vilnius University, Lithuania  
[lukas.matijosaitis@ff.stud.vu.lt](mailto:lukas.matijosaitis@ff.stud.vu.lt)

It is known since the early examinations of solid-state luminaires in street lighting applications that one day light-emitting diode (LED) based lamps will replace high pressure sodium (HPS) ones. Today LED based lamps does not offer significantly higher energy efficiency compared to HPS, although, solid-state light sources has unique properties, such as instantaneous and efficient dimming, improved flux directionality and variable spectral power distribution. Also intelligent control can be adapted using pedestrian movement detection, light sensors and weather monitoring, since wet or snowy surfaces are up to three times more luminous than dry ones [1]. These are the key features highly increasing solid-state street lighting energy savings today.

Although solid-state street lighting and dynamic control realization would require huge investment to new data and power lines infrastructures. We offer autonomous intelligent street lighting controller which does not require any infrastructure modifications.

Controller has inputs for external movement sensors, up to four independent outputs for luminaire intensity control and programmable calendar for custom date and time dependent street illumination.

Module is compatible with internal luminaire DC power source. Controller does not require constant power source or synchronization since global positioning system's (GPS) receiver is used for automatic and exact time synchronization from satellites.

Module's settings are configured via custom made JAVA based user interface. Using this software time and date dependent street lighting protocols are configured. There is ability to set different lighting regimes for every day of the week separately and additionally up to 20 custom holidays. Each day can be programmed up to four different light intensity modes. When all required data is uploaded controller can work autonomously.

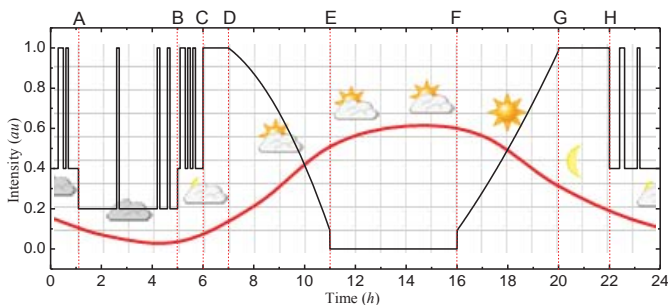


Fig. 1. Solid-state luminaire's twenty-four hour light intensity cycle (thin line) and road illumination from natural sources (thick line) graphs.

One day module's work cycle is depicted in figure 1. In example from A to B constant illumination level is set to 20%. Spikes in intensity chart shows triggered movement detectors. From D to E constant surface illumination level is maintained with respect to road luminance measurement.

By employing intelligent street lighting module it is expected to achieve up to five times reduced total energy consumption for streets illumination.

[1] L. Guo, "Intelligent road lighting control systems experiences, measurements, and lighting control strategies", PhD Dissertation, Helsinki University of Technology (2008).

## CHARACTERIZATION OF THE CELLS ISOLATED FROM HUMAN ARTICULAR CARTILAGE

Virginija Plungytė<sup>1</sup>, Aušra Ungurytė<sup>2</sup>

State Research Institute, Center for Innovative Medicine, Lithuania

*[Virginija.plungyte@gf.stud.vu.lt](mailto:Virginija.plungyte@gf.stud.vu.lt)*

Human articular cartilage covers the joints between bones and contains no blood vessels, lymphatic vessels, or nerve fibers. It is composed of only one specialized cell type, the chondrocytes which produce and maintain the extracellular matrix of cartilage, i.e. collagen and proteoglycans. Due to the lack of chondroprogenitor cells and poor regenerative capabilities of chondrocytes the articular cartilage is hard to repair. The most common procedure is the replacement of damaged cartilage chirurgically, but the procedure is very invasive and difficult. Therefore intensive research is carried out in tissue engineering for cartilage repair. One of them is using cells isolated from human cartilage. It was shown by Diaz-Romero et al. <sup>1</sup> that cells isolated from human articular cartilage and cultivated in monolayer undergo changes in phenotype and gene expression known as "dedifferentiation." The expression of surface markers of MSC suggested that dedifferentiation leads to reversion to a primitive phenotype (MSC - Mesenchymal stromal cells). Still there is too little information about cells isolated from human cartilage.

The aim of our study was to isolate cells from human articular cartilage and sort them into two populations of cells: ALDH positive and ALDH negative; then determine their potential of adipogenic and osteogenic differentiation. ALDH (aldehyde dehydrogenase) activity is one hallmark of human bone marrow (BM) umbilical cord blood (UCB) and peripheral blood (PB) primitive progenitors presenting high reconstitution capacities *in vivo* <sup>2</sup>. But it has not yet been studied in cells isolated from human cartilage.

We isolated cells by enzymatic digestion of cartilage samples and cultivated them in monolayer for 2-4 weeks. Then cells were sorted according to the expression of ALDH using fluorescence-activated cell sorting (FACS) and cultivated in monolayer until they reached confluence. The differentiation to adipocyte and osteogenic lineages proceeds for 21 d. And we are still in the process of determining the differentiation potential of sorted cells.

---

<sup>1</sup> Diaz-Romero J, Gaillard JP, Grogan SP, Dobrila N, Trub T, Varlet PM. Immunophenotypic analysis of human articular chondrocytes: changes in surface markers associated with cell expansion in monolayer culture. *J. Cell. Physiol.* 2005; 202:731–742.

<sup>2</sup> Vauchez K, Moarolleau J, Schmid M, Khattar P, Chapel A, Caterlain C, Lecourt S, Larghero J, Fiszman M, Vilquin J. Aldehyde Dehydrogenase Activity Identifies a Population of Human Skeletal Muscle Cells With High Myogenic Capacities. *Mol Ther.* 2009;17(11):1948-58

## PATTERN RECOGNITION IN SYNERGETIC COMPUTER

Igor Sivak, George Krylov

Belarusian State University, Republic of Belarus  
sidsivak@gmail.com

Generally the image may be separated into differential characteristics and details and put the symbol  $q_i$  in accordance to each characteristic. Under such approach the vector of the image  $q = (q_1, q_2, \dots, q_n)$  will correspond to the whole image (figure 1). It is clear that instead of the vector it can be examined his end – the point in the multidimensional space. Therefore, to each image we put a vector or point. In Figure 1 the ends of the vectors indicate the image of the prototype, while the points located in the vicinity of the ends are slightly different from the prototype and still have similarities to him.

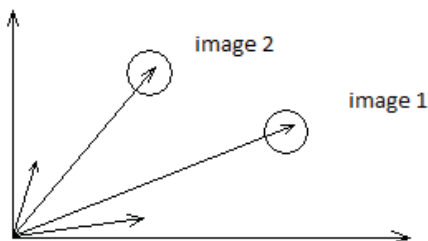


Fig. 1. Visualization space characteristics.

As our programme operates with quite primitive images, it is quite sufficient to present the image as a vector, which elements are 0 and 1 (0 – uncolored pixel, 1 – colored pixel).

Under the same pattern the vector of recognition image is built.

$$\dot{q} = \sum_k \lambda_k v_k (v_k^+ q) - B \sum_{k' \neq k} (v_k^+ q)^2 (v_k^+ q) v_{k'} - C(q^+ q) q + F(t) \quad (1)$$

[1] Haken H. Synergetic Computers and Cognition a Top-Down Approach the Neutral Nets. – Berlin, 1991

[2] Haken H. Secrets of perception: synergy as the key to the brain. - Mir, 2002

[3] LD Landau, EM Lifshitz Statistical Physics, 3rd ed., Part 1. - Moscow: Nauka, 1976

## SMART SOLID-STATE LIGHTING WITH AN OPTIMAL COLOUR SATURATION AND MINIMAL PHOTOCHEMICAL DAMAGE

Justas Trimailovas, Andrius Petrušis

Institute of Applied Research, Vilnius University, LT-10222 Vilnius, Lithuania

[j.trimailovas@gmail.com](mailto:j.trimailovas@gmail.com)

Coloured objects suffer from the light damage during exposure [1]. We trace that paper becomes yellowish, photographs lose their true colour and become dull, printed documents lose their contrast and could be hardly readable after prolonged exposition to the light [2]. Chromacity coordinates measurements show that aged and damaged inkjet colour print examples become a lot whiter and duller in colour. By incorporating light source composed of 623 nm red (R), 597 nm pc amber (A), 523 nm green (G) and 455 nm royal blue (B) light emitting diodes (LEDs) we are able to change various lighting parameters, such as colour rendering, correlated colour temperature (CCT), intensity [3] and make a suitable light source for a gamut and white point corrections.

Direct-emission LEDs usually have a very narrow spectrum (15-40 nm width at half maximum). As the band of LED spectrum becomes narrower, the colour saturation index (CSI) increases greatly [3]. Multicolour RAGB cluster helps to shift illuminated object colour coordinates to the saturated or dulled values and increase CCT. Practical example is shown (fig. 1) with 6500 K RGB cluster compared to a common 2950 K halogen lamp.

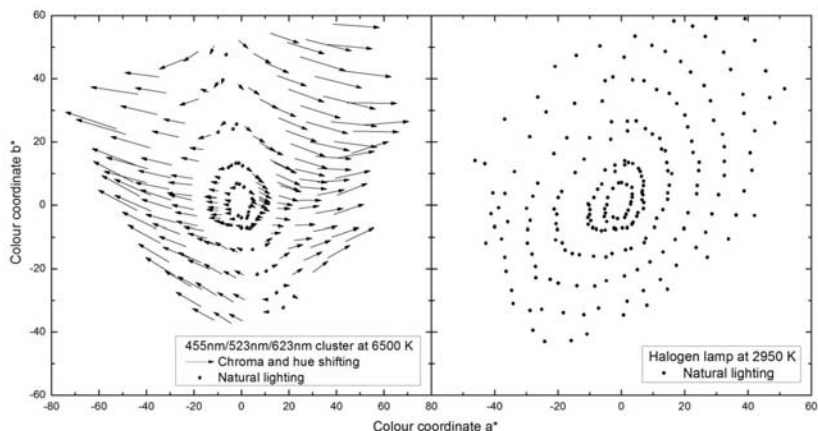


Fig. 1. CIELAB a\* and b\* colour coordinates comparing 6500 K saturating LED cluster (left) with a common 2950 K halogen lamp (right).

Ability to control illuminated surfaces chromatic saturation, allows restoring damaged objects colour gamut, shifting white point to a quasi-white light with lower yellow spectral component to decrease yellowish colours appearance. While changing spectral power distribution composition, photochemical damage index (DI) (1) is calculated and optimized to keep the lowest DI for the selected scene:

$$DI = \frac{\int_{300}^{780} \exp(-b(\lambda - 300)) S(\lambda) d\lambda}{\int_{380}^{780} V(\lambda) S(\lambda) d\lambda}, \quad (1)$$

Here  $b$  depends on an illuminated material. Solid-state lighting technology with multicolour LED clusters present a perfect light source with adjustable lighting parameters for the sensitive illuminated objects.

[1] A. Venosa, D. Burge, D. Nishimura, Effect of Light on Modern Digital Prints, Studies in conservation 56, 267-280, 2011.

[2] F. Viénot, G. Coron, B. Lavédrine, LEDs as a tool to enhance faded colours of museums artefacts, Journal of Cultural Heritage 12, 431-440, 2011.

[3] A. Žukauskas, R. Vaitiekus, M. Shur, Solid-state lamps with optimized colour saturation ability, Optics Express 2295, 2010.

## PHYTOPLASMA INFECTION IN CURONIAN SPIT

Indrė Urbonaitė<sup>1</sup>

<sup>1</sup> Phytoviruses laboratory, Nature Research Centre, Akademijos str. 2, LT-08412, Vilnius, Lithuania  
[indre.urbonaite@gf.stud.vu.lt](mailto:indre.urbonaite@gf.stud.vu.lt)

Phytoplasmas are unculturable plant pathogenic bacteria responsible for yellowing diseases. These microorganisms inhabit plant phloem tissue and are transmitted from one plant to another by phloem sap feeding insects. The pathogenic bacteria causes disbalance of plant metabolites and phytohormones, causing these symptoms in angiosperms: yellowing, plant stunting, little leaf, proliferation, witches'-broom, phyllody, virescence. To this day, studies have focused on angiosperms, but data concerning gymnosperms is lacking. Phytoplasma infection symptoms in gymnosperms include yellowing symptoms and prolific branching of small shoots, dwarfed needles. Phytoplasmas are associated with diseases in about a thousand plant species, causing economic losses worldwide.

Curonian Spit is an unique landscape that is included in UNESCO world heritage list. The sand dunes are under constant threat of wind and tide, it is only by continuing reforestation and stabilization efforts, Curonian Spit erosion is kept at bay.

In this study, samples from Curonian Spit pine trees that were showing symptoms were examined using molecular methods. DNA was extracted and 16S rRNA gene was amplified using PCR and nested-PCR reactions. PCR products were checked during gel electrophoresis and phytoplasma infection was confirmed. Aquired products were digested with specific restriction endonucleases to identify phytoplasma 16Sr XXI group. We are currently under the investigation if this particular phytoplasma belongs to „*Candidatus phytoplasma pini*“ species.

# MODELING OF THE ABSORPTION SPECTRUM OF PHOTOSYNTHETIC LH2 COMPLEX BASED ON THE ALTERNATIVE CRYSTAL STRUCTURE

Valdas Eimontas, Olga Rancova

Department of Theoretical Physics, Physics faculty, Vilnius University

Valdas.Eimontas@ff.stud.vu.lt

Photosynthesis is Nature's most efficient way to obtain energy from distant light sources so it is of high importance to perform research in this field in order to make use of it in energy production. The peripheral light harvesting complex (LH2) which is under investigation is part of *purple bacteria Rhodoblastus acidophilus* strain 10050, which is capable of producing energy through photosynthesis. The structure of this complex was found using different methods of crystallization [1,2].

The main objective of this work is to compare the properties of spectra, depending on the way the structure of a light harvesting complex was obtained. The structure used in this work was obtained through a crystallization method called *in meso* [2]. Unfortunately, applying X-ray diffraction on crystallized considerably large molecular complexes some information about the complex is lost and the position of hydrogen atoms is not even found. Therefore crucial data about the electrostatic environment within this photosynthetic complex is gone and has to be modeled additionally.

The spectral properties of photosynthetic complexes are calculated using Frenkel exciton approximation. The properties of this complex are defined through Frenkel exciton Hamiltonian in pigment excitation representation [3]:

$$\hat{H} = \sum_m E_m \hat{B}_m^\dagger \hat{B}_m + \sum_{m,n} V_{mn} \hat{B}_m^\dagger \hat{B}_n \quad (1)$$

Where  $E_m$  denotes site energies of the pigments,  $V_{mn}$  – excitonic coupling between pigments. Since the photosynthetic complex is ~9000 atoms excluding hydrogen, only approximate methods can be used to evaluate the elements of the Hamiltonian (1).  $E_m$  is calculated using CDC method and  $V_{mn}$  using TrEsp method [4]. Charge layout for this modeling is adapted from [5], where properties of the same LH2 complex are found based on another structural file[1].

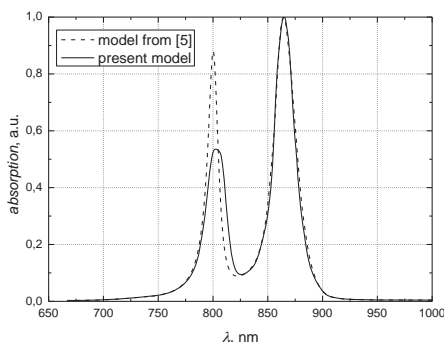


Fig. 1. Simulated absorption spectra of LH2 complex.

As seen in fig. 1, the exactly same model applied to different structural files gives somewhat different absorption spectra. In this research we look for the reasons of this mismatch investigating the differences in two structural files. In this way we try to clarify the structure-function relationship within photosynthetic pigment protein complexes.

- 
- [1] Papiz, M.; Prince, S.; Howard, T.; Cogdell, R.; Isaacs, N.; The Structure and Thermal Motion of the B800–850 LH2 Complex from *Rps. acidophila* at 2.0 Å Resolution and 100 K: New Structural Features and Functionally Relevant Motions, *J. Mol. Biol.*, **326**, 1523–1538 (2003).  
 [2] Cherezov, V.; Clogston, J.; Papiz, M. Z.; Caffrey, M.; Room To Move: Crystallizing Membrane Proteins In Swollen Lipidic Mesophases, *J. Mol. Biol.*, **357**, 1605–1618 (2006).  
 [3] van Amerongen, H.; Valkunas, L.; van Grondelle, R. *Photosynthetic Excitons*; (World Scientific: Singapore, New Jersey, London, Hong Kong, 2006); p 590; Abramavicius, D.; Palmieri, B.; Voronine, D. V.; Sānda, F.; Mukamel, S.; Coherent Multidimensional Optical Spectroscopy of Excitons in Molecular Aggregates: Quasiparticle versus Supermolecule Perspectives, *J. Chem Rev.*, **109**, 2350–2408 (2009).  
 [4] Renger, T., Theory Of Excitation Energy Transfer: From Structure To Function, *Photosynth. Res.*, **102**, 471–485 (2009).  
 [5] Rancova, O.; Sulskus, J.; Abramavicius, D., Insight into the Structure of Photosynthetic LH2 Aggregate from Spectroscopy Simulations, *J. Phys. Chem. B*, **116**, 7803–7814 (2012).

## INVESTIGATION OF PHOTO-EXCITATION PROCESSES IN ORGANIC COMPLEXES WITH IRIIDIUM USING QUANTUM CHEMICAL METHODS

Vadim Gerasimov<sup>1</sup>, Juozas Šulskus<sup>1</sup>, Stepas Toliautas<sup>1</sup>

<sup>1</sup> Department of Theoretical Physics, Physics Faculty, Vilnius University, Lithuania

[Vadim.Gerasimov@ff.stud.vu.lt](mailto:Vadim.Gerasimov@ff.stud.vu.lt)

One of the problems in creating light emitting diodes (LED) is optimizing their colour properties. Based upon that, organic molecules with heavy metals are used as LED's active material. This particular work is about theoretically investigating the structural and spectral properties of such a molecule – (acetylacetonate)bis(2-phenylbenzo[d]thiazole) with iridium (see Fig. 1) – and its constituents.

The goal of this work is to investigate the dependence of the properties of a (pbt)<sub>2</sub>Ir(acac) complex on the basis function set and on the method of calculation. The work was performed using computational chemistry methods. One of the methods used was the Model Core Potential with large basis function set. Assortment of Density Function Theory functionals was used in calculations as well. All of it was executed on a computation cluster at Physics Faculty of Vilnius University [1]. The results were compared to the earlier theoretical studies and completed experiments.

The results yield that the molecule has three stable conformers. Optimized geometric parameters of the singlet ground state (S0) and lowest triplet state (T1) differ only by a minute amount for the most stable structures. The compared functionals show that it is better to use the B3LYP functional for absorption spectra calculations. Estimated phosphorescence wavelength differs from the experimental results, but may be accepted as the fringe wavelength. Compiled bundles of results of the excited states using S0 and T1 geometries show that the excited states rearrange at different minima (see Fig. 2).



Fig. 1 (acetylacetonate)bis(2-phenylbenzo[d]thiazole) with iridium

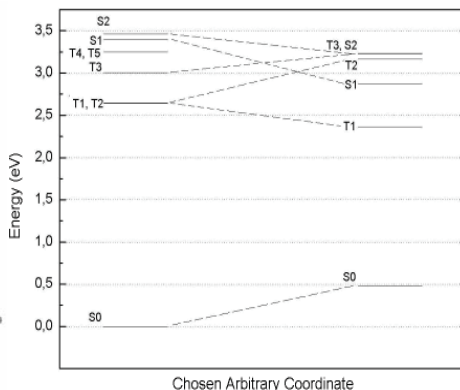


Fig. 2 Energy levels at S0 and T1 equilibrium geometries

In order to fully explain the results shown in Fig. 2 and to gain an insight on how the molecule's emitting mechanism really works deeper research of the competing transition processes (involving higher electronic states) is needed.

[1] <http://supercomputing.ff.vu.lt>



# 1/f noise with double power law from nonlinear stochastic differential equations

Rytis Kazakevičius<sup>1</sup>, Bronislovas Kaulakys<sup>1</sup>

<sup>1</sup>Institute of Theoretical Physics and Astronomy, Vilnius University, Lithuania

[Rytis.Kazakevicius@ff.stud.vu.lt](mailto:Rytis.Kazakevicius@ff.stud.vu.lt)

One of the principal statistical features characterizing the activity in financial markets is the distribution of fluctuations of market indicators such as the indexes. Frequently heavy-tailed long-range distributions with characteristic power-law exponents are observable. Power laws appear for relevant financial fluctuations, such as fluctuations of number of trades, trading volume and price. The well-identified stylized fact is the so-called inverse cubic power-law of the cumulative distributions, which is relevant to the developed stock markets, to the commodity one, as well as to the most traded currency exchange rates. The exponents that characterize these power laws are similar for different types and sizes of markets, for different market trends and even for different countries – suggesting that a generic theoretical basis may inspire these phenomena [1, 2].

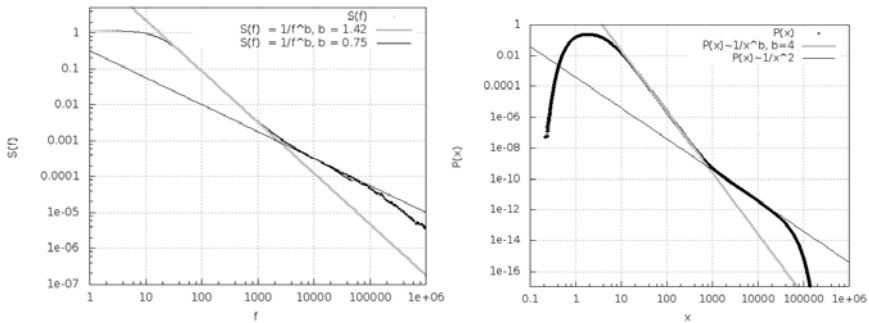


Fig. 1. Power spectral density  $S(f)$  (left) and steady-state distribution of the intensity of the process  $P(x)$  (right). Parameters  $x_{min} = 1$ ,  $x_{max} = 10^5$ ,  $x_0 = 5$ ,  $x_c = 1000$ .

The empirical data of trading activity for 26 stocks traded on NYSE was modeled by point process model as the Poissonian-like stochastic sequence with slowly diffusing mean rate. The proposed scaled stochastic differential equation provides the universal description of the trading activities with the same parameters applicable for all stocks [3]. In proposed model the fractured power-law distribution of spectral density with two different exponents  $\beta_1$  and  $\beta_2$  arise.

Starting from the concept of the point processes we proposed process driven by the nonlinear stochastic differential equation Eq. (1). This may serve as a possible model of the flow of points or events in the physical, biological and social systems when their statistics exhibit power-law scaling.

$$dx = \left\{ \left[ 1 - \exp \left( - \left( \frac{x}{x_c} \right)^2 \right) \right] (x_0 + x)^3 + \left( \frac{x_0^4 x_{min}^2}{x^3} - \frac{x^5}{x_{max}^2} \right) \right\} dt + (x_0 + x)^2 dW. \quad (1)$$

Here  $x(t)$  is a signal (flow of events) and  $W(t)$  is a standard Wiener process. Signal value is restricted in interval  $x \in [x_{min}, x_{max}]$ . Parameters  $x_0$ ,  $x_c$  characterize steady-state distribution of the intensity of the process  $P(x)$ .

Numerically calculated power spectral density and steady-state distribution of the intensity of the process  $x(t)$  are plotted in Fig. 1. Signal intensity is distributed by  $q$ -exponential distribution, when  $x \in [x_{min}, x_c]$ . If signal intensity varies between  $x_0$  and  $x_c$ ,  $P(x) \sim 1/x^4$ , when  $x \in [x_c, x_{max}]$ ,  $P(x) \sim 1/x^2$ . Power spectral density is inverse proportional to frequency  $f$  in power of  $\beta$  ( $S(f) \sim 1/f^\beta$ ). There are observable two different exponents  $\beta_1 = 1.42$  and  $\beta_2 = 0.75$  like in empirical data. Eq. (1) generates  $1/f^\beta$  noise with  $q$ -exponential distribution (also  $q$ -Gaussian distribution is possible) and double power law.

- [1] V. E. Plerou, P. Gopikrishnan, L. Amaral, X. Gabaix and E. Stanley, Economic fluctuations and anomalous diffusion, Phys. Rev. E **62** R3023 (2000).
- [2] S. Solomon, P. Richmond, Power Laws of Wealth, Market Order Volumes and Market Returns Physica A **299** (1-2) **188** (2001).
- [3] V. Gontis, B. Kaulakys, and J. Ruseckas, Trading activity as driven Poisson process: Comparison with empirical data, Physica A **387** (15), p. 3891 (2008).

# REVISED IDENTIFICATION OF THE AUTOIONIZING STATES OF RUBIDIUM ATOM

Gintaras Kerevičius<sup>1</sup>

<sup>1</sup>Department of Theoretical Physics, Faculty of Physics, Vilnius University, Saulėtekio Ave. 9, LT-10222, Vilnius, Lithuania

[gintaras.kerevicius@ff.stud.vu.lt](mailto:gintaras.kerevicius@ff.stud.vu.lt)

The autoionizing states of doubly excited Rb atom were observed and their energy spectra measured in [1, 2]. In [1] the experimental spectra were registered at 75° polar angle with respect to the incident beam of electrons of 27 and 400 eV kinetic energy. This spectra are not fully identified until now. Theoretical studies of these states were made in [2, 3, 4]. So far, the most reliable published identification was made in paper [2]. More accurate attempts to identify this spectra are made in paper [4], where the first attempts to reliably identify the autoionizing states of doubly excited Rb were made by taking into account the asymmetry of the angular distribution of Auger electrons ejected from these states with respect to the incident beam of electrons. In the case of the spectra measured at various polar angles with respect to the incident beam of electrons of various kinetic energies, we are able to make a more fail-safe identification. There are published spectra measured at 75° [1] and 54.7° 'magic' [2] polar angles with incident beam of electrons of 27 and 400 eV; 16.7, 18.8 and 49.4 eV energy, respectively, which is only a few. There are no known published papers, where an experimental energy spectrum of autoionizing states of Rb was measured at a fixed polar angle with respect to the incident beam of electrons of more than three different kinetic energies, or vice versa. However, having in mind that the latter experimental spectra of papers [1, 2] were measured at different polar angles, we could simulate a theoretical ejected Auger electron spectrum for fixed parameters (angle of detection and incident electron energy) and compare the relative intensities of respective spectral lines in both spectra. By taking into account the asymmetry of angular distribution, we could relate most of the experimentally measured spectral lines to the theoretically calculated ones.

For the simulation of an Auger electron intensity spectrum we need to calculate the autoionization state energy, excitation cross section, radiative and autoionization probability values. It is known that the probability of a radiative decay is much smaller than the probability of an Auger decay from the autoionizing states of doubly excited Rb atom. Therefore, ejected Auger electron spectrum intensities of respective spectral lines are proportional to the excitation cross sections. Keeping in mind all the ideas mentioned previously we can write the differential cross section of a two step ionization process, where non-polarized atoms in the ground state are excited by non-polarized incident electrons to the doubly excited states as follows [5]:

$$\frac{d\sigma(\alpha_0 J_0 \rightarrow \alpha_1 J_1 \rightarrow \alpha_2 J_2)}{d\Omega} = \frac{\sigma(\alpha_0 J_0 \rightarrow \alpha_1 J_1 \rightarrow \alpha_2 J_2)}{4\pi} \left[ 1 + \sum_{K>0, \text{even}} \beta_K P_K(\cos \theta) \right]. \quad (1)$$

Here  $\sigma(\alpha_0 J_0 \rightarrow \alpha_1 J_1 \rightarrow \alpha_2 J_2)$  is the total cross section of a two step process, where  $\alpha_0 J_0$  defines ground,  $\alpha_1 J_1$  – excited states of an atom and  $\alpha_2 J_2$  – ground state of an ion;  $P_K(\cos \theta)$  is a Legendre polynomial; the asymmetry parameter of angular distribution of Auger electrons ejected from the autoionizing states of an atom is  $\beta_K = A_K \alpha_K = A_K \cdot \text{Const}$  [6], because the Auger decay from these states of Rb atom is only possible to the ground state of Rb ion (decays to the excited states of Rb ion are energetically forbidden). This means that the angular distribution of Auger electrons ejected from the autoionizing states of Rb atom depends only on the alignment parameter  $A_K$ .

We have calculated that the asymmetry parameters  $\beta_K$  for the autoionizing states  $4p^5 n l n' l'$  LSJ weakly depend on both orbital L and spin S angular momenta, but strongly depend on the total angular momentum J. Furthermore, we have shown that the angular distribution of Auger electrons ejected from the electron impact-excited autoionizing states could depend on the energy of impacting electrons even for the states with total angular momentum  $J > 3/2$ , when the respective spectral lines are measured at the 'magic' polar angle with respect to the incident electron beam.

- 
- [1] V. Pejčev, D. Rassi, K. J. Ross and T. W. Ottley, High-resolution ejected-electron spectrum of rubidium vapour autoionising levels excited by electrons with kinetic energies in the range 27 to 400 eV, *J. Phys. B: At. Mol. Phys.* **10**, 1653–1659 (1977).
  - [2] A. Borovik, V. Roman and A. Kupliauskienė, The  $4p^6$  autoionization cross section of Rb atoms excited by low-energy electron impact, *J. Phys. B: At. Mol. Opt. Phys.* **45**, 045204 (6pp) (2012).
  - [3] S. Kaur and R. Srivastava, Excitation of the lowest autoionizing  $np^5(n+1)s^2$ ,  $^2P_{3/2,1/2}$  states of Na ( $n=2$ ), K ( $n=3$ ), Rb ( $n=4$ ) and Cs ( $n=5$ ) by electron impact, *J. Phys. B: At. Mol. Opt. Phys.* **32**, 2323–2342 (1999).
  - [4] A. Kupliauskienė and G. Kerevičius, Theoretical study of the  $4p^5 n l n' l'$  autoionizing states of Rb excited by electron impact, submitted to *Physica Scripta* (2013).
  - [5] A. Kupliauskienė and V. Tutlys, Properties of Auger electrons following excitation of polarized atoms by polarized electrons, *Nucl. Instr. Meth. Phys. Res. B* **267**, 263–265 (2009).
  - [6] A. Kupliauskienė, Fluorescence of polarized atoms excited by polarized electrons, *Nucl. Instr. Meth. Phys. Res. B* **267**, 266–269 (2009).

# AB INITIO SIMULATION OF TWO-DIMENSIONAL MOLYBDENUM DISULFIDE WITH VACANCY CLUSTERS

Olga Kozlova<sup>1</sup>

<sup>1</sup> Department of Micro- and nanoelectronics, Belarusian State University of Informatics and Radioelectronics, Belarus  
[olga.bsuir@gmail.com](mailto:olga.bsuir@gmail.com)

Two-dimensional materials are attractive for the application in nanoelectronic devices because of their extraordinary properties manifestation at the near atomic scales. Molybdenum disulfide ( $\text{MoS}_2$ ) is one of such materials. Monolayer of  $\text{MoS}_2$  (Fig. 1) has a direct band gap. Thus it can be used to construct interband tunnel FETs with lower power consumption than classical transistors. Monolayer  $\text{MoS}_2$  could also complement graphene in applications that require thin transparent semiconductors, such as optoelectronics and energy harvesting [1]. Further progress in understanding of physical phenomena at the nanoscale level may be realized by use of *ab initio* simulation [2] taking into account difficulties of experimental nanoobjects investigations.

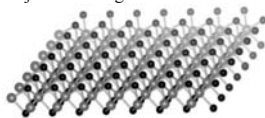


Fig. 1. Crystallographic structure of two-dimensional  $\text{MoS}_2$

This work is dedicated to the electronic and magnetic properties study of two-dimensional  $\text{MoS}_2$  structure with S- and Mo-vacancy clusters. Simulation was carried out by the means of the *ab initio* and molecular dynamics approaches realized in the program package VASP (Vienna *Ab initio* Simulation Program) [3]. The interaction between the ions and electrons in the simulated system is described by the Plane Augmented Waves (PAW) method. With the use of program package VASP it is possible to calculate the forces and stresses, which are used to relax atoms into their ground state. GGA-PBE pseudopotentials were applied for description of the interaction between the atomic cores and electrons. The calculations were performed using periodic conditions, therefore  $4 \times 4$  supercell of  $\text{MoS}_2$ , corresponding to  $12.64 \times 12.64 \text{ \AA}$ , was used to exclude the effect of vacancies on each other. In order to remove the interaction between  $\text{MoS}_2$  plates, vacuum gap of  $10 \text{ \AA}$  was inserted between them. The sampling for Brillouin zone integrations is performed using the Gamma Scheme with a regular  $4 \times 4 \times 1$  k-point grid.

The results of densities of electron states (DOS) and energy bands calculation are presented (Fig. 2). Analysis of the calculated electronic properties and their dependencies from the size and type of vacancy clusters are performed.

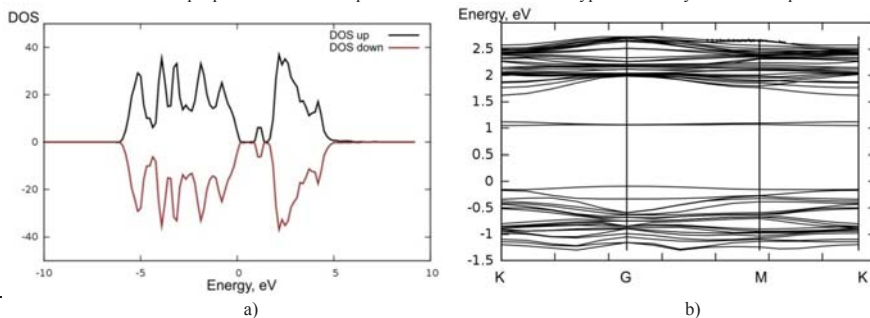


Fig. 2. DOS (a) and energy bands (b) of two-dimensional  $\text{MoS}_2$  structure with two S-vacancy clusters

Analysis of the DOS and energy band calculations of the studied structures shows the appearance of additional energy levels in the band gap, which can be used as trap levels in laser technology. However, it's worth noting a slight change of the band gap value from  $1.71 \text{ eV}$  (perfect two-dimensional structure) to  $1.64 \text{ eV}$  with increasing S-vacancy cluster. While the Mo- vacancy cluster increase causes a sharp narrowing of the band gap to  $0.11 \text{ eV}$  and increasing of the magnetic moment value from  $0.0008 \mu\text{B}$  (perfect two-dimensional structure) to  $1.89 \mu\text{B}$ . This fact suggests the possibility of using two-dimensional  $\text{MoS}_2$  as a structural element for sensors and spintronic devices.

This work was carried out under the Governmental Scientific Research Program of Belarus, Project 1.6.06 "Functional and engineering materials, nanomaterials".

- [1] B. Radisavljevic, A. Radenovic, J. Brivio, V. Giacometti, *Single-layer  $\text{MoS}_2$  transistors*, *Nature Nanotechnology*, 2011, Vol. 6, P. 147–150.
- [2] G. Kresse, J. Joubert, *From ultrasoft pseudopotentials to the projector augmented-wave method*, *Phys. Rev. B*, 1999, Vol. 59, P. 1758–1765.
- [3] G. Kresse, *VASP the guide: tutorial*, Austria, University of Vienna, 2003, P. 94 – 104.

## Simulation of Environmental Influence on Electronic Spectra of Bacteriochlorophyll Molecules by FMO Method

Rūta Tolytė<sup>1</sup>, Juozas Šulskus<sup>1</sup>, Stepas Toliautas<sup>1</sup>

<sup>1</sup> Department of Theoretical Physics, Faculty of Physics, Vilnius University, Saulėtekio al. 9-III, LT-10222 Vilnius, Lithuania

[rutos.tolytes@gmail.com](mailto:rutos.tolytes@gmail.com)

Bacteriochlorophyll-a molecules are part of the LH2 complex. LH2 complex acts as an antenna that absorbs solar energy which is subsequently transferred to the reaction center. LH2 complex is composed of two kinds of polypeptides that form a cylinder connecting the edges of the membrane. Within this cylinder two rings of bacteriochlorophyll molecules can be found. Bacteriochlorophyll molecules are in close proximity with histidine groups from both chains of polypeptides, which affects bacteriochlorophyll group magnesium atom. Entire LH2 complex is shown in Figure 1 [1].

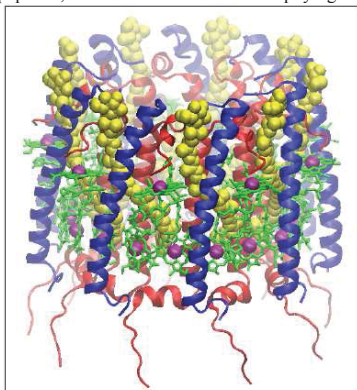


Fig. 1. LH2 complex

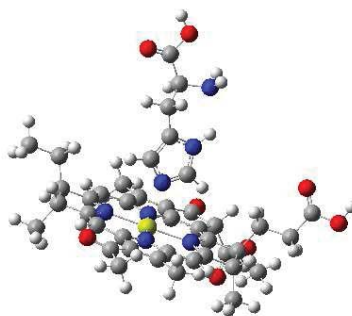


Fig. 2 Histidine and bacteriochlorophyll from LH2 complex

Histidine is one of the 20 neutral amino acids [2]. Imidazole ring of histidine chain is chemically unstable. It may have different tautomers with regard to its protonation and act as a proton donor, acceptor or proton-transfer agent. There are four different imidazole ring protonation forms (i.e. formally anionic imidazolate form).

This work is based on the interaction between bacteriochlorophyll-a and neutral histidine molecules from the LH2 complex. The structure used was taken from the LH2 complex in Protein Data Bank [3]. Bacteriochlorophyll-a (structure called bcl1601) and histidine ( $\beta$ -his30) are shown in Fig. 2. For visualization, the GaussView program was used [4].

The main goal of this study is the investigation of the influence of histidine molecules to bacteriochlorophyll spectrum. The distance between protein chains bearing histidine and bacteriochlorophyll were fixed at different distances and the geometry of remaining dimer structure was optimized. For this purpose, several methods have been used: BOP TDDFT with LC correction, TDDFT B3LYP, and FMO [5]. Gaussian and GAMESS quantum chemistry packages [6,7] of Vilnius University Physics faculty supercomputer [8] were used in this work.

It was determined that the TDDFT BOP/6-311 method with LC correction gives the electronic excitation energies closest to experimental results. Five different structures were selected by varying the distance between protein chains. It was determined that the energies and oscillator strength of the two lowest electronic excitations practically do not change during the investigated deformations. The distance between the magnesium atom of bacteriochlorophyll and the nitrogen atom of histidine in the most stable histidine-bacteriochlorophyll dimer is 2.19 Å.

The work is still expected to continue by changing the histidine tautomers and by using the FMO method in order to take into account the influence of the surrounding protein environment to BChl.

[1] <http://www.ks.uiuc.edu/Training/CaseStudies/pdfs/lh2.pdf>

[2] Protein-induced geometric constraints and charge transfer bacteriochlorophyll–histidine complexes in LH2 Piotr K. Wawrzyniak, A. Alia, Roland G. Schaap, Mattijs M. Heemskerk, Huub J. M. de Groot and Francesco Buda 10 (2008) 6971

[3] <http://www.rcsb.org/pdb/explore/explore.do?structureId=3eoj>

[4] [http://www.gaussian.com/g\\_prod/gv5.htm](http://www.gaussian.com/g_prod/gv5.htm)

[5] *The Fragment Molecular Orbitals Method: Practical Application to Large Molecular Systems*, Edited by Dmitri G. Fedorov, Kazuo Kitaura. CRC Press, Boca Raton, London, New York. 2009. 276.

[6] Schmidt M. W. et al. *J. Comp. Chem.* 1993, 14, 1347-1363.

[7] Frisch M. J. et al. *Gaussian 03, Revision D.01* (2004), Gaussian, Inc., Wallingford CT.

[8] <http://supercomputing.ft.vu.lt>

## COMPRESSION PLASMA FLOWS AS PERSPECTIVE TOOL FOR SILICON-BASED MATERIALS SYNTHESIS

Vladimir V. Uglov<sup>1</sup>, Nikolai T. Kvasov<sup>2</sup>, Raman S. Kudaktsin<sup>2\*</sup>, Yury A. Petukhou<sup>2</sup>

<sup>1</sup> Department of Physics, Belarussian State University, Belarus

<sup>2</sup> Department of Physics, Belarussian State University of Informatics and Radioelectronics, Belarus

[uglov@bsu.by](mailto:uglov@bsu.by)

Nowadays new materials are in demand in the majority of human life activities. Various new material properties are needed for ecological safety and for material usability improving. One of the methods for new material production is modification of pre-surface layers by means of chemical, heat, radiation action and high energy flows. The use of compression plasma flows is of a great interest due to high energy density and short action time.

Compression plasma flows (CPF) are flows of compressed plasma generated by means of electrical discharge in the orifice gas atmosphere [1]. During treatment vacuum camera is filled by orifice gas (nitrogen, hydrogen, helium and etc.). Sample is placed against electrodes at the distance 8-20 cm. Plasma is formed by means of gas discharge while voltage supplying (1-5 kV). This plasma flows towards the sample and is compressed by its magnetic field. Therefore this plasma is compressed. The energy density near sample varies from 3 to 30 J/cm<sup>2</sup> and action time is ~100 μs.

One of the CPF application is silicon based solar energy materials. It was discovered that compression plasma flows treatment of single-crystalline p-silicon (boron-doped) leads to the appearance of photovoltaic effect. The magnitude of free circuit voltages in this case is 150 – 300 mV. The advantages of this method in comparison with other is low vacuum requirements and short treatment time (~100 μs). The usual value of plasma modified silicon area is 1-2 cm<sup>2</sup>. This effect is observed when orifice gas is nitrogen. We suppose this effect to be connected with nitrogen penetration to the pre-surface layer and subsequent formation of n-layer because of nitrogen is donor for silicon.

Another CPF application is the use for silicide layer formation. CPF action on silicon with pre-deposited metal coating leads to pre-surface silicide layer formation up to 30 μm depth. Modification process can be divided into two stages. On the first stage silicon and coating melt and intermixing takes place. It was found that intermixing mechanism depends upon plasma energy density  $Q$  [2]. If only diffusion takes place ( $Q = 3-5$  J/cm<sup>2</sup>) structured interlayers of thickness 1 – 3 μm form (fig. 2a). If also convection takes place ( $Q > 5$  J/cm<sup>2</sup>) the layer of thickness up to 30 μm forms (fig. 2b). The second stage is rapid cooling and solidification of the melted surface layer. The one leads to constitutional supercooling and subsequent formation of silicon dendrites with metal silicide (Ti<sub>5</sub>Si<sub>3</sub>, ZrSi<sub>2</sub>, CrSi<sub>2</sub> and etc.) in interdendritic space. The tip radius of dendrites is typically 0.4 – 1 μm. The primary spacing is 0.5 – 1 μm.

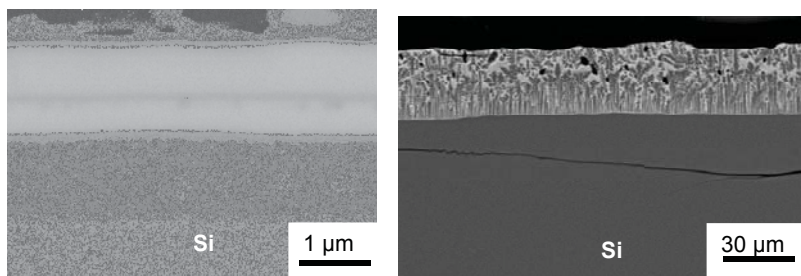


Fig. 2 The Ti-Si system treated by CPF: (a) –  $Q = 4$  J/cm<sup>2</sup>, (b) –  $Q = 8$  J/cm<sup>2</sup>

Thereby CPF is a perspective tool for formation of silicon-based photovoltaic structures and silicide layers of thickness up to 30 μm. The formed silicides CrSi<sub>2</sub> and ZrSi<sub>2</sub> are perspective materials for electronic for interconnections, Ti<sub>5</sub>Si<sub>3</sub> is of great interest as material for high temperature applications.

[1] V.V. Uglov, N.T. Kvasov et al., Structural Phase Changes in a Titanium–Silicon System Modified by High-Current Electron Beams and Compression Plasma Flows, *Journal of Surface Investigation. X-ray, Synchrotron and Neutron Techniques* **6**(2), 296–302 (2012).

[2] V.V. Uglov, R.S. Kudaktsin et al., Mass transfer in “metal layer–silicon substrate” systems under the action of compression plasma flows, *Applied Surface Science* **258**, 7377–7383 (2012).

# Index

## A

Aberfelds, Artis .....	162
Abramavičius, Darius .....	52
Abromavičius, Ignas .....	141
Adelbergytė, Karolina .....	163
Adomėnas, Povilas .....	157
Adomenienė, Ona .....	157
Aidas, Kęstutis .....	192
Albino, Marjorie .....	117
Aleknavičius, Justinas .....	109
Aleksa, Valdemaras .....	96, 100
Aleksejeva, Jelena .....	30
Algueró, M. ....	149
Amorín, H. ....	149
Andrijauskas, Tomas .....	53
Anisimovas, Egidijus .....	53, 143
Antonovaitė, Nelda .....	64
Araminaitė, Rūta .....	43
Arbačiauskienė, Eglė .....	159
Archipovaitė, Giedrė Marija .....	81
Arlauskas, Kęstutis .....	152
Armakavičius, Nerijus .....	75
Arnatkevičiūtė, Aurina .....	110
Arnold, Cord .....	66

## B

Bacevičius, Vytautas .....	97
Bajarūnas, Darius .....	111
Balakauskas, Saulius .....	142
Balčiūnas, Sergejus .....	149
Balčytis, Armandas .....	27
Balevicius, Saulius .....	146
Balevicius, Vytautas .....	37, 91, 190
Baliulytė, Laura .....	50
Baltakytė, Evelina .....	89
Banys, Jonas Povilas .....	90
Banys, Jūras .....	93, 117, 118, 136, 149, 155, 158
Barkauskas, Jurgis .....	187
Baronas, Paulius .....	150
Barre, Maud .....	148
Bedulin, Alexandr .....	185
Bellucci, Stefano .....	158
Belov, Maxim .....	49
Belovickis, Jaroslavas .....	112
Berzinš, Jonas .....	65
Bieliauskas, Aurimas .....	159
Blaževič, Dominyka .....	89
Bobić, Jelena .....	118
Boboriko, Natalia .....	36
Bogdanchuk, Kseniya .....	92
Bogush, Andrew .....	186
Bohnke, Odile .....	160

Bonifacio, Piercarlo .....	164
Borisevich, D. V. ....	91
Botyriūtė, Akvilė .....	40
Brazaitis, Andrius .....	169
Brilius, Edvinas .....	167
Brinkus, Mindaugas .....	100
Bučinskas, Kęstutis .....	93
Budriūnas, Rimantas .....	66
Bulai, Pavel .....	172
Burakevič, Marek .....	151
Buscaglia, Vincenzo .....	136
Butkus, Simas .....	19
Buzelis, Rytis .....	79, 84

## C

Cał, Dariusz .....	195
Callens, Freddy .....	125
Castro, A. ....	149
Cēbers, Andrejs .....	156
Celzard, Alain .....	158
Chაževskis, Gediminas .....	67
Cicėnas, Paulius .....	113

## Č

Čeponis, Tomas .....	113, 145
Čeponkus, Justinas .....	89, 99
Čerkauskaitė, Aušra .....	68
Čibiraitė, Dovilė .....	105
Čiučiulkaitė, Agnė .....	94

## D

Dabašinskas, Laurynas .....	198
Dakševič, Justina .....	187
Darginavičius, Julius .....	71
Daškevičienė, Marytė .....	22
Daujotis, Vytautas .....	194
Denafas, Gintaras .....	95
Dichenko, Yaroslav .....	168
Dimanta, Ilze .....	42
Dmitry, Gorbach .....	82
Dmukauskas, Mantas .....	25
Dobrovolskis, Pranciškus .....	114
Dobužinskas, Rokas .....	152
Drazdys, Ramutis .....	80, 84
Dudutis, Juozas .....	69
Dvinelis, Edgaras .....	115
Dzelme, Valters .....	106

## E

Eicher-Lorka, Olegas .....	95
Eidikas, Paulius .....	153
Eikevičius, Adomas .....	116

Eimontas, Valdas .....	203
Eljišiotė, Erika .....	95
Elksnis, Eriks .....	154
Elste, Liene .....	33
Ergin, Fahrettin Gökhan .....	156
Ērglis, Kaspars .....	156

## F

Filippenko, Volha .....	56
Franckevičius, Marius .....	73

## G

Gabalīs, Martynas .....	72
Gabrielaitis, Dainius .....	117
Gailevičius, Darius .....	70
Gajdosik, Thomas .....	54
Garancis, Valerijs .....	33
Garejev, Nail .....	71
Gaubas, Eugenijus .....	111, 113, 120, 125, 130, 145
Gečys, Paulius .....	69, 78
Gedvilas, Mindaugas .....	65
Gėgžna, Vilmantas .....	169, 182
Geļinis, Andrius .....	52
Geļinytė, Kristina .....	133
Gerasimov, Vadim .....	204
Getautis, Vytautas .....	22
Gylytė, Joana .....	39
Goldman, Nathan .....	53
Golubeva, Elena N. ....	170, 174
Gontis, Vygintas .....	57
Gražulevičius, Juozas Vidas .....	121, 150
Gražulevičiūtė, Ieva .....	72, 171
Grigalaitis, Robertas .....	93, 117, 118, 136
Grigalevičius, Saulius .....	101
Grinys, Tomas .....	189
Griškonis, Egidijus .....	95
Gulbinas, Vidmantas .....	73
Gustainytė, Aušra .....	73
Gvozdas, Eduardas .....	26

## H

Halavanau, Alex .....	49
Hliatsevich, Maryna .....	172

## I

Indrišiūnas, Simonas .....	74
Ivanov, Maksim .....	93, 149

## Y

Yantsevich, Aleksei .....	168
---------------------------	-----

Yermalovich, Anton .....196

## J

Jablonskas, Džiugas .....155

Jakovels, Dainis .....32

Jankauskaitė, Viktorija .....118

Jankauskas, Vyginas .....157

Jankūnaitė, Dalia .....95

Janonis, Vytautas .....119

Janulevičius, Gytautas .....188

Jasiūnas, Arnoldas .....120

Jazdauskaitė, Edita .....45

Jonavičius, Tomas .....17

Jonušas, Justinas .....43

Jonušauskas, Linas .....20

Josse, Michaël .....117

Jovaišaitė, J. ....121

Jóźwiak, Andrzej .....195

Juknius, Tadas .....171

Jurkevičiūtė, Aušrinė .....75

Juršėnas, Saulius .....22, 121, 129,  
150, 157, 159

Juškevičius, Kęstutis .....86

Juzeliūnas, Gediminas .....53

## K

Kadys, Arūnas .....25

Kalendra, Vidmantas .....113

Kalpakovaitė, Agnė .....189

Karabanovas, Vitalijus .....43, 46

Karaliūnas, Mindaugas .....139, 143

Karitāns, Varis .....47

Karpicz, Renata .....101

Kašalynas, Irmantas .....26, 103, 122

Kaščionis, Povilas .....96

Kaulakas, Bronislovas .....205

Kaveckytė, Vaiva .....122

Kazakevičius, Rytis .....205

Kaziulionytė, Eglė .....16

Kazlauskas, Karolis .....22, 121,  
150, 157, 159

Kazlauskas, Saulius .....147

Kazlauskas, Arūnas .....181

Kazokaitė, Justina .....173

Kerevičius, Gintaras .....206

Khrol, Helen .....190

Kičas, Simonas .....79, 80

Kinka, Martynas .....117

Kirpich, Julia .....174

Kiršanskė, Gabija .....17

Kišonaite, Migle .....197

Kitenbergs, Guntars .....156

Kleperis, Jānis .....42

Klevas, Jonas .....164

Klimavičius, Vytautas .....191

Klimienė, Irena .....171

Kolomiecias, Edgaras .....165

Komskis, Regimantas .....157

Kononovicius, Aleksejus .....57

Kovalenkovas, Deividas .....123

Kozlova, Olga .....207

Kozlovskaya, Ekaterina .....37

Kranauskaitė, Ieva .....158

Kravecov, Oleg .....124

Kreiza, Gediminas .....159

Krylov, G.G. ....76

Krylov, George .....200

Krylova, L.G. ....76

Krylova, Nina .....174, 183

Krot, Vladimir .....176

Krzyszczonik, Anna .....38

Kučikas, Vytautas .....64

Kučinskas, Arūnas .....164, 165

Kudaksin, Raman S. ....209

Kulahava, Tatsiana .....174

Kulvietis, Vytautas .....45

Kuokšis, Edmundas .....143

Kuprevičiūtė, Austė .....155

Kurtinaitis, Jaunius .....169

Kusakovskij, Jevgenij .....125

Kvasov, Nikolai T. ....209

Kviesis, Edgars .....33

## L

Lackus, Žygimantas .....97

Lange, Marta .....32

Laure, Ajja .....60

Lauwaert, Johan .....132

Lavrova, Olga .....126

Lengvinaitė, Dovilė .....192

Levchuk, Elena .....126

Lewkowski, Jarosław .....38

Lis, Tadeusz .....38

Lyvens, Karolis Manfreds .....61

Ludwig, Hans-Günther .....164

Lukševičiūtė, Viktorija .....96

Luse, Kaiva .....184

## M

Mackoit, Mažena .....127

Macutkevič, Jan .....158

Madeikis, Karolis .....128

Maglione, Mario .....117

Maigytė, Lina .....70

Majus, Donatas .....83

Makarenko, Leonid .....126

Makauskas, Benas .....88

Malevich, Alex .....37, 91, 190

Malinauskas, Mangirdas .....16, 17, 20,  
70, 87

Malinauskas, Tadas .....22, 123

Marinkevičiūtė, Agnė .....77

Marcinonytė, Raminta .....44

Markauskas, Edgaras .....78

Matijošaitis, Lukas .....198

Matukas, Jonas .....29, 105, 151

Matulionytė, Marija .....44, 179

Matulis, Daumantas .....39, 173, 197

Matusevičius, Algimantas Petras .....171

McNally, Tonny .....155

Mekys, Algirdas .....135, 144

Melnikas, Simas .....79

Merzliakovaitė, Rita .....129

Meškauskaitė, Dovilė .....130

Miasojedovas, Arūnas .....159

Michailovas, Andrejus .....18

Michailovas, Kirilas .....18

Mikolajūnas, Eimantas .....131

Mikučiūnas, Mykolas .....181

Millkus, Valdemaras .....54

Milto, Katažyna .....193

Minchenya, Vladimir .....92

Minkevičius, Linas .....29, 128

Mitoseriu, Liliana .....136

Mitrofanov, Jevgenij .....80

Muižnieks, Indriķis .....42

Muliuk, Grigorij .....132

Muravitskaya, Alina .....98

## N

Nanni, Paolo .....136

Narbutis, Donatas .....61

Narmontas, Andrius .....81

Naujalis, Paulius .....31

Naujalis, Rokas .....166

Nazarov, Sergey .....82

Nomeika, Kazimieras .....133

Novičkovas, Algirdas .....144

## P

Paipulas, Domas .....19, 67, 68

Panke, Karola .....47

Pauraitė, Julija .....175

Peckus, Martynas .....70

Perzynski, Regine .....156

Petrichenko, Oksana .....156

Petrovič, Mirjana Vijatović .....118

Petrulionis, Dalius .....160

Petrulis, Andrius .....153, 201

Petruškevičius, Raimondas .....27, 72

Pileckis, Emilis .....83

Pitsevich, George .....37, 91, 185, 186, 190

Pleshko, Nadya .....176

Plotka, Mieczysław W .....195

Plungytė, Virginija .....199

Podlipskas, Žydrūnas .....134

Porvanekas, Narūnas .....169

Poškus, Andrius .....152



Prakapavičius, Dainius .....	164
Pralgauskaitė, Sandra .....	105
Pučetaitė, Milda .....	89, 90, 104
Pulmanas, Arūnas .....	194
Puodžiūtė, Ieva .....	99
Purlys, Vytautas .....	70

## R

Ragauskas, Mantas .....	29, 151
Raišys, S. ....	121
Raišys, Steponas .....	22, 121
Ramanenka, Andrei .....	98
Rancova, Olga .....	203
Rastenienė, Loreta .....	73
Reghu, R. ....	121
Rekštytė, Sima .....	16
Rimeika, Romualdas .....	112
Rimkus, Renaldas .....	157
Rödel, Jürgen .....	93
Rotomskis, Ričardas .....	177
Rubenis, Oskars .....	33
Rumbauskas, V. ....	135
Rutkauskas, Danielis .....	31

## S

Sablinskas, Valdas .....	37, 89, 90, 91, 104, 190
Sabonis, Deividas .....	177
Sabulis, Algimantas Kostas .....	59
Sakanas, Aurimas .....	136
Sakavičius, Andrius .....	137
Saknité, Inga .....	32, 33
Samulionis, Vytautas .....	117, 155
Sapper, Eva .....	93
Serevičius, Tomas .....	157
Simachova, Olga .....	178
Sirutkaitis, Valdas .....	19, 77
Sivak, Igor .....	200
Skiriutė, Daina .....	181
Skudra, Atis .....	154
Ślepokura, Katarzyna .....	38
Slivka, Mindaugas .....	84
Smilgevičius, Valerijus .....	18, 85, 141
Smirnovas, Vytautas .....	40, 193
Songaila, Ramūnas .....	138
Spigulis, Janis .....	32, 33
Staliūnas, Kęstutis .....	70
Stalnionis, Marius .....	179
Stanislovaitytė, Paulius .....	85
Stankevičius, Mantas .....	100
Stankevičiūtė, Karolina .....	77
Stankevičiūtė, Rūta .....	35
Stasiūnas, Marius .....	139
Statkutė, Urtė .....	46
Steffen, Mathias .....	164

Stepanenko, Dmitry .....	92
Steponkevičius, Kęstutis .....	88
Stojanović, Biljana .....	118
Stonys, Darius .....	51
Stonkutė, Rima .....	166
Stramkaļs, Artūrs .....	58
Streikaite, Simona .....	101
Subačius, Andrius .....	86
Svagere, Anda .....	102
Svekla, Alina .....	140
Svirbutavičius, Ernestas .....	179
Svirskas, Šarūnas .....	155

## Š

Šačkus, Algirdas .....	159
Šetkus, Vytautas .....	85
Šimatonis, Linas .....	75
Šimkevičius, Vytautas .....	63
Šoliūnas, Martynas .....	142
Špogis, Gediminas .....	180
Šulskus, Juozas .....	204, 208
Šuminas, Rosvaldas .....	77

## T

Tamošaitytė, Sandra .....	89
Tamošiūnas, Stasys .....	167
Tamošiūnas, Vincas .....	142, 144
Tamulevičienė, Asta .....	94
Tamulevičius, Sigitas .....	72, 75, 171
Tamulevičius, Tomas .....	72, 75, 171
Tamulienė, Jelena .....	50
Tatulchenkov, Andrei .....	156
Terbetas, Gunaras .....	182
Teteris, Janis .....	30
Tikiušis, Kristupas Kazimieras .....	87
Tokarz, Paweł .....	38
Tolenis, Tomas .....	84
Toliautas, Stepas .....	204, 208
Tolytė, Rūta .....	208
Tomašiūnas, Rolandas .....	27
Tomkevičienė, Ausra .....	150
Trimailovas, Justas .....	201
Tumas, Vytautas .....	143
Tumėnas, Saulius .....	116, 138
Tumonis, Laurynas .....	103
Tuzikas, Arūnas .....	198

## U

Uglov, Vladimir V. ....	209
Ulevičius, Vidmantas .....	175
Ungurytė, Aušra .....	199
Urbanaitė, Indrė .....	202
Urbanas, Darius .....	72
Usanov, Sergei .....	168

## V

Vaišnoras, Rimas .....	73
Vaitkevičius, Augustas .....	24
Vaitkienė, Paulina .....	181
Vaitkūnas, Andrius .....	144
Vaitkus, Juozas Vidmantis .....	135, 182
Vaitkuviienė, Aurelija .....	182
Valiulytė, Indrė .....	181
Valkūnas, Leonas .....	52
Valušis, Gintaras .....	26, 29, 103, 128, 151
Varanias, Darius .....	182
Vasiliauskas, Andrius .....	94
Vasilyeu., Nikita .....	183
Velička, Arūnas .....	145
Velička, Martynas .....	104
Venckevičius, Rimvydas .....	103
Venckutė, Vilma .....	114
Vengelis, Julius .....	77
Viksna, Arturs .....	154
Virganavičius, Dainius .....	75, 171
Vizbaras, Augustinas .....	115
Vizbaras, Kristijonas .....	115
Vyšniauskas, Artūras .....	105
Voisiat, Bogdan .....	74
Vrielinck, Henk .....	125, 132

## W

Watz, Bo Beltoft .....	156
------------------------	-----

## Z

Zabillūtė, Akvilė .....	23
Začs, Laimons .....	60
Začs, Laimons .....	162
Zagórski, Piotr .....	195
Zaharans, Eriks .....	33
Zaharans, Janis .....	33
Zinge, Madara .....	106
Zubovas, Kastytis .....	59
Zubrienė, Asta .....	39, 197
Zurauskaitė, Laura .....	146
Zutere, Brigita .....	184
Zvejnieks, Rolands .....	102

## Ž

Žalga, Artūras .....	35, 188
Žeimys, Ernestas .....	88
Žemaitytė, Audronė .....	147
Žukauskaitė, Loreta .....	148
Žukauskas, Albertas .....	87
Žukauskas, Tomas .....	107



# PHAROS

## High-power Industrial Femtosecond Lasers



- 200 fs-10 ps pulse duration adjustable
- Up to 1.5 mJ pulse energy
- Single pulse to 1 MHz
- Up to 15 W average power
- Industrial, sealed design
- Compact, modular setup
- Yb based with SSLD pumping
- Complete range of harmonic converters and OPA's available



LIGHT  
CONVERSION

For more information, contact  
Light Conversion  
Sauletekio al. 10,  
LT-10223 Vilnius,  
LITHUANIA  
Tel: +370 5 2491830  
E-mail: [company@lightcon.com](mailto:company@lightcon.com)  
[www.lightcon.com](http://www.lightcon.com)

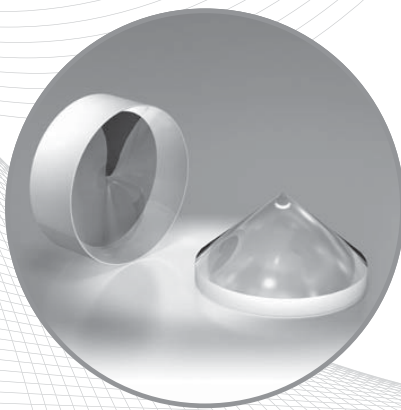
# ALTECHNA

**UAB Altechna** is a laser technology company operating in the fields of photonics and laser research since 1996.

**Altechna** is a reliable supplier of laser products: laser optics, crystals, lasers and optomechanics.

## Our products:

- ❖ Lasers and their equipment
- ❖ Spectroscopes
- ❖ CCD cameras
- ❖ Positioning systems
- ❖ Laser crystals and optics
- ❖ Other laboratory equipment



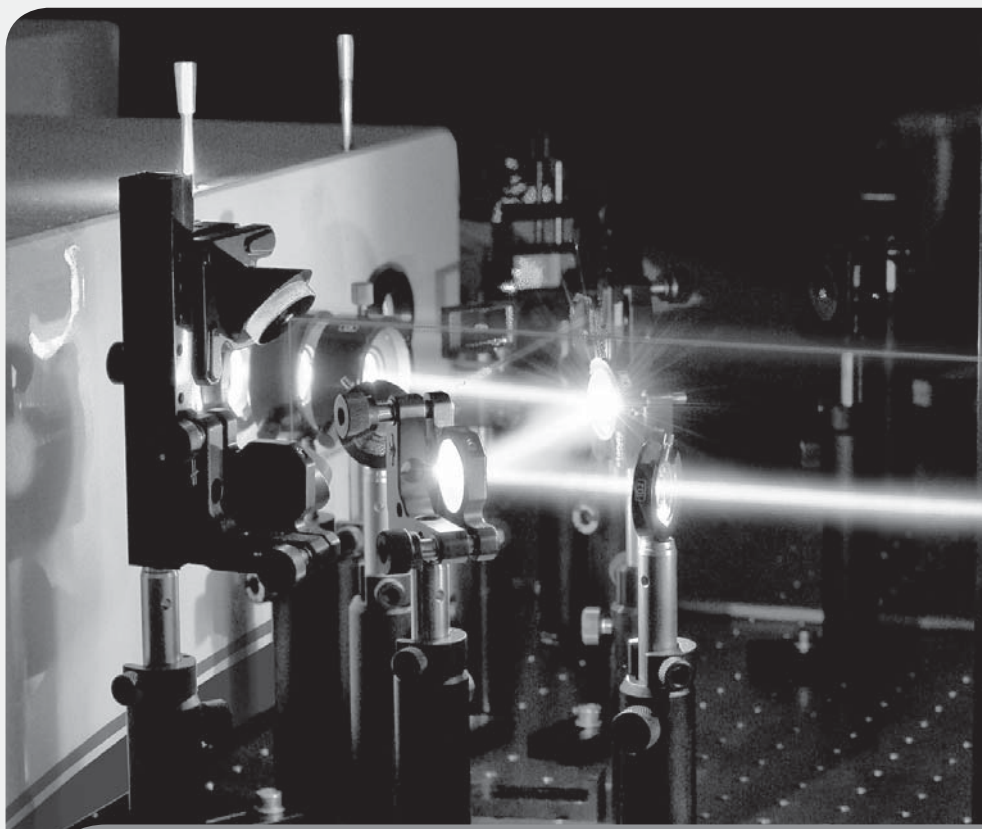
**Altechna represents:**



**UAB Altechna** • Konstitucijos ave. 23C, LT-08105 Vilnius, Lithuania  
Tel. +370 5 2725738 • Fax +370 5 2723704 • E-mail: [info@altechna.com](mailto:info@altechna.com)  
[www.altechna.com](http://www.altechna.com)



## ADVANCED LASER TECHNOLOGIES



Lasers | Laser systems | Optoelectronics

[www.ekspla.com](http://www.ekspla.com)



Ruptela is young company, which seeks to help people and organizations to manage their property effectively, while using the latest communication technologies. Our main objective is to provide high quality services. By doing this we ensure the peace of mind of our clients.

Ruptela has a professional team with strong background of communications technologies (GSM, 3G, GPS), electronics and software systems. About company

**Our vision** – Business and society, effectively managing current resources.

**Our mission** – To give an opportunity to companies and people to monitor their most valuable asset in real time.

**Our values:**

- Inovative services and products of high quality
- Responsible attitude towards customer and employee.
- Long-term and reliable partnership.

**Strategic objectives and directions of activity:**

- To continously improve quality management system;
- To foresee and set the demand of clients;
- Systemically improve the qualification of employees;
- To affirm responsibility of each employee according to duties and competence.

**Our geography:**

